



University
of Glasgow

Witte, Christian (2015) *Micromanipulation in microfluidics using optoelectronic and acoustic tweezing*. PhD thesis.

<http://theses.gla.ac.uk/6391/>

Copyright and moral rights for this thesis are retained by the author

A copy can be downloaded for personal non-commercial research or study, without prior permission or charge

This thesis cannot be reproduced or quoted extensively from without first obtaining permission in writing from the Author

The content must not be changed in any way or sold commercially in any format or medium without the formal permission of the Author

When referring to this work, full bibliographic details including the author, title, awarding institution and date of the thesis must be given

Micromanipulation in microfluidics using optoelectronic and acoustic tweezing

Christian Witte

Submitted in the fulfilment of the requirements for the
Degree of Doctor of Philosophy

School of Engineering
College of Science and Engineering
University of Glasgow

2014

Abstract

Micromanipulation platforms have gained increased attention over recent decades. They enable the handling of particles in minute samples within microfluidic compartments and demonstrate promising routes to enhance procedures in important fields such as analytical chemistry and medical diagnosis. Non-contact approaches based on externally applied force fields allow researchers to probe and alter particle states in a gentle, precise and controlled manner. Among them, especially forces generated by acoustic and electric fields received the attention of researchers developing Lab on a chip, micro total analysis and point of care systems. This is evident by the vast amount of literature dealing with physical phenomena such as dielectrophoresis and acoustophoresis applied in miniaturised systems. Each of these methods has its merits, ideally, a system that combines it all would be of great benefit for the scientific community.

The thesis introduces a concept for a unified platform that enables the use of acoustic and electric fields for particle manipulations in microfluidic environments. In particular, optoelectronic tweezing (OET), also known as light induced dielectrophoresis is fused with acoustic tweezing, also known as acoustophoresis, on a versatile system. The system can be divided into two individual physical units. The first one represents the OET unit which integrates light induced electric fields into a robust microfluidic chip. The OET chip not only operates as a device for electric field generation but also as a transverse resonator to confine acoustic fields. These fields are the result of travelling surface acoustic waves excited by a piezoelectric transducer which defines the second unit. The developed platform is applied to a range of applications such as particle trapping, transporting, focussing, sorting as well particle alterations in form of cell lysis and microbubble insonation.

Author's Declaration

I declare that, except where explicit reference is made to the contribution of others, that this dissertation is the result of my own work and has not been submitted for any other degree at the University of Glasgow or any other institution.

Acknowledgement

First of all, I want to say a special thank you to Miriam. This adventure would not have happened without you. I will be forever grateful.

The biggest thank you to my parents Erhard and Jutta, my sister, Ivonne, my brother in law, Jan, and my nephews Lip and Max, for their love and support. I miss you guys.

I would like to thank my supervisors Prof. Jonathan M. Cooper and Dr. Steven L. Neale. It was their guidance, perspective and most off all their patience that shaped the outcome of this work.

A big thank you for the effortless help, stimulating and fruitful discussion and collaboration goes to Dr. Andrew Glidle, Dr. Julien Reboud, Dr. Rab Wilson, Dr. Helen Mulvana and Dr. Norbert Klauke.

For your help, advice, support and friendship I want to thank my labmates Abeer, Yannik, Chiara, Kwang, Niall, Allan, Anoop, Shahid and the rest of the workgroup. Many thanks to the staff of the James Watt Nanofabrication centre for their steady help and support in the countless hours I spent in the cleanroom. I also want to acknowledge the James Watt Scholarship program which has generously funded three years of my life as PhD student and enabled me to attend a conference in San Francisco to present my research work.

Finally, I would like to thank Kimia and Higgs for giving me so much love, happiness and lightness. I am so grateful to have you in my life.

Publications

Christian Witte, Julien Reboud, Robert Wilson, Jonathan M. Cooper, Steven L. Neale, “Microfluidic resonant cavities enable acoustophoresis on a disposable superstrate”, 2014, *Lab Chip*, doi: 10.1039/C4LC00749B

Christian Witte, Clemens Kremer, Mayuree Chanasakulniyom, Julien Reboud, Robert Wilson, Jonathan M. Cooper, Steven L. Neale, “Spatially selecting a single cell for lysis using light induced electric fields”, 2014, *SMALL*, doi: 10.1002/smll.201400247

Clemens Kremer, Christian Witte, Steven L. Neale, Julien Reboud, Michael P. Barrett, Jonathan M. Cooper, “Shape-Dependent Optoelectronic Cell Lysis”, 2014, *Angewandte Chemie*, doi: 10.1002/anie.201307751

Christian Witte, Clemens Kremer, Jonathan M. Cooper, Steven L. Neale, “Continuous cell lysis in microfluidics through acoustic and optoelectronic tweezers”, 2013, *Proc. SPIE 8615, Microfluidics, BioMEMS, and Medical Microsystems XI*, doi: 10.1117/12.2004814

Christian Witte, Robert Wilson, Jonathan M. Cooper, Steven L. Neale, “OET meets acoustic tweezing”, 2012, *Proc. SPIE 8458, Optical Trapping and Optical Micromanipulation IX*, doi: 10.1117/12.928698

Steven L. Neale, Christian Witte, Yannyk Bourquin, Clemens Kremer, Anoop Menachery, Yi Zhang, Julien Reboud, Robert Wilson, Jonathan M. Cooper, “New optical, acoustic, and electrical diagnostics for the developing world”, 2012, *Proc. SPIE 8251, Microfluidics, BioMEMS, and Medical Microsystems X*, doi:10.1117/12.924357

Conferences

SPIE Optics + Photonics, 2012, San Diego, USA, “OET meets acoustic tweezing”, poster presentation.

Photonics West, 2013, San Francisco, USA, “Continuous cell lysis in microfluidics through acoustic and optoelectronic tweezers”, oral presentation.

Microbubble Symposium: Fabrication, Characterisation and Translational Applications, 2013, Leeds, UK, “Integrated optoelectronic tweezing and surface acoustic wave device for single microbubble investigation”, poster presentation.

Abbreviations

aSi	Amorphous silicon
AT	Acoustic tweezing
BAW	Bulk acoustic wave
CM	Clausius-Mossotti
DEP	Dielectrophoresis
IDT	Interdigitated transducer
ITO	Indium tin oxide
MB	Microbubble
MCF 7	Michigan Cancer Foundation 7, breast cancer cell line
MEMS	Microelectro-mechanical systems
OET	Optoelectronic tweezing
OT	Optical tweezer
PAR	Primary acoustic radiation
PS	Polystyrene
RBC	Red blood cell
SAR	Secondary acoustic radiation
SAW	Secondary acoustic radiation
SAW	Surface acoustic wave
SSAW	Standing surface acoustic wave

List of Figures

Figure 1-1: Schematic of the structure of an optoelectronic tweezing (OET) device. A typical device consist of transparent top and bottom indium tin oxide (ITO) coated glass electrodes while one of the electrodes (bottom) is covered with a photoconductor such as amorphous silicon (aSi). A liquid medium is sandwiched between the electrodes and contains the particles to be manipulated. A voltage is applied between the ITO electrodes and a light source such as a data projector or laser provides selective illumination of the photoconductor. In the illuminated regions a change in the conductivity of the photoconductor takes place and transfers the voltage into the liquid layer. This creates a non-uniform electric field which interacts with the particles in the liquid in the form of positive or negative dielectrophoresis (DEP).	8
Figure 1-2: OET device operation simplified as equivalent circuit model. (a) In the dark state (no illumination) an applied AC voltage signal drops mainly across the photoconductors impedance Z_p which dominates over the impedance of the liquid Z_m . (b) In the light state, the Z_p is decreased, Z_m dominates and more voltage drops across the liquid layer.	10
Figure 1-3: Positive and negative DEP of particles more and less polarisable than the surrounding medium.....	13
Figure 1-4: Real part of the Clausius-Mossotti factor as a function of frequency for a 6 μm polystyrene particle suspended in liquid medium of varying conductivity.....	15
Figure 1-5: Frequency dependent real part of the CM factor for a red blood cell (erythrocyte) suspended in 10 mS/m liquid medium.	16
Figure 1-6: Schematic of boundary conditions and subdomains used for simulations of electric field and potential distributions in the OET device.	21
Figure 1-7: 2D cross-section model (31 μm x 50 μm) of OET device with 1 μm thick aSi layer and 30 μm thick liquid medium of 5 mS/m conductivity. The photoconductor is modelled with a 5 μm virtual electrode and an AC signal of 10 V at 100 KHz is simulated for the OET device. (a) Simulated voltage distribution in the OET device. Change in the conductivity in the aSi layer by an virtual electrode reduces the voltage drop across the aSi layer in that region which in turn switches more voltage into the liquid medium. (b) Simulated switched voltage in the liquid medium along the aSi surface including the virtual electrode. (c) Magnitude of the electric field E created by virtual electrode in the liquid medium (aSi layer suppressed). (d) Streamline representing electric field lines in the liquid medium and demonstrate the non-uniformity of the field with sharp gradient close to the surface and edge of the virtual electrode. (e) X-component E_x of the electric field E . (f) Y-component E_y of the electric field E	24
Figure 1-8: (a) Square of the gradient of the electric field ∇E^2 and (b) direction of the DEP force acting on an insulating particle which is less polarisable than surrounding medium. (c) Magnified view virtual electrode and liquid interface region representing the magnitude and the direction of the DEP force. The size of the virtual electrode is 5 μm in the simulations.	25
Figure 1-9: Schematic showing one dimensional pressure standing wave created by two counter propagating pressure waves in an enclosed system.	28
Figure 1-10: Schematic showing pressure, velocity and acoustic force fields in a cavity at a resonance which supports half a wavelength of the acoustic pressure wave (fundamental frequency). The sign of the acoustic contrast factor dictates the direction of the field. A negative sign means particles move towards the pressure antinode and <i>vice versa</i> for a positive sign.	31
Figure 1-11: Secondary acoustic radiation force (Bjerknes force) becomes dominant at close particle distance. At the pressure nodal plane particles line up and create chain-like structures.....	32
Figure 1-12: Schematic showing inner and out streaming rolls (vortex flows) around the pressure node in a standing wave.....	33

Figure 1-13: (a) Schematic (adapted from ¹³¹) of longitudinal wave travelling along the bulk of a material. (b) Schematic of an acoustic tweezing concept based on BAW transducer attached to a microfluidic chip.....	35
Figure 1-14: (a) Schematic (adapted from ¹³¹) of a Rayleigh wave travelling along a solid substrate with longitudinal and transverse component (adapted from Wikipedia.org). (b) SAW transducer with interdigitated electrodes producing a SAW along the aperture with wavelength λ defined by the pitch and gap of the IDT.....	38
Figure 1-15: SAW transducer types used for microfluidic actuation. (a) Conventional SAW transducer for single frequency actuation defined by straight electrode fingers. Gap and pitch size of the IDT defines the wavelength. (b) Chirped IDT with electrode pitch and gap gradient for multiple frequency excitation along the IDT aperture. (c) Slanted IDT with changing electrode pitch and gap along the aperture for multiple frequency excitation confined by the local electrode dimensions.....	39
Figure 1-16: (a) SAW radiates energy into a liquid on the piezoelectric surface in the form of a longitudinal pressure wave. Acoustic attenuation results in acoustic streaming which drives a bulk fluid flow. (b) Standing surface acoustic wave (SSAW) produced by a pair of identical SAW transducer excited at the same frequency. A PDMS channel precisely placed relative to the pressure nodal planes enables particle manipulation by the PAR force.	40
Figure 2-1: Fabrication process for SAW device. (1) Cleaned lithium niobate wafer is spin coated with S1818 resist and softbaked for 5 min at 90°C. (2) Transfer of slanted electrode pattern by UV exposure for 4.3 s. (3) Development of exposed resist. (4) Deposition of 10 nm NiCr layer and 100 nm Au layer. (5) Metal-lift off in Acetone for 30 min to 60 min at 50°C.	51
Figure 2-2: SAW device based on slanted interdigitated electrodes deposited on a three inch lithium niobate wafer. The SAW device is designed for a bandwidth of 3.5 MHz to 5.5 MHz (Scale bar: 2 cm).	52
Figure 2-3: Fabrication process for superstrate with embedded microchannel. (1) A cleaned microscope slide was spin coated with SU8 3050 resist and placed on a 95°C hotplate (2) A cleaned cover slip with predrilled holes for outlet and inlet is immediately but carefully placed on top of the freshly prepared SU8 film and the structure is softbaked for 25 min at 95°C. (3) The mask for the microchannel is placed on the top substrate and exposed with UV for 60 s. (4) After a postexposure bake at 65°C for 2 min and at 95°C for 6 min the superstrate is developed with EC Solvent.	54
Figure 2-4: Transmission spectrum for ITO coated glass substrates (provided by Diamond Coatings Ltd, UK).....	55
Figure 2-5: (a) a 1 μm amorphous silicon layer evaporated on ITO coated glass slide and (b) cross section of substrate showing 0.3 μm ITO and 1 μm aSi layer.....	56
Figure 2-6 (a) 1.5 μm aSi layer evaporated on ITO coated slide. (b) Same substrate after standard cleaning procedure in ultrasonic bath using acetone, isopropanol and deionized water.	56
Figure 2-7: Layout of the OET chip. Overhang of each substrate for wire connections to ITO layer... 57	57
Figure 2-8: (a) OET setup based on Olympus microscope BX51 showing data projector (1), CMOS camera (2), dual port for simultaneous image projection and video recordings (3), syringe pump (4), light source (5), stage for OET chip (6), function generator (7). (b) Schematic of the optical path through the OET system.	59
Figure 2-9: Photoconductor conductivity depending on light intensity produced by different objectives (4x, 10x, 20x, 40x).....	60
Figure 3-1: Schematic of composite structure used to create OET chip.....	68
Figure 3-2: (a-c) Example SEM images showing cross-sections of microchannels fabricated using SU8 3000 series spin coated at different speeds. In detail, (a) SU8 3050, 500/1500 rpm, (b) 3050, 500/4000rpm, (c) 3025, 500/4500rpm. (d) SEM image shows magnified channel wall with a curved shape. (e) SEM image shows open microchannel section from top. The top cover slip has been removed to enable thickness measurements using the Dektak profilometer. (f)	

Example Dektak measurements showing profile along a path of an open microchannel section for samples spin coated with different SU8 versions and spin-coating speeds.	71
Figure 3-3: Samples spin coated with (a) SU8 3050 (4000 rpm) and (b) SU8 3025 (4500 rpm) showing relative homogenous thickness along substrate width.....	72
Figure 3-4: (a) Examples of fabricated composite chips with simple microfluidic channel geometries. For the OET chips, ITO and aSi electrodes overlap on the sides to provide connections for wires. (b) Microscopic image of a microfluidic channel with junction. Scale bar: 100 μm	73
Figure 3-5: Trapping of polystyrene beads (10 μm) against fluid flow for different voltages at 50 KHz in medium with conductivity of 5 mS/m and an optical power of 2 W/cm^2 . (a) Image from experiment showing beads hold against the fluid flow at virtual electrode of 45 μm width (Scale bar: 200 μm). (b) Velocity of trapped beads and imposed DEP force against voltage applied to the OET device.....	75
Figure 3-6: A 2D models simulating electric field in the OET device of 40 μm height and a 45 μm virtual electrode pattern at 50 KHz and 20 V in a 5 mS/m conductivity solution. (a) Simulation showing the gradient of the electric field squared $\log \nabla E^2 $ as surface plot where the colour bar represents the magnitude. The black arrows show the direction of the DEP force for particles less polarisable than the surrounding medium. (b) Electric field (∇E^2) distribution at different distances above the photoconductor and along the 45 μm virtual electrode pattern. (c)The field components ∇E_x^2 and ∇E_y^2 at the edge of the virtual electrode are simulated for different voltages and different distance to the aSi surface.	76
Figure 3-7: (a) Simulated voltage drop across the photoconductor for various liquid conductivities when an AC signal of 50 KHz at 20 V is applied and a light intensity of 2 W/cm^2 is used. (b) Simulated real part of the CM factor of different bead sizes as a function of liquid conductivity at 50 KHz.....	77
Figure 3-8: Trapping performance and DEP forces induced on 10 μm beads at 50 KHz (20 V) for various liquid conductivities.....	79
Figure 3-9: Simulated electric field magnitude as a function of the gap between the electrodes for a virtual electrode width of 20 μm , an AC signal of 20 V at 100 KHz and a liquid medium conductivity of 5 mS/m. (a) Logarithm of the square of the electric field gradient ∇E^2 within the first 15 μm above the illuminated (edge) aSi layer for different gap heights. (b) ∇E^2 in the centre of the channel cross section above the illuminated (edge) aSi layer for various gap heights.	80
Figure 3-10: Trapping of 6 μm beads under continuous flow at 100 KHz for different voltages in medium with 5 mS/m conductivity and light intensity of 2 W/cm^2 . (a) Image from trapping experiment showing virtual electrode and trapped beads in 15 μm high channel (Scale bar: 100 μm). (b)) Velocity of trapped beads and imposed DEP force against voltage applied to the OET device of different channel heights.....	81
Figure 3-11: Influence of the width of the virtual electrode pattern on bead trapping at 100 KHz (15 V, 5mS/m, 10x objective). (a) Images from the experiment showing 3 different electrode width and 6 μm beads trapped along the edge (Scale bar: 100 μm). (b) Results of the trapping experiments for various electrodes widths. (c) Simulated values for ∇E^2 across the height of the microchannel and above the edge of the virtual electrode. ∇E^2 is shown for various virtual electrode widths.	82
Figure 3-12: Influence of the transparency (set by imaging software) of the virtual electrode pattern (30 μm) on bead trapping at 100 KHz (10 V, 5mS/m, 10x objective). (a) Images from the experiment showing the virtual electrodes unaltered (0 %) and with increased transparency (60 %). Scale bar: 50 μm	83
Figure 3-13: Particle focussing using oblique virtual electrodes to produce a net force as the sum of DEP and Stokes drag force to align particles towards a single stream.....	85
Figure 3-14: Focussing of polystyrene beads in an OET device by oblique virtual electrodes. (a-e) Magnified view (40x objective) showing bead focussing for different electrode angles in the microchannel (Scale bar: 50 μm). (f) Stable bead focussing at different bead velocities	

dependent on the electrode angle at 100 KHz in 15 μm height channel (Beads suspended in 5 mS/m conductive medium). (g) Stable focussing at different bead velocities and for several electrode angles dependent on applied voltage.....	86
Figure 3-15: Lateral deflection of beads along the microchannel using oblique electrodes (100 KHz, 10 V, 5mS/m, Scale bar: 50 μm).....	87
Figure 3-16: Principle of size based bead separation using OET. Beads are first focused into a stream followed by a filtering step along an oblique virtual electrode. The electric field magnitude and hence the DEP force are adjusted at the particular electrode by controlling the line width or the transparency.....	88
Figure 3-17: Separations of beads of various sizes by adjusting the DEP force using virtual electrodes of certain width and transparency. (a) Guiding and Separation of 6 μm and 3 μm beads into virtual microchannels at 100 KHz, 15 V (5 mS/m, 40x objective). An oblique virtual electrode of 22 μm width imposes a larger DEP force on 6 μm particles which were deflected along the electrode while 3 μm particles pass the virtual electrode with minor deflection. Scale bar: 50 μm . (b) Focussing and separation of 6 μm and 3 μm beads using an oblique virtual electrode of reduced light intensity (25 % transparency) to reduce the DEP force imposed on the 3 μm beads (100 KHz, 10V, 5mS/m, 10x objective). Scale bar: 100 μm . (c) Guiding of 10 μm , 6 μm and 3 μm particles towards a virtual electrode with an light intensity gradient (27 %, 40 %, 70 % transparency) to achieve size based sorting into virtual microchannels (50 KHz, 16V, 5 mS/m, 10x objective). Scale bar: 100 μm	89
Figure 3-18: Time-lapse showing image sequences of a sorting experiment where smaller beads are loaded on larger beads due to mutual DEP. Scale bar is 50 μm . Red arrows point towards smaller beads which were loaded onto larger beads.	90
Figure 3-19: Electric field distribution in the presence of a particle (bead). (a) Electric field magnitude around an insulating 6 μm polystyrene bead subjected to uniform electric field (20 V, 100 KHz, 5 mS/m) when the aSi layer is not selectively illuminated (dark state). Colours in the scale bar and around the bead indicate electric field magnitude with blue being lower than red. (b) Corresponding representation of the electric field lines around the bead. For an insulating bead, the field bends around the particle. The bead is less polarisable than the surrounding medium. The results are lower field magnitudes at the poles of the bead compared to the sides. (c) The electric field distribution around the bead induces a DEP force on adjacent beads. This is called mutual DEP. The black arrows in the simulation represent the direction and magnitude of the DEP force imposed on an adjacent insulating bead. (d) The dipole within the bead induced by the electric field combined with mutual DEP leads to dipole-dipole-interactions between beads. This is also called pearl chaining because of beads lining up along the electric field lines.	91
Figure 3-20: Voltage leakage effect induces the creation of an electric field in the liquid layer. This resulted in bead-bead interaction also known as pearl chaining. Top image shows randomly distributed 6 μm beads in the OET device without illumination and electric signal applied. The middle image demonstrates the stacking effect induced by the leakage field (no illumination). The bead concentration visually decreases as the beads were parallel aligned to the electric field lines. This becomes evident when the electric signal was switched off again and fluid flow driven separation occurred which revealed a line style bead arrangement.	93
Figure 3-21: Influence of the leakage field (no illumination) on the bead distribution in the microchannel when a continuous flow was applied. (a) Distribution of 6 μm beads across the microchannel in absence of an AC signal. Voltage drop across the aSi layer in the dark state for an applied AC signal of 100 KHz at 20 V resulted in the displacement of beads towards (b) the microchannel centre and (c) the microchannel wall. The focal plane in (c) was change to improve the bead observation at the wall (Scale bar: 50 μm).....	94
Figure 3-22: The curved microchannel wall acts as a shield preventing nearby beads from being manipulated by light induced DEP. (a) Absence of the AC field where beads were distributed randomly. (b) AC signal of 20 V at 100 KHz was applied leading to sufficient guiding of 6 μm	

along the virtual electrode. However, beads close to the channel wall (c) escaped the influence of the light induced DEP force due to the shielding effect of the insulating SU8 which resulted in bead motion toward the channel wall. Here, the focus was slightly changed for enhanced bead visibility by bringing the light pattern out of focus. (Scale bar 50 μm , flow from bottom to top).... 94

Figure 4-1: Superstrate with embedded microchannel (b) SEM cross section of microchannel. (c) Superstrate placed in front of a slanted SAW device on a piezoelectric wafer. 100

Figure 4-2: Tracking of 3 μm particles over time using video analysis software Tracker. (a) Dimensions and coordinate system were calibrated and defined. Beads of interest were marked and the auto tracking function was applied to monitor the bead position once acoustic actuation was on. (b) Beads were pushed towards the pressure node. The paths of individual beads were marked and can be seen by the different colour coding. 102

Figure 4-3: Tracking of 1 μm bead in vortex flow to determine streaming velocity for different applied voltages. Software Tracker was used to mark beads of interest and monitor position over time. The red path shows the circular motion of a 1 μm bead in the vortex flow. A coordinate system (violet) and image scale (blue line) were defined beforehand. The pressure nodal plane is shown on the left hand side of the image. It contains stationary 6 μm beads which were focussed upon ultrasound activation. 103

Figure 4-4: Fluidic domain of the microchannel in the superstrate used for simple 2D model..... 105

Figure 4-5: Extended 2D model containing solid domain (SU8) surrounding the fluidic domain. 105

Figure 4-6: (a) Standing surface acoustic waves generated by a pair of identical SAW transducer exciting the same frequency. A PDMS channel is aligned and bonded with respect to the pressure landscape on the piezoelectric material. (b). Alternative concepts proposed in this study where a superstrate with embedded microchannel acts as transversal resonator. A single SAW transducer provides an ultrasound signal which is coupled into the superstrate creating standing waves upon resonance. 107

Figure 4-7: Eigenmodes of the pressure field in a simple liquid filled microchannel (green: zero, blue: negative, red: positive) as solutions to the Helmholtz equation with different boundary conditions where (a) depicts hard wall, (b) soft wall and (c) a lossy wall. 109

Figure 4-8: Eigenmodes of the pressure field in an extended 2D model including the SU8 as material surrounding the liquid filled microchannel. Eigenmodes are presented for hard wall (green: zero, blue: negative, red: positive). 110

Figure 4-9: Eigenmodes of the pressure field in an extended 2D model including SU8 layer modelled as soft boundary..... 110

Figure 4-10: Eigenmodes of the pressure field in an extended 2D model including SU8 layer modelled as lossy boundary. 111

Figure 4-11: (a) SAW device with slanted interdigitated transducer design on LiNbO₃. (b) Broadband frequency response of SAW device. (c) Infrared images of transducer when actuated in the frequency bands with lowest frequency of 3.70MHz, centre frequency of 4.55MHz and highest fundamental frequency of 5.50MHz. 113

Figure 4-12: (a) Superstrate with microchannel placed on piezoelectric wafer. The marking on the superstrate correspond to the microscopic pictures (1,2) when the SAW transducer was actuated at the resonance frequency. The first image (1) shows the start of the acoustophoretic movement of 3 μm polystyrene beads towards the pressure node. Image 2 shows a stable stream of focussed beads further down the microchannel. Scale bar 100 μm . (b) Infrared image of the SAW device when the resonance frequency of 4.138 MHz at 15 V was applied. (c) Image stack obtained from confocal microscopy showing the channel cross-section and the one-dimensional character of the standing wave. 115

Figure 4-13: Experimentally observed resonance frequencies with strong transverse mode leading to alignment of beads in the pressure nodal plane. Images taken (a) 3 s and (b-c) 2 s after activating the SAW transducer (10 V) at the particular frequency shown. (d) Acoustic actuation at 4.138 MHz and 10 V under continuous flow (Scale bar: 1 mm). (e) Coupling of the initial incident

narrow (~ 2 mm to 3 mm) SAW beam caused a wider acoustic manipulation region (~ 6 mm) along the channel length.	116
Figure 4-14: Visualisation of the surface displacements induced by a SAW on the LiNbO ₃ substrate and the bottom glass slide of the superstrate within the microchannel region after coupling of the SAW. (a) SAW excitation at the resonance frequency of the superstrate visualised by thermal imaging. (b) Displacement on the surface of the LiNbO ₃ along the SAW beam (Scale bar: 2 mm) and corresponding graph which shows the surface displacement amplitudes along the center of the SAW beam. (c) Surface displacement on the bottom substrate of the superstrate within the microchannel region (Scale bar: 1 mm). The color plots in (b) and (c) represent maximum (red), minimum (blue) and zero (green) displacements.	118
Figure 4-15: (a) Lateral displacement of 3 μm bead when SAW device was actuated with 15V at 4.138MHz (b) Calculated velocity and force based on lateral displacement of 3 μm bead using 15V at 4.138 MHz.	120
Figure 4-16: (a) Acoustic energy density determined from 3 μm bead tracking experiments using a set of voltages at 4.138 MHz. (b) Corresponding pressure amplitude.	120
Figure 4-17: (a) Focusing of differently sized beads towards the pressure node using 10 V at 4.138 MHz. Scale bar is 25 μm. (b) Lateral displacements of various beads using 10 V at 4.138 MHz and (c) corresponding PAR force.	121
Figure 4-18: Acoustic streaming in microchannel (a) Channel filled with suspension of 1 μm and 3 μm beads. (b) Acoustic actuation leading to alignment of 3 μm bead in pressure node while 1 μm beads stay mainly in bulk vortex flow. (c) Frame overlay producing streamlines to visualize 1 μm bead movement in vortex flow. Scale bar 50 μm. Frequency 4.138 MHz.	122
Figure 4-19: Example of the motion of 1 μm diameter beads in vortex flow. (a) Lateral displacement of bead over time in vortex flow when 40 V were applied (4.138 MHz) and (b) corresponding maximum bead velocity.	123
Figure 4-20: (a) Velocity of 1 μm beads depending on displacement in vortex flow (40V, 4.138 MHz). (b) Velocity of 1 μm bead for different voltages. Largest bead displacements were considered for velocity measurement (4.138 MHz).	124
Figure 4-21: Temperature increase on top of the bottom glass substrate after coupling of the SAW (4.138 MHz) with different voltages applied to the transducer. Measurements were taken with an infrared camera.	125
Figure 4-22: Reduced complexity in system assembly. (a) Superstrate can be misaligned by up to 30° without affecting the formation of the standing wave (Scale bar: 100 μm). (b) Comparison of acoustic energy density of superstrate close to SAW device and at a distance of 1 cm (10 V at 4.138 MHz).	126
Figure 4-23: Multi pressure node arrangements in the microchannel using 3 μm beads. The frequency of SAW device was tuned to several resonance points of the superstrate, where (a) 4.138 MHz, (b) 8 MHz, (c) 12.514 MHz (10 V, Scale bar 50 μm), led to varying standing wave pattern confined to the straight channel section (d-f, scale bar 250 μm, static fluid).	127
Figure 4-24: Adjustment of the SAW transducer frequency to match the resonance of different channel widths. For 280 μm channel width, the frequencies for (a) 2 and (b) 4 pressure nodal planes were found to be 4.878 MHz and 9.807 MHz, respectively (Scale bar: 100 μm). For a 350 μm channel width the frequency for (c) 2 and (d) 4 pressure nodes were 3.791 MHz and 8.301 MHz (Scale bar 100 μm).	128
Figure 4-25: Patterning of red blood cells using a single SAW device with wide frequency range. (a) 4.138 MHz, (b) 8 MHz, (c) 12.514 MHz, (d) 20.504 MHz. The transducer was actuated with 10 V. The patterning was performed without fluid flow (Scale bar: 50 μm).	129
Figure 4-26: Red blood cell patterning time versus applied voltage for different resonance frequencies.	130
Figure 4-27: Fusion of patterned cells by switching between resonance frequencies. (a) RBCs in microchannel before acoustic actuation. (b) 8 MHz were applied to create 2 pressure nodes. (c-	

g) Switch to 4.138 MHz to merge cell pattern into single pressure node. No fluid flow (Scale bar: 50 μm).	130
Figure 4-28: Fusion of patterned cells by switching between resonance frequencies. (a) RBCs in microchannel before acoustic actuation. (b) 20.514 MHz were applied to create 5 pressure nodes. (c-g) Switch to 8 MHz to merge cell pattern into two pressure nodes. No fluid flow (Scale bar: 50 μm).	131
Figure 4-29: Displacement of RBCs and trypanosomes induced by acoustic forces. (a) RBCs and trypanosomes were randomly distributed in the microchannel channel (no acoustic actuation). (b) Channel is acoustically excited (30 V) producing a standing pressure wave with single pressure node. Blood cells were pushed toward the pressure node by primary acoustic radiation force. Trypanosomes experienced a drag force induced by acoustic streaming (Scale bar: 50 μm).	132
Figure 4-30: Setup for separation of trypanosomes from a blood sample based on acoustic streaming induced displacement. (i) Sample was hydrodynamically focussed to achieve initial sample flow along the channel wall. (ii) Without acoustic actuation, the sample was leaving via outlet 1. Acoustic actuation switched the sample into the laminar stream of the buffer which resulted in the sample leaving via outlet 2. Switching time was about 300 ms for 4.138MHz and 40V. (iii) Trypanosomes and red blood cell displacement under flow in straight channel section. Flow rates are 0.2 $\mu\text{l}/\text{min}$ and 0.4 $\mu\text{l}/\text{min}$ for sample and buffer inlet, respectively.	134
Figure 4-31: (a) Separation of the parasite from a blood sample at the microfluidic junction (Scale bar: 100 μm). (b) Close up of junction showing separation of both cell types into different outlets. Arrows show positions of trypanosomes (Scale bar: 50 μm). Flow rates are 0.2 $\mu\text{l}/\text{min}$ and 0.4 $\mu\text{l}/\text{min}$ for sample and buffer inlet, respectively.	135
Figure 4-32: Separation of parasite from blood sample in straight channel using the PAR force to trap blood cells while trypanosomes subjected to acoustic streaming flow along the channel. (a) Schematic of the setup containing superstrate, SAW device and actuation area. (b) Sample acoustically focused by applying 30 V at 4.138 MHz. (c) Increased voltage (60 V) created a hot spot where blood cells aggregated and were trapped against the flow while trypanosomes followed fluid flow along the channel as well as the flow pattern of the vortex rolls. (d-g) Zoom into the trapping site which shows increasing blood cell aggregation over time. The trypanosomes pass the blood cell aggregate and get separated. Flow direction from bottom to top. Flow rate 0.4 $\mu\text{l}/\text{min}$. Scale bar: 50 μm .	136
Figure 4-33: Interference of pressure waves (fundamental and 1 st harmonic) and modulation of pressure node position by pressure amplitude control of the fundamental frequency. (a-d) The amplitude of the 1 st harmonic is constant while the pressure amplitude of the fundamental frequency increases until a pressure node in the channel centre is formed.	138
Figure 4-34: (a) Schematic showing the principle of superposition of two standing waves. In this case the fundamental frequency f_0 was superimposed to the 1 st harmonic. (b-e) Image sequence is shown starting with 1st harmonic frequency (8 MHz, 20 V where 2 pressure nodes were created and then the pressure distribution was altered by superimposing the fundamental frequency (4.138 MHz, 1 V – 25 V) which led to merging of the separated bead (3 μm) streams. Flow rate applied was 2 $\mu\text{l}/\text{min}$ (Scale bar: 100 μm).	139
Figure 4-35: Lateral displacement of bead streams aligned in two pressure nodes when 1st harmonic (8 MHz, 20V) was applied and the fundamental frequency (4.138 MHz) was superimposed. Voltage range corresponds to fundamental frequency. The displacement at 3 different positions along the stream is plotted.	139
Figure 4-36: Superposition of fundamental frequency (8 MHz, 20 V) and 1 st harmonic (4.138 MHz, 8 V) around a loose pinching region where the pressure amplitude for the 1 st harmonic is low. This led to a localised denting effect when the fundamental frequency was superimposed (Scale bar 100 μm).	140
Figure 4-37: Superposition fundamental f_0 and $f_{2\text{nd}}$ harmonic frequency for particle pre-focussing and sorting. (a) Schematic of SAW electrodes with superstrate in-between, as well as microchannel	

images at 3 positions along the channel, with (i) showing the inlet junction where a bead sample was hydrodynamically focussed using the center buffer inlet. (ii) Shows the transition from hydrodynamically to stronger acoustically focussed bead streams using a frequency of 12.514 MHz (20 V). (iii) Outlet junction and exit of bead streams via outer outlets. (b) Superstrate was actuated with two resonance frequencies to achieve superposition of standing waves (4.138 MHz, 8 V; 12.514 MHz, 20 V). Image shows separation of previously focussed 6 μm and 3 μm beads. The fundamental frequency was tuned to an amplitude which enabled the translation of 6 μm beads towards the centre pressure node. The red circle marks several 6 μm beads moving towards the centre node. (c) Image shows the situation at the outlet junction after superimposing to standing waves for bead separation. 6 μm beads exit via the centre outlet while 3 μm beads, still being focussed exit via the outer channel outlets. The applied flow rate was 3 $\mu\text{l}/\text{min}$ and 1 $\mu\text{l}/\text{min}$ for the buffer inlet and the sample inlet, respectively (Scale bars: 100 μm)...... 142

Figure 4-38. Superposition of fundamental f_0 and 2nd harmonic resonance frequency $f_{2\text{nd}}$ to suppress acoustic streaming induce particle displacement. (a) Schematic of SAW transducers showing approximated position of wave propagation into the superstrate. (b) Situation in microchannel filled with 1 μm and 3 μm diameter beads when the fundamental frequency f_0 (4.138MHz, 20 V), 2nd harmonic $f_{2\text{nd}}$ (12.514MHz, 30 V) and both f_0 and $f_{2\text{nd}}$ were applied to the transducer (Scale bar: 50 μm , static fluid). 144

Figure 4-39: Sorting of 1 μm and 3 μm beads using the principle of superimposing the 2nd harmonic frequency to suppress acoustic streaming induced displacement. (a) 2nd harmonic frequency (12.514 MHz, 20 V) was applied leading to pre-focussing of injected sample along pressure nodes close to channel wall. All beads exit chip via outlet 2. (b) Superimposing the fundamental resonance frequency (4.138MHz, 10 V) resulted in lateral movement of 3 μm beads towards the pressure node in the centre of the channel. 1 μm beads exit via outlet 2 while 3 μm beads left via outlet 1 (Scale bar: 50 μm). Flow rates for buffer and bead sample were 4.5 $\mu\text{l}/\text{min}$ and 2.1 $\mu\text{l}/\text{ml}$, respectively. (c) Bead concentration in outlet 1 and (d) outlet 2 for sorting experiment. Initial bead concentrations were 83.9 % and 16.1 % for 1 μm and 3 μm beads, respectively. The data shown in (c) and (d) was obtained from bead count analysis in a haemocytometer (see chapter 2.4.1). 145

Figure 4-40: (a) Fundamental frequency (4.138 MHz, 25V) applied to the superstrate induced alignment of blood cells in the pressure node, while the parasite underwent acoustic streaming induced vortex motion. (b) 2nd harmonic frequency (12.514 MHz, 25V) was applied, followed by the alignment of blood cells and parasites in pressure nodes. No vortex induced parasite movement was observed. Experiment conducted without external flow applied. The red arrows mark position of parasites (Scale bar: 50 μm). 146

Figure 4-41: Sorting of trypanosomes and red blood cells using the principle of superimposition. (a) 2nd harmonic frequency (12.514 MHz, 20 V) was applied leading to pre-focussing of injected sample along pressure nodes close to the channel wall. Trypanosomes and blood cells exit chip via outlet 2. Red arrows mark position of parasites. (b) Superimposing of the fundamental resonance frequency (4.138MHz, 15 V) resulted in the movement of blood cells towards the pressure node in the centre of the channel. Blood cells exit channel via outlet 2, while trypanosomes exit via outlet 1 (Scale bar: 50 μm). Flow rates for buffer and blood sample were 6 $\mu\text{l}/\text{min}$ and 3 $\mu\text{l}/\text{ml}$, respectively. (c) Cell concentrations in outlet 1 and (d) outlet 2 for sorting experiment. Initial cell concentrations were 97.2 % ($169 \cdot 10^6$ cells/ml) and 2.8 % ($4.7 \cdot 10^6$ cells/ml) for blood cells and trypanosomes, respectively. The data shown in (c) and (d) correspond to the data in table 4-1 and represents the analysis of cell counts performed in a haemocytometer after sample collection at the outlets. 147

Figure 5-1: Assembled setup on the microscope stage showing OET chip (superstrate) placed onto the piezoelectric wafer close to the SAW transducer. 151

Figure 5-2: Influence of leakage field and acoustic field on particle (3 μm beads) interaction with channel wall. (a) OET chip acoustically (8 MHz, 10 V) and electrically (100 KHz, 20V) actuated to

demonstrate dominating particle-wall interaction induced by a leakage field. (b) OET chip acoustically (8 MHz, 15 V) and electrically (100 KHz, 10V) actuated but this time tuned to the point where the PAR force overcame particle wall interactions (Scale bar: 50 μm ; flow rate: 0.5 $\mu\text{l}/\text{min}$). 153

Figure 5-3: Influence of leakage field and acoustic field on particle (3 μm beads) alignment in pressure node. (a) Acoustic actuation at fundamental frequency using 20 V. (b) Electrical signal (100 KHz, 20 V) applied to OET chip while being acoustically actuated (no illumination). The resulting leakage field promoted partially tighter bead focusing due to pearl chaining. (c) Same conditions as (b), however, some beads were repelled by electric interactions arising from tight bead stream and potentially due to secondary acoustic radiation forces in the pressure node. Red arrows mark the beads which were not able to enter the central bead stream due to an electric and acoustic barrier (Scale bar: 50 μm ; flow rate: 0.5 $\mu\text{l}/\text{min}$). 154

Figure 5-4: Deflection of particles (6 μm beads) into channel outlets using dynamic virtual electrode arrangements that deflect particles to a desired outlet (flow from bottom to top). (a) Acoustic actuation (4.138 MHz, 15 V) focused particles along the channel center followed by the particles exiting via the central outlet. (b-c) Additional application of virtual electrode (70°, 15 μm width, 50 KHz) provided dynamic particle switching into the side outlets. (Scale bar: 100 μm , solution conductivity 5mS/m, 20 x objectives). (d) Voltage needed to switch particles to side outlets when different flow rates were used. 156

Figure 5-5: Sorting different sized particles into outlets using the PAR and DEP force combined with hydrodynamic force (flow from bottom to top). Bead mixture consisting of 6 μm and 3 μm were first concentrated within a pressure node by applying the fundamental frequency (4.138MHz, 15 V) followed by tuning the size dependent DEP force (50 KHz, 16 V) to enable size selective guiding of 6 μm bead into a side outlet. (Scale bar: 100 μm , 5mS/m, 20x objective, 0.5 $\mu\text{l}/\text{min}$). 157

Figure 5-6: Acoustic sorting of 3 μm and 6 μm beads supported by virtual electrodes (flow from right to left). (a) The bead mixture was acoustically (4.138 MHz, 5 V) focused into a single pressure node in the channel center. An oblique virtual electrode (75°) was projected into the channel crossing the pressure nodal plane. (b) The activation of the electrode (15 V, 100 KHz) deflected the beads along the length of the electrode and therefore out of the pressure nodal plane. (c) Once the influence of the virtual electrode was overcome, the PAR force pushed particles back to the pressure node. The movement towards the channel center was size dependent due the PAR force scaling with the radius of the particle and lead to varying displacement times between the bead sizes. This difference was used to sort the bead mixture into virtually defined channels using (d) low (10^5 beads/ml) and (e) high (10^5 beads/ml) bead concentrations (Scale bars: 50 μm , flow rate: 0.5 $\mu\text{l}/\text{min}$, 5mS/m). 158

Figure 5-7: A 270 μm wide microchannel in an OET chip acoustically excited at the resonance frequencies of (a) 4.782 MHz and (b) 10.002 MHz (Scale bar: 50 μm). 161

Figure 5-8: A sequence of continuous bead (3 μm) manipulation using OET and acoustic tweezing. Beads focused into 4 streams by the PAR force at 10.002 MHz at 20 V followed by virtual electrode activation (100 KHz, 20 V) to partially merge two streams by deflecting beads along the edge of the electrode due to negative DEP (Scale bar: 50 μm , flow rate: 0.5 $\mu\text{l}/\text{min}$, medium conductivity: 5 ms/m, 20x objective.)..... 161

Figure 5-9: Manipulation sequence of 3 μm beads by acoustic and optoelectronic tweezing under continuous flow (flow from bottom to top). The OET chip was first acoustically actuated using the 3rd harmonic resonance frequency (10.003 MHz, 5 V) followed by activation of the virtual electrode (50 KHz, 10V) to trap particles in front of the virtual electrode (25 μm wide) within the pressure node. (a) OET off, ultrasound on. (b-d) Activated electrode led to accumulation of particles over time while being confined to the pressure node (Scale bar: 50 μm , flow rate: 0.1 $\mu\text{l}/\text{min}$, 20x objective, 5 mS/m) 162

Figure 5-10: Virtual trapping sites defined by virtual electrodes for array-like capturing of 3 μm beads focussed in pressure nodes under continuous flow (flow from bottom to top). (a) Beads flowing through the microchannel. No actuation. (b) Acoustic actuation at 3 rd harmonic resonance (15 V, 10.003 MHz), followed by (c) activation of OET (100 KHz, 20 V, 20x objective) to create trapping sites on demand (Scale bar: 50 μm , flow rate: 0.25 $\mu\text{l}/\text{min}$, 20x objective).	163
Figure 5-11: Trapping and fusion of bead aggregates along a virtual electrode (30°, 25 μm wide) under continuous flow (flow from bottom to top). (a) Acoustic actuation using the 3 rd harmonic resonance frequency (10.003 MHz, 15 V). (b) Activation of OET (17 V, 100 KHz, 20x objective) induced bead aggregation in front of the virtual electrode. (c-d) Bead aggregates released from trap after switching off acoustic actuation followed by flow induced movement along electrode which led to fusion of bead agglomerations. (e) Activation of ultrasound induced movement of fused beads back into pressure node (Scale bar: 50 μm , flow rate: 0.1 $\mu\text{l}/\text{min}$, 20x objective). 164	164
Figure 5-12: Sorting of particles into pressure node using a virtual electrode. (a) A bead mixture (3 μm and 6 μm suspended in 5 mS/m solution) was hydrodynamically focussed along one side of the channel before (b) concentrated into a pressure node created by applying the first harmonic frequency (4.782 MHz, 20V) to the OET chip with a 270 μm channel width. (c) An activated oblique virtual electrode (45°, 18 μm width, 100 KHz, 25 V, 20x objective) was used to guide 6 μm beads into the adjacent pressure node (Scale bar 50 μm , flow rate: 0.5 $\mu\text{l}/\text{min}$).	165
Figure 6-1: (a) Schematic of a cell exposed to an external electric field applied between two parallel electrodes and (b) corresponding potential along the y-axis of the cell highlighting the voltage drop across the membrane.	168
Figure 6-2: (a) SAW transducer with OET chip clamped on piezoelectric wafer for combined acoustic and electrical actuation. (b) Cross-section of OET channel chip showing sandwiched SU8 3025 between ITO/glass and aSi/ITO/glass substrates to produce a 15 μm spacer.	171
Figure 6-3: (a-b) Intensity of the electric field across a 15 μm liquid gap for short (2.5 μm) and wide (50 μm) photoconductor illuminations (20V, 25 KHz, 10 mS/m). (c) Electric field strength across a 15 μm liquid gap for different illumination lengths (25 KHz, 20 V, 10 mS/m) determined from the center of the light pattern. (d) Electric field strength versus liquid gap within the OET chip for a range of voltages when a wide field illumination (> 50 μm) is applied at 25 KHz, 10 mS/m.	174
Figure 6-4: Electric field strength versus medium conductivity for a 15 μm (black line) and 100 μm (red line) thick microchannel illuminated with a wide light pattern (25 KHz, 20V).	175
Figure 6-5: (a) Simulated potential plot (in V) of 15 μm high microchannel in the presence of a red blood cell for 20 V, 25 KHz, 10mS/m. (b) Cross section plot through the centre of a red blood cell (indicated in Figure 6-5a as dotted line) showing voltage drop of 1.7 V across the membrane (20 V, 25 KHz, 10 mS/m).	176
Figure 6-6: (a) Simulated transmembrane potential for a cell centred in a microchannel with changing vertical dimensions (Illumination pattern: 50 μm , 20 V, 25 KHz, 10 mS/m). (b) Influence of a 2.5 μm light spot and the vertical cell position on the transmembrane potential compared with a 50 μm light spot. Dotted line represents the threshold voltage for irreversible pore formation.	177
Figure 6-7: Conventional OET device made by double sided tape creating a liquid gap of about 100 μm between the electrodes. (a) Homogeneous distribution of red blood cells settled on the photoconductor (b) Light spot and a electric signal of 20 V at 25 KHz was applied. (c) Lysis was achieved after ~ 60 s of exposure to the electric field. Scale bar: 100 μm	178
Figure 6-8: Lysis of red blood cells floating above the surface. Lysis was triggered by 100 ms light pulse and an applied electrical signal of 25 KHz and 10 V in 10 mS/m conductivity buffer	178
Figure 6-9: Converting of greyscale image to binary image by threshold functions in ImageJ.	179
Figure 6-10: Example for time versus intensity plot monitored for two red blood cells after a 100 ms light pulse at 25 KHz, 20 V in 10 mS/m buffer. Sequence below graph shows lysis stages according to numbering in graph for original images and threshold image.	180
Figure 6-11: Lysis time of red blood cells for different exposure times. (a) Example pixel intensity versus time plot for 10 ms (black), 100 ms (red) and 500 ms (blue) pulse at 20 V, 25 KHz in 10	

mS/m buffer. (b) Average lysis time of red blood cells for different exposure times at 25 KHz, 20 V, 10 mS/m.....	181
Figure 6-12: Light pulse time of 10 ms and the corresponding illumination area was not homogenous over time.....	181
Figure 6-13: Lysis time of RBC for different voltages and exposure times. (a) Example pixel intensity versus time plot for 100 ms pulses with applied voltage of 5 V (black) and 20 V (red). Inset shows RBCs after 5 V, 100 ms exposure. Lysis was not complete, indicating reversible electroporation. (b) Lysis times for different applied voltages and corresponding exposure times of 10 ms (black bar), 100 ms (grey bar) 500 ms (white bar). A frequency of 25 KHz was used.	182
Figure 6-14: Change of red blood cell morphology after light pulse (25 KHz, 20 V, 10 ms pulse). Scale bar is 10 μ m.	183
Figure 6-15: (a) Sequence of induced lysis in Jurkat cells after a 10 ms light pulse at 25 KHz, 20 V. Scale bar: 20 μ m. (b) Comparison of lysis times between red blood cells and Jurkat cells using a 10 ms light pulse at 25 KHz and 20 V.	185
Figure 6-16: Blood cell concentration change over time due to settling of cells in tubing. Sampling time for quantification of cell concentrations was set to 2 min.	186
Figure 6-17: Focussing of blood cells towards the pressure node for a frequency of 4.138 MHz and an applied voltage of 20 V. (a) No flow, cells randomly distributed, and acoustics off. Scale bar: 50 μ m. (b) Acoustic actuation pushed cells towards the pressure node by the PAR force. (c) Focussing under flow (flow from top to bottom), 5 μ l/min, and aligning of sample within 2 mm for 4.138 MHz, 20 V. Scale bar: 100 μ m.	187
Figure 6-18: Change in acoustic contrast factor due to lysis of red blood cell. (a) RBCs in microchannel. (b) Acoustic actuation forced cells into pressure node (Target cells marked in red circle). (c) A light pulse created an electric field for localised cell lysis. (d) Lysis process induced in cells and change in intracellular and mechanical properties (density). (e-h) Cells started to move towards pressure anti-node due to sign change in acoustic contrast factor. Scale bar 50 μ m.	188
Figure 6-19: Focussed blood cells undergo dielectrophoretic movement when passing the illuminated region. (a) Electric field was switched off and cells experienced PAR and stokes drag force. (b) At 25 KHz (20 V, 10 mS/m) negative DEP force was dominating over stokes drag force leading to trapping of blood cells at the light pattern edge. (c) Negative DEP force dominated over PAR and drag force which led to lateral displacement of cells. (d) DEP force pushed red blood cells towards the channel top (cells out of focus). Lysis was induced but not completed when light pattern was passed by cells. Scale bar: 50 μ m. Flow from right to left.	190
Figure 6-20: Collected blood samples after (a) pumping through the channel without acoustic or electric actuation, (b) after applying an ac signal of 25 KHz and 20 V, (c) after acoustic actuation at 20 V, and 4.138 MHz and (d) after optoelectrical actuation at 25 KHz, 20V.....	191
Figure 6-21: Lysis efficiency under continuous flow (5 μ l/min) in 15 μ m high channel with 30 ms exposure times when lysis was triggered by optically induced electric fields. C – Control (control run, no actuation, conducted after every actuation run), E – power on (20 V, 25 KHz), no light, no sound, AT – acoustic actuation on (20 V, 4.138 MHz), OET – light induced electric field (20 V, 25 KHz) only, O-A – acoustic and electric actuation for cell concentrations of 17 \cdot 10 ⁶ cells/ml, 60 \cdot 10 ⁶ cells/ml, 150 \cdot 10 ⁶ cells/ml. The lysis efficiency was obtained from cell count analysis in a haemocytometer after injecting cells into the microchannel and collecting samples from the outlet.....	191
Figure 6-22: (a) Accumulation of red blood cells at the channel wall under a low flow rate when 20 V were applied at 25 KHz without light or acoustic actuation. Red blood cells moved toward insulating SU8 wall where electric field strength was lower creating a dielectrophoretic effect due to voltage leakage into the liquid despite no illumination. The photoconductor was not a perfect insulator in its dark state, especially at high voltage a significant voltage dropped across the	

liquid is observed (b) This led to non-uniform electric fields along the channel wall due to a curved channel wall which acted as insulator.	194
Figure 6-23: Jurkat cells sampled after acoustic actuation at 20 V, 4.138 MHz in 0.5 mg/ml of 3 kDa FITC-dextran DEP-buffer solution. (a) Bright field image (b) Fluorescence imaging (excitation at 495 nm) measured direct after sampling. Scale bar: 50 μ m.	196
Figure 6-24: Lysis of densely packed cells using an increased exposure time. (a) Cells were trapped at electrode edge due to negative DEP force (20V, 25 KHz). (b) Applied voltage was switched off to release cells and allow movement towards the illuminated area.(c) 2 s after the electric signal (20 V, 25 KHz) was switched on again. (d) 7 s after lysis was induced (Scale bar 50 μ m). The focus in the images (b-d) was changed towards a higher plane to observe the lysis process as negative DEP pushed the cells upwards.....	198
Figure 6-25: Alternative configuration to optimize lysis of high cell concentrations based on multiple pressure nodes. (a) Two pressure nodes at 8 MHz, (b) three pressure nodes at 12.541 MHz (Scale bar 50 μ m). Distribution of high cell concentrations over several pressure nodes might help to prevent dense cell aggregates and therefore electric shielding by surrounding cells. ...	199
Figure 6-26: (a) Simulated non-uniform electric field (kV/cm) created by a 2.5 μ m spot in microchannel with 35 μ m distance between ITO electrode and photoconductor when a voltage signal of 20 V and 25 KHz is applied. (b) Corresponding FWHM of the area of higher electric field created by the 2.5 μ m light spot. Measurement was taken at 100 nm above the photoconductor surface.	201
Figure 6-27: (a) Simulated potential distribution in the presence of a red blood cell (V) for 20 V and 25 KHz. (b) Cross section potential plot through the center of the red blood cell showing voltage drop of 0.3 V and 2.1 V across the furthest and closest membrane site relative to the photoconductor surface for 20 V, 25 KHz. (c) Transmembrane potential for different voltages and changing electrode distances (25 KHz). Simulations considered a low conductivity buffer of 10 mS/m.	201
Figure 6-28: Single cell lysis using 2.5 μ m light pattern at 25 KHz and 20 V in 10 ms buffer solution. (a) 2.5 μ m beam spot close to RBC. (b) Beam spot was focused on the centre of the cell and a voltage of 20 V was applied. (c) Cell after 14 s. (d) Lysis complete after 20 s. (e) Cell lysis times for a range of beam spot sizes. Scale bars: 20 μ m.	202
Figure 6-29: Single cell lysis at 25 KHz and 20 V in 10 mS/m buffer solution. (a) 2.5 μ m beam spot (marked by black arrow) was used for selective lysis of target cells (red arrow). (b) Beam spot was focused on the center of first target cell and a voltage of 20 V was applied. (c) First target cell after 20 s of electric field exposure. (d) After 35 s, second target cell lysis was started. (e) 27 s after inducing lysis in second target cell. (f) 50 s after inducing lysis in second target cell. (g) Simulated change in transmembrane potential with increasing vertical and horizontal distance of the cell to the light spot center (25 kHz, 20 V, 10 mS/m). Scale bar: 20 μ m.	203
Figure 6-30: (a) Comparison of simulated electric field strength created by a 2.5 μ m beam spot in low (10 mS/m, black curve) and high (PBS, 1.4 S/m, red curve) conductivity buffer. Inset shows detailed view of red curve. (b) Modelled transmembrane voltage of a red blood cell in PBS buffer. The distance between the cell and the photoconductor surface was varied between 5 nm and 640 nm. (c) Potential plot of a red blood cell with 5 nm distance to the photoconductor at the closest (edge of red blood cell).	205
Figure 6-31: Single cell lysis at 25 KHz and 20 V in PBS buffer. (a) 2.5 μ m beam spot (marked by black arrow) is used for selective lysis of target cell (red arrow). (b) Beam spot was focused on the centre of cell and a voltage of 20 V was applied. (c) Lysis complete after 25 s. Scale bars: 25 μ m.	205
Figure 6-32: MCF7 cells adhered to the surface of the photoconductor and immersed in cell culture medium inside the OET chip. (a-c) A 5.5 μ m light beam spot was used to achieve lysis of a cluster of cells within 80 s (25 KHz, 20 V). (d-g) A cell in the centre of a cell cluster was targeted and lysis was induced using 20 V at 25 KHz. Lysis was achieved after 35 s (Scale bars: 30 μ m).	207

Figure 7-1: Schematic of microbubble based drug carrier systems. (A) A MB design with lipid monolayer shell which stabilises a gas mixture core. The shell can also be modified with ligands (antibodies, peptides) to enable targeted microbubble accumulation at desired tissues (B) MB as carrier of drugs or DNA on the shell surface by electrostatic interaction. (C) Integration of lipophilic drugs into the shell of MBs. (D) Incorporation of hydrophobic drugs in a thickened oil shell. (E) Attachment of drug-filled liposomes on the MB surface. Ultrasound exposure causing mechanical oscillation of the MB disrupts the liposomes. (F) Incorporation of drugs and MB in liposome. Stimulation with ultrasound ruptures MB and liposome. Schematic and description from Ibsen et al. ³²²	211
Figure 7-2: (a) Transparent piezoelectric substrate (Lithium niobate) with slanted interdigitated electrodes (IDT, SAW device). (b) Frequency spectrum for SAW device in x-propagation direction. (c) Schematic of the setup showing SAW device and OET chip filled with microbubbles. Here, the photoconductor was used as top substrate compared to the previous setup where it was on the bottom.	215
Figure 7-3: SonoVue microbubbles for drug delivery. Image depicts the non-uniformity when working with microbubble samples. Scale bar: 50 μm	219
Figure 7-4: Simulated real part of the Clausius-Mossotti factor for various MB diameters (0.25 - 10 μm) in DEP buffer (10mS/m).	220
Figure 7-5: Simulated ∇E^2 for a ring trap. Scale bar shows the magnitude of the gradient of the electric field squared and the black arrows show the direction of the DEP force for an insulating MB. A negative DEP force points away from high field regions. However, the use of a ring trap results in the DEP force pointing towards the centre of the ring. Hence, the result is a stable MB trap which can be used to select and move single MBs.	221
Figure 7-6: (a-d) Selective trapping and moving of 7 μm microbubble using a light induced dielectrophoretic trap at 70 KHz and 10 V. Scale bar: 50 μm	222
Figure 7-7: 2D cross section model of the electric field strength distribution when a ring pattern illumination was used with 70 KHz and 10 V applied to the OET chip. The colours represent the electric field strength in kV/cm. (b) Cross section plot of the electric field strength along the ring pattern 10 nm above the aSi layer. Peak values of 7.4 kV/cm and 5.6 kV/cm correspond to outer and inner edge of the ring pattern. (c) Decay of the electric field at the outer edge of the ring pattern with increasing distance to the aSi layer.	223
Figure 7-8: Velocities of various sizes of microbubbles when trapped and moved in ring pattern applying 10 V and 70 KHz.	224
Figure 7-9: Microscopic images show inhomogeneous acoustic pressure distribution. (a) Chip filled with microbubble suspension. (b) Accumulation of microbubble in local pressure maxima after coupling of ultrasound into the chip at 2.8 MHz and 50 V. Scale bar: 100 μm	224
Figure 7-10: Microbubble (7 μm) response after activation of acoustic transducer (2.8 MHz, 60V, burst mode, 300ms) where (e) is 0 s, followed by 37 s (f), 73 s (g) and 86 s (h). Scale bar: 20 μm	225
Figure 7-11: (a) Trapping of different sized microbubbles in dielectrophoretic trap at 70 KHz and 10 V. (b-d) Insonation (2.8 MHz, 60V, burst mode 12 cycles, 300 ms) of microbubbles (b) after 1.21 min (c) 1.45 min and (d) 3.45 min. Scale bar 200 μm	227
Figure 7-12: Change in microbubble diameter over time when acoustically actuated at 2.8 MHz using 60 V. Microbubbles were kept in dielectrophoretic trap at 70 KHz and 10V.	227

Contents

Abstract.....	i
Author's Declaration.....	ii
Acknowledgement.....	iii
Publications.....	iv
Conferences.....	iv
Abbreviations.....	v
List of Figures.....	vi
1. Introduction.....	1
1.1. Microfluidics and force fields to manipulate particles.....	3
1.2. Optoelectronic tweezing.....	7
1.2.1. Principle of optoelectronic tweezing (OET).....	8
1.2.2. Device structures and systems for optoelectronic tweezing.....	11
1.2.3. Dielectrophoresis.....	13
1.2.4. Other electrokinetic effects in optoelectronic tweezing.....	18
1.2.5. Applications of OET.....	18
1.2.6. Model and simulations.....	20
1.3. Acoustic tweezing.....	27
1.3.1. Acoustophoretic particle manipulation a.k.a. acoustic tweezing.....	27
1.3.2. Primary acoustic radiation force.....	28
1.3.3. Secondary acoustic radiation force.....	32
1.3.4. Acoustic streaming.....	33
1.3.5. Acoustic tweezing in microsystems.....	34
1.3.6. Bulk acoustic wave transducer for acoustic tweezing.....	34
1.3.7. Surface acoustic wave transducer for acoustic tweezing.....	37
1.3.8. Applications of acoustic forces in microsystems.....	41
1.4. Combination of force fields – “eierlegende Wollmilchsau”.....	45
1.5. Aim of this work.....	49
2. Materials and Methods.....	50
2.1. Fabrication and characterisation of SAW transducer.....	50
2.1.1. Mask for photolithography.....	50
2.1.2. SAW device.....	50
2.1.3. SAW device frequency response.....	52
2.1.4. SAW device actuation.....	52

2.1.5.	Visualization of surface acoustic wave emission	52
2.2.	Microchannel fabrication for resonator and OET chip	53
2.2.1.	Superstrate concept	53
2.2.2.	Fabrication of amorphous silicon substrates	55
2.2.3.	OET chip fabrication	56
2.2.4.	Scanning electron microscope and Dektak profilometer	57
2.3.	OET setup.....	59
2.4.	Particle and cell samples	60
2.4.1.	Polymer beads.....	60
2.4.2.	Microbubbles	61
2.4.3.	Blood cells	61
2.4.4.	Breast cancer cell line MCF 7.....	61
2.4.5.	Jurkat cells.....	62
2.4.6.	<i>Trypanosoma Cyclops</i>	62
2.5.	Software.....	62
2.5.1.	Video and image analysis.....	62
2.5.2.	Modelling and data analysis software.....	63
3.	Optoelectronic tweezing integrated into microfluidics	64
3.1.	Introduction	64
3.2.	Materials and Methods	67
3.3.	Results and Discussion	68
3.3.1.	Integration of OET into microfluidics.....	68
3.3.2.	Characterisation and application of fabricated OET devices.....	74
3.3.3.	OET for particle handling under continuous flow	84
3.3.4.	Limitations of the current OET device	90
3.4.	Conclusion	96
4.	Acoustic tweezing using ultrasound standing waves	97
4.1.	Introduction	98
4.2.	Materials and Methods	100
4.2.1.	Slanted SAW device.....	100
4.2.2.	Superstrate with embedded microchannel - fabrication	100
4.2.3.	SAW device and superstrate	100
4.2.4.	Acoustic energy densities and pressure amplitudes in the microchannel	101
4.2.5.	Acoustic streaming induced bead movement in microchannel.....	102
4.2.6.	Model and simulations of pressure eigenmodes	103

4.3.	Results and Discussion	106
4.3.1.	Device concept.....	106
4.3.2.	Modelling pressure eigenmodes in simplified microchannels.....	107
4.3.3.	SAW transducer design.....	112
4.3.4.	Acoustic actuation of the superstrate using a SAW transducer.....	114
4.3.5.	Characterisation of acoustic energy density and pressure amplitude	119
4.3.6.	Acoustic streaming	122
4.3.7.	Temperature change induced by coupling losses	124
4.3.8.	Superstrate position.....	125
4.3.9.	Tuneable pressure distribution	126
4.3.10.	Acoustic tweezing for dynamic particle manipulation.....	128
4.4.	Conclusion	148
5.	Combined use of optoelectronic and acoustic tweezing	149
5.1.	Introduction	149
5.2.	Materials and Methods	151
5.3.	Results and Discussion	152
5.3.1.	Influence on leakage field on particle-particle interactions.....	152
5.3.2.	Dynamic sorting into channel outlets using virtual electrodes	154
5.3.3.	Acoustic sorting supported by virtual electrodes	157
5.3.4.	Particle handling in multipressure nodal planes using virtual electrodes	160
5.4.	Conclusion	165
6.	Cell lysis through the combination of electric and acoustic fields	166
6.1.	Introduction	166
6.1.1.	Cell lysis in microfluidics.....	166
6.1.2.	Electropermeabilization of the cell membrane.....	167
6.1.3.	Light induced electric fields for lysis and electroporation	169
6.2.	Material and Methods	170
6.2.1.	SAW transducer and OET chip - setup	170
6.2.2.	Cells and sample preparation.....	170
6.2.3.	Image analysis and modelling of transmembrane potentials.....	171
6.3.	Results and Discussion	173
6.3.1.	Electric field characterisation in OET chip for continuous lysis	173
6.3.2.	Modelling the transmembrane voltage in OET	175
6.3.3.	Cell lysis under static conditions to investigate time scales	177
6.3.4.	Jurkat cell lysis compared to red blood cell.....	184

6.3.5. Continuous lysis of red blood cells	185
6.3.6. Single Cell lysis	199
6.4. Conclusion	207
7. Microbubble actuation in microfluidics using optoelectronic tweezing and surface acoustic wave transducer.....	209
7.1. Introduction	209
7.2. Materials and Methods	214
7.3. Results and Discussion	218
7.4. Conclusion	229
8. Summary.....	231
9. Conclusion	238
10. References.....	241

1. Introduction

*'How many times when you are working on something frustratingly tiny like your wife's wrist watch, have you said to yourself, "If I could only train an ant to do this!" What I would like to suggest is the possibility of training an ant to train a mite to do this. What are the possibilities of small but movable machines? They may or may not be useful, but they surely would be fun to make.'*¹

Richard Feynman's amusing and inspiring speech heralds the start in the field of miniaturization and the establishment of new ways to fabricate tiny things. It took a couple of decades after his visionary speech before a new field known as microelectro-mechanical systems (MEMS) was established and allowed a step change in the miniaturisation of machines.

However, the quote above highlights an essential problem when working at small scales. It is the lack of control of small objects, their motion, position and state. Today, several micromanipulation methods exist, each having its benefits and shortcomings. This thesis starts by introducing several strategies based on force fields to control particles of micrometer dimensions and turns the focus on acoustic and electric fields in particular (**Chapter 1**) before outlining experimentally a route to combine these into microfluidics.

Chapter 2 presents the materials and methods used within this work. **Chapter 3** describes the development of a fabrication protocol to integrate OET into a microfluidic chip (substrate). This chip is also used as a resonator structure to enable the creation of standing wave patterns in the microfluidic compartments. Furthermore, the OET devices are characterised, potential applications are demonstrated and device properties are critically discussed.

The **Chapter 4** introduces a novel device concept which enables the coupling of acoustic energy from a surface acoustic wave (SAW) transducer into the fabricated microfluidic chip to create flexible standing wave patterns. The SAW transducer is characterised and the acoustic energy coupled into the chip is quantified. Moreover, potential applications of this concept for continuous particle manipulation such as sorting are outlined.

In **Chapter 5**, OET and acoustic tweezing are combined to demonstrate versatile particle manipulations by globally applied acoustophoretic and locally applied dielectrophoretic forces. The developed OET chip serves as superstrate which is acoustically actuated by the developed SAW transducer. It is shown that careful control of the force fields enables particle trapping, aggregation and fusion. The sequential use of the forces is utilized to concentrate particle prior to precise particle guiding into channel outlets, virtual channels or adjacent pressure nodes to achieve sorting and fractionation of mixtures.

The following **Chapter 6** applies both concepts to perform lysis of cells with high efficiencies under continuous flow and presents a unique feature of OET that allows precise single cell lysis.

Chapter 7 uses the platform for selective manipulation of therapeutic microbubbles (MB). MB positions are controlled by OET and MBs are insonified by ultrasound excitation from the SAW transducer.

Chapter 8 ends this thesis by giving a summary of the results and an outlook for further research.

1.1. Microfluidics and force fields to manipulate particles

Microelectro-mechanical systems deliver a vast amount of new device technologies in numerous fields that surrounds our daily life (e.g. inkjet printers). In the 1990s the know-how of fabricating these microsystems started to increasingly be applied to the handling of minute amounts of liquid. It was the field of analytical chemistry, with particular focus on separation processes (e.g. chromatography), that demonstrated first the advantages of scaling down and injecting liquids into small channels.² It was the birth of microfluidics and the start of a new research field that was energised by ideas to miniaturize laboratory functions and create novel tools to study fundamental physical aspects (e.g. single molecule, single cell)^{3, 4} and provide new kinds of reaction vessels (e.g. drug discovery)⁵ and total analysis system (e.g. sample to answer systems)⁶.

In general, microfluidic platforms comprise small channel systems connected to liquid reservoirs (e.g. by tubing systems linked to syringes) mainly fabricated by photolithography on substrates such as glass, silicon or polymers.⁷ The sizes of the channels are in the range of hundreds to a few of micrometers enabling the handling of volumes from micro- to femtoliters. The downscaling benefits from a significant reduction in the sample consumption and reduced sampling times. The use of small volumes and the increased surface to volume ratio facilitate fast (e.g. short diffusion length) and controlled transport times of mass and heat. The fluid flow in such systems is dominated by surface forces such as viscous force and surface tension rather than inertial forces, gravity and buoyancy.⁵ The Reynolds number, which is defined as the ratio of inertial and viscous forces, is low (<1) promoting sleek and constant fluid motion known as laminar flow. The fluid velocity of a laminar flow varies from zero at solid boundaries to a maximum along the centre of the bulk fluid volume creating a parabolic profile (Poiseuille flow).

The flow of microparticles such as beads or cells suspended in a liquid inside a microchannel is dominated by viscous interactions at low Reynolds numbers (< 1). A particle accelerates to the local fluid velocity due to the viscous drag of the fluid over the particle's surface almost instantly.⁸ The drag force F_S for a homogeneous spherical particle in a viscous fluid can be described by Stoke's law:

$$F_S = 6\eta\pi a u \quad (1.1)$$

where η is the viscosity of the fluid medium, a the particle radius and u the velocity of the particle. A particle subjected to viscous drag force under continuous flow remains positioned in a laminar streamline. However, the increase in the Reynolds number (>> 1) gives rise to additional hydrodynamic effects which includes inertial lift and Dean drag forces.

Microchannel geometries are specifically designed to control the influence of these force fields and induce particle motion across laminar streamlines.⁸

In many microfluidic applications, the adjustment of the fluid flow field and the associated drag forces combined with precise laminar streamlines and certain microchannel designs has been applied to control particle positions within a microfluidic channel and achieve particle and cell separation. The common examples include particle focusing by sheath⁹ and inertial focussing flows¹⁰, particle separation using pinched flow fractionation¹¹, hydrodynamic filtration¹² and deterministic lateral displacements¹³. For instance, pinch flow fractionation is based on particle wall interactions¹⁴ and the spreading of laminar streamlines (profile) after opening of a narrow (pinching region) microchannel section into a wider one. A particle mixture is first hydrodynamically focused along a wall in the pinching region by a particle free stream. The size (radius) of the particle then determines the center distance to the wall and hence the location within a particular streamline. Once the particles past the pinching region, the spreading of the laminar streamlines leads to the particle separation. Such hydrodynamic methods are easy to implement, cheap and have been shown to be valuable tools for a range of applications, especially where fast and high throughput is required. However, a continuous flow is always needed to process a sample which impedes selective and individual particle handling in dense samples. Also, often high flow rates (ml/min) are the basis to make use of hydrodynamic effects (e.g. Dean drag force for separations¹⁵) which requires large sample sizes (several milliliters) or accepting sample dilution with potential sample losses. Separation of particles takes place based on size and shape but may not be successful when for instance dead and viable cells need to be discriminated since their size or shape are similar. Therefore, a greater benefit arises with the ability to integrate additional force fields into microfluidic systems that allow the manipulation and control of small objects under varying conditions (e.g. static fluid, low sample volume) based on different physical criteria such as the chemical, electrical, magnetical or mechanical properties of particles.

Many micromanipulation concepts have been introduced to microfluidics in recent decades. These concepts make use of non-inertial force fields including optical gradient force¹⁶, magnetic force¹⁷, dielectrophoretic¹⁸ and acoustophoretic forces¹⁹. The methodology behind these manipulation approaches is often simply depicted as tweezers which are able to grab tiny objects without mechanical contact. Optical tweezer (OT, single beam) for instance uses highly focused laser beams to create an optical gradient force that is able to hold and move particles in three dimensions. The laser light is typically focused through a microscope objective with high numerical aperture into a microfluidic compartment. The energy and

momentum carried by the light beam is transferred to a particle upon refraction and reflection of the light on the particle's surface. The interaction gives rise to a net force which is the sum of the scattering force and the gradient force. The scattering force arises from the refraction and reflection of the light beam. The gradient force, which is the result of the gradient of the light intensity profile, is directed towards the centre of the light beam. A particle subjected to the gradient force experiences a restoring force with a movement towards the beam center. The scattering force can push particles in any direction. In order to achieve a stable trap a single laser beam is tightly focused where the gradient force dominates over the scattering force so that the resulting net force acts as restoring force towards the beam center. OT is not restricted to a single trap but able to create multiple beams to trap more than one particle at the same time by using different configurations which include rapid laser beam movement (μs), beam splitting and computer generated holograms (interference patterns).²⁰ A big advantage of OTs is the ability to tune the optical force dynamically in time and space which has been utilized for trapping²¹, moving²² and rotating²³ of single particles as well as probing mechanical properties by deforming cells and molecules to characterize forces in biological matter^{24, 25}. OTs manipulate particles from nanometer scales up to hundreds of micrometers using forces from femto- to nanonewtons.²⁶ Moreover, optically induced separation under continuous flow in microfluidic channels has been demonstrated using a static three dimensional optical lattice or an array of optical traps produced by light interference patterns.^{27, 28} Separation was achieved by deflecting particles selectively along the optical pattern depending on their affinity to the optically generated force and the hydrodynamic force. This kind of optical fractionation is extremely versatile and applicable to various particle mixtures as wavelength, intensity and geometry of the traps can be adjusted and optimized to fit many conditions. Overall, since the introduction in 1986, OT has become an important tool for micromanipulation and for gaining fundamental insights in diverse micro- and nanoscale processes which cover many research fields including biology, physical chemistry and soft matter physics.²⁶

In the last 15 years magnetic fields have been increasingly applied in microfluidics to handle particles based on their magnetic susceptibility. Particles subjected to a non-uniform magnetic field experience a gradient force which depends on the volume of the particle, the magnetic susceptibility of the particle relative to the medium as well as the gradient and the strength of the magnetic field. Particles are either forced towards field maxima or minima based on their field permeability which is classified as diamagnetic, paramagnetic or ferromagnetic. For instance, most materials such as cells, polymers, water, DNA have a low susceptibility and are classified as weak diamagnetic or non-magnetic. An imposed external

magnetic field creates an opposing magnetic field inside the material which results in a very small magnetic force acting towards field minima. The opposite behaviour can be observed for paramagnetic materials such as oxygen or platinum while ferromagnetic materials have a strong susceptibility and experience a strong force towards field maxima within a non-uniform field. For ferromagnetic microparticles typical forces are in the range of a few piconewtons to ten of piconewtons²⁹ well defined to the high field region but decay rapidly with increasing distance to it. A benefit of magnetic manipulation includes that magnetic interactions are not influenced by surface charges, pH, medium conductivity or temperature, however, magnetic interactions often need to be enhanced by altering the medium properties^{30, 31} or label^{32, 33} objects of interest (e.g. cells, except of red blood cells due to paramagnetic hemoglobin³⁴) with magnetic particles to generate appropriate forces for manipulation. An advanced method of labelling cells includes the use of magnetic nanoparticles (< 0.5 μm) modified with cell specific antibodies which can bind to the surface of a target cell. The labelled cells can be separated from non-labelled cells upon activation of a magnetic field. This process is known as magnetic-activated cell sorting (MACS).³⁵ The magnetic fields can be generated by small (severall millimeters) permanent magnets³⁶ or electromagnets³⁷ placed outside the microchip or even fabricated onto the microchip substrate^{37, 38} for a spatially more confined field or complex field pattern. Under the influence of magnetic fields particles can be trapped, transported and sorted within microfluidic compartments. For instance, a sequence of tapered electromagnets outside a capillary have been used to trap magnetic beads (2.8 μm) followed by the transport along the capillary length induced by switching the external field to an adjacent magnet.³⁹ Through integration of current carrying planar electrodes, magnetic fields have been generated inside microfluidic compartments. A pair of ratchet electrodes have been used to transport magnetic beads along the electrodes when an alternating current was applied to induce switching of high field regions along the electrode pair.⁴⁰ A dense mesh of individual addressable gold electrodes has been applied to produce magnetic fields locally. This has been used to trap magnetic particles and labelled cells as well as transporting in all directions by careful electrode actuation.⁴¹ Separations of magnetic, magnetically labelled and non-magnetic particles have been demonstrated under continuous flow with externally or internally produced magnetic fields deflecting particles based on size or magnetic susceptibility into side channels or adjacent laminar streams.⁴²⁻⁴⁴ Magnetic particles are often used for bioassays where they serve as solid supports for immobilised biomolecules such as DNA or proteins. In continuous flow application such functionalized particles are trapped prior to reactions with a sample liquid containing disease related biomarkers. The trapped particle agglomerate increases the surface area and decreases diffusion and

reaction times to speed up the analysis process.^{45, 46} Overall the use of magnetic fields in microfluidics has shown to be a promising route to integrate various lab functions into miniaturized systems.

Electric fields and acoustic fields have found extensive use in microfluidic systems. In particular dielectrophoretic particle manipulation in non-uniform electric fields⁴⁷⁻⁴⁹ and acoustophoretic manipulation within a standing wave field⁵⁰⁻⁵³ became very popular in the lab on a chip community. In the following chapters a detailed introduction to these methods is given with special focus on light induced electric fields and ultrasound generated standing pressure waves.

1.2. Optoelectronic tweezing

The principle of optoelectronic tweezing (moving particle with light patterned electric fields) and the forces associated with it are introduced in this chapter. An overview of potential applications for light induced particle manipulation is presented. In addition, simulations of an OET device are shown which help to understand the device characteristics.

Optoelectronic tweezing

Optoelectronic tweezing (OET) is a micromanipulation method where focused light is applied to pattern electric fields which interact with microparticles suspended in a liquid medium. In particular, the electro kinetic motion of polarisable particles under the influence of a non-uniform electric field between electrodes is the principle behind OET. The essential element in an OET system is a photoconductive material which absorbs some frequencies of electromagnetic radiation and changes resistivity due to electron-hole pair generation. The electric field pattern is then the result of an applied AC voltage accompanied with local changes in the photoconductivity induced by patterned light illumination. The illuminated area, producing the high electric field region, is called a virtual electrode. A typical OET device consists of a photoconductor such as amorphous silicon (aSi) deposited on an indium tin oxide electrode (ITO) and a second ITO electrode separated by tens of micrometers to create a microfluidic manipulation volume. Figure 1-1 shows a schematic diagram of a typical OET device similar to those used in this work. The electric field polarises particles suspended in the liquid medium. The gradient in the non-uniform field produces unequal forces on the poles of the dipole created and this induces movements towards regions of high or low electric field strength depending on the electrical properties of the liquid medium and the particle. The electro kinetic motion produced by the electric gradient force is called dielectrophoresis (DEP).

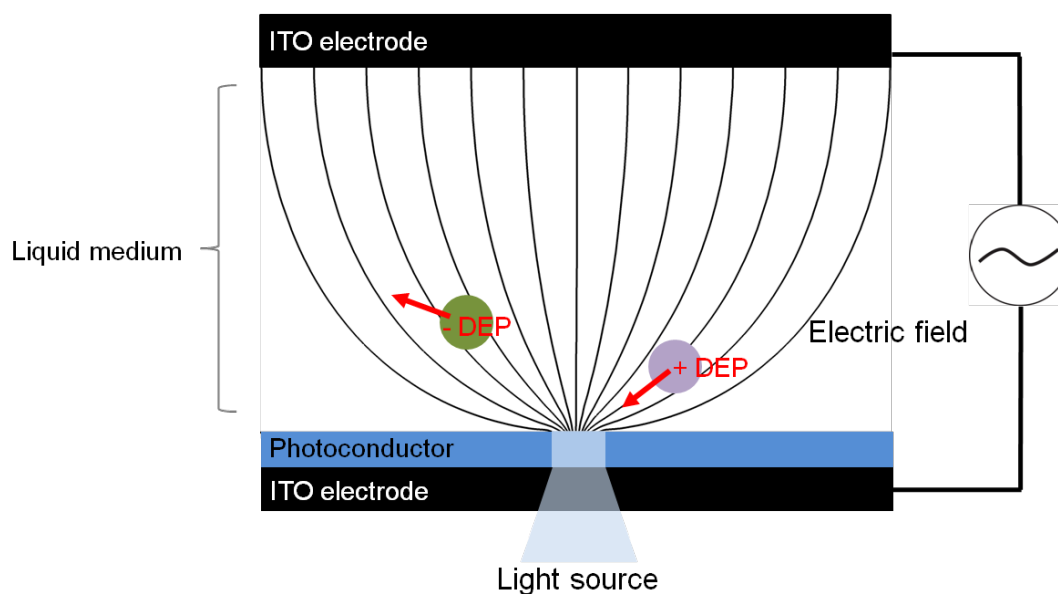


Figure 1-1: Schematic of the structure of an optoelectronic tweezing (OET) device. A typical device consist of transparent top and bottom indium tin oxide (ITO) coated glass electrodes while one of the electrodes (bottom) is covered with a photoconductor such as amorphous silicon (aSi). A liquid medium is sandwiched between the electrodes and contains the particles to be manipulated. A voltage is applied between the ITO electrodes and a light source such as a data projector or laser provides selective illumination of the photoconductor. In the illuminated regions a change in the conductivity of the photoconductor takes place and transfers the voltage into the liquid layer. This creates a non-uniform electric field which interacts with the particles in the liquid in the form of positive or negative dielectrophoresis (DEP).

1.2.1. Principle of optoelectronic tweezing (OET)

The use of light to create altered electric fields for particle manipulation was first introduced by Hayward *et al.*, who demonstrated the patterning of charged colloids on indium tin oxide electrodes (ITO) illuminated by UV light.⁵⁴ The current across the ITO surface has been altered by different light intensities causing particles to assemble in the light-patterned areas when a dc voltage was applied between two ITO electrodes. This phenomenon is related to electrostatic forces in a uniform electric field and is widely known as electrophoresis.

The term OET was first introduced by Chiou *et al.* in 2005.⁵⁵ In this work photoconductive aSi combined with ITO was used to massively manipulate particles simply by the projection of patterned light. Compared to the work by Hayward *et al.*, an alternating voltage was applied between the photoconductor and the ITO plate. As long as the light was off, most of the voltage dropped across the aSi, ideally. But when switched on, the conductivity of the aSi layer increased by several orders of magnitudes and caused the voltage to switch into the liquid medium.⁵⁶ The result was a localised electric field gradient inducing DEP as a

result of the interaction between the non-uniform field and the polarised particle. This allowed Chiou *et al.* to show that by changing the light pattern the pattern of forces could be changed, giving continuous control of the particles, a significant advantage of OET over DEP based on metal electrodes.

The operation of an OET device relies on the impedance of the photoconductive layer and the impedance of the liquid medium being chosen correctly. While the electrical properties of the liquid stay constant, the impedance of the photoconductor can be adjusted as a function of light intensity. For instance, the conductivity of amorphous silicon (used in this study) increases linearly with increasing light intensity (0.1 – 100 W/cm²) for a given wavelength of 632 nm.⁵⁶ An amorphous silicon layer of 1 µm thickness has a conductivity of approximately 1 · 10⁻⁶ S/m in the dark state (no illumination). But when illuminated (light state), electron-hole pair carriers are generated in the photoconductor and the conductivity increases to up to 1 · 10⁻³ S/m depending on the light intensity (several W/cm²). The light absorption coefficient of amorphous silicon depends strongly on the wavelength of the illuminated light.⁵⁷ In the visible spectrum the aSi absorption coefficient is around 10⁻⁴ /cm, resulting in a 90 % attenuation length within a 1 µm aSi layer.⁵⁸ Furthermore, the light state as the result of selective illumination and the dark state in aSi are well confined. The diffusion length (ambipolar diffusion) of the light induced charge carriers due to an applied electric field is in the order of 115 nm for aSi.⁵⁹ This means that patterned light which acts as a virtual electrode has a resolution limit mainly defined by the optical diffraction limit,⁶⁰

$$d = \frac{\lambda}{2N.A.} \quad (1.2)$$

where λ is the wavelength of the light and $N.A$ the numerical aperture of the objective. For instance, in this work the wavelength was around 600 nm and the numerical aperture of an objective (10x) was 0.25 resulting in minimum virtual electrode size of 1.2 µm.

The OET device structure in Figure 1-1 can be represented in form of an equivalent circuit consisting of two impedance elements (Figure 1-2). One represents the frequency dependent impedance of the photoconductor and one the impedance of the liquid. In the dark state the impedance of the photoconductor dominates and most of the voltage drops across it creating a weak field in the liquid medium. In the light state the impedance of the photoconductor is reduced resulting in an increased voltage drop across the liquid medium and a stronger electric field suitable to operate the OET in form of light induced dielectrophoresis. However, care must be taken in selecting a suitable liquid conductivity. A

high liquid conductivity decreases the voltage switched into the liquid.⁵⁶ The majority of the voltage drops across the photoconductor due to the decreased impedance of the liquid. Conversely, if the liquid impedance is too high, the voltage will be dropped across the liquid in both light and dark regions producing no field gradient. The optimal liquid conductivity to enable light induced dielectrophoresis is typically in the range of 0.1 mS/m to 20 mS/m.⁶¹⁻⁶⁵ It also should be noted that as impedance is a combination of resistance and reactance, and only reactance can be light patterned, care must be taken to not allow reactance to dominate the impedance of the photoconductor.

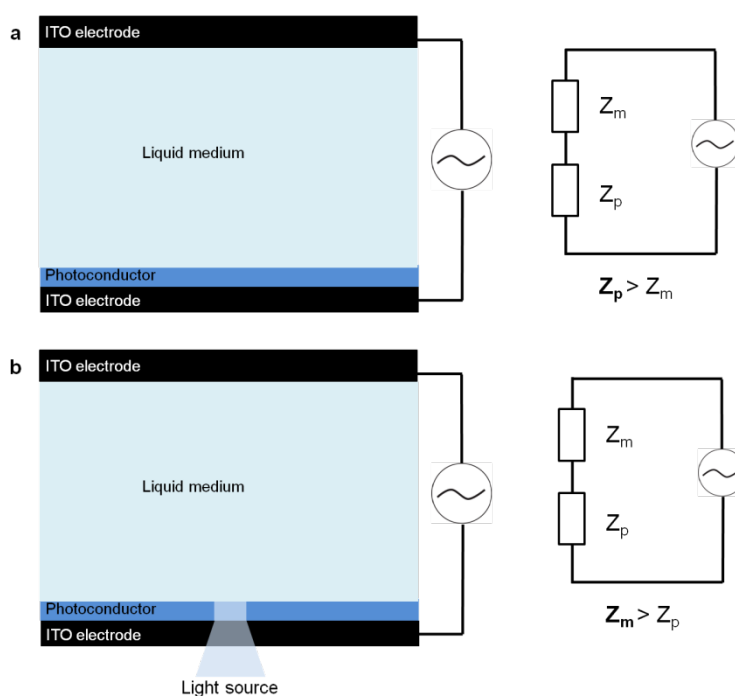


Figure 1-2: OET device operation simplified as equivalent circuit model. (a) In the dark state (no illumination) an applied AC voltage signal drops mainly across the photoconductors impedance Z_p which dominates over the impedance of the liquid Z_m . (b) In the light state, the Z_p is decreased, Z_m dominates and more voltage drops across the liquid layer.

For this the frequency range for OET operation needs to be considered as well. This is linked to the device structure and its frequency dependent impedance elements. While the photoconductor impedance is dominated by the resistive term of the impedance at low frequencies, the capacitance term dominates at higher frequencies. This means the voltage drop into the liquid is not only triggered by the liquid properties and the illumination of the OET, but also by the frequency of the applied AC signal. For instance, at a high frequency the photoconductor impedance is low, even in the dark state, due to the decreased capacitance resulting in a voltage drop across the liquid medium which creates a uniform field across the device. Only at low frequencies, is the voltage drop efficiently triggered by the light pattern and the liquid conductivities (see above) to enable sufficient generation of

non-uniform electric field regions in an OET chip. Based on the literature, OET for cell and particle manipulation based on DEP is mainly applied in the frequency range from 10 KHz to 300 KHz.^{61, 64, 66-71}

1.2.2. Device structures and systems for optoelectronic tweezing

The most common device structure for OET is based on the parallel arrangement of the electrode substrates as shown in Figure 1-1 where the electric field is patterned upon illumination from a light source perpendicular to the photoconductor electrode and a second electrode (e.g. ITO). However, several groups have adjusted the original design to allow functions and obtain benefits for particle manipulation and device integration. For instance, Hwang *et al.* developed an OET device where parallel oriented substrate electrodes were both modified with a photoconductive layer (aSi) which they called 3D OET device.⁷² This device was developed for the need to avoid non-specific interactions (hydrophobic, electrostatic etc.) of particles with the surface which would otherwise limit the manipulation efficiency. By applying a single illumination pattern, two virtual electrodes were created on each photoconductive layer resulting in a strong field gradient close to the surface of the electrodes. This was followed by the movement of polystyrene particles towards low field region in the bulk of the liquid by negative DEP and produced a 3D particle focussing effect.

An alternative OET device has been shown by Ohta *et al.* where the parallel electrode arrangement was replaced by a planar one on a single substrate.^{67, 70} The device was called lateral OET (LOET). The name originated from the fact the non-uniform electric field in the device was parallel to the substrate compared with the common design. This was achieved by etching aSi and the underlying ITO into a interdigitated electrode array. The advantage here is that the gap between the electrodes can be easily defined by standard photolithography which means the lateral electric field gradient can be tuned by the array geometry and allows, for instance, the orientation of nanowires parallel to the substrate.¹⁷

A floating electrode OET device (FOET) was developed by Park *et al.*⁷³ Similar to the LOET device, a single electrode substrate was used, however, instead of an ITO layer underneath the photoconductor, aSi was directly deposited onto a simple glass substrate. On top of the aSi layer a pair of aluminium electrodes separated by 5 μm were deposited. These electrodes were used to create a lateral electric field across the whole FOET device with uniform character in the centre of the device. This resulted in no net force in the presence of particles (in this case water/oil droplets). However, the selective illumination of the aSi

perturbed the uniformity and formed a dipole in the particles which were then able to be actuated.

Another important development used a phototransistor based OET (Ph-OET)⁷⁴ device to overcome operational limitations of OET associated with high conductivity liquid media, as discussed above. In this work a substrate with single-crystalline bipolar junction transistors was used to increase the photoconductivity to $1 \cdot 10^1$ S/m - $1 \cdot 10^2$ S/m. The transistor substrate was parallel to an ITO electrode and the field was created perpendicular to the electrode substrates.

The Ph-OET device demonstrated an alternative to the common amorphous silicon photoconductor. However, the phototransistor device and the common aSi are expensive, requiring specialised equipment for fabrication. To overcome this issue, a couple of groups introduced cheaper polymer based photoconducting materials which can be spin coated onto substrates. For instance, Wang *et al.* used poly(3-hexylthiophene) and [6,6]-phenyl C61-butyric acid methyl ester coated onto ITO as photoconductor and demonstrated light induced DEP on polystyrene beads.⁷⁵ A study by Yang *et al.* applied low cost titanium oxide phthalocyanine (TiOPc) in a similar manner which proved to be a viable alternative to aSi by showing particle and cell manipulations based on DEP.⁷⁶

An OET device is usually placed under a microscope for monitoring the light induced particle actuation. The objective used for observations or an additional objective can be used to enable the focussing of patterned light onto the photoconductor at low optical powers (< 1 W/cm²). As optical source for providing virtual electrode patterns, light-emitting diodes (LED) or halogen lamps combined with digital micromirror devices,^{55, 66, 67} data projectors,^{61, 77} liquid crystal displays (LCD)^{78, 79} and microLEDs^{80, 81} have been used. LCD and microLED based OET systems show the feasibility of miniaturisation of a rather complex optical setup into a more portable configuration which may be used in the field. With new developments in the area of miniaturized data projectors, system as small as a brief case can be obtained.⁸²

1.2.3. Dielectrophoresis

Dielectrophoresis describes the interaction of a non-uniform field with the induced dipole in a particle. In general, an electric field induces the formation of a dipole within a material and an accumulation of charges at the material's surface (polarisation). A particle subjected to a uniform electric field experiences a Coulomb force and the forces on the charges on either side of the particle are equal and in opposite directions. The result is a zero net force acting on the particle. But in the case of a non-uniform electric field where the magnitude varies in the area around the particle the Coulomb force acting on the dipole sides is unequal. The net force is the electrical gradient force or dielectrophoretic force (DEP force) and the action of movement is called dielectrophoresis.⁸³ The movement of a particle or cell towards regions of strong electric fields or repulsion from these regions depends on the polarisability of the particle relative to the suspending medium (Figure 1-3). Attraction or repulsion refers to positive and negative DEP forces and has been first investigated by Herbert A. Pohl in 1951, although the term DEP was introduced later.¹⁸ In general, the magnitude of the force is strongly related to the applied frequency, the electrical properties of the suspending medium and the particle as well as the particle's size and shape.

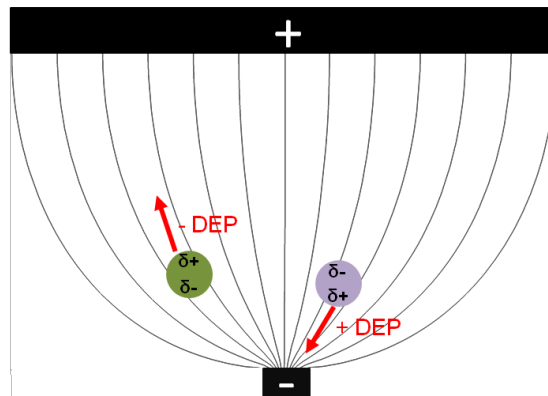


Figure 1-3: Positive and negative DEP of particles more and less polarisable than the surrounding medium.

In a non-uniform electric field (E), a dipole moment (μ) is induced in the particle. The dipole experiences a net force related to the gradient of the electric field which is called the electric gradient force or DEP force and can be approximated as:⁸⁴

$$F = (\mu \cdot \nabla)E \quad (1.3)$$

Typically, a spherical particle immersed in a dielectric liquid medium and subjected to a non-uniform electric field is used as simplified model to describe the DEP force. In this model several assumptions are made which include that the particle undergoing DEP is a homogenous dielectric.⁴⁹ The polarization induced in the particle is assumed to be a simple

dipole and the electric field in the infinite dielectric medium is not perturbed by the presence of boundaries such as other polarisable particles. Then the time-average DEP force on a sphere can be expressed as:⁴⁹

$$\langle F_{DEP} \rangle = 2\pi a^3 \varepsilon_r \varepsilon_0 \text{Re}[K(\omega)] \nabla E^2 \quad (1.4)$$

Here, a is the radius of the particle. $\varepsilon_r \varepsilon_0$ is the absolute permittivity of the medium with ε_r being the relative permittivity of the material (liquid medium) and ε_0 the permittivity of vacuum. ∇E^2 is the gradient of the electric field squared. $\text{Re}[K(\omega)]$ is the real part of the Clausius-Mossoti factor (CM) which is defined through frequency dependent properties of the materials (particle/medium). The CM factor determines whether the DEP force is directed towards regions of low (negative DEP) or strong (positive DEP) electric fields and is given by:⁴⁹

$$K(\omega) = \left(\frac{\varepsilon_p^* - \varepsilon_m^*}{\varepsilon_p^* + 2\varepsilon_m^*} \right) \quad (1.5)$$

Here, ε_p^* and ε_m^* are the complex permittivity of the particle and the medium which are given by:

$$\varepsilon_{p/m}^* = \varepsilon_r \varepsilon_0 - j \left(\frac{\sigma}{\omega} \right) \quad (1.6)$$

Here, ε_r is the relative permittivity of the material (particle or liquid medium). The conductivity of the material is defined by σ and ω is the angular frequency. The current in a particle can be considered to be associated with field-induced movements of free charges and field induced perturbations of bound charges.⁴⁹ At high frequencies the particle acts like a capacitor (no moving charges, displacement current) while at low frequencies a particle acts like an insulator or conductor as the conduction of free charges dominates. Therefore, the DEP force depends on the conductive properties of the particle and the surrounding medium at low frequencies. At high frequencies the permittivity values of the materials are important and at intermediate frequencies the conductive and dielectric properties of the medium and the particle determine the magnitude and the direction of the DEP force.⁴⁹ The CM factor takes values between +1 and -0.5 which represents if a particle is more or less polarisable than the surrounding medium. A positive CM factor means that particles move to a region of highest electric field. Conversely, particles are repelled from these regions for a negative CM factor. Figure 1-4 shows values of the CM factor as a function of frequency for a 6 μm polystyrene particle ($\sigma = 1 \cdot 10^{-13}$ mS/m, $\varepsilon_p = 2.5$) suspended in a liquid medium of different conductivities (0.1 mS/m, 1 ms/m, 10 mS/m, $\varepsilon_m = 79$).

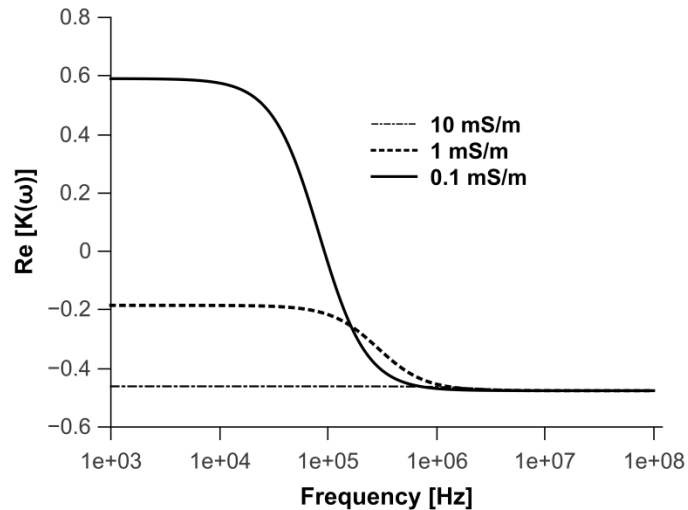


Figure 1-4: Real part of the Clausius-Mossotti factor as a function of frequency for a 6 μm polystyrene particle suspended in liquid medium of varying conductivity.

As seen in Figure 1-4, the CM factor varies as a function of frequency and media conductivity. A significant change in the CM factor over the frequency range can be observed for the lowest conductivity. At low frequencies the CM factor is positive and a positive DEP force is induced followed by the particle being attracted to regions of high electric fields. However, at higher frequencies a transition (crossover frequency) takes place where the particle's CM factor becomes negative followed by repulsion from high electric field regions due to negative DEP. As the conductivity of the liquid medium increases positive DEP disappears and is completely replaced with negative DEP as the result of the medium being more polarisable relative to the particle. It may be worth noting that conductivities as low as 0.1 mS/m are hard to achieve, practically, polystyrene particles usually experience negative DEP except when small enough for surface conductance to dominate.

While large polystyrene beads can be considered as homogenous throughout the volume, particles like biological cells are not homogenous due to components such as the cell membrane and the cytosol. The complex permittivity of the cell and hence the CM factor are therefore more difficult to estimate. However, a simple single shell model can be used to predict the frequency dependent dielectrophoretic response of cells. The model considers the complex permittivity of the cell's membrane (thin shell) and the complex permittivity of the cell interior (cytosol). Although being greatly simplified, empirical studies⁸⁵⁻⁸⁷ have shown that a single shell model gives good agreement with the dielectric response of a cell. The single shell model is given by.⁸³

$$\varepsilon_p^* = \varepsilon_m^* \left[\frac{\left(\frac{a}{a-d}\right)^3 + 2 \left(\frac{\varepsilon_{cyt}^* - \varepsilon_{mem}^*}{\varepsilon_{cyt}^* + 2\varepsilon_{mem}^*}\right)}{\left(\frac{a}{a-d}\right)^3 - \left(\frac{\varepsilon_{cyt}^* - \varepsilon_{mem}^*}{\varepsilon_{cyt}^* + 2\varepsilon_{mem}^*}\right)} \right] \quad (1.7)$$

Where ε_{cyt}^* and ε_{mem}^* are the complex permittivities of the cytosol and membrane and d is the thickness of the membrane. Although the model is derived for perfect spherical single shelled particles, it has been shown that it can be used to approximate the CM factor for discoid-shaped human erythrocyte (red blood cell, RBC).⁴⁹ The cytosol of RBCs has no compartmental structures but is composed of a homogenous haemoglobin suspension making it a reasonably good model system.⁸⁸ The frequency dependent real part of the CM factor is shown in Figure 1-5. Here a membrane thickness of 7 nm was considered accompanied by permittivities and conductivities for membrane and cytosol of 12.5 and $1 \cdot 10^{-6}$ mS/m as well as 60 and 0.8 mS/m, respectively (values obtained from Menachery *et al.*⁸⁹). At low frequencies and a medium conductivity of 10 mS/m the CM factor is negative. Here, the insulating properties of the cell membrane, despite being very thin, dominate. The cell is less polarisable than the surrounding medium. However, a transition takes place at higher frequencies where the conductive properties of the cell interior start to dominate over the capacitive membrane leading to a positive DEP response. The dielectric response is cell specific due to varying intrinsic properties (e.g. cell size). This can be used to separate different cell types from each other for instance.

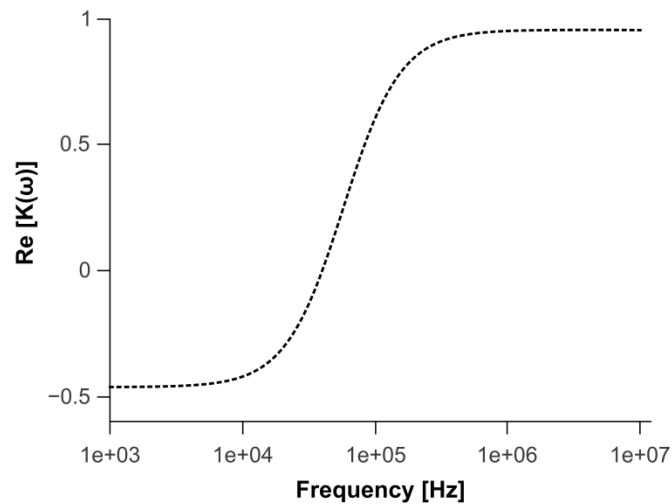


Figure 1-5: Frequency dependent real part of the CM factor for a red blood cell (erythrocyte) suspended in 10 mS/m liquid medium.

For small particles the surface conductance imposed by the liquid medium can influence the CM factor. The polarisation of a particle in an electric field induces the formation of an electrical double layer at the liquid/solid interface due to electrostatic interactions of charges on the particle's surface and the ions in the liquid medium. These ions are mobile under the influence of an electric field and give rise to a surface conductance K_s (~ 1 nS) which

influences the overall polarisability of a particle and can exceed its bulk conductivity σ_{bulk} .⁴⁹ Therefore, the total conductivity of a particle should be described as the sum of bulk and surface conductivity,

$$\sigma_p = \sigma_{bulk} + \frac{2K_s}{a} \quad (1.8)$$

The surface conductance dominates significantly for nanoparticles where the width of the electric double layer becomes the same size or larger than the particle's diameter. For instance, an insulating latex bead of 216 nm diameter suspended in a liquid medium of 10 mS/m experiences positive DEP (up to 10^7 Hz).⁸³ The double layer conductance results in the particle being more polarisable than the medium.

In summary, from equation 1.4 one can state that the DEP force is zero for a uniform field. The CM factor determines the direction and partially the magnitude of the DEP force. The DEP force scales with the particle's volume. Moreover, the DEP force is proportional to the square of the gradient of the electric field magnitude, which means the DEP force is also proportional to the square of the amplitude of the applied voltage. The electrode geometry and the gap between electrodes, which triggers the gradient of the electric field, are important experimental factors. The DEP force can be considered as a small range force as the electric field gradient decays exponentially with the distance of the electrode and remains strong only close to the electrode.

A common way to estimate the DEP force in microfluidic channels is by balancing it against the viscous drag imposed on a particle under fluid flow. This means a dielectrophoretic trap (positive or negative DEP) is generated at the electrode and the electric field is varied until a trapping of approaching particles is achieved. The measured velocity of a homogenous spherical particle within a laminar flow corresponds to the fluid velocity when viscous drag force dominates over inertial forces at low Reynolds number (<1). Then the velocity of a particle is proportional to the drag force F_s and given by Stokes law (equation 1.1). However, a more accurate result can be obtained when the particle position relative to the microchannel wall is known. The fluid flow that surrounds the particle in the presence of a wall is different compared to the flow in the bulk liquid and hence Faxen's correction⁹⁰ may be introduced to equation 1.1 when the particle-wall distance is determined precisely.

1.2.4. Other electrokinetic effects in optoelectronic tweezing

When using OET, care must be taken to ensure that operations are carried out in a regime where DEP is dominant. Valley *et al.* have shown that the DEP force is overcome by other physical effects when changes in voltage, frequency and optical power occurred.⁵⁶

Electrolysis describes a process where oxidation and reduction reactions of solvent compounds take place at electrode surfaces driven by a DC current. Although OET usually operates with AC signals, at lower frequencies (<1 KHz) and high electrode potentials electrolysis of water into hydrogen and oxygen can occur. The result is the creation of gas bubbles in the OET device and damaging of the photoconductor.

An electrode with an applied potential placed in an electrolyte induces the formation of an electric double layer at the electrode/electrolyte interface as the result of electrostatic interactions of ions in the solution and charges at the electrode surface. In the presence of a tangential electric field component with sufficiently low frequency, the Coulomb force pushes ions in the double layer and generates a fluid flow. This effect is described as electro-osmosis. In an AC electric field, the double layer acts as a capacitor which changes polarity in response to the field resulting in a steady motion of the solvent-ions. However, electro-osmosis is frequency dependent and only occurs at sufficiently low frequencies (<10 KHz) where the double layer is able to sustain the field induced polarisation. The induced fluid flow is strong enough to enable an efficient transport of particles independent of their size and electrical properties.

Furthermore, electro-thermal effects have been observed when operating with high optical power (>100 W/cm²) and high electrical fields (>20 V). Phonon scattering and Joule heating as heat sources generate gradients in electrical permittivity and conductivity in the solution which then interact with the electric field producing an external fluid flow driven by a body force.⁵⁶

1.2.5. Applications of OET

The advantage of OET based electrokinetic manipulations compared to the conventional method of using fixed metal electrodes is the flexible and dynamic arrangement of virtual electrodes of any, 2D, geometry. Therefore, the described electrokinetic effects in an OET device have been used for a range of different applications in microfluidics. For instance, the light induced DEP force was applied to select and move individual particles such as cells, polystyrene beads and gas bubbles attracted to virtual electrodes (positive DEP) or trapped

in it (negative DEP).^{55, 65, 75, 80, 91, 92} Even actuation of submicrometer particles such as carbon nanotubes and DNA using positive DEP has been demonstrated.^{71, 93} For instance, Chiou *et al.* impressively showed the parallel manipulation of up to 15,000 microparticles using a LED as light source and a digital micromirror spatial light modulator (DMD device) to pattern virtual electrodes on the photoconductor.⁵⁵ Single polystyrene beads of 4.5 μm were trapped and moved by negative DEP in individual virtual ring patterns of 4.5 μm diameter across an area of 1.3 mm x 1.0 mm. The achieved particle trap density was 11,500 traps per mm^2 . Zhu *et al.* used light induced DEP to characterise the frequency dependent behaviour of various microparticles.⁶⁵ A conventional OET device stimulated by a DMD device was used first to trap particles of various sizes in optical ring patterns followed by linear motions of the pattern to determine the maximum particle velocity (before particles escaped from the trap) for a range of frequencies. The obtained velocity spectra can be used distinguish microparticles, for instance. Yang *et al.* applied OET to manipulate gas picobubbles suspended in silicon oil. The picobubbles were less polarisable than the suspending medium due to the insulating gas. This enabled the attraction to virtual electrodes by positive DEP in frequency range of 1 Hz to 20 MHz. DEP forces of up to 160 pN could be achieved when bubbles of 300 pL volume were manipulated. Furthermore, this study demonstrated that individual controlled bubbles undergo fusion when brought in contact. The manipulation of nano-objects by OET has been demonstrated by Pauzauskie *et al.*.⁷¹ Multiwalled carbon nanotubes (~ 80 nm diameter, several hundred nanometer in length) were attracted to high field regions generated by virtual electrodes on an aSi coated substrate. The nanotubes aligned parallel to the electric field lines when trapped and their positions within the OET device was controlled by translating the virtual electrode patterns with manipulation speeds of up to 200 $\mu\text{m}/\text{s}$.

As the DEP force scales with the volume of the particle, this has been applied to samples of different sized beads and droplets to achieve separations and sorting functions.^{64, 94-96} For instance, Lin *et al.* used focused light of different wavelengths to create moving virtual electrodes on a aSi layer.⁶⁴ Each wavelength was associated with a particular electric field strength due to a difference in the generation of charge carriers in the aSi layer. The resulting DEP force was large enough to move large beads while small beads were left behind. Alternatively, sieve like light pattern structures can be generated which are able to trap large particles while smaller particles can pass them, as shown by Ohta *et al.*.⁶⁶

The light induced DEP has also been applied to analyse and pattern biological cells. Dead and viable B lymphocyte cells have been discriminated by exploiting the difference in the

dielectrophoretic response at a particular frequency.⁶⁷ While dead cells experienced negative DEP which pushed them from a virtual ring pattern, viable cells were stepwise attracted to it and concentrated. A similar dielectrophoretic behaviour has been found for viable and non-viable sperm cells which can help to improve fertilisation experiments.⁹⁷ Moreover, Valley *et al.* showed that OET is a promising tool to distinguish developmental stages in embryos which can be used to enhance the outcome of *in vitro* fertilisation where the most mature embryos increase the success rate of live birth.⁹⁸ Valley found that the dielectrophoretic response changes from positive DEP in the early stages to negative DEP in the mature stages of the embryo. The work is a good example which shows that probing the dielectric properties of a cell using OET is significantly simplified by virtual electrodes compared to fixed metal electrodes. OET can be a useful tool to pattern cells or cell-constructs in arbitrary ways for subsequent cell behaviour studies. For instance, Lin *et al.* showed a perfusion system for bottom-up tissue engineering where OET was applied to arbitrary arrange alignate microbeads with encapsulated cells.⁹⁹ The beads were of 80 μm in diameter and loaded with cell concentrations of up $1 \cdot 10^7$ cells/ml. A positive DEP force was used to generate 3D sheet-like cell culture constructs.

As described above, other electrokinetic effects are present in an OET device and in particular, light induced electro-osmosis has been used for concentrating small particles (0.2-3 μm)^{63, 69, 100} and even molecules such as dextrans¹⁰¹, proteins¹⁰² and DNA.¹⁰³ At low frequencies (<10 KHz), the tangential field at the edge of a virtual electrodes induces a fluid flow directed towards the centre of the light pattern. The maximum flow velocity can be found at the electrode edge while a stagnation point is setup in the centre of the electrode.⁶⁹ The results are vortex flows on the electrode edges which drive particles and molecules into the stagnation point.

OET can also be used to create strong electric fields which enable the selective poration¹⁰⁴ and lysis^{105, 106} of cells which can be applied to transfer molecules into a cell, analyse cells in regards to particular intracellular biomarkers or enrich a particular cell type. Cell lysis using OET was studied within this work and a detailed introduction to this topic can be found in Chapter 6.

1.2.6. Model and simulations

In order to understand the device characteristics of a micro scaled OET device a range of simulations were undertaken using the finite-element modelling software COMSOL

Mutliphysics (v3.5). A simple 2D cross-section model which depicts the liquid layer and the photoconductor layer in the OET device and their actual thicknesses is used to introduce field distributions, magnitudes and components in the microdevice before the influence of parameters such as the conductivity of the liquid medium and the photoconductor, vertical channel dimensions, electrode pattern sizes as well as potential drops across the layers are specifically explored in chapter 3 by experiments and simulations. In the following example the geometry, layer properties and parameter values resemble a typical configuration for a conventional OET device.

The AC/DC module (In-plane electric currents) in COMSOL was applied and 2D cross-section geometries of the OET chip with specific boundary conditions were implemented. The Figure 1-6 shows a schematic of the geometry with defined boundary conditions. To simplify the model the ITO layer was removed as the potential change across it is negligible. The sides of the cross-section were assumed to be electric insulators owing to the fact that a polymer (SU8) was used as microchannel wall in this work. The upper side of the geometry was given an electric potential ($V = V_0$), while the lower side of the photoconductor was set as ground ($V = 0$). The enclosed sides (Interfaces to layers) were subjected to the continuity boundary condition. The layers of the OET device were defined as subdomains and specified by defining geometrical and electrical parameters.

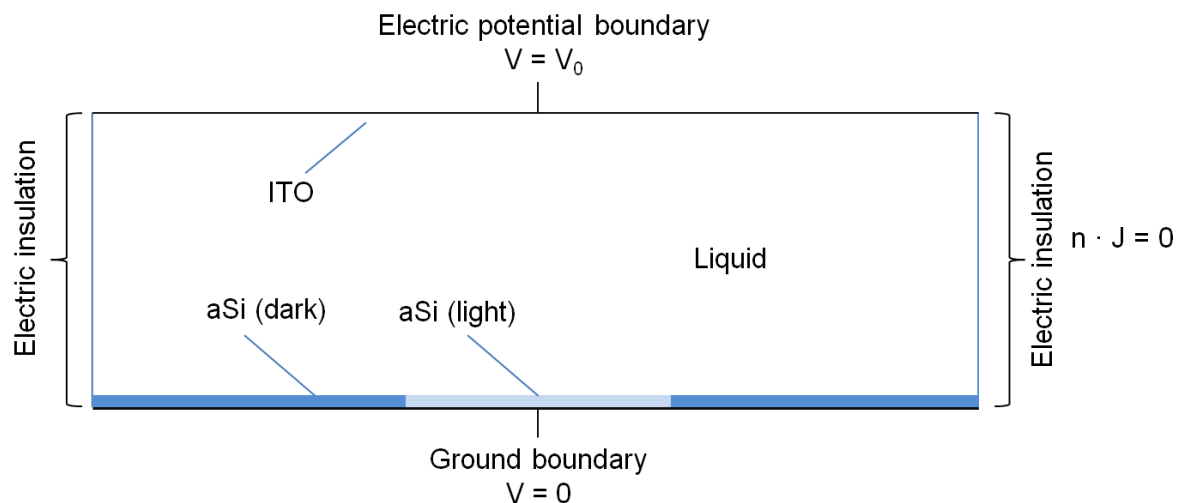


Figure 1-6: Schematic of boundary conditions and subdomains used for simulations of electric field and potential distributions in the OET device.

An overview of the parameters for the different materials is shown in table 1-1. The photoconductive effect was modelled as a change in the electrical conductivity of the aSi layer. The microscope in this work was equipped with a set of different objectives leading to different optical powers and hence different light intensities (see Figure 2-8 in Chapter 2).

The influence of light intensity on the conductivity of the aSi layer was considered by defining values for the dark- and light-state for each objective.

Table 1-1: Parameters used for simulations.

Thickness liquid domain	5 – 300 μm
Thickness aSi	1 μm
Conductivity σ liquid medium	0.005 – 0.1 S/m
Conductivity σ aSi (light state)	$4 \cdot 10^{-4}$ S/m (10x), $8.5 \cdot 10^{-4}$ S/m (20x), $1.4 \cdot 10^{-3}$ S/m (40x)
Conductivity σ aSi (dark state)	$5.7 \cdot 10^{-6}$ S/m (10x), $1.1 \cdot 10^{-5}$ S/m (20x), $1.8 \cdot 10^{-5}$ S/m (40x)
Permittivity ε liquid medium	79
Permittivity ε aSi	14

The electric field distribution is computed for the applied potential V by solving the continuity equation:

$$\nabla J = \frac{\partial \rho}{\partial t}, \quad (1.9)$$

$$J = J_c + J_d = \sigma E + \frac{\partial D}{\partial t} \quad (1.10)$$

$$E = -\nabla V. \quad (1.11)$$

J is the current density, J_c is the conduction current, J_d is the displacement current, ρ is the charge density, E is the electric field, t is the time, V is the electrical potential, and D is the displacement field. A quasistatic regime is considered for the modelled system owing to the fact the electromagnetic wavelength (2250 m, 100 KHz) is much larger compared to the system with electromagnetic fields propagating instantaneously. In particular, an electro-quasistatic system is considered which includes capacitive but not inductive effects. The magnet field induced currents in the electrodes are assumed to be negligible due to small absolute magnitudes of the current flow. Then the constitutive relation between the displacement field D and the electric field E is given by:

$$D = \varepsilon_r \varepsilon_0 E \quad (1.12)$$

In Figure 1-7 2D cross-section (31 μm x 50 μm) models of an OET device are shown which include a 1 μm thick aSi layer and a 30 μm thick liquid medium layer. The device response is modelled for an applied AC signal of 10 V at 100 KHz and aSi conductivity states (dark/light) corresponding to 10x objective (see table 1-1). In detail, Figure 1-7a shows the simulated voltage distribution in the amorphous silicon layer and the liquid medium. The illuminated area, virtual electrode, in the centre of the aSi layer induces a higher voltage switch into the liquid layer due to the increased conductivity upon illumination. Figure 1-7b shows the simulated voltage switch into the liquid medium along the surface of the aSi layer including the virtual electrode. In fact, a voltage drop of 4.5 V takes places in the light activated region of increased conductivity while approximately 8 V drop across the aSi layer in the dark state regions. The voltage switch is not only influenced by the properties of the aSi layer, the conductivity of liquid medium plays a significant role when operating the OET device. An increase in the liquid medium increases the voltage drop across the aSi layer and less is switched into the medium. Therefore, the medium conductivity is an important experimental factor which should be considered when operating OET. An example of an OET device response towards increasing medium conductivity is shown in Chapter 3.

The applied voltage and the induced voltage switch upon illumination create an electric field E distribution in the liquid medium. In Figure 1-7c the magnitude of the resulting electric field as the sum of the electric field components in all directions ($E = \sqrt{E_x^2 + E_y^2}$) is shown. For the given conditions an electric field magnitude of up to $1.1 \cdot 10^6$ V/m is simulated. The highest magnitudes are confined to the surface of the aSi layer in the area of the virtual electrode owing to the non-uniform profile of the field with the strongest gradient close to the edge of the virtual electrode as shown in form of streamlines in Figure 1-7d. Component analysis of the electric field in x- and y-direction is shown in Figure 1-7e and 1-7f. The lateral component of the electric field E_x has the highest magnitude of $8.9 \cdot 10^5$ V/m at the edges of the virtual electrode. This strong electrical field in a well localised area with lower field regions close by produces a large electrical gradient (strong lateral gradient). The vertical component E_y of the electric field shows the highest magnitude of $8.1 \cdot 10^5$ V/m around the centre of the vertical electrode.

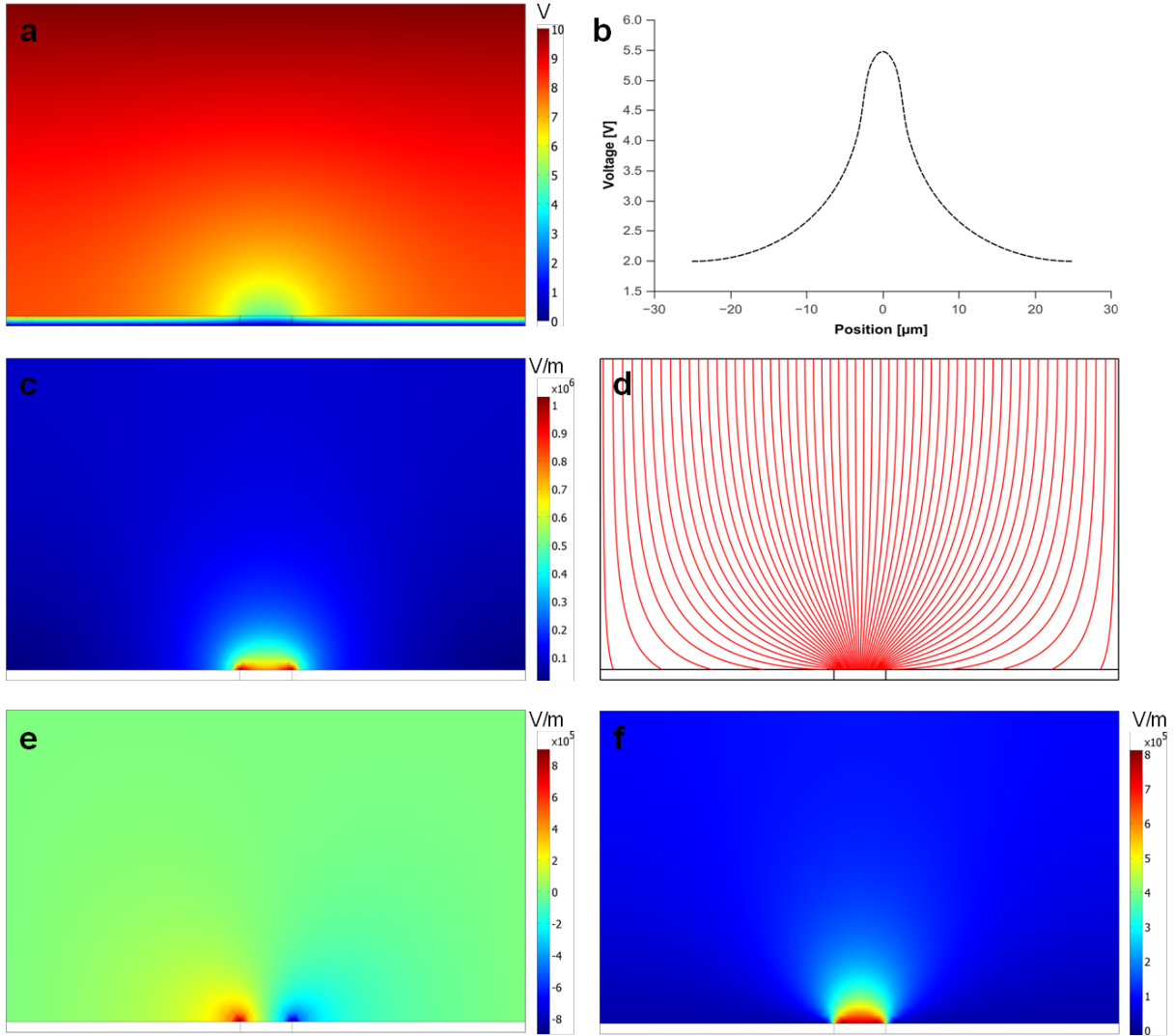


Figure 1-7: 2D cross-section model ($31 \mu\text{m} \times 50 \mu\text{m}$) of OET device with $1 \mu\text{m}$ thick aSi layer and $30 \mu\text{m}$ thick liquid medium of 5 mS/m conductivity. The photoconductor is modelled with a $5 \mu\text{m}$ virtual electrode and an AC signal of 10 V at 100 KHz is simulated for the OET device. (a) Simulated voltage distribution in the OET device. Change in the conductivity in the aSi layer by an virtual electrode reduces the voltage drop across the aSi layer in that region which in turn switches more voltage into the liquid medium. (b) Simulated switched voltage in the liquid medium along the aSi surface including the virtual electrode. (c) Magnitude of the electric field E created by virtual electrode in the liquid medium (aSi layer suppressed). (d) Streamline representing electric field lines in the liquid medium and demonstrate the non-uniformity of the field with sharp gradient close to the surface and edge of the virtual electrode. (e) X-component E_x of the electric field E . (f) Y-component E_y of the electric field E .

The DEP force is directly proportional to the gradient of the square of the electric field ∇E^2 . In Figure 1-8a a surface plot of ∇E^2 for the above mentioned conditions is shown. As already implied, a strong lateral electric field gradient ($\nabla E_x^2 = 1.69 \cdot 10^{18} \text{ V}^2/\text{m}^3$) dominates ∇E^2 compared to the vertical component ($\nabla E_x^2 = 7.78 \cdot 10^{17} \text{ V}^2/\text{m}^3$) and generates high electric field magnitudes at the edges of the virtual electrode close to the surface of the aSi. The vertical and lateral components of the field decay sharply in all directions. In an experiment using the OET device, this results in attraction of particles in proximity to the virtual electrode

caused by positive DEP towards the electrode edges or away from that under negative DEP. An example for the direction of the DEP force for a particle that is less polarisable than surrounding medium is shown in Figure 1-8b. A magnified view of the simulation showing the magnitude and the direction of the DEP force is shown in Figure 1-8c.

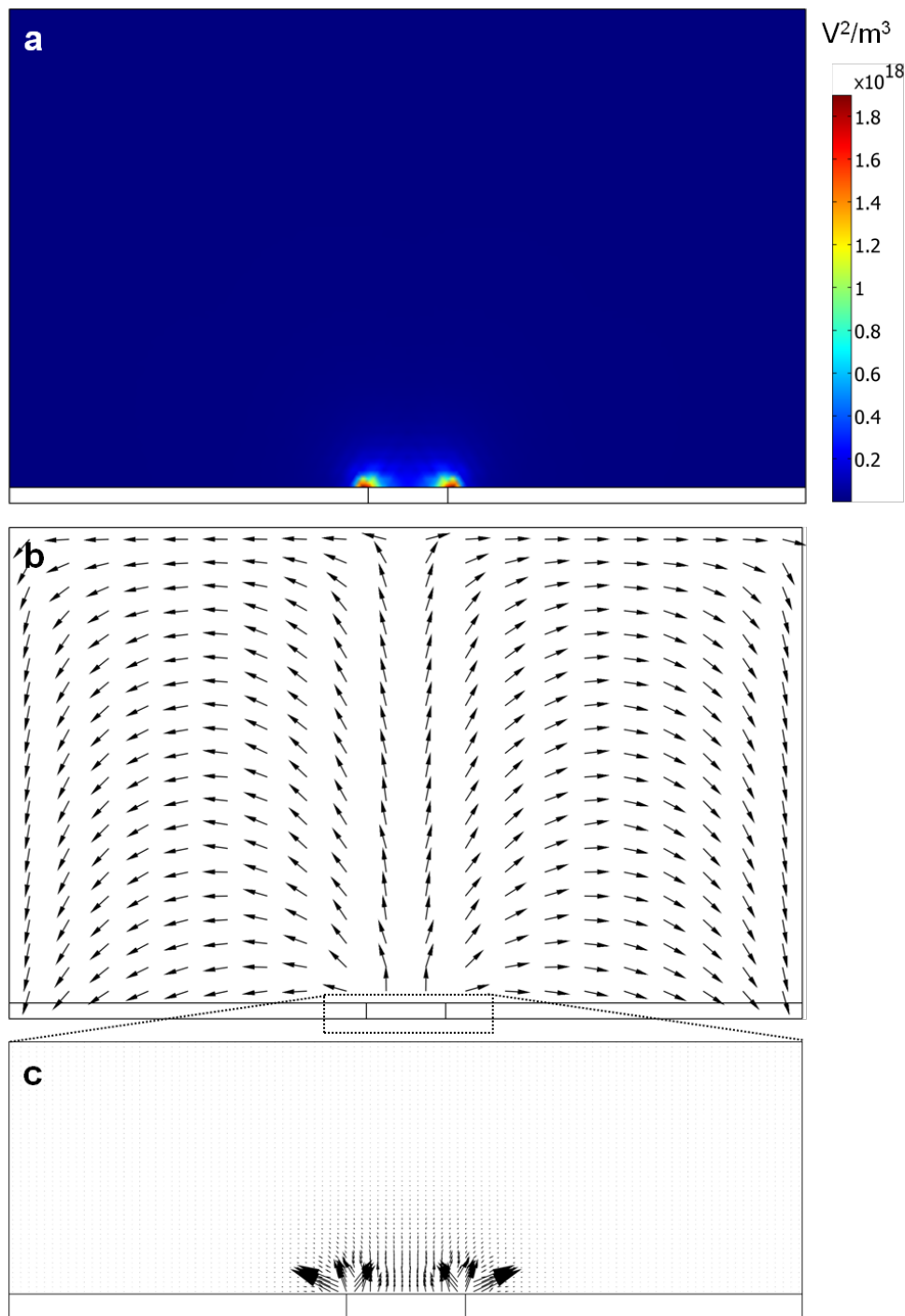


Figure 1-8: (a) Square of the gradient of the electric field ∇E^2 and (b) direction of the DEP force acting on an insulating particle which is less polarisable than surrounding medium. (c) Magnified view virtual electrode and liquid interface region representing the magnitude and the direction of the DEP force. The size of the virtual electrode is $5 \mu\text{m}$ in the simulations.

Based on the simulation it can be concluded that the electric field is well defined to the surface of the virtual electrode and rapidly decays towards the bulk of the liquid. Hence, the DEP force decays accordingly (Figure 1-8c) and can be considered as small range force spatially defined to the virtual electrode. This is important when considering the lateral and vertical positions of particles relative to the electrode and the induced polarisation. For instance, a particle experiencing negative DEP can be levitated (due to vertical component of the electric field) when placed above the virtual electrode and can overcome the influence of the field by moving towards low field regions (Figure 1-8b). However, the same particle surrounded by virtual electrodes and placed in low field region can be trapped. Alternatively, the gap between the electrodes can be decreased to increase the magnitude of the electric field in the bulk liquid and hence the magnitude of the DEP force on particles (see Chapter 3).

1.3. Acoustic tweezing

The principle of acoustic tweezing is introduced in this chapter. An overview of transducer concepts for acoustic actuation in microfluidic environment and related applications for sound mediated particle manipulation are presented.

1.3.1. Acoustophoretic particle manipulation a.k.a. acoustic tweezing

Acoustophoresis, also known as acoustic tweezing, describes the manipulation of particles using sound waves under acoustic resonance conditions. Early investigations of this phenomena date back to 1874 when Kundt and Lehmann investigated the effects of travelling sound waves.¹⁹ To show that sound is mediated by travelling pressure variations, Kundt and Lehmann used an air filled tube modified with a vibrating metal rod as sound source and a piston on each end to change its length. The tube was filled with dust particles and during the experiments the position of the piston was changed until a regular particle accumulation pattern could be observed as the result of interfering travelling sound waves. At that point, the rod oscillation matched the resonance frequency of the tube or in other words the wavelength of the excited longitudinal sound wave fitted the length of the tube.

A plane travelling sound wave is defined by the acoustic pressure amplitude p_{ac} , the frequency f via the angular frequency $\omega = 2\pi f$ and the wavelength λ via the wavenumber $k = 2\pi/\lambda$. The variation of the pressure wave in time and space along the propagation direction can be described by a sinusoidal function:

$$p(y, t) = p_{ac} \sin(\omega t - ky) \quad (1.13)$$

At resonance, in Kundt's experiments, the incoming wave is reflected at the surface of the piston and travels in the opposite direction with the same frequency. The interference (superposition) of counter propagating waves forms a one dimensional pressure standing wave which can be described as:

$$p = p_{ac} \sin(\omega t - ky) + p_{ac} \sin(\omega t + ky) = 2p_{ac} \sin(\omega t) \cos(ky) \quad (1.14)$$

The pressure amplitude of the standing wave varies along the length of the tube. In a Kundt's experiment, particle accumulation takes place at characteristic points separated by half a wavelength. The pressure at these points is at minimum while the fluid velocity (fluid displacement) is at maximum. These pressure nodal planes are separated by points of maximum pressure and minimum fluid velocity, the pressure antinodal planes. Figure 1-9 shows a schematic of a one-dimensional wave in a closed system like the Kundt's tube. The

particle movement towards pressure nodes or antinodes is called acoustophoresis. It is the result of wave scattering on the particle's surface which imposes a force in the direction of wave propagation. In fact, Kundt and Lehmann used the standing wave induced particle pattern to measure the speed of sound c in the surrounding medium applying equation 1.15.

$$c = \lambda f \tag{1.15}$$

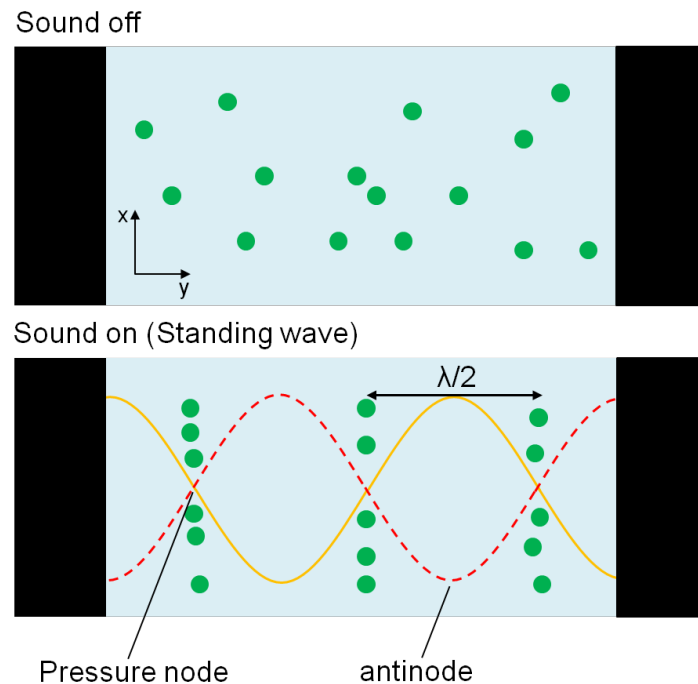


Figure 1-9: Schematic showing one dimensional pressure standing wave created by two counter propagating pressure waves in an enclosed system.

1.3.2. Primary acoustic radiation force

In an acoustic standing wave field, particles suspended in a liquid medium experience a gradient force along or against the acoustic pressure gradient depending on their mechanical properties. The gradient force on the particle is called primary acoustic radiation (PAR) force and arises due to a mismatch in the acoustic properties between the particle and the surrounding liquid medium. In particular, this results in a local distortion of the acoustic field in form of scattering around the particle's surface. The pressure difference on the surface of the particle triggers its motion.

The (PAR) force is a function of the acoustic properties (density, compressibility) of the particle relative to the properties of the liquid medium as well as the generated pressure and velocity field in the liquid. First theoretical descriptions of the acoustic radiation pressure on

an incompressible sphere in a plane standing wave were derived by King in 1934.¹⁰⁷ The theory was extended for compressible spheres by Yosioka and Kawasima in 1955¹⁰⁸ before Gorkov, in 1962, derived the expression for the PAR force on a compressible sphere in a arbitrary acoustic field. The time average acoustic radiation force is a gradient of a potential:¹⁰⁹

$$\langle F_{rad} \rangle = -\nabla U \quad (1.16)$$

where U is the acoustic force potential which is given by

$$U = V \left[\frac{f_1}{2\rho_m c_m^2} \langle p^2 \rangle - \frac{3f_2 \rho_m}{4} \langle |v|^2 \rangle \right] \quad (1.17)$$

with p and v being the pressure and velocity field in the particle's surroundings; V the volume of the particle and ρ_m and c_m the density and speed of sound in the (e.g. liquid) medium. The acoustic properties of the medium and particle join as the compressibility factor f_1 and the density factor f_2 which are given as¹¹⁰

$$f_1 = 1 - \frac{1}{\gamma\beta^2} \quad f_2 = \frac{2\gamma-2}{2\gamma+1} \quad (1.18)$$

where γ and β are the speed of sound ratio and density ratio of the particle (c_p, ρ_p) and medium (c_m, ρ_m), respectively

$$\beta = \frac{c_p}{c_{pm}} \quad \gamma = \frac{\rho_p}{\rho_m}. \quad (1.19)$$

In a miniaturized system for acoustophoretic particle manipulation any resonance results from a complex 3D resonance. However, a strong one dimensional coupling effect at single frequency excitation is usually observed. Then an approximation of the PAR force to a one dimensional plane standing wave can be made by assuming that the chosen frequency supports a strong resonance field in only one direction (axial) and that the wavelength is much longer than the particle radius. Then the axial component of the PAR force is given by:¹¹⁰

$$F_y^{rad} = 4\pi\Phi k_y a^3 E_{ac} \sin(2k_y y) \quad (1.20)$$

Where k_y is the wave number ($k_y = 2\pi/\lambda$); a is the radius of the particle; Φ the acoustic contrast which is described by:¹¹⁰

$$\Phi = \frac{5\gamma-2}{2\gamma+1} - \frac{1}{\gamma\beta^2} \quad (1.21)$$

and E_{ac} is the acoustic energy density which is given as:¹¹⁰

$$E_{ac} = \frac{p_{ac}^2}{4\rho_m c_m^2} \quad (1.22)$$

From equation 1.20, one can see that the force scales with the radius of the particle and frequency. The latter one is of great benefit when working with microfluidic systems, as the reduced length scale requires smaller wavelengths which are achieved with frequencies in the Megahertz range. Moreover, the direction and magnitude of the PAR force is also triggered by the acoustic contrast factor which depends on the particles density and compressibility in relation to the suspending medium. For example, a solid particle is less compressible and has a higher density than the surrounding aqueous media. This results in a positive contrast factor which forces particles to move to the pressure nodes. In contrast, a gas bubble can have a high density and high compressibility. Then the contrast factor becomes negative and the force is directed towards the antinodes. Figure 1-10 shows the acoustic force, pressure and velocity field at resonance (fundamental frequency) in a cavity (resonator) which supports half a wavelength, a common case in many microfluidic applications. The maximum pressure (antinode) is situated at the boundaries while the minimum pressure (node) is in the centre. The PAR force on a particle is zero at the boundary and maximal at the centre point between the pressure node and antinode. Depending on the acoustic contrast factor particles move either to the boundary or the centre.

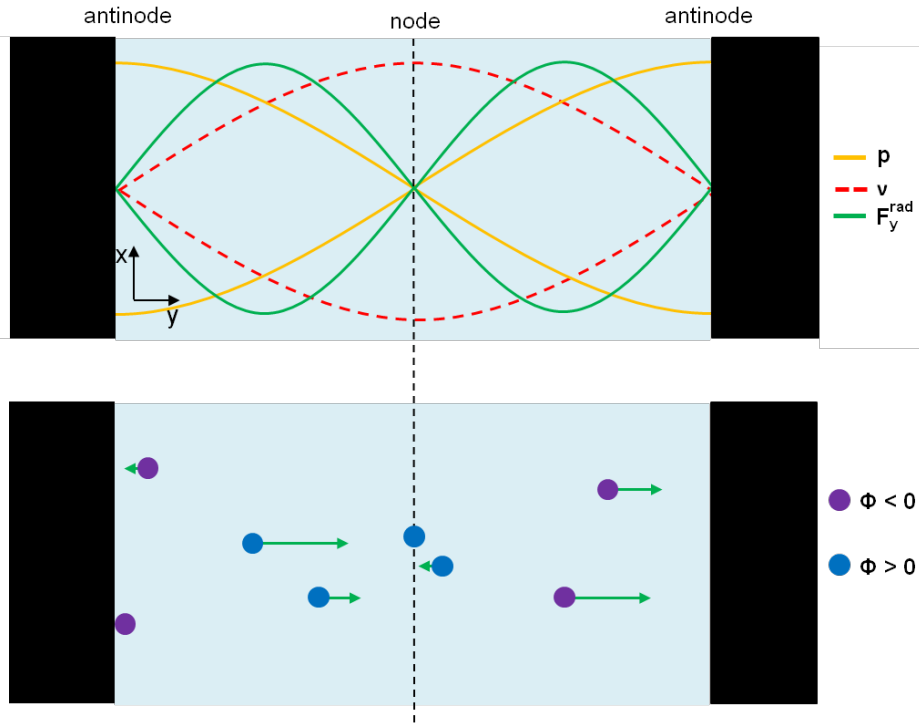


Figure 1-10: Schematic showing pressure, velocity and acoustic force fields in a cavity at a resonance which supports half a wavelength of the acoustic pressure wave (fundamental frequency). The sign of the acoustic contrast factor dictates the direction of the field. A negative sign means particles move towards the pressure antinode and *vice versa* for a positive sign.

Apart from the axial component of the PAR force which is based on both pressure and velocity gradients in the standing wave, it has been shown that large velocity gradients give rise to a significant lateral component of the PAR force.¹¹¹ This effect drives particles together generating a two dimensional manipulation effect (pseudo one dimensional resonance¹¹²). The lateral force component of the PAR force is given by:¹¹¹

$$F_{Lat} = \pi\rho\omega^2 a^2 s_0 s_e \quad (1.23)$$

Where s_0 is the fluid displacement amplitude through the centre of the particle and s_e the difference in displacement amplitude at the edge of the particle compared to the centre. The lateral force component is not as size dependent as the axial component in equation 8. Therefore, a strong lateral force requires large lateral gradients.

1.3.3. Secondary acoustic radiation force

The scattered acoustic field around particles interacts with nearby particles and gives rise to a secondary acoustic radiation (SAR) force. When the distance between particles becomes smaller, e.g. after particle alignment in the pressure nodal plane, interparticle forces, also called Bjerknes forces, influence the particles motion. This force can be expressed as:¹¹³

$$F_B = 4\pi a^6 \left(\frac{(\rho_p - \rho_m)^2 (3\cos^2\theta - 1)}{6\rho_m d^4} v^2(y) - \frac{\omega^2 \rho_m (\beta_p - \beta_m)}{9d^2} p^2(y) \right) \quad (1.24)$$

Where d is the center to center distance of the particles; β_p and β_m are the compressibility of the particles and the liquid medium; ω is the angular frequency; θ is the angle between the particles and the propagation direction of the incident sound wave.

The assumptions made in equation 1.24 include that there is a standing wave in y-direction and that the particles as well as the distance between them are much smaller than the acoustic wave length. The force can either be attractive (negative sign) or repulsive (positive sign) depending on the particles orientation with respect to the direction of wave propagation. If particles are aligned parallel to the wave propagation direction ($\theta = 0^\circ$) the first term of equation 1.24 becomes positive, while at a perpendicular orientation ($\theta = 90^\circ$) it becomes negative. At the pressure nodal plane the second term vanishes and particles are aligned perpendicular to the wave propagation which leads to an attractive force (Figure 1-11). The influence of the SAR force is very weak and becomes only important at short distances between particles when it dominates over the PAR force (e.g. at the pressure nodal plane a chaining of particles can take place).

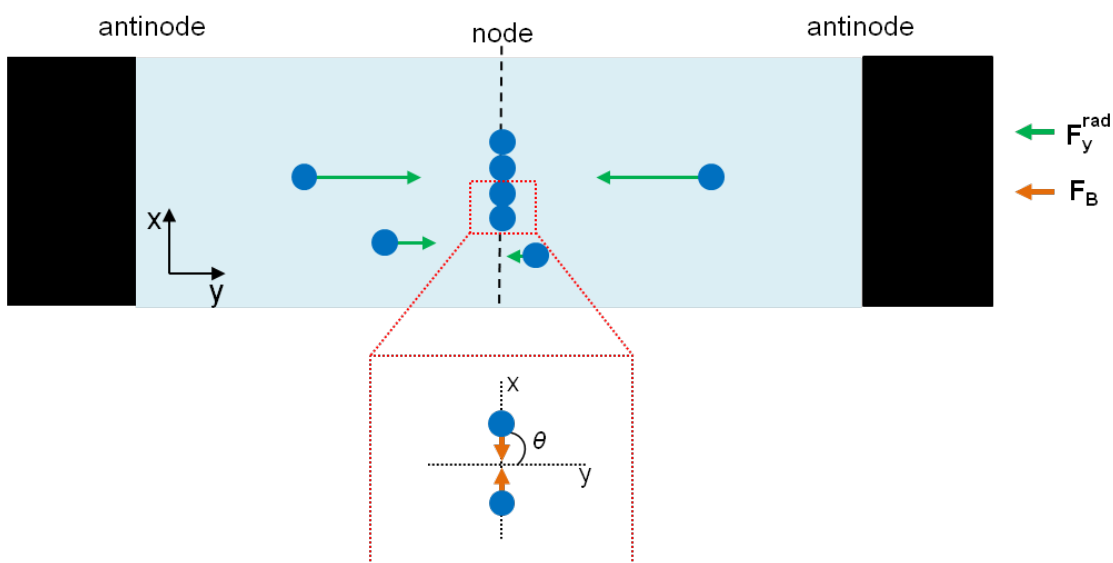


Figure 1-11: Secondary acoustic radiation force (Bjerknes force) becomes dominant at close particle distance. At the pressure nodal plane particles line up and create chain-like structures.

1.3.4. Acoustic streaming

The acoustophoretic movement of particles in microchannels is influenced by the particle size. Large particles (e.g. polystyrene beads) $> 2 \mu\text{m}$ move towards the pressure nodal plane due to the PAR force. However, smaller particles of less than $< 2 \mu\text{m}$ can be subjected to acoustically generated fluid vortex flows in the bulk of the liquid medium. These vortex flows are associated with acoustic streaming as a result of the absorption of acoustic energy in the medium. The streaming induced drag force dominates over the PAR force for small particles. In general three types of streaming can be distinguished:¹¹⁴ Inner and outer boundary layer streaming, Eckart streaming and cavitation micro streaming. The boundary layer streaming is induced by standing waves between parallel substrates (Figure 1-12). The inner boundary layer describes a fluid layer which is characterised by a higher viscosity compared to the bulk fluid because of its vicinity to a bounding surface. Acoustic energy dissipates into the inner boundary layer along this solid/fluid interface and generates strong vortices which drive subsequent bulk fluid vortices in the outer boundary layer. This type of streaming is the most common one seen in microfluidic resonator structures and is especially pronounced in shallow microchannels where the influence of the submicron thick inner boundary layer is stronger. A recent study by Barkholt *et al.* showed that outer boundary layer streaming can be suppressed by increasing the aspect ratio (~ 2) of the microchannel and likewise enhanced by decreasing it.¹¹⁵ In a laminar flow regime streaming can be used to mix fluids. The induced bulk fluid vortices have the maximum fluid velocity near the top and bottom wall of the resonator while decaying towards the centre of the vortex.

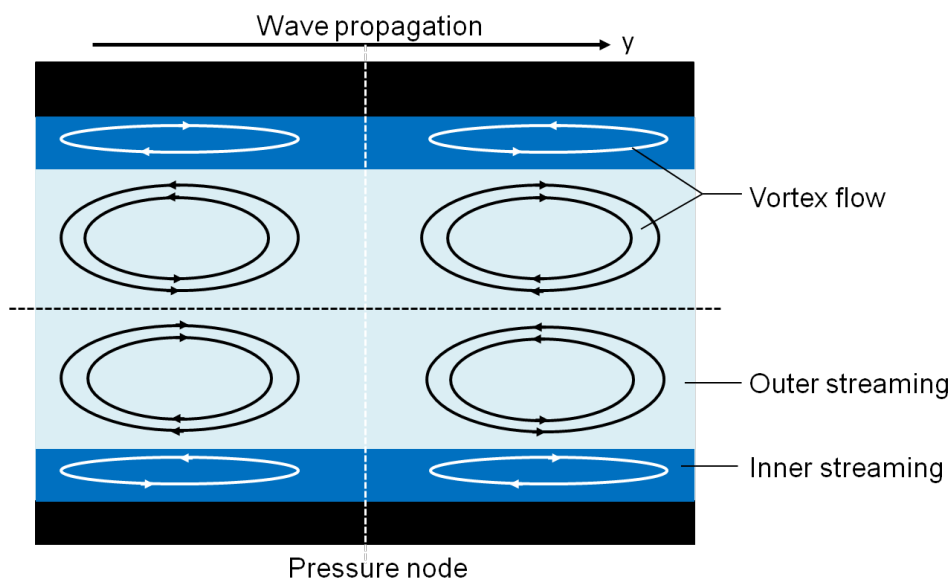


Figure 1-12: Schematic showing inner and out streaming rolls (vortex flows) around the pressure node in a standing wave.

Eckart streaming is the result of acoustic energy absorption in the bulk of a fluid when an acoustic wave travels through it. This usually occurs in standing waves at high frequencies where the microfluidic channel dimensions are large (several millimetres) as this supports sufficient wave attenuation in the bulk liquid. Last but not least, the interaction of oscillating gas filled microbubbles with acoustic waves can lead to cavitation microstreaming. Acoustic energy losses in the boundary layer of the microbubble combined with the stable oscillation generate amplified vortex flows which are several orders of magnitude larger compared to those around solid particles.¹¹⁴

1.3.5. Acoustic tweezing in microsystems

The transfer of the acoustic tweezing concept towards microsystems benefits from the fact that the PAR force is proportional to the frequency. An increased frequency increases the magnitude of the force to a level where efficient manipulation of particles is feasible.¹¹¹ Piezoelectric transducers are able to produce pressure waves in the ultrasonic range (100kHz – 100MHz) with corresponding wavelengths of millimeter to tens of micrometer and so are ideal for microfluidic channels. The forces are typically in the range of 10^{-12} N to 10^{-10} N for particles sizes of 1 μ m to 20 μ m in diameter.¹¹⁶⁻¹¹⁸

It is essential to create an acoustic resonance field and to do so, two main approaches for sound wave actuation have been established in the field of microfluidic acoustophoresis. These are based on piezoelectric materials and the inverse piezoelectric effect¹¹⁹ and can be divided into surface acoustic wave (SAW) and bulk acoustic wave (BAW) transducers. Here, pressure waves are produced by applying an oscillating electric field to electrodes on the piezoelectric substrate. This causes a mechanical deformation in the material as the result of the alignment of molecules with the electric field. Subsequently, a translation into a mechanical wave which propagates on the substrate's surface (SAW) or through the bulk of the substrate (BAW) takes place. In the following section, an introduction to micromanipulation systems using BAW and SAW transducers is given.

1.3.6. Bulk acoustic wave transducer for acoustic tweezing

Bulk acoustic wave transducers are typically made from piezo ceramics such as lead zirconate titanate (PZT). The transducer's resonance frequency is inversely proportional to the thickness of the piezoelectric material; and hence the device works best at one particular frequency. The transducer is modified with electrodes to enable the application of an electric

signal which is translated into a mechanical motion and induces a travelling sound wave. The wave propagates in form of longitudinal (Figure 1-13a) and transverse waves. BAW transducers are usually connected to the microfluidic chip via a coupling layer (e.g. glue, water) to enable the transmission of the acoustic wave. The microfluidic chip acts as acoustic resonator and its dimensions are chosen to match a certain resonance condition. This means a frequency is chosen which generates a plane standing wave across the width of the microfluidic channel. The most common resonator designs employ dimensions to support half a wavelength where a single pressure nodal plane is generated in the centre of the microchannel, while resonances in the vertical direction are suppressed by the geometrical mismatch.^{51, 120-126} This refers to the fundamental frequency of the resonator. However multiple pressure nodal planes at higher harmonic frequencies are used as well, depending on the application. An often used resonator design^{120, 127, 128}, called transverse resonator, is shown in Figure 1-13b. The BAW transducer is attached to the resonator from the bottom, although the position can be arbitrarily chosen as long as the frequency matches the resonance condition.¹¹¹ And even two opposing transducers excited at the same frequency may be used.^{129, 130} Nonetheless, in the most common designs, a longitudinal pressure standing wave is formed as the result of interfering counter propagating waves reflected at the microchannel wall.

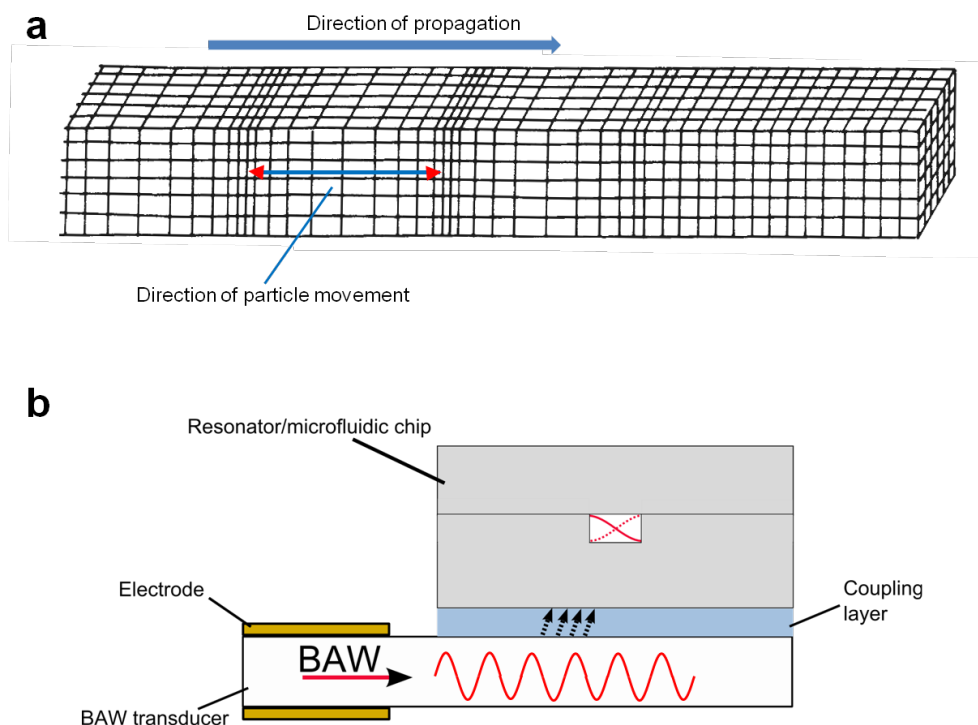


Figure 1-13: (a) Schematic (adapted from ¹³¹) of longitudinal wave travelling along the bulk of a material. (b) Schematic of an acoustic tweezing concept based on BAW transducer attached to a microfluidic chip.

The geometrical dimensions and the material properties are the key aspects when designing the transverse resonator, as they govern the fundamental acoustic forces.⁵¹ The material should provide the transmission of the acoustic energy into the manipulation medium at low loss (low damping) and exhibit good acoustic reflection properties to support a standing wave. The Q-factor is an indicator for the energy transmission into a resonator. It describes the ratio of the energy stored in the actuated resonator to the energy losses during an actuation cycle (damping) at certain resonance frequencies. A high Q-factor device resonates with larger amplitudes at the resonance frequency and produces larger acoustic forces for smaller power inputs compared to a low Q-factor device. However, low Q-factor devices can have a larger bandwidth at which they resonate compared to high Q devices. The Q-factor is highly material dependent and the fact that particle manipulation takes usually place in aqueous solutions, a sufficient difference in the acoustic impedance between the liquid and the resonator material is a good indicator for an appropriate material. The acoustic impedance Z is proportional to the speed of sound c and density ρ of the material (equation 1.25).

$$Z = \rho c . \quad (1.25)$$

The characteristic acoustic impedance of adjacent materials is helpful to estimate the pressure reflection coefficient R_p and transmission coefficient T_p using equation 1.25 and 1.26,¹¹¹

$$R_p = \frac{Z_2 - Z_1}{Z_1 + Z_2} \quad (1.26)$$

$$T_p = 1 - R_p \quad (1.27)$$

where Z_1 and Z_2 are the acoustic impedances of the materials. For instance, steel ($\rho = 7890 \text{ kg/m}^3$, $c = 5790 \text{ m/s}$) has an acoustic impedance of $46 \cdot 10^6 \text{ kg/sm}^2$ which is compared to water ($\rho = 1000 \text{ kg/m}^3$, $c = 1450 \text{ m/s}$) which has $1.45 \cdot 10^6 \text{ kg/sm}^2$, 30 times higher. This will result in high reflection and low transmission with a reflection coefficient of 0.93, in particular (maximum is 1 and means total reflection). Moreover, it is suggested that flat and parallel microchannel walls assist the creation of acoustic standing waves.⁵¹ Steel has ideal material properties but is hardly used in microfluidic applications as it is difficult to machine at these small length scales. Instead, silicon^{110, 127, 132, 133} and glass^{120, 134, 135} based microfluidic resonators fulfil the above mentioned requirements as well and are widely used. Polymer based devices are considered less suited due to their high acoustic losses and low reflection coefficients,⁵¹ however, despite this, glass-polymer¹³⁶⁻¹³⁸ or pure polymer^{139, 140} resonators have proven to be viable alternatives, which also benefit from easier fabrication (no etching

required, no anodic bonding), lower costs and mass production potential (e.g. moulding). The actual coupling of the acoustic energy from the piezoelectric transducer into the resonator is an additional factor that can be optimised to improve the energy transmission. This often involves acoustic impedance matching and the introduction of a matching or coupling layer between the resonator and transducer or in general between two adjacent layers to reduce acoustic losses due to reflections. A matching layer should have a lower characteristic acoustic impedance compared to the transducer but a higher acoustic impedance than the material that surrounds the microfluidic channel.¹¹¹

1.3.7. Surface acoustic wave transducer for acoustic tweezing

Surface acoustic waves (SAWs) propagate at the surface of a solid substrate. In miniaturized systems, SAW devices generate periodic deformation of a piezoelectric material which translates into a coherent travelling SAW with nanometer amplitude.¹⁴¹ The SAW has the form of a Rayleigh wave which is characterised by a longitudinal and a transverse component (Figure 1-14a).⁵³ The displacements decay exponentially with increasing distance from the surface into the substrate. Most of the acoustic energy ($\sim 95\%$) is confined within a depth equal to one wavelength.¹⁴² A SAW transducer consist of an interdigitated electrode (IDT) with a certain number of electrode fingers (Figure 1-14b) deposited (e.g. by metal evaporation) onto a single crystal piezoelectric substrate. Common piezoelectric materials are lithium niobate (LiNbO_3) and lithium tantalite (LiTaO_3). The application of an alternating electric signal to the IDT produces a SAW perpendicular to the electrodes and along the electrode length (aperture) as shown in Figure 1-14b. The signal matches the operation frequency of the SAW device which is chosen to match the electrode pitch and the gap of the IDT. This means the resonance frequency of the SAW device and the resulting wavelength of the propagating Rayleigh wave is governed by the geometry of the IDT and the speed of sound of the SAW substrate (e.g. 3965 m/s for LiNbO_3 , 128° Y-cut, propagation in x-direction). The pitch and the gap are typically of $\lambda/4$ and by using equation 1.15 SAW devices of particular working frequencies can be designed.

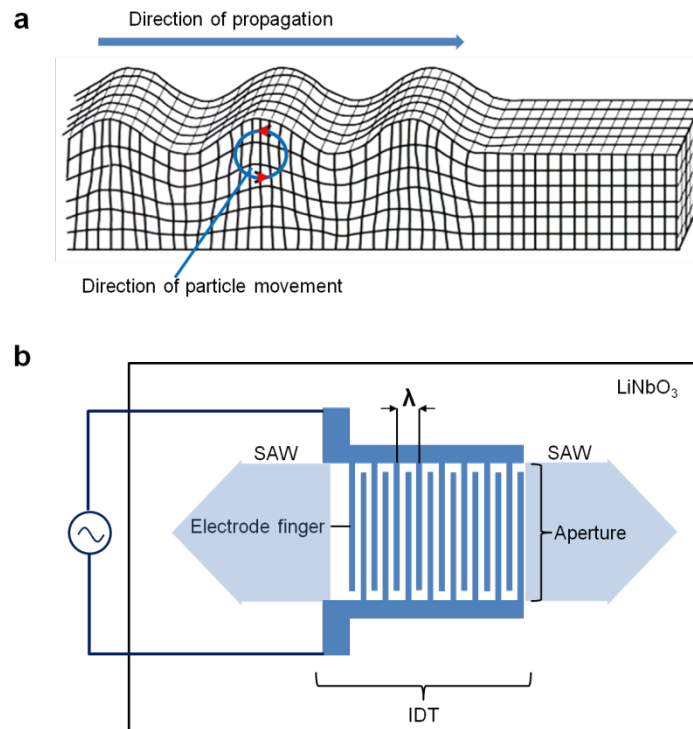


Figure 1-14: (a) Schematic (adapted from ¹³¹) of a Rayleigh wave travelling along a solid substrate with longitudinal and transverse component (adapted from Wikipedia.org). (b) SAW transducer with interdigitated electrodes producing a SAW along the aperture with wavelength λ defined by the pitch and gap of the IDT.

A conventional SAW transducer consist of straight electrodes and works best at a particular frequency (Figure 1-15a), though higher harmonics can be excited, too. However, an advantage of a SAW transducer compared to a BAW transducer is that the bandwidth can be tuned by structuring of the IDT. For instance, a chirped IDT design consists of an electrode pitch gradient along the SAW propagation direction and allows SAW generation over a wide frequency range (Figure 1-15b).¹⁴³ The electrode width can also be changed perpendicular to the wave propagation along the aperture of the transducer. This type is called slanted IDT and creates narrow SAW beams of varying frequency along the electrode length (Figure 1-15c).¹⁴⁴

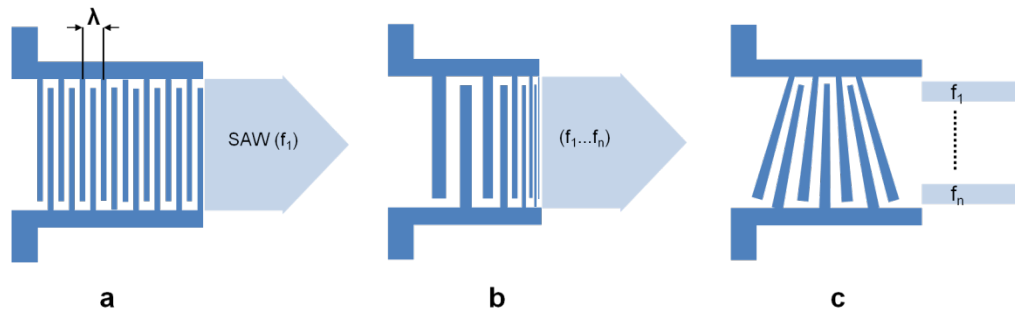


Figure 1-15: SAW transducer types used for microfluidic actuation. (a) Conventional SAW transducer for single frequency actuation defined by straight electrode fingers. Gap and pitch size of the IDT defines the wavelength. (b) Chirped IDT with electrode pitch and gap gradient for multiple frequency excitation along the IDT aperture. (c) Slanted IDT with changing electrode pitch and gap along the aperture for multiple frequency excitation confined by the local electrode dimensions.

A single transducer can be applied to actuate fluids (e.g. droplet) on top of the piezoelectric substrate. When a travelling SAW comes in contact with the fluid, acoustic energy diffracts into it due to a mismatch between the acoustic properties of the piezoelectric substrate and the fluid (Figure 1-16a). Diffraction occurs at a certain angle (Rayleigh angle, $\theta_R = c_m/c_s$) defined by the ratio of the sound velocities in the fluid and substrate and gives rise to a longitudinal pressure wave front that drives bulk liquid recirculation or acoustic streaming.¹⁴⁵ The energy transfer into the liquid and the creation of a longitudinal pressure wave is used for precise particle actuation on the surface of the piezoelectric substrate by means of standing surface acoustic waves (SSAW). This requires a pair of identical transducers to produce two counter propagating travelling SAWs.⁵³ The interference results in a one-dimensional SSAW (Figure 1-16b). Along the distance between the SAW transducer pair, the SSAW creates a series of nodes and antinodes on the surface. A microfluidic channel, usually made from PDMS, is precisely bonded with respect to the node and antinode position to bring a sample fluid in contact with the SSAW. It is understood that the pressure distribution on the substrate surface dictates the pressure distribution in the liquid. The wall of the PDMS channel may reduce the magnitude of the pressure but does not influence node or antinode position in form of reflections for instance. The pressure node and antinode position in the fluid corresponds to the acoustic field on the substrate.¹⁴⁶

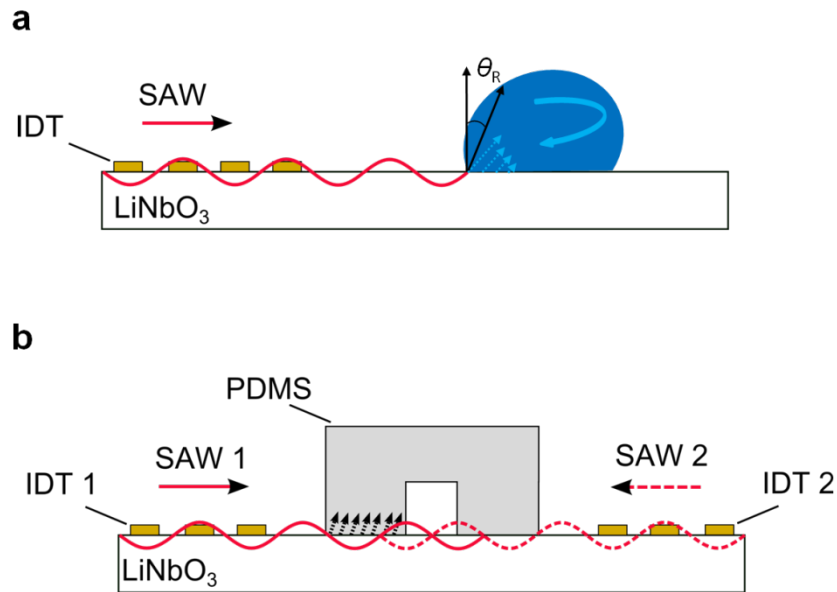


Figure 1-16: (a) SAW radiates energy into a liquid on the piezoelectric surface in the form of a longitudinal pressure wave. Acoustic attenuation results in acoustic streaming which drives a bulk fluid flow. (b) Standing surface acoustic wave (SSAW) produced by a pair of identical SAW transducer excited at the same frequency. A PDMS channel precisely placed relative to the pressure nodal planes enables particle manipulation by the PAR force.

SAW transducers for microfluidic applications have several advantages compared to BAW transducers. This include a better control of the excitation frequency in a wider range as well as high frequency actuation enabling a versatile and flexible approach and allows a more precise and controllable manipulation of fluids and suspended particles.⁵³ Furthermore, the fact that the acoustic field is confined to the substrate surface makes the use of a cheap polymer based microchannel feasible. Last but not least, the versatile nature of SAWs has been demonstrated in many applications which not only involve the manipulation of fluids and particles using travelling and standing waves but also sensing application to detect biological and chemical compounds.¹⁴⁷

However, one can see a disadvantage in the fact that the particle manipulation using SSAW needs to be carried out directly on the piezoelectric substrate. This impedes the development of disposable units considering the price of piezoelectric materials (e.g. ~ \$50 for a single LiNbO₃, y-cut 128°, 3 inch wafer of 0.5mm thickness from <http://www.pmoptics.com/>). The bonding step of the microchannel (e.g. PDMS), has to be very precise in respect to the position of nodes and antinodes. This can lead to fabrication problems when lateral channel geometries reach scales down to tens of micrometers. The sample throughput by means of standing wave based manipulation is low compared to BAW approaches. BAW actuation has been shown to process liquids with flow rate of ml/min^{148, 149} while SAW based processes work with µl/min rates which is most likely associated with low

bonding strength of PDMS to the piezo surface (leakage problems) but also with the fact that the acoustic field is confined to the substrate surface making shallow microchannels (20 μm – 50 μm)¹⁵⁰⁻¹⁵³ necessary.

1.3.8. Applications of acoustic forces in microsystems

Acoustic tweezing is commonly used for focussing, patterning enrichment, sorting and trapping of particles. The PAR force is used to precisely define the position of particles and cells in a microsystem under static conditions or continuous flow. The transfers of particles between fluids or their retention against the fluid are promising strategies to replace common benchtop methods used for washing and purification. Moreover, the acoustic properties of individual particle types can be addressed to enable sorting and enrichment. Last but not least, acoustic streaming induced drag forces can also be applied to achieve sorting of particles and the mixing of fluids. The following section focuses on applications in enclosed microfluidic channels. However, it should be mentioned that SAW and BAW can be applied for open microfluidics where sample liquid droplets with suspended particles (e.g. blood samples) are processed by fluid actuation such as mixing,¹⁵⁴ concentrating,¹⁵⁵ merging¹⁴⁴ or nebulisation¹⁵⁶, although the volume throughput is very low and precise particle handling is limited due to the induced streaming effects.⁵²

On chip microfluidic flow cytometry requires the focusing of particles into a single file for precise individual detection. This can be achieved hydrodynamically by sheath flows¹⁵⁷ but increases the complexity (several laminar flows) of the microsystems and can cause shear stress to sensitive particles such as cells. The PAR force has been applied to generate precise particle streams in microfluidic channels combined with optical detection using laser systems. Piyasena *et al.* used opposing bulk acoustic transducers attached to a machined aluminium frame sandwiched between glass slides to align cells and particles in pressure nodal planes.¹⁵⁸ The work demonstrated the creation of multiple particle streams (up to 37 pressure nodes) and their individual probing for particle counting. However, the one dimensional nature of the produced pressure nodes impeded the resolution of individual particles at higher concentrations. SSAW approaches were developed by several groups with a one dimensional single nodal plane^{151, 159} and even a three dimensional focusing strategy was proposed by using non-uniform acoustic fields.¹⁴⁶ The latter one has been explained by the presence of a weaker but still significant lateral acoustic force which acts perpendicular to the axial primary acoustic radiation force. Besides microfluidic cytometer, the concept of acoustic focusing has found its way into a conventional benchtop cytometer.

The Attune® cytometer developed by AB (Applied Biosystems, Thermo Fisher Scientific, USA) uses BAW transducer to focus samples in a capillary into a single stream.

Acoustic standing waves have also been used for one and two dimensional non-invasive patterning of particles in quiescent liquids. This can be beneficial for studying cell-cell interactions, the construction of microarrays or the generation of cell aggregates for tissue engineering. Wood *et al.* applied SSAW to form lines of particles in water on the surface of the piezo substrate sandwiched by a glass slide. This approach was extended by adding another pair of identical IDTs orthogonal to the first pair creating two SSAW for spot like patterning.¹⁶⁰ Shi *et al.* applied the same concept to pattern cells in PDMS channels¹⁶¹ and introduced slanted IDTs to enable adjustments of the distance between the patterned particles by frequency changes.¹⁶² Bulk acoustic transducer integrated in the channel wall of a square¹⁶³ or heptagonal¹⁶⁴ microfluidic cavity has been shown to produce particle and cell patterns. So far, the most sophisticated systems for particle and cell patterning as well as individual particle control in a quiescent fluid were developed by British Universities (Glasgow, Dundee, Bristol and Southampton) as part of the collaborative Sonotweezer project. These systems consist of multi-element transducer arranged to heptagonal (8 transducer)¹⁶⁵ or circular (16 and 64 transducer)^{166, 167} arrays. The individual control of these transducers has been utilized to generate arbitrary particle and cell patterns^{164, 168-170} as well as independent manipulation of multiple particles using Bessel-function acoustic pressure fields.¹⁶⁷

The trapping of particles (retention) against a flow in microfluidic compartments is of use for a range of applications. For instance, this enables microfluidic perfusion system that can be used to study the long or short term interaction of drugs, chemical or stimulants with non-adherent cells and the influence on cell-cell interactions. It can also be applied to extract particles from complex samples followed by enrichment and subsequent washing steps. So far, such systems have been developed using BAW transducers incorporated in channel walls^{116, 136, 137} or attached to microfluidic chips^{112, 134, 135}. For example, Evander *et al.* developed a concept which enabled the retention of yeast cells with subsequent culturing in an acoustic trap by perfusion with cell culture medium. The BAW transducer was integrated into the channel wall to generate a standing wave with an opposing glass reflector at a fundamental frequency. Interestingly, the trapping was achieved with a single transducer producing forces of up to 450 pN. The lateral component of the primary acoustic radiation force (equation 1.23) as well as interparticle forces (equation 1.24) were exploited to keep particles stably positioned within the nodal plane.¹¹⁶ Alternatively, two transducers and dual frequency excitation can be used to achieve two dimensional particle manipulation. This was

demonstrated by Manneberg *et al.* through creating plane standing waves across the width and the height of the microchannel using two BAW transducers.

The PAR force scales with the volume and the acoustic properties of the particles and its direction is governed by the acoustic contrast factor. This has been exploited to achieve the separation, enrichment and sorting of particles within microfluidic chips under continuous flow. For instance, the group around Thomas Laurell showed that blood cells can be separated from lipid particles in a blood sample using the difference in the acoustic contrast factors.^{121, 122, 124, 125} A BAW transducer attached to a silicon microchannel chip with three outlets generated a single pressure node in the channel centre. Blood cells were concentrated towards the channel centre while lipid particles were forced to the channel wall (antinode). The lipids left the chip separated from blood through the outer microchannel outlets with separation efficiencies close to 100 %. This concept gained much attention as it solves a major problem in surgery where lipid micro emboli in blood can cause severe damage to the patient's brain. The research led to a spin-out company AcouSort (www.acousort.com) which focuses on clinical product development based on acoustophoretic separation.

The size dependant transverse displacement of particles has been used to achieve sorting of particles into specific channels outlets. Sorting of complex bead samples has been demonstrated by Peterson *et al.*¹²³ Bead sizes of 2 μm , 5 μm , 8 μm and 10 μm were separated into four outlets with efficiencies up to 94 %. A wide microchannel with sample injection from side channels was used in conjunction with a single BAW transducer attached to the chip. Particles were pushed towards a single pressure node in the centre and the difference in the travelling time was utilized to guide particles into the outlets. Similar concepts with varying BAW transducer arrangements for bead separation can be found in the literature.^{130, 138, 140, 171} The same principle has been applied to enable the separation of various cell types. Liu *et al.* demonstrated separation of the waterborne parasites *Giardia lamblia* (15 μm) and *Cryptosporidium parvum* (5 μm) into different channels with efficiencies of up to 84%.¹⁷² Kumar *et al.* showed that small *Lactobacillus rhamnosus* bacteria can be separated from much larger hybridoma cells.¹⁷³ A SAW transducer approach was demonstrated by Ai *et al.* where a cell mixture containing *E.coli* bacteria and blood cells were first hydrodynamically focused in the channel centre followed by acoustic separation with efficiencies of more than 90%.¹⁷⁴ In this case the PDMS channel walls were placed along the pressure nodal plane. The larger bloods cells moved towards the channel wall while the bacteria remained located in the centre. The same device strategy was applied by Nam *et al.* to achieve separation of blood cells and platelets in whole blood samples with efficiencies of

74%.¹⁷⁵ Platelet-derived microparticles (0.1 μm to 1 μm) have been found to be involved in many physiological processes such as vascular disorders, tumor metastasis, osteoconduction and angiogenesis. However, platelets are very sensitive to shear stress and therefore sensible enrichment methods are required to enable the study of this cell type.

The magnitude of the PAR force is partially defined by the acoustic contrast factor. Particles of the same size but different densities experience a different PAR force. Jo *et al.* showed a SSAW based approach where equally sized polystyrene and melamine beads (10 μm) could be separated with efficiencies up to 98%.¹⁷⁶ In the setup, beads were first focused along the channel centre by one set of IDTs. This was followed by the separation step where a second pair of IDTs created pressure nodal planes close to the channel walls. The higher-density melamine (1.71 g/cm^3) beads were pushed to the channel sides while the lower-density polystyrene (1.05 g/cm^3) beads remained in the centre. A similar concept was applied by Nam *et al.*, where same sized alginate beads, filled with different amounts of cells, were separated with high efficiencies (97%).¹⁷⁷

Last but not least, acoustic streaming induced drag forces can be utilized for microfluidic manipulations. In resonator structures acoustic streaming is often an unwanted effect as it disrupts the particle movement. For small particles, the streaming induced drag force overcomes the PAR force making particle separation in microfluidic cavities difficult.¹¹⁵ However, streaming induced bulk liquid flows within standing wave fields can be applied for mixing purposes. For instance, Bengtsson *et al.* showed that bulk vortex flows enhanced mixing of adjacent laminar streams.¹⁷⁸ An otherwise diffusion limited enzymatic reaction could be enhanced by 20 % using ultrasound. Besides standing wave induced streaming in resonator structures, travelling surface acoustic waves can generate flow circulations when the SAW radiates energy in form of a longitudinal pressure wave into a liquid. Jo *et al.* showed that efficient mixing (up to 97%) of two laminar streams (one water, one dye) using SAW transducers is a promising route for the development of microreactors for chemical and biochemical applications.¹⁷⁹ Recently, acoustic streaming has been applied to sort cells and particles in a microfluidic chip. Franke *et al.* used acoustic streaming induced by a travelling SAW to deflect a hydrodynamically focused flow stream into a side channel achieving sorting rates of several KHz.^{180, 181}

1.4. Combination of force fields – “eierlegende Wollmilchsau”

The German term “eierlegende Wollmilchsau” is a colloquial figure of speech which describes a hybrid animal (pig, sheep, cow and chicken) that produces meat, wool, eggs and milk. The term is often used to outline a system that meets requirements or compensates shortcomings by introducing new developments. The introduction above presented a range of force fields used for various microfluidic manipulations and highlighted benefits and promising applications. However, all of these methods have shortcomings and limitations which may not be overcome easily by the technology itself but more likely by implementing and combining several novel technologies.

For instance, acoustic manipulation is well suited to manipulate large populations of particles fairly independent of medium conditions such as conductivity, pH or surface charges. The standing wave field and the forces associated with it can cover large manipulation areas and the whole volume of the sample liquid. Nevertheless, it is not yet possible to select an individual particle by an acoustic trap and move it around in arbitrary fashion within a microfluidic compartment. Single particle handling has been shown by Ding *et al.*¹⁴³ but the generated pressure landscape generated by 2 pairs of orthogonal chirped SAW devices made independent movement of several particles in the system impossible. It may require spatially localised pressure nodes generated by a focused ultrasound beam from a moveable external transducer or micron sized individually addressable piezoelements integrated in the chip substrate to obtain single particle precision for several particles simultaneously. In contrast, optical methods such as OET are able to generate a very localised force field to control one or multiple (or even thousands of⁵⁵) particles independently. OET is also able to cover large areas of a chip as long as the optical system provides a sufficient field of view¹⁸², however, the range of the force field decays sharply with increasing distance to the substrate surface, impeding particle manipulation in microchannels with large aspect ratios. In a conventional OET device, operation is also dependent on the medium conductivities. At high conductivities (>100 mS/m) the generated DEP force is too low for sufficient particle handling and throughput. Optical tweezing (OT) instead, can be truly considered as a method where contactless individual manipulation in three dimensions can be achieved as no contact to any other medium is required. However, massive or individual manipulation of particles over large areas is not easily achieved and requires sophisticated laser and optics systems that are limited to specialised laboratories. Magnetic field based approaches are able to produce very localised force fields similar to OET with individual and independent manipulation of several particles. The operation of such systems is fairly independent on medium properties (pH, conductivity) but many

particles of interests (e.g. mammalian cells, bacteria) are diamagnetic requiring magnetic labelling or changes to the magnetic properties of the surrounding medium to increase magnetic forces. Of course, the costs, the ability for miniaturization and ease of usage are criteria which impede the wide spread use and the combining of these technologies to overcome limitations.

Nonetheless in recent years researchers worked on integrating and combining various force fields into microfluidics and showed different functions successfully. For instance Thalhammer *et al.* combined acoustic fields with OTs in a single setup.¹⁸³ A capillary was used as microfluidic compartment attached to a BAW transducer and integrated into optical macro tweezer setup which applied holographically shaped laser beams. This work demonstrated that large particles ($> 50 \mu\text{m}$) and a motile organism (*Euglena gracilis*) can be trapped within pressure nodes of a standing wave parallel to the top and bottom surface of the capillary and importantly, in the same plane over a large area (several mm^2) of the microfluidic compartment. This enabled an easier addressing of individual particles with the OT due to the fixed focal point (all particles in the same plane) and a less complex laser beam adjustment due to the acoustic force acting as restoring force towards the focal point which reduced optimizations of the scattering force to hold particles stable in the trap. This work also showed that polystyrene beads aligned in several pressure nodal planes can be individually addressed by OT and when the optical gradient force dominated particles could be pushed individually into adjacent pressure planes. OT can be used to measure the acoustic forces exerted on a particle directly, when the optical forces are carefully calibrated as shown by Bassindale *et al.*¹⁸⁴ Then the particle displacements into an equilibrium point where acoustic and optical forces balance allow precise force quantification. A combination of OT and acoustic fields has also been used to investigate the interaction between cavitation microbubbles (MB) and cells to study sonoporation effects towards therapeutic MB mediated drug delivery.¹⁸⁵ The OT was used for precise positioning of MB close to adherent cells, while a BAW transducer generated an acoustic field to insonify the MB and induce MB collapse.

Magnetic field induced particle manipulation has been used in conjunction with OT and ultrasound induced acoustic forces. A study by Chung *et al.* demonstrated separation of magnetic and non-magnetic particles into specific microchannels using magnetic fields, OT or both combined.¹⁸⁶ An electro-magnet attached to the PDMS-Glass microchip (near an outlet junction) and a single beam laser (focused at the target outlet channel) were used to force particles into a channel by attraction to high magnetic field regions and/or to the optical trap. This kind of hybrid system is of advantage when specific particle properties (magnetic,

non-magnetic) can be addressed to enable separations and enrichments. A similar goal was followed by Adams *et al.* where an integrated acousto-magnetic manipulation device was applied for multiparameter particle sorting under continuous flow.¹⁸⁷ The device consisted of a microchannel chip made from silicon and glass. A BAW transducer and permanent magnet were attached to the top and bottom of the chip in a sequential manner to create individual stages for magnetic and acoustic separation. The permanent magnet provided a homogeneous field which was distorted by an array of angled nickel electrodes (ferromagnetic) deposited on the bottom substrate of the microchannel to generate a non-uniform field with high field regions along the electrode edges. A sample mixture containing magnetically labelled and unlabelled particles was injected into the chip and hydrodynamically focused along a channel wall before approaching the acoustic separation stage. A standing pressure wave with a single pressure node in the channel center was used to guide particles responding to the acoustic force into the pressure node while any other particles remained in the initial laminar stream and left the channel via a waste outlet. Magnetic particles within the pressure node were attracted to the high magnetic field regions when approaching the nickel electrodes and could be deflected towards a side channel while unlabelled particles in the pressure node were collected by a central outlet channel. A combination of magnetic and acoustic forces was also used to enrich tuberculosis bacteria from a sputum sample.¹⁸⁸ Magnetic beads modified with antibodies to capture bacteria were mixed with the sample and then injected into a microfluidic chamber. An attached BAW transducer was utilised to speed up bead agglomerations into pressure nodes while an attached magnet was used to pull down beads to the surface after acoustic actuation which enabled removal of the supernatant liquid and washing of the bead sample enriched with the bacteria. Afterwards, acoustic levitation into pressure nodes was used to detach beads from the surface before elution of the sample for further analysis steps.

The first demonstration of dielectrophoretic and acoustophoretic particle manipulation into a microfluidic device was shown by Wiklund *et al.*¹⁸⁹ The system consisted of a glass-silicon microchannel chip with curved and linear metal electrodes deposited on the bottom glass substrate to create non-uniform electric fields, while a BAW transducer attached to the top glass substrate enabled plane acoustic standing waves across the width of the microfluidic channel. A standing wave with multiple pressure nodes was created to align beads under continuous flow. Beads approaching the activated metal electrodes experienced a negative DEP force which led to trapping and eventual agglomeration in front of the electrodes and within pressure nodal planes. However, careful adjustment of the DEP force could be used to guide a particle towards a particular pressure node or induce fusion of particle

agglomerates originating from different pressure nodes. A device concept developed by Ravula *et al.* utilized interdigitated electrodes deposited on a glass substrate for DEP manipulation and a BAW transducer attached to the glass substrate to couple acoustic energy in a microfluidic channel. The microfluidic channel was defined by a glass chip bonded onto a glass substrate. The device was used to preconcentrate and align beads coarsely by the PAR force before achieving more precise focussing into fine bead streams by negative DEP along the electrode array. These studies demonstrated that the long range acoustic force can be used to rapidly arrange beads in a microfluidic device while the short range DEP force can be applied to perform much localised manipulation.

1.5. Aim of this work

The aim of the study is to develop a platform that enables the combined application of acoustic and electric fields for particle manipulation in a microfluidic chip. For the first time optoelectronic tweezing is being combined with acoustic tweezing to demonstrate selective particle handling based on their electrical and mechanical properties.

2. Materials and Methods

This chapter includes the design and fabrication of surface acoustic wave transducers, superstrates with embedded microchannels and optoelectronic tweezer chips. Furthermore the setup for acoustic and optoelectronic tweezing is presented and the protocols for the preparation of particle suspensions, cell culture and cell handling are described.

2.1. Fabrication and characterisation of SAW transducer

2.1.1. Mask for photolithography

Polymer-emulsion film masks were used for the fabrication of SAW devices and microchannels. The mask layout was designed using the editor software L-Edit (Tanner Research Inc., USA). Mask printings were performed by JD Photo-Tools (Photo Data Ltd., UK). The super-high resolution option with 128,000 dpi offered by JD Photo is suitable for a minimum feature size of 10 μm .

2.1.2. SAW device

The material of the surface acoustic wave device was a 3 inch, 0.5 mm thick lithium niobate wafer (LiNbO_3 , purchased from Roditi, UK). The piezoelectric substrate was characterised by a 128° Y-cut and wave propagation speeds of 3992 m/s and 3488 m/s in x- and y-direction, respectively. An interdigitated transducer of a slanted electrode design was transferred by standard photolithography. As shown in Figure 2-1, a cleaned wafer was first spin coated with S1818 resist at 4000rpm for 30 s. This was followed by a softbake at 90°C for 5 min. The coated wafer was exposed to UV light (i-line, 365 nm, Mask aligner MA 6, SÜSS MicroTec AG, Germany) for 4.3 s through a polymer-emulsion film mask containing the slanted electrode design. The exposed resist was developed in 1:1 Microdev (Microposit, Shipley, UK) and pure deionised water for 1.5 min. Afterwards metal deposition was performed using an electron beam evaporator (Plassys II, PLASSYS-BESTEK, France) to form the electrodes. First an adhesion layer of 10 nm NiCr was deposited followed by 100 nm layer of Au. The metal-lift off step was performed in Acetone at 50°C for 30 min to 60 min. Before using the device wires were connected with silver paint applied to the connection pad of the interdigitated electrodes.

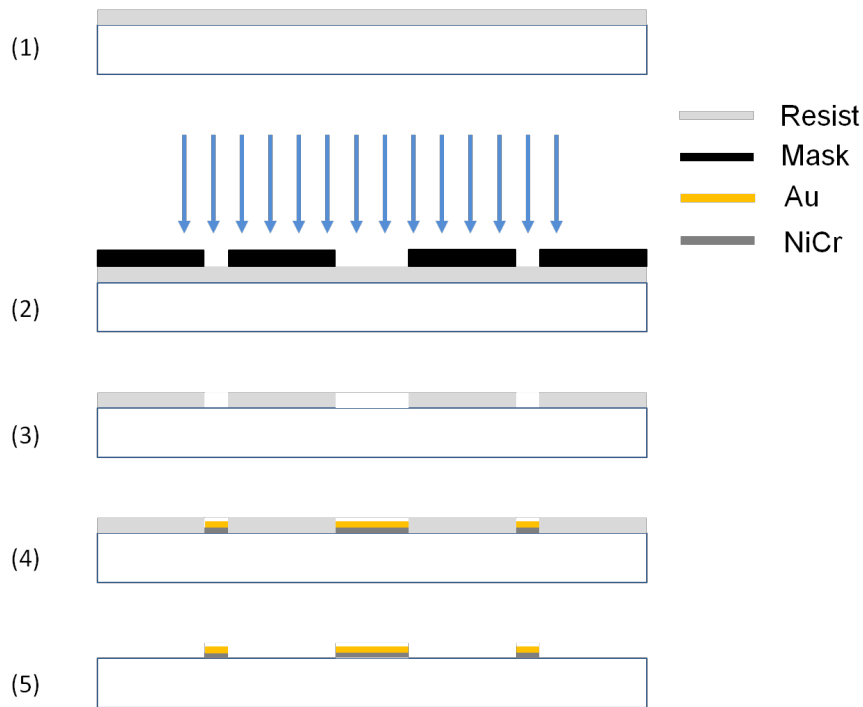


Figure 2-1: Fabrication process for SAW device. (1) Cleaned lithium niobate wafer is spin coated with S1818 resist and softbaked for 5 min at 90°C. (2) Transfer of slanted electrode pattern by UV exposure for 4.3 s. (3) Development of exposed resist. (4) Deposition of 10 nm NiCr layer and 100 nm Au layer. (5) Metal-lift off in Acetone for 30 min to 60 min at 50°C.

When designing a SAW transducer the crystal orientation is of major importance as the sound velocity varies in y-(3488m/s) and x-direction (3992m/s). Based on the simple relationship for the wavelength of a SAW¹⁹⁰

$$f = \frac{c}{\lambda},$$

$$\lambda = D$$

where f is the frequency, c the speed of sound in the material and D the pitch between adjacent electrode fingers, a transducer with a broad frequency range was developed. In particular, the electrode pitch and width of 18 electrode pairs within an aperture of 2 cm were varied linearly from 285 μm to 181 μm (x-direction) and 249 μm to 159 μm (y-direction), resulting in a theoretical bandwidth of 3.5 MHz to 5.5 MHz. A picture of a slanted interdigitated transducer is shown in Figure 2-2.

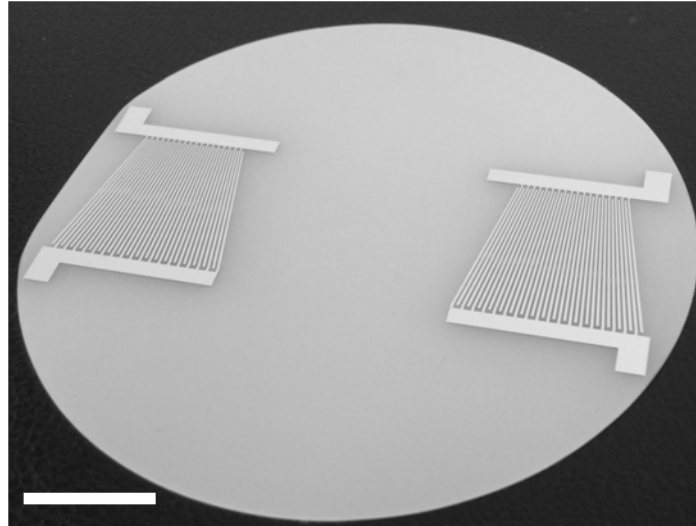


Figure 2-2: SAW device based on slanted interdigitated electrodes deposited on a three inch lithium niobate wafer. The SAW device is designed for a bandwidth of 3.5 MHz to 5.5 MHz (Scale bar: 2 cm).

2.1.3. SAW device frequency response

The reflection coefficient of the SAW device was measured using the scattering parameter (S-parameter) function of an Agilent Technologies E507C ENA series network analyzer. The S-parameter S_{11} measures the frequency dependence of the reflection and the corresponding radiation after applying power to the electrical network. This is recorded as spectra showing the delivered power (dB) against the chosen frequency band. The SAW device was connected to the network analyser, directly.

2.1.4. SAW device actuation

A signal generator (TG5011 TTI, UK) combined with an amplifier (Mini Circuits ZHL-5W-1) and a 3 A, ± 24 V DC power supply were applied to drive the SAW device.

2.1.5. Visualization of surface acoustic wave emission

An infrared camera (Ti 25, Fluke, USA) was used to visualize the surface acoustic wave emission and position along the aperture of the slanted interdigitated electrode. The piezoelectric substrate in front of the electrodes was coated with water-based jelly. The absorption of acoustic energy in the gel delivered by the travelling surface wave is converted to heat. The increase in temperatures can then be visualised using the infrared camera and the position dependent frequency response can be investigated. Furthermore, the SAW was visualized by its surface displacement using a Laser Doppler Vibrometer (Polytec.Germany). The vibrometer Laser was used to probe and scan the surface of the piezoelectric wafer after applying an electric signal to the SAW device. Using the Doppler Effect, the laser reflection induced by the surface displacement can be used to visualize the SAW amplitude

on the LiNbO_3 substrate. The vibrometer was also used to visualize the displacement in the microchannel integrated in the superstrate. In particular, the laser was focused onto the bottom slide of the superstrate and the displacement across the channel width and along the channel length was measured.

2.2. Microchannel fabrication for resonator and OET chip

2.2.1. Superstrate concept

The superstrate with embedded microchannels consisted of custom cut but standard microscope slide (bottom substrate, Menzel Glaser, H: 1 mm x D: 1.5 cm x L: 4 cm) and cover slip (top substrate, Menzel Glaser, H: 0.16 mm x D: 1.5 cm x L: 4 cm). Negative photoresist SU8 (MicroChem Corp., USA) was sandwiched inbetween and acted as a bonding agent between the substrates and defined the layout of the microchannels. Before the cleanroom fabrication process, the cover slip had inlet and outlet holes drilled according to the microchannel mask design. A Dremel drill (MultiPro, Robert Bosch GmbH, Germany) mounted to a work station for precise vertical adjustments and drilling was used in conjunction with Tungsten drill bits of 0.5 mm diameter (Diama, UK). To achieve good drilling results, the substrate was placed on a slightly wetted microscope slide and moved until a fixation due to the adhesion forces of water between the substrate and the slide was achieved. This prevented unwanted moving of the substrate and assured a homogenous and clean surface. The outlet and inlet positions were marked with a pen and a droplet of water was placed onto it. The drill bit was carefully moved towards the marked position and fully immersed in the water droplet. The water was used to avoid heat generation and fast wear of the drill bits. The driller was set to its highest speed and the vertical position was carefully changed until contact between drill bit and substrate was made. The drilling was performed in batches, slowly to avoid cracks in the glass cover slip. The clean room fabrication process is shown in Figure 2-3. In particular, the glass substrates were thoroughly cleaned in Acetone, Isopropanol for 5 min in an ultrasound bath, followed by rinsing with deionised water and blow drying. To make sure no water is left on the surface a dehydration bake at 180°C for 30 min was performed. Afterwards SU8 3050 was spincoated onto the bottom substrate using a two step protocol. First, SU8 was spread over the substrate with a coating speed of 500 rpm for 10s. Second, the speed was increased to 4000 rpm for 30s. After spincoating the substrate was placed on the hotplate at 95°C. The cover slip containing predrilled holes for inlets and outlets was bonded immediately onto the freshly prepared SU8 film by carefully placing it on top of the bottom substrate. This was

followed by a softbake at 95°C for 25 minutes. The photoresist was exposed (i-line, 365 nm, 200 mJ/cm³, Mask aligner MA 6, SÜSS MicroTec AG, Germany) through a polymer-emulsion film mask aligned to the predrilled holes in the cover slip for 60 seconds. A post-exposure bake at 65°C for 2 minutes and 95°C for 6 minutes was performed prior to developing the unexposed SU8 through inlet and outlet holes using Microposit EC solvent (Shipley, USA). The whole chip was placed in a beaker containing the developer. The developing process was monitored by observing the phase change (from solid to liquid) of the unexposed SU8 in the microchannel. A clear interface between the solid and the liquid phase was visible during this process. Once the interface vanished, the unexposed SU8 was fully dissolved. To remove any residues left in the channel structures, the chip was placed in an ultrasonic bath with acetone for 5 min to 10 min. Afterwards the chip was rinsed properly with Acetone, followed by blow drying until the acetone inside the chip is fully removed. The inlet and outlets were connected to PTFE tubing (#30, Cole and Parmer, UK) using shortened 10 µl pipette tips glued to the substrate.

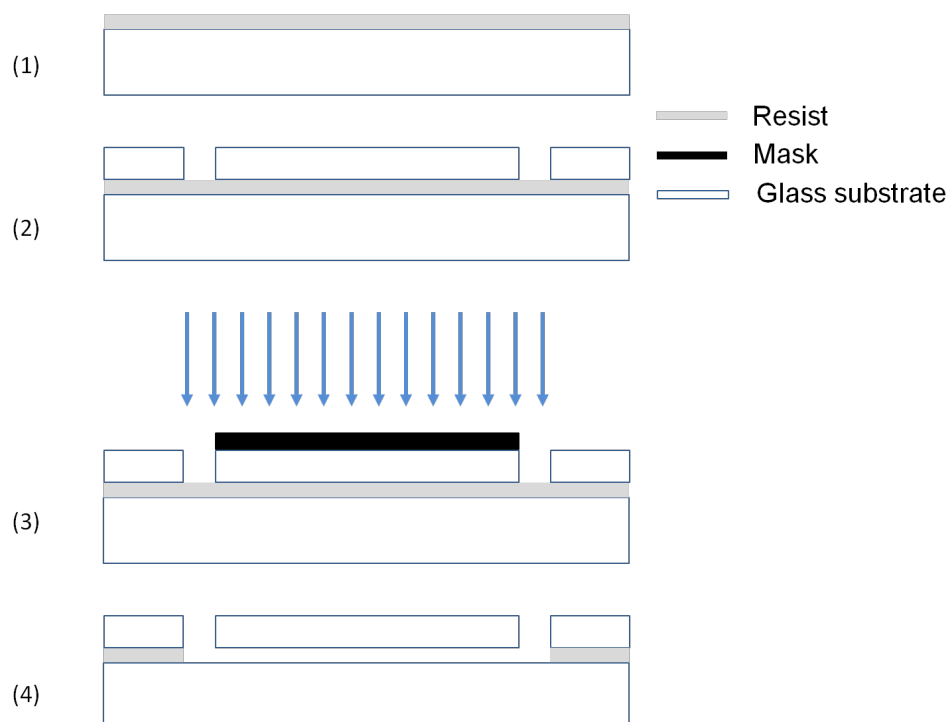


Figure 2-3: Fabrication process for superstrate with embedded microchannel. (1) A cleaned microscope slide was spin coated with SU8 3050 resist and placed on a 95°C hotplate (2) A cleaned cover slip with predrilled holes for outlet and inlet is immediately but carefully placed on top of the freshly prepared SU8 film and the structure is softbaked for 25 min at 95°C. (3) The mask for the microchannel is placed on the top substrate and exposed with UV for 60 s. (4) After a postexposure bake at 65°C for 2 min and at 95°C for 6 min the superstrate is developed with EC Solvent.

2.2.2. Fabrication of amorphous silicon substrates

Indium tin oxide (ITO) coated standard microscope slides (H: 1 mm x D: 25 mm x L: 75 mm) and cover slips (H: 0.16 mm x D: 22 mm x L: 40 mm) were purchased from Diamond Coatings Ltd. (UK). The thickness of the ITO layer was approximately 300 nm (measured from SEM images). The sheet resistance for the microscope slides and cover slips was between 15 ohm/square and 30 ohm/square. A transmission spectrum for the ITO coated glass substrate is shown in Figure 2-4. It can be seen that the transmission is highest between 525 nm and 600 nm (89%).

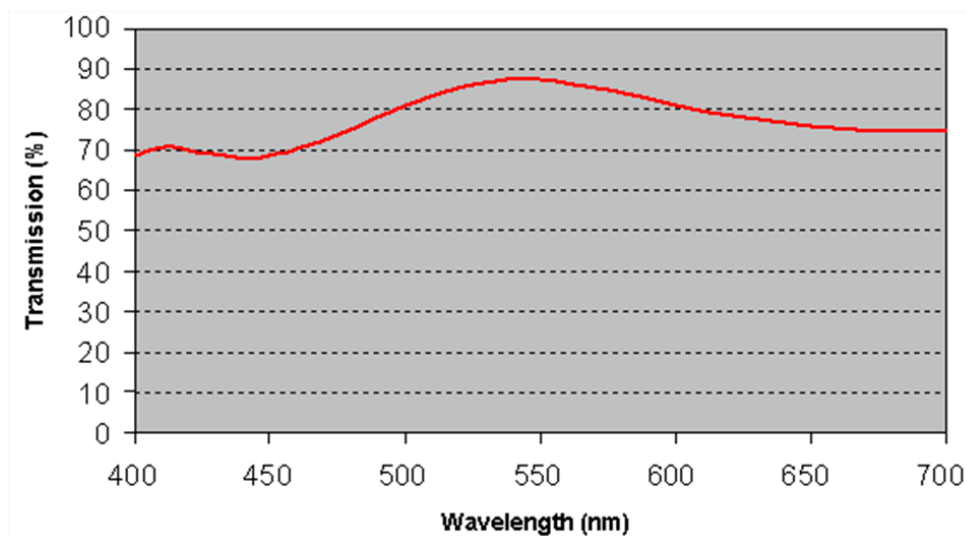


Figure 2-4: Transmission spectrum for ITO coated glass substrates (provided by Diamond Coatings Ltd, UK)

The photoconductor for the optoelectronic tweezer chip was amorphous silicon (aSi) and only microscope slide were used as photoconductor substrate. Prior to the deposition the ITO coated slides were thoroughly cleaned in Acetone, Methanol and pure deionised water. Afterwards the prepared substrates were coated with 1 μm amorphous silicon layer by plasma-enhanced chemical vapour deposition using pure silane gas (10 W, 300 mTorr, 250 $^{\circ}\text{C}$, 15sccm). A typical result after the evaporation process can be seen in Figure 2-5a. A homogenous aSi layer without contaminations or holes was obtained for the 1 μm process. A cross-section of the substrate is given in Figure 2-5b. Thicker layers of the photoconductor would reduce voltage drops in the dark state and so were also fabricated. The advantage would have been a reduced leakage of electric fields into the liquid when no illumination and only a voltage signal was applied. But the fabrication results were not promising for 1.5 μm and 2.0 μm aSi layer due to adhesion problems. The extra stress in the thicker film caused buckling and eventual de-lamination. In Figure 2-6a a 1.5 μm aSi sample substrate is shown. A smooth and homogenous layer could be fabricated using the evaporation process but after

cleaning the substrates prior to the OET chip fabrication a delamination could be observed indicating a weakened adhesion with increased aSi thickness (Figure 2-6b).

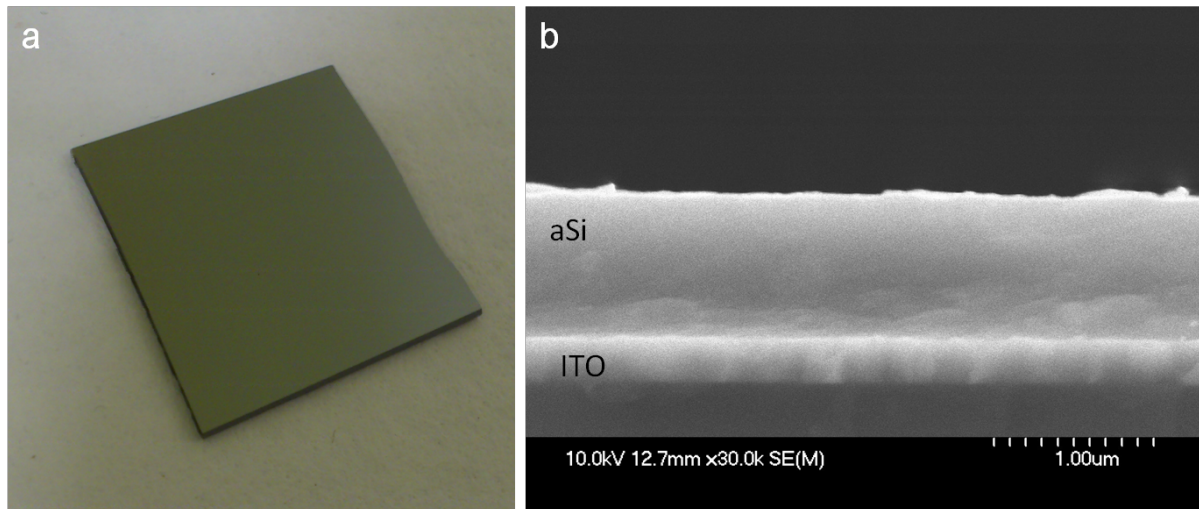


Figure 2-5: (a) a 1 μm amorphous silicon layer evaporated on ITO coated glass slide and (b) cross section of substrate showing 0.3 μm ITO and 1 μm aSi layer.

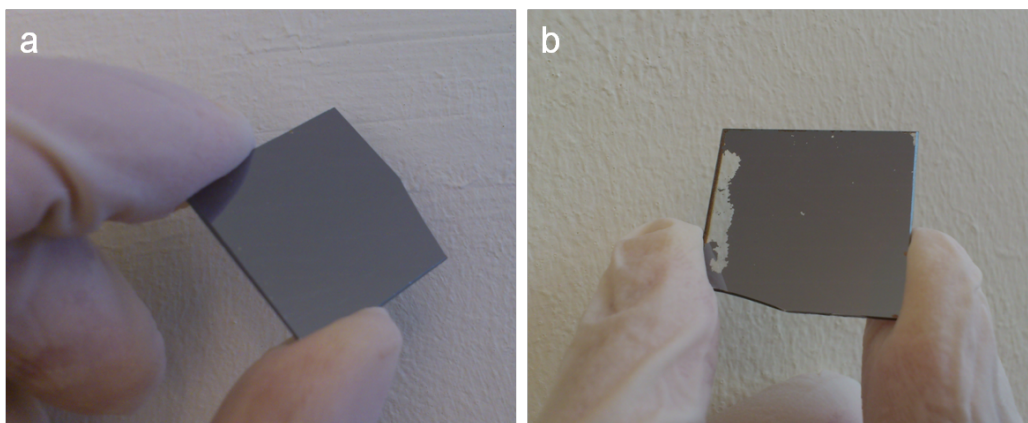


Figure 2-6 (a) 1.5 μm aSi layer evaporated on ITO coated slide. (b) Same substrate after standard cleaning procedure in ultrasonic bath using acetone, isopropanol and deionized water.

2.2.3. OET chip fabrication

The OET chip consisted of two electrode substrates. The bottom substrates were made of a standard but custom-cut microscope slide with a 0.3 μm ITO layer and an 1.0 μm aSi layer deposited on it. The top substrate was a standard cover slip coated with ITO. The OET chip fabrication followed the same fabrication steps as described above for the superstrate. Only a couple of modifications were made and included a change in the substrate layout, dehydration bake and an adjustment of the spincoating settings and type of SU8 resist. For the substrate layout an overhang of the bottom and top substrate as show in Figure 2-7 was introduced to allow wire connection to each electrode.

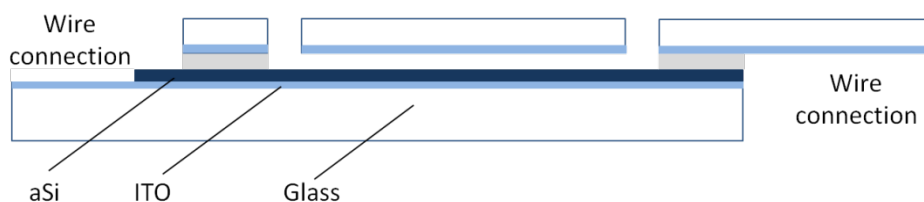


Figure 2-7: Layout of the OET chip. Overhang of each substrate for wire connections to ITO layer.

After cleaning of the substrates the temperature for the dehydration bake was reduced to 90°C and substrates were usually dried over night. The temperature reduction at this point is crucial as a change in the oxidation state of the ITO layer occurs at higher temperatures > 110°C and resulted in an increase in the sheet resistance. Furthermore to adjust the thickness of the SU8 layer sandwiched between the substrate different types of SU8 were used. SU8 3050 coated with spinning speeds of 1000 rpm and 4000 rpm for 30s with an initial coating step at 500 rpm for 10 s. At 4000 rpm, the following steps were as described above. For the 1500 rpm coating, the softbake time was increased to 45 min at 95°C. SU8 3025 was used to obtain more shallow microchannels. SU8 3025 was spincoated with an initial coating step of 10s at 500 rpm followed by 4500 rpm for 30 s. Afterwards the softbake was reduced to 20 min at 95°C. The exposure time was only adjusted for the substrates coated with spinning speeds of 1500rpm. Here, UV light exposure was set to 90s. It has to be noted that the overhangs of the top substrate with exposed ITO layer needed to be covered with mask material to avoid resist exposure at this particular area. The postexposure bake for the 1500 rpm and 4500 rpm (SU8 3025) coated substrates was set to 10 min and 5 min at 95 °C with an initial bake at 65°C for 2min. After resist development the wire connection areas were cleaned properly (wiped with acetone) and on the bottom substrate the aSi layer was removed by scratching open to achieve a connection to the ITO layer underneath. Wires were first connected with conducting silver paint and left for drying for one hour. A strong fixation was achieved by applying epoxy glue (BondLoc, UK) to the connection area. A TG5011 (TTi, UK) signal generator with high impedance load was used to apply AC signals to the OET chip.

An alternative and more conventional assembling process was used for experiments with microbubbles. Instead of SU8, double side tape was applied to the photoconductor as a spacer. The ITO electrode was simply pressed onto the tape to create a sandwich structure. The height of the tape was approximately 100 µm.

2.2.4. Scanning electron microscope and Dektak profilometer

An electron microscope (SEM Hitachi S4700, Japan) was used for visualization of ITO and amorphous silicon layers as well as for crossection images of the sandwich structure in the

superstrate and OET chip. A 45° holder was used for mounting the substrates. Prior to imaging, the substrate were coated with a 10 nm metal layer of Au/Pd (80/20) using a sputter coater (Agar Scientific, UK). The substrates were placed vertically to achieve an appropriate coating result of the crosssection. Afterwards Imaging was performed under high vacuum with an accelerating voltage of 10 kV and an emission current of 10 μ A.

Dektak Height Profiler (6M, Veeco, USA) was used to verify thicknesses of SU8, ITO and aSi layers. The surface contact measurements were performed using a diamond stylus of radius 12.5 μ m. A force of 7 mg was set to the stylus while measurement ranges were set to 65 kÅ and 655 kÅ.

2.3. OET setup

The system to run the optoelectronic tweezing chip is shown in Figure 2-8a. A microscope (BX51, Olympus, Japan) equipped with a dual port (U-DP, Olympus, Japan) attachment was used for observation of the micromanipulation and for camera recordings as well as image projection onto the photoconductor. The dual port allowed for simultaneous operation of camera and data projector for light projection. Cameras used within this study were an UC30 (Olympus, Japan), a FASTCAM SA3 model 120K-M3 (Photron), a Thorlabs CMOS Camera, (DCC1545M, UK), a MotionScope CMOS camera (M3, Redlake, USA) and an Orca Flash4.0 CMOS-camera (Hamamatsu, Japan). The data projector model was a Dell 1510X (USA). The projector was connected to a PC and images for light induced electric fields were created using Microsoft PowerPoint. The software was mainly used because of its availability and ease of creating arbitrary light patterns on the fly by making use of the drawing toolset. Figure 2-8b shows a schematic of the light path through the system.

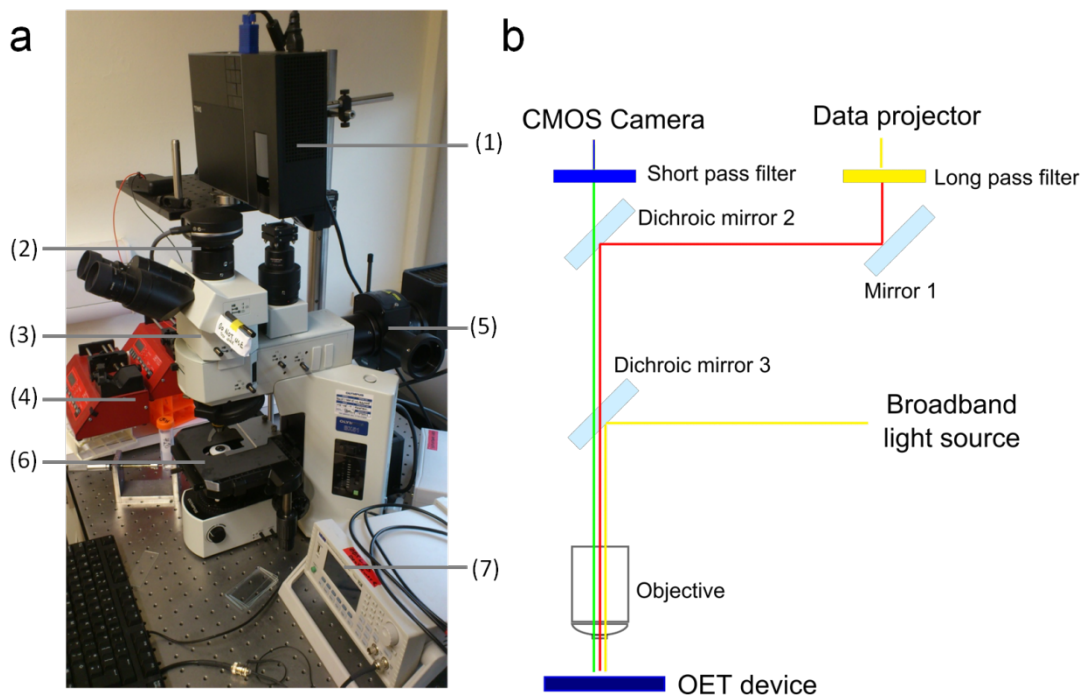


Figure 2-8: (a) OET setup based on Olympus microscope BX51 showing data projector (1), CMOS camera (2), dual port for simultaneous image projection and video recordings (3), syringe pump (4), light source (5), stage for OET chip (6), function generator (7). (b) Schematic of the optical path through the OET system.

The microscope was equipped with a 4x (NA: 0.1), 10x (NA: 0.4), 20x (NA: 0.4) and 40x (NA: 0.65) objective. An increase in the numerical aperture increased the sharpness of the light pattern as well as the light intensity. Measurements of the optical power using an optical power meter (Wilcom FM1318, USA) resulted in a power range given in table 2-1. These values were converted into optical intensities and then corresponding aSi conductivities were

obtained using a reference plot.⁵⁶ In Figure 2-9 the change in the conductivity of the photoconductor depending on the light intensity is shown. A linear increase in the conductivity for increased light intensities using the set of microscope objective was obtained.

Table 2-1: Optical power for different objectives.

Objective	Optical power [W]
4x	0.022
10x	0.03
20x	0.016
40x	0.007

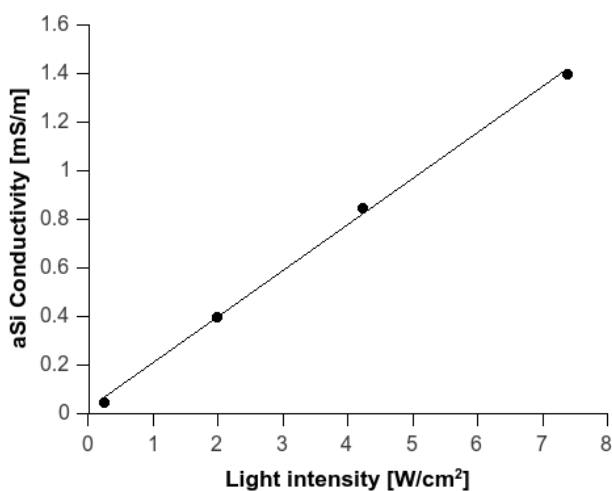


Figure 2-9: Photoconductor conductivity depending on light intensity produced by different objectives (4x, 10x, 20x, 40x).

2.4. Particle and cell samples

2.4.1. Polymer beads

Polystyrene beads (Bangs Laboratories) of different sizes (1 μm , 3 μm , 6 μm , 8 μm , 10 μm) were suspended in deionised water containing 0.1% Tween 20 to prevent aggregations of beads and unspecific binding to the substrate surface. The conductivity was adjusted by adding potassium chloride to a deionised water and Tween 20 suspensions prior to the addition of beads. Beads were injected into the chip manually using pipette or automatically using a syringe pump (NE-1000, New Era Pump Systems, USA). Continuous sorting experiments of 1 μm and 3 μm beads were conducted in chapter 4.3.10.4. Samples of 5 μl

were collected at the channel outlets and counted after 1:1 dilution in buffer using a haemocytometer (Neubauer, Marienfeld, Germany). It has to be noted that the counting of 1 μm and 3 μm using this kind of counting chamber is not trivial. To achieve a reasonable result a video of the counting chamber while focusing through the volume was taken. This assured that beads in different planes and normally out of focus could be identified.

2.4.2. Microbubbles

SonoVue (Bracco Suisse SA, Switzerland) MBs were purchased as a kit including a vial containing 25 mg of lyophilised sulphur hexafluoride (SF_6) powder and a pre-filled syringe with a 5 ml sodium chloride solution. The salt solution is usually used to dissolve the powder, instead DEP buffer (10 mS/m) was transferred into the vial followed by 20 seconds of shaking to mix all contents. MB samples were withdrawn into a syringe and then manually injected into the optoelectronic chip after further 1:10 dilution in DEP buffer.

2.4.3. Blood cells

Human blood samples were provided by the blood transfusion service (Glasgow) within 2 to 4 days after collection from the donor. These samples require an ethical approval which was obtained from Dr. Lisa C. Ranford-Cartwright (Institute of Biomedical and Life Sciences, Division of Infection and Immunity, Glasgow Biomedical Research Centre, University of Glasgow). The blood was stored at 4°C prior to usage. The total storing time was 5 days before new blood samples were collected. However, it has to be noted that the age of the blood cell population is not homogenous. A blood cell has a life span in the body of ~ 120 days. During that time its durability decreases due to repeated large deformations when circulating through microvessels. Blood cells were washed one time in PBS, followed by three washing steps in a buffer solution made of 8 % sucrose, 0.3% glucose and 3 mM HEPES (pH 7.4, 10mS/m) at 1500 rpm for 5 mins using a conventional centrifuge. For the experiments in PBS buffer, blood cells were only washed one time in PBS and then resuspended. Blood samples were manually injected using a pipette or automatically using a syringe pump (NE-1000, New Era Pump Systems, USA). For continuous lysis experiments blood samples were injected using a syringe pump. Continuous lysis experiments (Chapter 6.3.5) were carried out at flow rates of 5 $\mu\text{l}/\text{min}$. Volumes of 10 μl were sampled shortly after injection and used to quantify cell concentrations in a haemocytometer (Neubauer, Marienfeld, Germany).

2.4.4. Breast cancer cell line MCF 7

MCF 7 cells were cultured in cell media, DMEM, containing 10 % serum, 4.5 g/l Glucose, L-Glutamine, Penicillin and Streptomycin. After injection of the MCF 7 cells, the OET chip was

placed in a petri dish and incubated over night at 37 °C (5 % CO₂) to assure adherence to the photoconductor surface. Cell biology experiments are often conducted on flat surfaces in vitro. Hence, the cell line was used as a model to demonstrate the feasibility of lysis of a cell type that is cultured and adhered on the surface of the photoconductor inside the superstrate chip.

2.4.5. Jurkat cells

Jurkat cells were cultured in RPMI growth media containing 10 % serum, at 37 °C (5 % CO₂). Cells were washed one time in PBS, followed by three washing steps in a buffer solution made of 8 % sucrose, 0.3% glucose and 3 mM Hepes (pH 7.4, 10mS/m) at 1500 rpm for 5 mins. Jurkat cells are suspension cells of spherical shape with a diameter of 10 µm to 12 µm. Jurkat cells are suspension cells of spherical shape with a diameter of 10 µm to 12 µm. The cells were used to demonstrate the lysis of a different cell line and differences in the lysis times between cell types (e.g. red blood cells).

2.4.6. *Trypanosoma Cyclops*

The parasite was cultured in Cunningham's medium with 10% FCS at 27 °C and washed in PBS one time (5000 rpm, 5 mins) before being spiked into a prepared blood sample. Control experiments were carried out with heat inactivated non-motile parasite. The washed parasite sample was placed in a water bath two times for 10s at 95°C. Continuous sorting experiments were carried out to separate the parasite from a blood sample (Chapter 4.3.10.4.). The parasite was spiked into the blood sample followed by injecting the sample into the microchannel using a syringe pump. At the outlets, 10 µl of the processed sample was collected and then used to quantify cell concentrations in a haemocytometer (Neubauer, Marienfeld, Germany).

2.5. Software

2.5.1. Video and image analysis

Tracker v4.82

Tracker is an open source physics software developed by Douglas Brown. It was mainly used to analyse video sequences from acoustophoresis experiments. Videos were imported into the software and the automatic particle tracking function was used to monitor the bead movement over time. After defining dimensions and coordinates, this software was used to extract values for bead distance moved over time, velocities and accelerations. Tracker is written in Java and can be installed on any operating system.

ImageJ v1.47 and MBF plugin collection

ImageJ is an open source Java software environment for image and video processing. It is able to import a wide range of different file formats and provides a standard tool set for image analysis. However, its advantage lies in its extendibility by adding new plugins for more features and tool sets. ImageJ was used particularly for analysing feature sizes in microscopic images and for intensity analysis over time by applying tools in the MBF plugin.

The MBF plugin is a collection of 200 additional functions especially useful for data obtained from microscopy studies. The plugin enables the import of different microscope brand specific file formats and provides a number of time course processing and analysis routines.

2.5.2. Modelling and data analysis software

COMSOL Multiphysics

COMSOL (v3.5) is a finite element analysis simulator. The AC/DC module was used for simulations of electric field strength and transmembrane potentials in red blood cells (the chapters 1.2.6, 4.3.2). The pressure acoustic module was used to simulating the pressure distribution in the superstrate (see chapter 6).

GNU Octave

Octave (v3.6.4) is programming language intended for numerical computation. It is a free software and compatible with MATLAB. Octave was used to model the dielectrophoretic response of different sized particles under varying conditions.

3. Optoelectronic tweezing integrated into microfluidics

The integration of optoelectronic tweezing (OET) into a robust microfluidic chip is demonstrated, characterized and applied to particle manipulation. It is shown that several parameters (e.g. liquid medium conductivity, electrode gap) influence the electric field strength and hence the dielectrophoresis (DEP) force imposed on particles. The experimental results demonstrate fast and complex dielectrophoretic particle manipulation in microfluidic channels under pressure driven flow. However, voltage leakage effects and corresponding leakage fields in the microchannel have been found to be responsible for undesired particle movements which should be addressed to optimise OET based particle manipulation. Nonetheless, the developed concept is a vital step of combining OET with acoustic tweezers.

3.1. Introduction

So far, many microfluidic functions have been demonstrated using OET. Chiou *et al.* showed trapping and moving of polystyrene beads, *E.coli* and *HeLa* cells on the surface of the photoconductor.⁵⁵ The use of moving light patterns^{64, 66} or virtual sieves⁶⁷ has been beneficial for the separation of different bead sizes, bead - cell mixtures and different cell types. OET has also proven to be useful for cell analysis such as discriminating between dead and live cells⁶⁷ and developmental stages of complex systems like mouse embryos,⁹⁸ as well as being helpful for identifying viable motile sperm⁹⁷ and normal oocytes¹⁹¹ for fertilization experiments.

The examples mentioned above show that OET is mainly used as a manipulation tool for batch processes where a particle or cell sample is only injected between the electrode substrates and no sample collection is envisaged after manipulation. The most common approach to create OET chips is based on applying adhesive tapes to the electrodes to create liquid chambers with microfluidic volumes. This approach is cheap and fast to apply, however, it is less suited for approaches where pressure driven flow is needed. It is prone to fast liquid absorption into the adhesive tape which weakens the bonding between the electrodes and can be cumbersome to create well defined microfluidic channel geometries.

An attempt to integrate OET into microfluidics for continuous particle manipulation under pressure driven flow has been carried out only by a small number of studies.¹⁹²⁻¹⁹⁴ The reason for this is not necessarily associated with a low demand as there are many groups working on OET based micromanipulation. The reason is rather associated with the restriction of fabrication methods which makes the integration into robust continuous microfluidics channels challenging. For instance, anodic bonding of glass or silicon substrates containing etched microchannels is a common approach to create robust chips, however sputtering of aSi or ITO on such etched-structured substrates is difficult and the temperatures during the bonding process is very high, leading to changes in the chemical structure of aSi and ITO which effects the electrical properties. Polydimethylsiloxane (PDMS) is the material of choice for fast prototyping of microfluidic chips but not well suited for OET considering the conventional device structure. The PDMS moulding procedure results in partially enclosed microfluidic channels while OET devices typically require channels that expose the liquid sample to the electrode substrates to be able to generate electric fields. The same problem arises when considering other polymer materials (PMMA, PC) which require moulding techniques for structuring.

Alternatively, a lateral OET (LOET) device can be considered as shown in a study by Ohta *et al.*⁷⁰ Here the ITO and the aSi layer have been structured to create an interdigitated electrode array which resulted in electric field lines parallel to the photoconductor instead of a perpendicular arrangement in the conventional OET device. This is a way to open up the possibility of using materials like PDMS but it complicates the fabrication and spoils the flexibility of light induced electric fields as the field creation is restricted to the structured parts. Furthermore, the ITO electrodes are partially exposed leading to non-uniform electric fields independent of the light (similar to standard DEP with fixed electrodes).

Lin *et al.* showed an approach where SU8 was spincoated and photopatterned on an aSi substrate.¹⁹² A top ITO substrate was then placed on the SU8 layer and epoxy glue was applied around the edges of the substrates to seal the chip. However, the ITO substrate was not fully bonded, resulting in a thin gap between the SU8 and the ITO. Huang *et al.* investigated approaches where PDMS can be modified with transparent and conductive layers.^{193, 195} In particular a gold/titanium mesh as well as carbon nanotubes were deposited on the PDMS surface and particle manipulation (trapping and transporting) has been successfully shown. However, the manipulation speed of several $\mu\text{m/s}$ compared to the conventional OET device where tens of $\mu\text{m/s}$ can be achieved indicate a weak performance which might be attributed to the mesh structure of the gold layer compared to a homogenous ITO layer as well as the high sheet resistance (500 ohm/sq) in the nanotube layer. Last but

not least, Yang *et al.* used a similar approach to the one developed in this work. A photopatternable hydrogel solution (poly(ethylene glycol) diacrylate, PEGDA) was sandwiched between the electrode substrate followed by exposure to UV and developing through predrilled holes in the top ITO substrate. Instead of using amorphous silicon, a low cost and spin-coatable organic photoconductor, titanium oxide phthalocyanine (TiOPc), was used. Using this concept, Yang *et al.* were able to manipulate particles continuously by light induced electric fields. Particles were stepwise deflected along a series of virtual electrodes, resulting in lateral displacements of up to 90 μm . TiOPc is a cheap and easy to fabricate alternative to aSi, however, as Yang *et al.* described, TiOPc is very sensitive to organic solvents which makes cleaning of fabricated chips impossible as decomposition of the photoconductor would occur. Moreover, large water uptake in the hydrogel might be a major disadvantage during the experiments as well as for the entire chip structure because of increased swelling and possibly reduced bonding strength at the substrate interfaces.

In this work, the objective was first to integrate the conventional OET structure into a robust microfluidic chip using a material which provides appropriate sealing and bonding properties to connect electrode substrates and avoid leakage of sampling liquids. Furthermore, the material should withstand cleaning procedure using organic solvents. A certain flexibility in microchannel geometry to tune electric properties of the OET chip was also desirable. And last but not least, the used materials should have sufficient acoustic reflection properties to enable acoustophoretic particle manipulation (see Chapter 4).

For this work, we decided to use SU8 3000 series to create microfluidic channels and integrate OET into a chip format. SU8 is a photopatternable negative resist with good bonding strength to glass and silicon substrates. As shown in previous studies, SU8 has good mechanical and chemical stability making it an excellent material for many microelectromechanical system applications.¹⁹⁶ Moreover, lithography-defined SU8 structures and layers have shown to be biocompatible^{197, 198} making it a suitable material for biological cell handling applications. Last but not least, a SU8/PMMA microchannel structure has been used for acoustic particle manipulation indicating suitable mechanical properties for particle manipulation based on standing acoustic waves.¹⁴⁰

3.2. Materials and Methods

ITO coated glass slides and cover slips were used as primary electrode substrates. ITO coated glass substrates were modified with amorphous silicon (aSi) to obtain a photoconductive layer (see, Chapter 2 for fabrication). The aSi modified substrates and ITO coated cover slips were assembled to microfluidic sandwich composite structures using the negative photoresist SU8 (3000 series, see Chapter 2 and below for more details). All of these materials have been used in cell biology experiments before including cell viability studies which indicated that the materials (SU8^{197, 198}, Menzel glass¹⁹⁹, ITO^{200, 201}, aSi^{202, 203}) are biocompatible.

The fabricated OET chips were characterized using scanning electron microscopy, profilometer and standard upright brightfield microscopy.

An Olympus microscope (BX53, Olympus, Japan) equipped with one of the following cameras; an UC30 CMOS camera (Olympus, Japan), a FASTCAM SA3 model 120K-M3 (Photron), a Thorlabs CMOS Camera, (DCC1545M, UK), a MotionScope CMOS camera (M3, Redlake, USA) and an Orca Flash4.0 CMOS-camera (Hamamatsu, Japan) were used to monitor and record experiments for particle manipulation. The microscope was also connected to an data projector (1510X , DELL, USA) to project images generated in PowerPoint (Microsoft, USA) through a set of objectives (10x, 20x, 40x, Olympus) onto the photoconductor electrode.

The OET chip was directly connected to a signal generator (TG5011, TTI, UK) to apply voltages in the range of 5 V to 20 V (peak to peak) at frequencies of 50 KHz and 100 KHz.

Polystyrene beads of various sizes were suspended in aqueous solutions of different conductivities and with 0.1 % (v/v) Tween 20. The conductivity of each solution was adjusted by adding potassium chloride to deionised water. The conductivity was measured using a conductivity meter. Beads were injected into the OET chip at varying flow rates using a syringe pump.

Electric fields and potentials in the chip for various conditions were modelled using COMSOL (v3.5, UK). Details to the 2D model including boundary conditions and subdomain settings can be found in chapter 2.

Recordings of bead manipulation experiments were analysed using ImageJ (v1.47). The velocities of moving beads under various conditions were extracted to quantify trapping and focussing capabilities and DEP forces in the developed OET chips.

3.3. Results and Discussion

3.3.1. Integration of OET into microfluidics

An unusual microfabrication approach was developed to integrate OET into a robust microfluidic chip. As described in Chapter 2, a photoresist layer (SU8) acts as bonding agent and microchannel defining structure. SU8 was spin coated onto the aSi substrate and the ITO electrode substrate was immediately placed onto the fresh SU8 layer resulting in a composite sandwich structure of glass-polymer-glass (Figure 3-1).

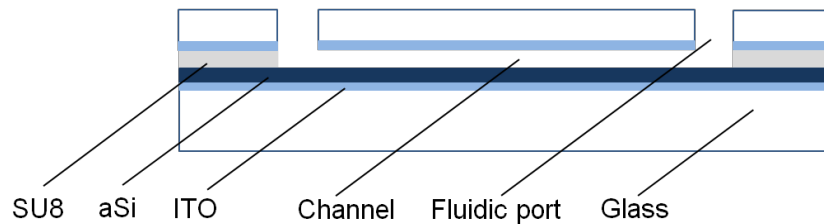


Figure 3-1: Schematic of composite structure used to create OET chip.

Normally, photoresists are exposed through a mask which is in contact or proximity with the resist. However, here, the exposure took place through an additional ITO-glass cover slip separating the resist from the mask by approximately 160 μm to 190 μm . This needs to be considered when designing microfluidic features as the refraction of light through the cover slip but also the absorption of ITO in the UV-light range affect the resulting channel geometry and exposure times in the final protocol. For instance, 30 s exposure time (200 mJ/m^3) for a free standing SU8 (3050, spin-coated at 3500 rpm) film of 50 μm thickness is sufficient to induce crosslinking in the exposed regions and generate a stable microstructure after developing. In this work the protocol needed to be changed to account for the above mentioned reasons. The exposure was doubled to 60s for resist thicknesses < 50 μm . For thicker films > 60 μm it was increased to 90 s. Moreover, the feature size defined by the polymer-emulsion film mask differed from the resulting feature size in the fabricated chip. This was attributed to the unusual fabrication procedure but also due to refraction issues when light exposure takes place through different layers (quartz plate, air, polymer-emulsion film mask, air and glass cover slip) before reaching the resist. Overall, this led to increased feature sizes by up to 10 % relative to the initially designed feature size.

Another significant adjustment was made towards the pre-exposure baking times on the hotplates. In general this process step involves the reduction of the solvent in the spin-coated SU8 film by evaporation. It results in a volume change of the SU8 film and effects the diffusion and reaction times of the photo-activated triarylsulfonium salt which catalyses the polymerisation and cross-linking of SU8. In this work the SU8 layer was sandwiched

between two substrates restricting the solvent evaporation to the parts of the sandwich structure where the SU8 was exposed to the surrounding air. These parts include the side sections of the chip and the drilled holes (inlet/outlet ports) in the cover slip. Therefore, the evaporation process was slowed and more time for the pre-exposure bake was needed. For instance, the common SU8 protocol suggests 10 minutes at 95°C for thickness of 50 μm . Here, we found 20 to 25 minutes for SU8 thickness of < 50 μm and 45 minutes for thickness of > 60 μm to be sufficient for substrate areas up to 8 cm^2 . Following the conventional protocol, resulted in solvent left in the SU8 layer. This affected the cross linking after exposure to be weakly defined by the mask because of the diffusion of the catalyst into unexposed parts and poor bonding of the substrates to the SU8 film due to limited adhesion triggered by the remaining solvent.

Last but not least, the development of the unexposed structured was realised via the drilled holes in the ITO coated glass cover slip. Compared to a free standing resist layer such as in conventional processes, the SU8 developer has only access from these particular points to dissolve the uncrosslinked resist. This led to increased developing times and can be considered as the bottleneck of the overall process. The developing time was strongly dependent on the microchannel geometry. In general, it was observed that the developing time increased with decreasing channel width and increasing channel length. For instance, a microchannel with dimensions of 20 mm x 0.170 mm x 0.04 mm (length x width x height) took up to 3 days to develop while a microchannel of 10 mm x 5 mm x 0.04 mm (length x width x height) was developed over night when placed in the developer bath. An attempt to decrease the developing time has been undertaken by applying ultrasound (KHz range) during incubation in the developer solution. However, it was found that the developing could not be improved due to the creation of cavitation bubbles in developed regions of the microchannel. These prevented diffusion of the developer further into the unexposed resist as well as exchange of the resist/developer mixture from the chip. Moreover, prolonged ultrasound treatment for several days induced mechanical stress to the composite structure which resulted in debonding of the SU8 at the interface to the substrates. An alternative, which was not tested but may improve the developing time and avoids cavitation bubbles, is the application of ultrasound in the Megahertz range. As shown by Williams and Wang²⁰⁴ for high aspect ratio SU8 structures, faster and more gentle developing was achieved using this method.

Several samples following the protocol described above have been characterized using a profilometer, scanning electron microscopy (SEM) and brightfield microscopy. The profilometer was used for the measurement of the SU8 thickness. SEM was used to

investigate the cross-section of the microchannels and the composite structure. A standard microscope was used for general microchannel inspections from the top.

The results of the thickness measurement for several samples fabricated at different spin coating speeds are shown in table 3-1. Using a spin coating speed of 1500 rpm for SU8 3050 resulted in SU8 layer thicknesses of 62 μm to 70 μm . An increase in the spin coating speed to 4000 rpm resulted in decreased SU8 layer thickness of 32 μm to 40 μm . To obtain thinner layers of SU8, the 3025 version was applied at spin coating speeds of 4500 rpm which resulted in thickness of 15 μm to 23 μm .

Table 3-1: Thicknesses of microchannel when using SU8 sandwiched between glass substrates.

Sample	SU8	Spin coating speed [rpm]	Thickness [μm]
1	3050	500/1500	62
2	3050	500/1500	70
3	3050	500/4000	32
4	3050	500/4000	35
5	3050	500/4000	40
6	3025	500/4500	15
7	3025	500/4500	20
8	3025	500/4500	23

In Figure 3-2 (a-c) the cross-sections of fabricated OET composite structures are shown where Figure 3-2a shows 70 μm (SU8 3050, 1500 rpm), Figure 3-2b a 35 μm (SU8 3050, 4000 rpm) and Figure 3-2c a 20 μm (SU8 3025, 4500 rpm) thick channel. It is clear from these images that the fabrication process resulted in non-rectangular microchannels as seen from the curved SU8 channel wall (Figure 3-2d) which could be attributed to a combined effect of sandwiching the resist between two substrates and refraction issues while UV-exposure through different material layers. Overall, this affected the lateral microchannel

dimensions as being different from the actual mask design. For instance, microchannel designs with a width of 160 μm ended up being increased by 5 % to 10%. Figure 3-2e shows an angled top view of a microchannel where the cover slip was snapped off for thickness measurements while the graph in Figure 3-2f shows some example profiles of microchannels obtained from the profilometer.

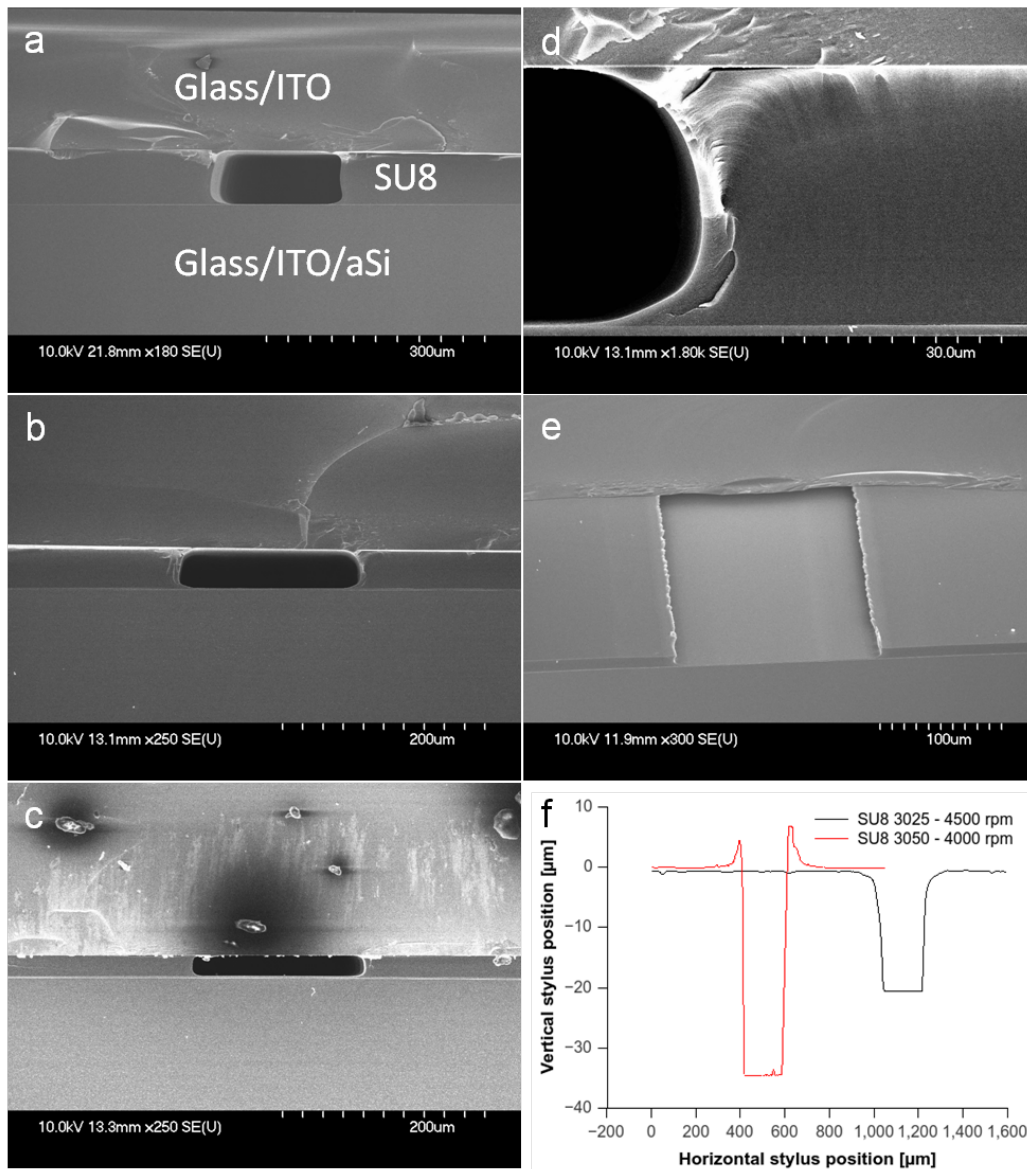


Figure 3-2: (a-c) Example SEM images showing cross-sections of microchannels fabricated using SU8 3000 series spin coated at different speeds. In detail, (a) SU8 3050, 500/1500 rpm, (b) 3050, 500/4000rpm, (c) 3025, 500/4500rpm. (d) SEM image shows magnified channel wall with a curved shape. (e) SEM image shows open microchannel section from top. The top cover slip has been removed to enable thickness measurements using the Dektak profilometer. (f) Example Dektak measurements showing profile along a path of an open microchannel section for samples spin coated with different SU8 versions and spin-coating speeds.

Thickness variations of SU8 along the cross-sections of two samples were investigated at random by scanning around ~ 5 mm along the width of sandwich structure using the SEM.

Based on the images shown Figure 3-3a and 3-3b, we found a homogenous SU8 layer along the scanning length. It has to be noted that a proper quantification of the thickness along the width is difficult to conduct due to angled and uneven sample positions and cross-section breaking points, however, simple observations indicate sufficient precision for the region of interest which lies within the centre of the substrate.

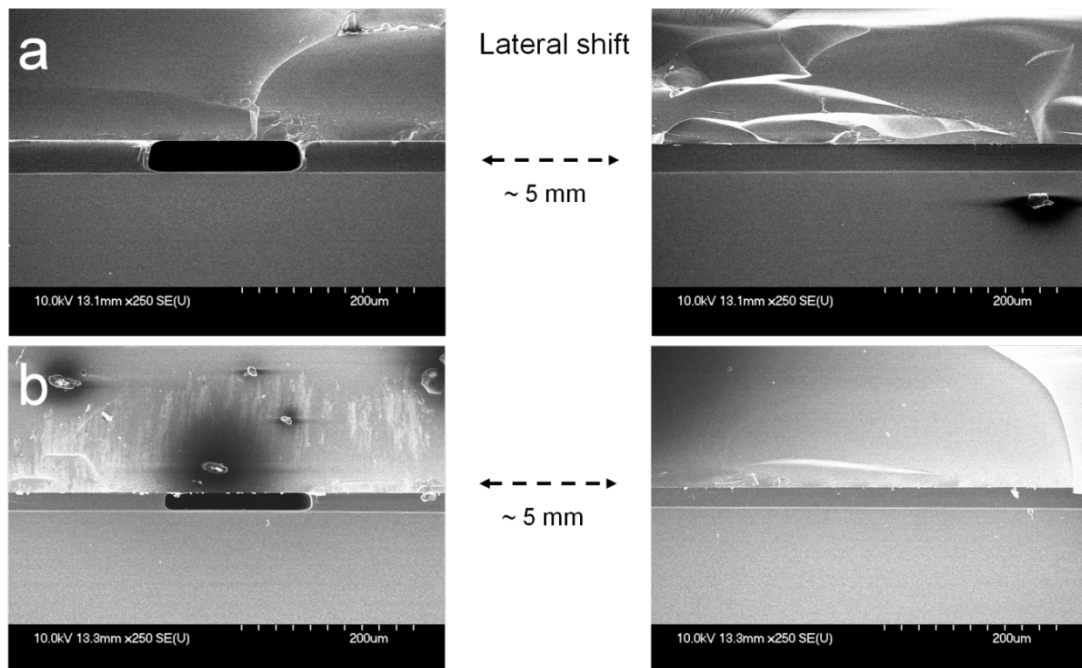


Figure 3-3: Samples spin coated with (a) SU8 3050 (4000 rpm) and (b) SU8 3025 (4500 rpm) showing relative homogenous thickness along substrate width.

Examples of fabricated OET chip as well as chips made from unmodified glass substrates are shown in Figure 3-4. As can be seen from the images, the used fabrication process resulted in homogenous bonding areas across the entire chips. OET chips contained overlaps of the electrode substrates to one of the sides to be able to connect wires to the ITO layer. The drilled holes served as ports to connect the chip to the world via shortened pipette tips glued to the port and attached PTFE tubing. Figure 3-4b shows a brightfield topview image of a microchannel junction with three channels connected to a single channel. Here, it needs to be highlighted that the fabrication process resulted in residue-free microchannels which means that the unexposed SU8 was developed leaving no debris behind. This is important because any thin insulating layer left on the photoconductor alters the electric field generated inside the microchannels. However, the channel walls were curved as seen in Figure 3-2d. The curved shape resulted in a thin SU8 layer reaching into the channel at the channel wall interface as shown in Figure 3-4b. Due to the insulating properties of SU8 the electric field is perturbed at these points which can influence the manipulation of particles or cells.

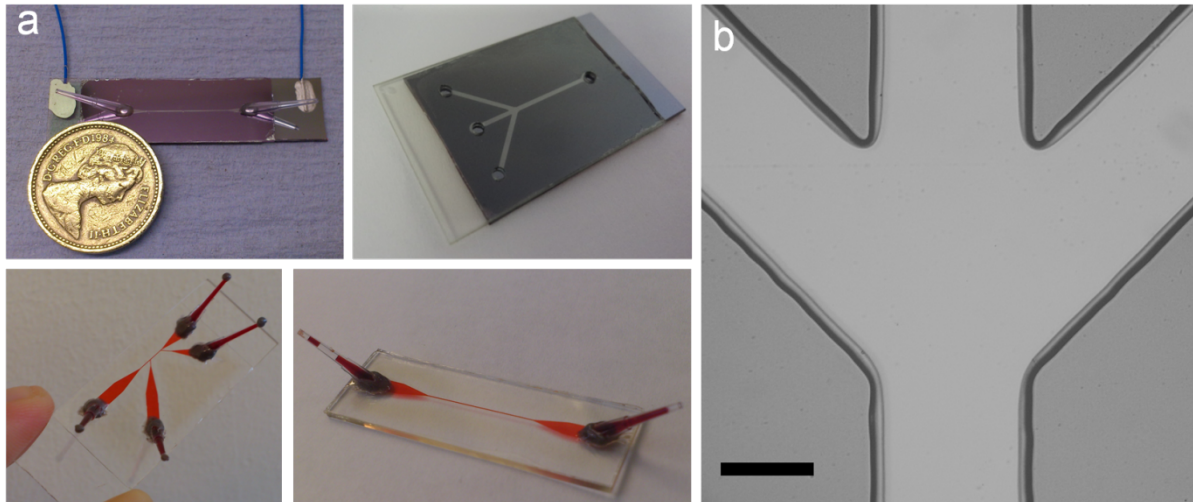


Figure 3-4: (a) Examples of fabricated composite chips with simple microfluidic channel geometries. For the OET chips, ITO and aSi electrodes overlap on the sides to provide connections for wires. (b) Microscopic image of a microfluidic channel with junction. Scale bar: 100 μm

In summary, the developed fabrication protocol led to a successful integration of the OET electrode substrates into simple microfluidic chips with adjustable vertical dimensions. In the course of this study many chips have been fabricated and used for different manipulation purposes involving polystyrene bead samples but also biological samples. Fouling and wearing of microchannel chips is a typical result after experiments with such samples. However, we found that the fabricated microchannels can be cleaned from minimal biological and artificial residues by rinsing with organic solvents such as 70% ethanol and acetone without destroying the SU8 layer or its adhesion properties in the short term. These chips were used for several experimental days before changes in the channel outline were observed which were associated with uptake of liquid into the SU8 layer at the channel wall/liquid interface. However, this had no effect on the bonding strength and the adhesion of the substrate, in fact under pressure driven flow, the weakest component which showed leakage of sample liquids from time to time was found to be the inlet-ports at the interconnection between the chip and the tubing. A quantification of the bonding strength using pressure test, pull test or shear test²⁰⁵ was not undertaken but can be included for future characterisation studies. The influence of the liquid uptake requires also further investigation as this could affect the insulating behaviour at the channel wall and the resonance frequency condition during acoustic actuation. The “soaked” interface may decrease the insulating properties which can result in a stronger penetration of the electric field into the interface region. The water uptake may also change the acoustic impedance properties of the channel wall which can alter the resonance frequency of the microchannel. The reflections of the acoustic wave may not take place at the interface region but instead at regions further into the SU8 layer which is not affected by the water uptake. This can result

in pressure anti-node positions that are within the “soaked” SU8 layer and pressure node positions that are closer to the channel wall.

3.3.2. Characterisation and application of fabricated OET devices

3.3.2.1. Microparticle trapping under continuous flow

The manipulation speed or how fast microparticles can be moved using virtual electrodes is a common figure of merit in the literature as it gives an estimation of the DEP force and hence can be used as a measure of the performance of the device. Several parameters such as the applied voltage signal, liquid conductivity, virtual electrode pattern, electrode gap and light intensity affect the performance.

The typical approach involves the measurement of the particle velocity which is the result of positive or negative DEP induced by moving the virtual electrode pattern or the stage with an OET device while the virtual electrode is fixed. The DEP force is then estimated by balancing it against the drag force imposed on the particle. The velocities are typically in the range of tens of micrometer for bead diameters of 10 μm - 20 μm , applied voltages of 10 V - 20 V (50 - 100 KHz), optical powers of approximately 1 W/cm^2 and liquid conductivities of 0.2 mS/m - 10 mS/m .^{66, 78}

In this work the performance depending of several parameters (voltage, conductivity etc.) was characterized by trapping particles against the hydrodynamic flow induced by a syringe pump connected to the OET device. A virtual electrode was simply placed across the channel width (Figure 3-5a) accompanied with an AC signal. The velocity of the particles was adjusted using the syringe pump's flow rate settings and the voltage amplitude was varied until the negative DEP force imposed on the particles balanced the drag force.

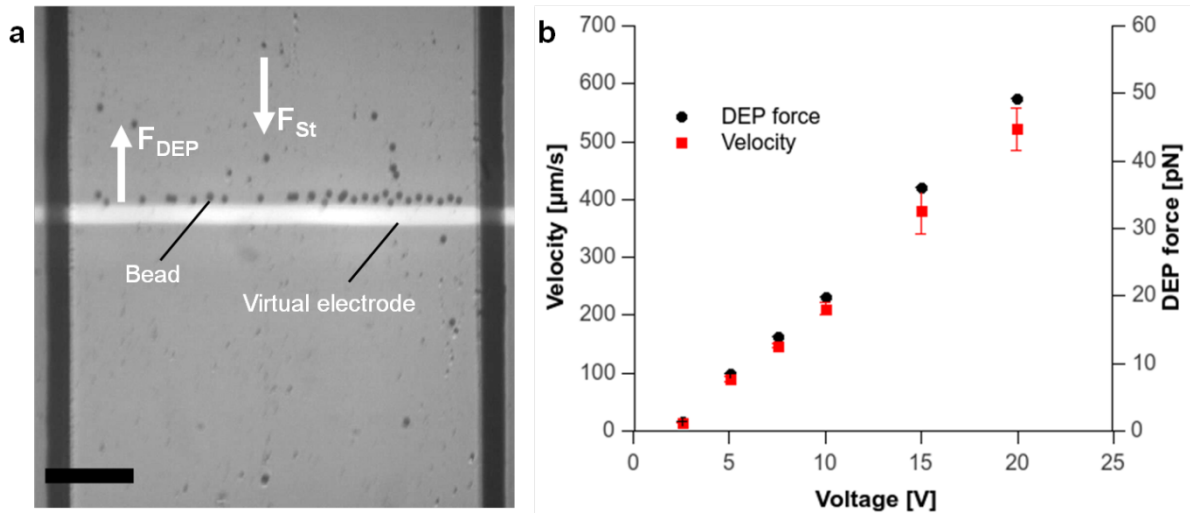


Figure 3-5: Trapping of polystyrene beads (10 μm) against fluid flow for different voltages at 50 KHz in medium with conductivity of 5 mS/m and an optical power of 2 W/cm^2 . (a) Image from experiment showing beads hold against the fluid flow at virtual electrode of 45 μm width (Scale bar: 200 μm). (b) Velocity of trapped beads and imposed DEP force against voltage applied to the OET device.

Figure 3-5a shows an image of an experiments where 10 μm polystyrene beads were trapped at a 45 μm wide light pattern at 50 KHz and 10 V due to a negative DEP force (CM factor: - 0.43, liquid conductivity 5 mS/m). Here, a 40 μm high channel was used and trapping was conducted for varying bead velocities using a light intensity of 2 W/cm^2 . A voltage range from 2.5 V to 20 V was used to investigate the device performance. Figure 3-5b shows the result of these trapping experiments. An increase in the applied voltage increases the velocity at which beads can be trapped. A linear relationship between the applied voltage and the bead trapping velocity was found. Trapping velocities of 15 $\mu\text{m}/\text{s}$ to 522 $\mu\text{m}/\text{s}$ were achieved which corresponds to DEP forces of 1.4 pN to 49.0 pN. The electric field gradient under these conditions is shown in the simulations in Figure 3-6a for a voltage amplitude of 20 V. The highest field magnitudes at distances of 2.5 μm to 5 μm to the aSi surface vary between $2.2 \cdot 10^{17} \text{ V}^2/\text{m}^3$ to $8.0 \cdot 10^{15} \text{ V}^3/\text{m}^3$ and can be found at the edges of the virtual electrode. The direction of the DEP force for insulating particles is indicated by black arrows in the surface plot. A negative DEP force with lateral and vertical components is acting on the polystyrene beads resulting in repulsion from high field regions.

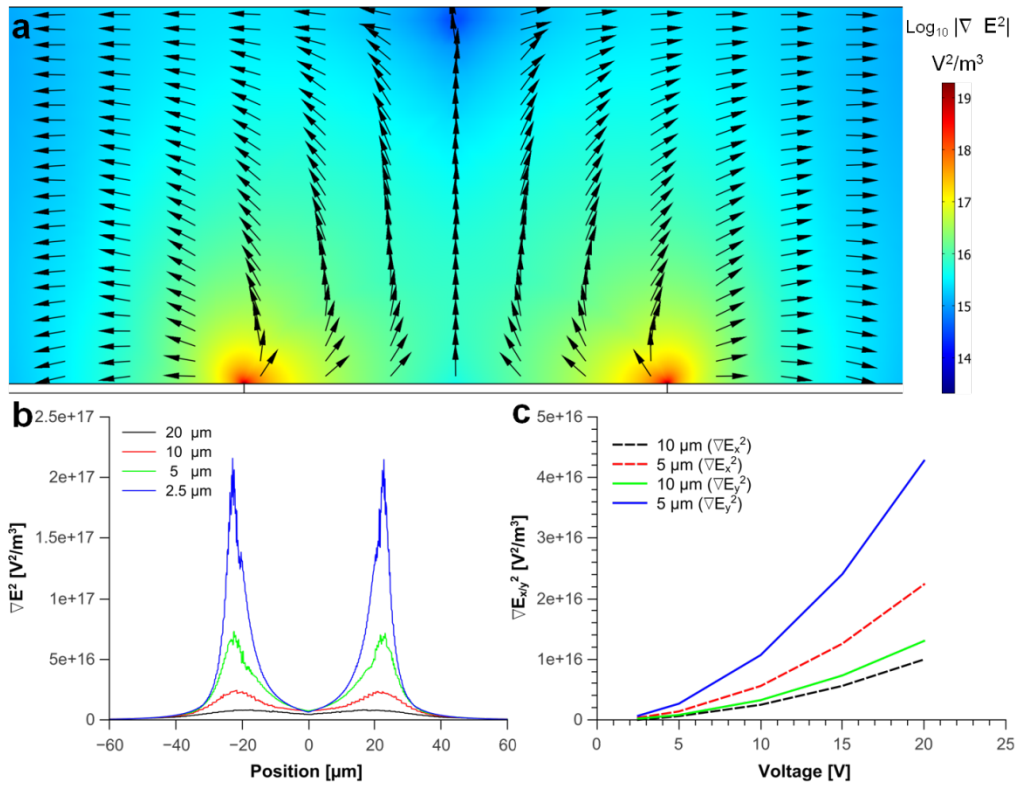


Figure 3-6: A 2D models simulating electric field in the OET device of 40 μm height and a 45 μm virtual electrode pattern at 50 KHz and 20 V in a 5 mS/m conductivity solution. (a) Simulation showing the gradient of the electric field squared $\log |\nabla E^2|$ as surface plot where the colour bar represents the magnitude. The black arrows show the direction of the DEP force for particles less polarisable than the surrounding medium. (b) Electric field (∇E^2) distribution at different distances above the photoconductor and along the 45 μm virtual electrode pattern. (c) The field components ∇E_x^2 and ∇E_y^2 at the edge of the virtual electrode are simulated for different voltages and different distance to the aSi surface.

The DEP force scales with the square of the gradient of the electric field. Hence, the field should be proportional to the square of the applied voltage. However, the results demonstrated a rather linear relationship in the developed OET device. The exact reason for this behaviour was not known and requires more investigations. However, one may attribute this effect to the particles being unable to experience the full force as at higher speeds they were forced up, over the barrier. The vertical and the lateral field components scale both with the applied voltage while having a similar magnitude. Under the influence of the negative DEP force a lifting of particles attributed to the vertical field component may reduce the trapping effect induced by the lateral field component. This would result in a movement of particles towards lower field regions near the top electrode allowing particles to pass the virtual electrode by the induced fluid flow. The described behaviour is supported by simulations of the components of ∇E^2 . In Figure 3-6c, ∇E_y^2 and ∇E_x^2 were determined for different heights and voltages above the virtual electrode edge in the aSi layer. At distances relative close to the aSi surface, where the DEP force has its maximum, ∇E_y^2 is dominates

over ∇E_x^2 . This might promote the lifting of particles over the potential barrier which decreases the trapping force.

3.3.2.2. Influence of the liquid medium conductivity

The liquid medium conductivity is a crucial parameter when operating an OET device. From the introduction, we learned that the device can be modelled as simple lumped equivalent circuit containing impedance elements which represent the photoconductor and the liquid layer. An increase in the conductivity of the medium decreases the impedance of this layer and induces a higher voltage across the photoconductor. Figure 3-7a shows simulation results (see model above) of the voltage drop across the centre of a illuminated aSi layer for medium conductivities of 5 mS/m to 100 mS/m using an AC signal of 20 V at 50 KHz and a light intensity of 2 W/cm² (corresponding to 10x objective). AT low conductivities (5 mS/m) the voltage drops mainly across the liquid layer resulting in a strong non-uniform electric field in the sample. At high medium conductivities (1000 mS/m, e.g. physiological conditions) the voltage drops mainly over the photoconductor producing a low electric field magnitude in the liquid layer.

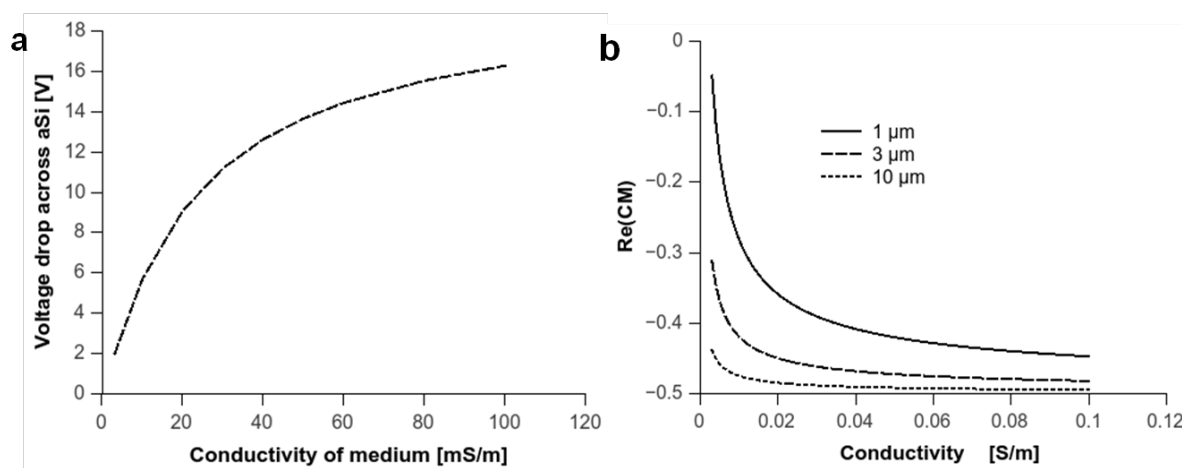


Figure 3-7: (a) Simulated voltage drop across the photoconductor for various liquid conductivities when an AC signal of 50 KHz at 20 V is applied and a light intensity of 2 W/cm² is used. (b) Simulated real part of the CM factor of different bead sizes as a function of liquid conductivity at 50 KHz

The performance of the OET device was tested at varying liquid conductivities using the trapping method described above. It has to be noted that an appropriate particle size should be used for this experiment. From equation 1.5, it is known that the CM factor is dependent on the frequency and the complex permittivity of particle and medium. When the liquid conductivity increases the CM factor decreases. From equation 1.4 it is clear that the CM factor partially contributes to the DEP force. Furthermore, for small particles the surface

conductance effect in the electric double layer (equation 1.8) influences the particles conductivity and hence the DEP response. The width of the electric double layer is altered with changing ion concentration in the solution which again influences the CM factor. Hence, when relating measured particle velocities to the device performance it should be verified that the DEP response of the particle is not altered by increasing conductivities. A large particle ($\geq 10 \mu\text{m}$) has a relative constant CM factor (only $\sim 10\%$ change on CM) for increasing conductivities (Figure 3-7b), while smaller particles ($\sim 1 \mu\text{m}$) can undergo significant changes ($> 100\%$).

The trapping performance of the OET device for various conductivities is shown in Figure 3-8. Velocities of $522 \mu\text{m/s}$ to $17 \mu\text{m/s}$ were measured for the range of conductivities used which corresponded to DEP forces of 49 pN to 1.6 pN . A sharp drop in the DEP force occurred within the range from 5 mS/m to 30 mS/m before it levelled off slightly towards higher conductivities up to 100 mS/m . This compares well with simulations of the voltage drop across the aSi layer, where more than half of the applied voltage drops across the layer within 30 mS/m to 40 mS/m before a levelling can be observed. These results give insight in the operation limits of the OET device in terms of liquid conductivities. This is of importance especially when dealing with biological cells suspended in buffer solutions where certain parameters such as pH, ion concentrations or osmolarity are adjusted to maintain a viable cell population. A cell sample is usually suspended in specialised cell media or buffer solutions with high conductivities of $\geq 1 \text{ S/m}$. These media are not applicable for a conventional OET device. The electric field in the liquid layer would become 3 to 4 magnitudes lower ($\nabla E^2 \sim 10^{13} - 10^{14} \text{ V}^2/\text{m}^3$) resulting in DEP forces not sufficient for continuous particle manipulation. However, a Ph-OET (see chapter 1) was recently introduced which is capable of overcoming this restriction and enables cell and particle handling in cell culture medium, though the fabrication complexity and costs of it are high which restricts a widespread use.⁷⁴

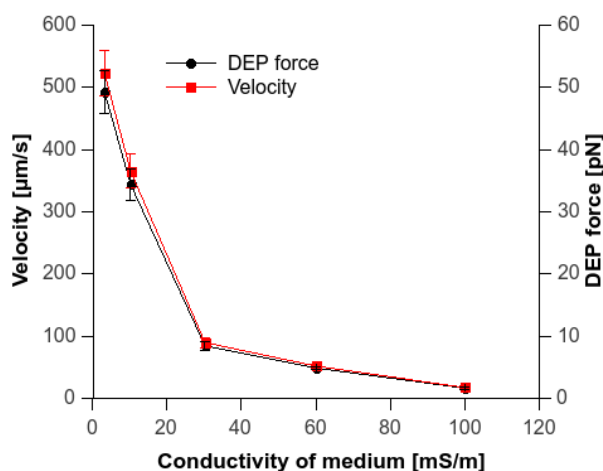


Figure 3-8: Trapping performance and DEP forces induced on 10 µm beads at 50 KHz (20 V) for various liquid conductivities.

3.3.2.3. Influence of the gap between the electrodes

The performance of the OET chip can be improved by considering how the electric field is dependent on the gap between the parallel electrodes. The voltage drop across the liquid layer reduces while the electric field magnitude increases when decreasing the gap between the photoconductor and the ITO electrode. The device fabrication method introduced above enables the construction of variable and well controlled SU8 thickness and hence gaps between the electrodes. The performance change was tested by creating channels with heights of 70 µm and 15 µm. A 20 µm virtual electrode (2 W/cm^2) and an AC signal of various voltages at 100 KHz was used to trap 6 µm polystyrene beads against various flow velocities of the liquid medium (5 mS/m).

Simulations of the electric field gradient ∇E^2 were carried out to obtain insight into the significance of channel heights in the OET device. In Figure 3-9a and b, ∇E^2 is shown for varying electrode gaps. In particular, Figure 3-9a shows the decay of ∇E^2 above the edge of a virtual electrode for electrode gaps of 15 µm to 110 µm. The field distribution is shown for the first 15 µm above the illuminated aSi layer. The simulation results show that the increase in the channel height decreases the field magnitude and promotes a steeper decay above the photoconductor. Furthermore, considering that particles occupy the fluid volume in the centre of the microchannel cross-section, the change in the magnitude becomes even more pronounced as shown in Figure 3-9b. Therefore, the OET device performance is significantly influenced by the device structure.

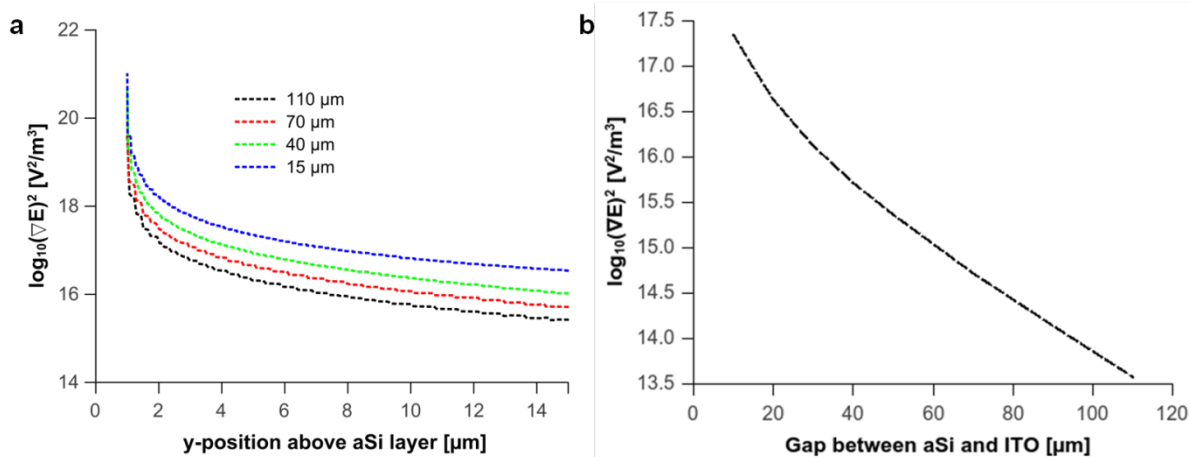


Figure 3-9: Simulated electric field magnitude as a function of the gap between the electrodes for a virtual electrode width of 20 μm , an AC signal of 20 V at 100 KHz and a liquid medium conductivity of 5 mS/m. (a) Logarithm of the square of the electric field gradient ∇E^2 within the first 15 μm above the illuminated (edge) aSi layer for different gap heights. (b) ∇E^2 in the centre of the channel cross section above the illuminated (edge) aSi layer for various gap heights.

Figure 3-10a and b show the results of the trapping experiments in OET devices with different channel heights. As expected, the differences in the trapping forces for 70 μm and 15 μm channel heights were significant. At a channel height of 15 μm the obtained DEP forces for voltages of 6.5 V to 20 V were 5.5 pN to 44 pN while at a gap of 70 μm the obtained DEP forces were only 1 pN to 7 pN.

The results indicate that relatively fast manipulation of small particles using OET is feasible but requires dimensional control of the OET device. However, reducing the electrode gap in the OET device is also accompanied with an increased shear stress imposed onto particles. While this is less important for artificial particles, biological cells might be affected, although some cells (e.g. red blood cells) are able to withstand higher shear rates. Furthermore, high sample concentration (10^7 - 10^8 beads/ml with bead diameter > 5 μm) should be avoided as channel blocking by particle aggregates inhibits efficient manipulations. Nonetheless, this can be used for improved particle manipulation functions (e.g. focussing), faster than previously shown for an OET device.

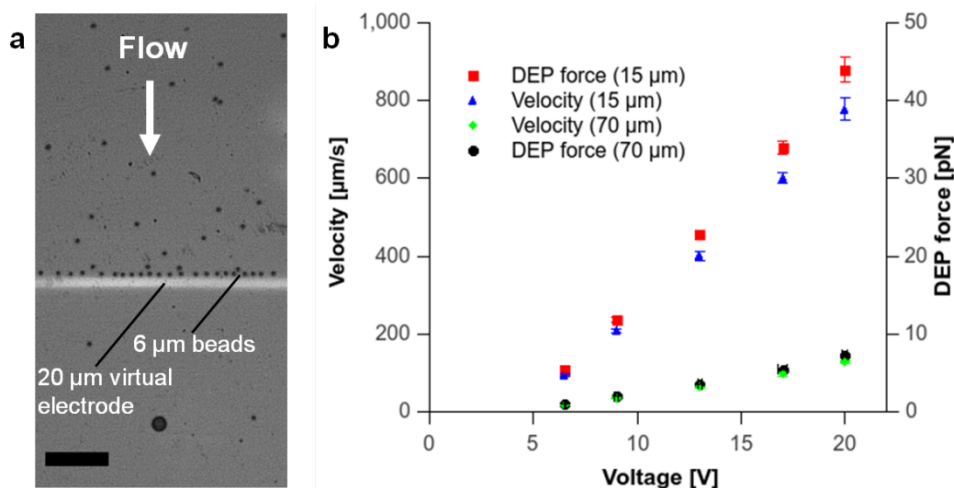


Figure 3-10: Trapping of 6 μm beads under continuous flow at 100 KHz for different voltages in medium with 5 mS/m conductivity and light intensity of 2 W/cm^2 . (a) Image from trapping experiment showing virtual electrode and trapped beads in 15 μm high channel (Scale bar: 100 μm). (b) Velocity of trapped beads and imposed DEP force against voltage applied to the OET device of different channel heights.

3.3.2.4. Influence of the virtual electrode pattern

The device performance is dependent on several factors as shown above which need to be adjusted to obtain forces of appropriate scale for particle manipulation. The virtual electrode projected on to the photoconductor also has a significant effect. Firstly, the magnitude of the light intensity which is projected onto the photoconductor through an objective effects the magnitude of the electric field in the sample. In chapter 2, it was shown that the light intensity increased with increasing magnification and hence increased the conductivity of the aSi layer. Also, the dimension of the electrode (e.g. width) as well as the pixel intensity of the virtual electrode defined by the imaging software (e.g. PowerPoint) influence the electric field created in the liquid medium. Here, it is shown that virtual electrode width and transparency (pixel intensity) can be used to tune the electric field magnitude and hence the DEP force imposed on beads. Experiments were carried out with increasing electrode width (7 μm to 120 μm) and increasing electrode transparency (0 % to 60 %). As shown previously, 6 μm beads suspended in 5 mS/m conductive medium were trapped against the flow and velocities and DEP forces were measured. The gap between the electrodes was 15 μm and an applied AC signal of 10 V to 15 V at 100 KHz was used to trap beads while the light was projected through a 10x objective.

Figure 3-11 shows the result of the influence of the virtual electrode width which varied between 7 μm and 120 μm . The measured velocities for the width range were between 54 $\mu\text{m/s}$ and 300 $\mu\text{m/s}$ which corresponded to DEP forces of 3 pN to 17 pN.

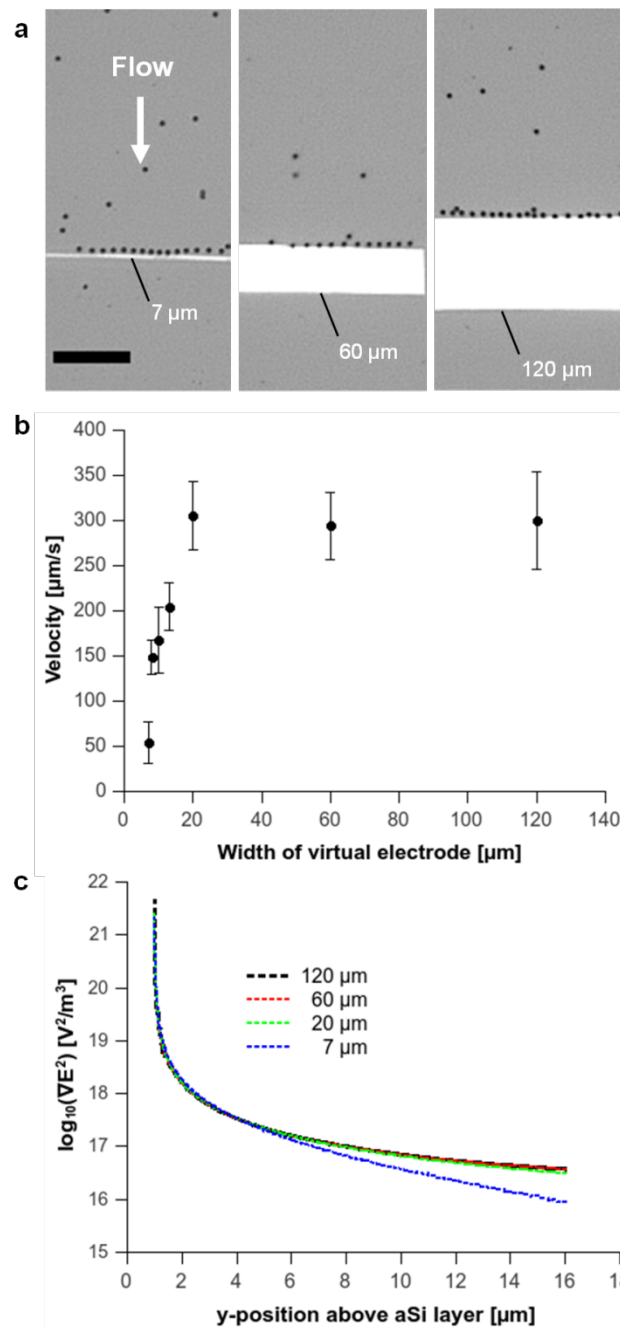


Figure 3-11: Influence of the width of the virtual electrode pattern on bead trapping at 100 KHz (15 V, 5mS/m, 10x objective). (a) Images from the experiment showing 3 different electrode width and 6 μm beads trapped along the edge (Scale bar: 100 μm). (b) Results of the trapping experiments for various electrodes widths. (c) Simulated values for ∇E^2 across the height of the microchannel and above the edge of the virtual electrode. ∇E^2 is shown for various virtual electrode widths.

The results in Figure 3-11b show a rapid increase in the trapping velocity when doubling the virtual electrode width (7 μm to 20 μm) before an asymptotic behaviour is observed for width of $>20 \mu\text{m}$. At that point any further increase of the particle velocity overcame the trapping by the negative DEP force. The cause of this difference may be associated with the change of the gradient of the electric field across the channel height. Figure 3-11c shows a simulation of ∇E^2 for different electrode widths. The cross-section plot represents the magnitude determined from the edge of the virtual electrode towards the top end of the microchannel. The electrode patterns share a similar magnitude of ∇E^2 close to the aSi surface ($< 5 \mu\text{m}$). However, ∇E^2 decays much steeper across the channel height for 7 μm electrode compared to wider virtual electrodes. The simulation also shows that the increase of the electrode width results in a convergence of ∇E^2 which agrees well with the asymptotic behaviour observed in the experiments.

In addition, refraction at the interfaces in the OET device may alter the light intensity which reaches the photoconductor. This influence may be pronounced when using small virtual electrode patterns and could affect the photoconductivity of the aSi layer. The influence of an altered light intensity is shown in Figure 3-12. The light intensity was adjusted (but not measured in this case) by modifying the transparency of the electrode pattern in the imaging software (PowerPoint). Increasing the transparency from 0 % (unaltered) to 60 % resulted in changes of trapping velocities from 190 $\mu\text{m/s}$ to 37 $\mu\text{m/s}$ which corresponded to DEP forces of 11 pN to 2 pN.

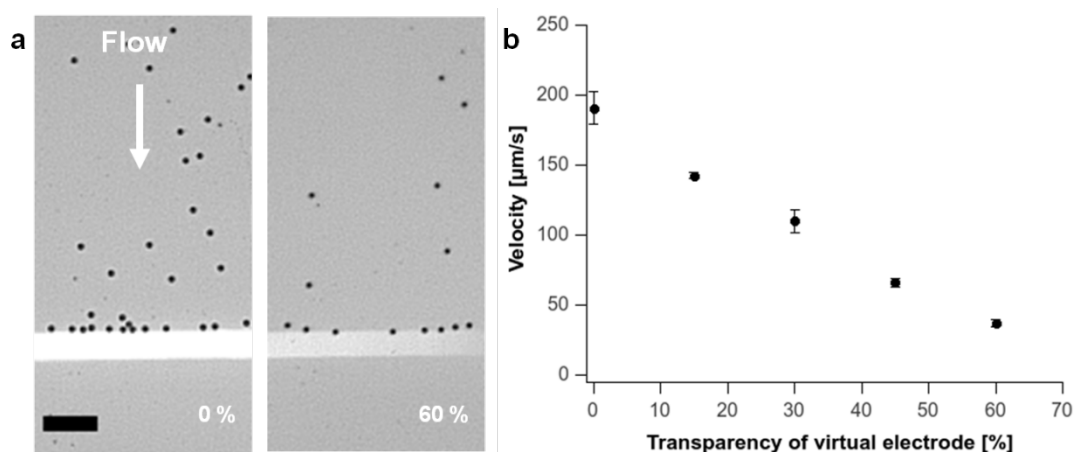


Figure 3-12: Influence of the transparency (set by imaging software) of the virtual electrode pattern (30 μm) on bead trapping at 100 KHz (10 V, 5mS/m, 10x objective). (a) Images from the experiment showing the virtual electrodes unaltered (0 %) and with increased transparency (60 %). Scale bar: 50 μm .

The presented results show the significance of the virtual electrode pattern in terms of electrode size and transparency and should give guidance when working with the OET device. In fact, this dependency is of advantage as it enables the generation of tuneable electric field gradients with corresponding DEP forces at arbitrary positions in the OET device, while other parameters (e.g. voltage, frequency, objective) are kept constant. For instance, this can be used to selectively manipulate particles of different sizes as shown later in this chapter.

3.3.3. OET for particle handling under continuous flow

Conventional dielectrophoresis with fixed metal electrodes is commonly applied for different microfluidic operations under pressure driven flows. Examples include focussing of particles into a single stream^{206, 207} or separation of a particle mixture²⁰⁸ based on their properties (e.g. volume). In the following it is shown that the developed OET device is capable to provide analog functions for microfluidic operations and that certain limitations associated with the device structure need to be overcome to enhance its overall usability.

3.3.3.1. Focussing of beads into single streams

Particle focussing into tight streams is an essential step in microfluidic flow cytometer^{157, 209, 210} where the properties (e.g. fluorescence) of single particles are investigated prior to subsequent handling processes (e.g. separation, detection). It is also used to concentrate particles into specific regions in the microchannel for counting, detecting, enrichment purposes²¹¹ or to separate the particles from a carrier liquid into a different liquid²¹²⁻²¹⁴ (e.g. washing, functionalisation).

The focussing performance in the developed OET device was investigated using oblique virtual electrode patterns projected on to the photoconductor. The schematic in Figure 3-13 describes the general concept of the focussing process. A pressure driven flow imposed on a sample delivers particles to the virtual electrodes. The DEP and Stokes drag force experienced by the particles combine to a net force which guides them along the virtual electrode. At the end of the virtual electrode particles line up and the hydrodynamic force under laminar flow maintains a stable and tight stream of particles.

Particle focussing was characterized in an OET device of 15 μm height. Oblique virtual electrode patterns (10 μm width) of different angles (15° to 75°) were used to align 6 μm beads into a tight single stream. A light intensity of 2 W/cm^2 combined with a set of voltages at 100 KHz were used to investigate particle velocities at which stable single stream

focussing can be achieved. The polystyrene beads were suspended in liquid medium of 5 mS/m conductivity.

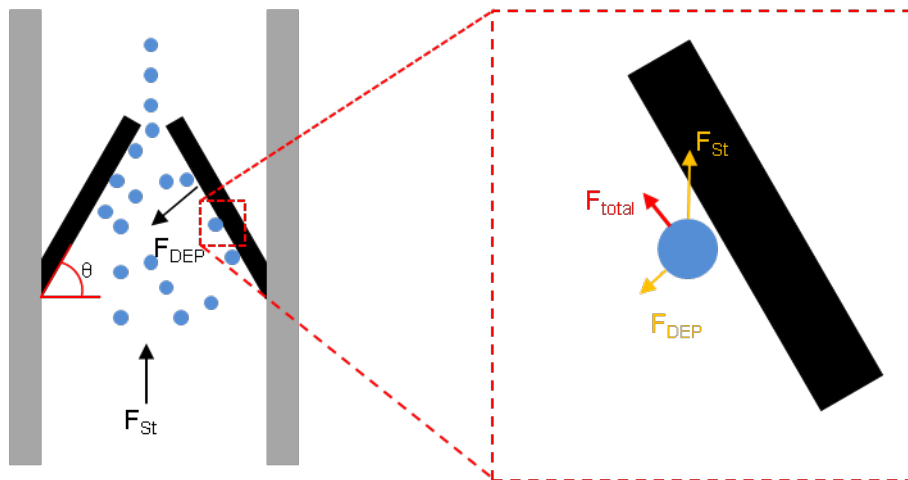


Figure 3-13: Particle focussing using oblique virtual electrodes to produce a net force as the sum of DEP and Stokes drag force to align particles towards a single stream.

Figure 3-14 (a-e) shows magnified images (40x) of focussing experiments with electrode angles of 75° (a), 60° (b), 45° (c), 30° (d), and 15° (e). A tight single stream of one particle width can be obtained with different electrode angles. However, the net force to guide beads along the virtual electrode varies with the angle. This has been investigated by measuring the velocities obtainable with stable bead focussing. Figure 3-14f shows velocity values obtained for different electrode angles and for different voltages (10 V, 20 V) applied to the OET device. The velocity increased with increasing electrode angle. For instance, the velocities achieved for an applied voltage of 20 V were in the range of 0.9 mm/s to 5.2 mm/s for angles of 15° to 75° . The DEP force necessary for guiding beads along the electrode decreases with increasing angle. Moreover, the particle velocities increased linearly with the applied voltage as in shown Figure 3-14g. The highest velocities were achieved with a 75° electrode. When voltages of 5 V to 20 V were used velocities of 0.4 mm/s to 5.1 mm/s have been measured. This could be even improved using virtual electrodes of increased width (see above) as long as the channel dimensions allow for it. Again, a linear relationship between the bead velocity and the applied voltage was found. This may be associated with the vertical field gradient levitating beads over the potential barrier, as described earlier.

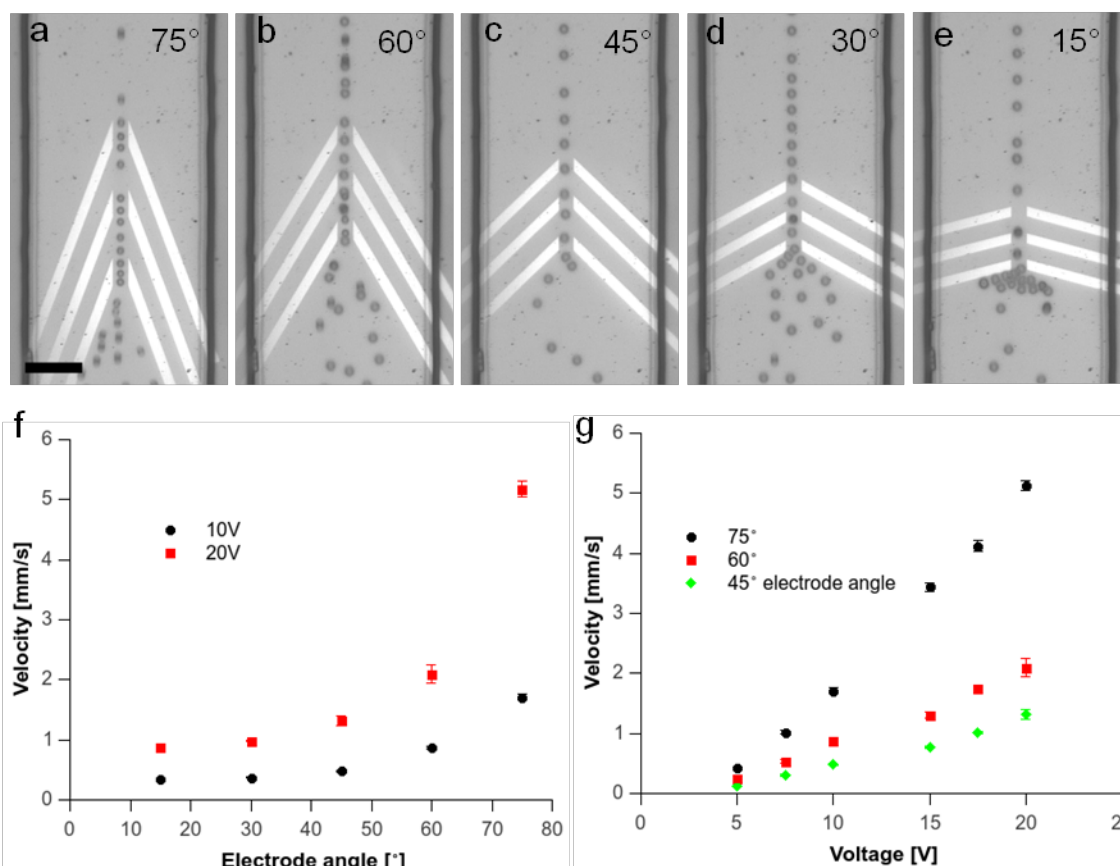


Figure 3-14: Focussing of polystyrene beads in an OET device by oblique virtual electrodes. (a-e) Magnified view (40x objective) showing bead focussing for different electrode angles in the microchannel (Scale bar: 50 μm). (f) Stable bead focussing at different bead velocities dependent on the electrode angle at 100 KHz in 15 μm height channel (Beads suspended in 5 mS/m conductive medium). (g) Stable focussing at different bead velocities and for several electrode angles dependent on applied voltage.

These results show for the first time that an OET device is capable of fast particle manipulation with velocities in the mm/s range when oblique virtual electrodes combined with a shallow microchannel geometry are applied. This might be of interest for the development of microfluidic flow cytometer where flexible electrode arrangements suited for different kinds (e.g. size) of particles is desired, though state of the art flow cytometer use velocities of 1 m/s to 10 m/s for high throughput analysis (500000 particles/s).¹⁵⁷ However, OET can not only be used to focus particles, it also enables sorting of them, as shown later, which may reduce the complexity of the cytometer setup. Furthermore, oblique electrodes can also be used to deflect particles laterally in a microfluidic channel as shown in Figure 3-15. This could be used for automated biological assays integrated into continuous microfluidic assays. Such a concept has been shown using solid rails which guide particle across several adjacent laminar streams.²¹³ Each stream can carry a certain reagent to wash

and modify (e.g. protein coupling, surface functionalisation) particles prior to a reaction in another laminar stream which carries a sample liquid (e.g. blood) with an analyte of interest.

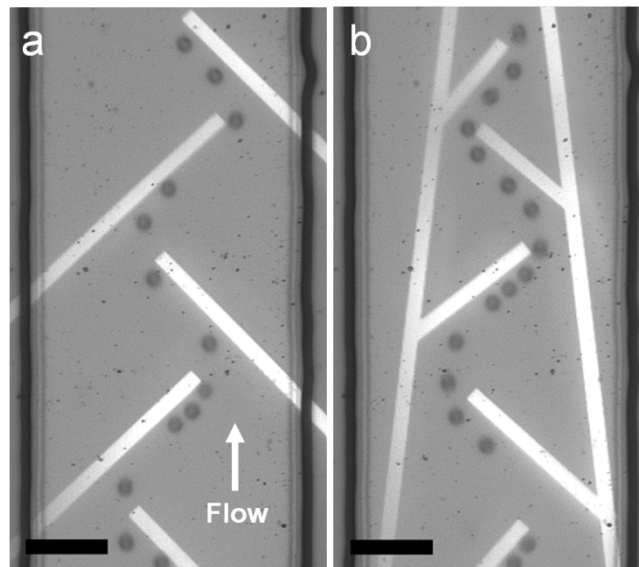


Figure 3-15: Lateral deflection of beads along the microchannel using oblique electrodes (100 KHz, 10 V, 5mS/m, Scale bar: 50 μ m).

3.3.3.2. Continuous separation of focussed bead mixtures

The DEP force scales with the size of the particle and can be controlled by adjusting the voltage, line width or transparency of the virtual electrode as shown before. The latter ones can be used to achieve separation and sorting of beads in a mixture based on how much force the bead experiences which is strongly dependent on size while parameters such as frequency, voltage, flow rate are kept constant. A schematic of the process is shown in Figure 3-16. A bead sample is first concentrated and focused in a laminar stream by an oblique virtual electrode before approaching a second oblique virtual electrode where the separation takes place. The separation is controlled by adjusting the DEP force imposed on the particle using either a certain line width or transparency to alter the electric field distribution in the channel. While a big particle experiences a larger DEP forces and gets deflected along the electrode edge, a smaller particle gets less deflected due to a lower DEP force and eventually passes the virtual electrode.

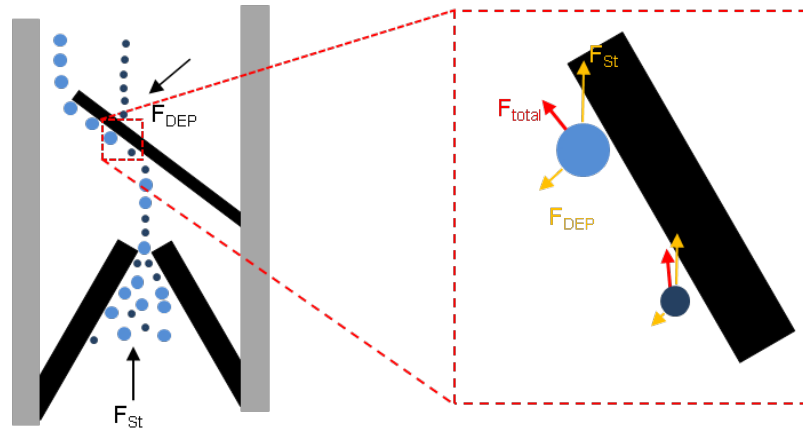


Figure 3-16: Principle of size based bead separation using OET. Beads are first focused into a stream followed by a filtering step along an oblique virtual electrode. The electric field magnitude and hence the DEP force are adjusted at the particular electrode by controlling the line width or the transparency.

The feasibility of this concept is demonstrated in Figure 3-17 (a-c) which depicts stills from experiments where the line width and light intensity were modified to achieve the separation of bead mixtures. The electric field gradient was adjusted during the experiment by changing line width and transparency of the virtual electrodes until a separation could be observed. For instance, Figure 3-17a shows the sorting of 6 μm and 3 μm into virtual channels controlled by the line width while voltage, flow rate and light intensity were kept constant. While all beads were guided towards the sorting regions by wide electrodes (30 μm), the sorting took place at the oblique electrode of 22 μm which created a force strong enough to deflect 6 μm beads but permitted guiding of 3 μm beads. As shown before, the angle of the electrode can be used as an additional parameter to trigger the separation. At lower angles, the DEP force to guide particles has to be higher compared to higher angles.

In Figure 3-17b, altered light intensity (transparency) of the virtual electrode is used for bead separation. First beads of 6 μm and 3 μm diameter were focussed into a single stream to translate them towards the separation region. An oblique virtual electrode of increased transparency (25 %) generated a DEP force sufficient to guide 6 μm beads but passed through 3 μm beads. In Figure 3-17c, the light intensity approach was used to separate polystyrene beads of 3 μm , 6 μm and 10 μm . Here, the bead mixture was guided towards a single oblique virtual electrode with a light intensity gradient. The electric field along the electrode was altered stepwise by changing the transparency of the virtual electrode pattern in the imaging software. The transparency properties of the virtual electrodes were defined in percentage where 0 % meant fully illuminated while 100 % meant no light at all. In particular, the transparencies were set to 27 %, 40 % and 70 % to pass through 3 μm beads first, followed by 6 μm and 10 μm beads to achieve sorting into virtual microchannels and hence fractionation of the sample.

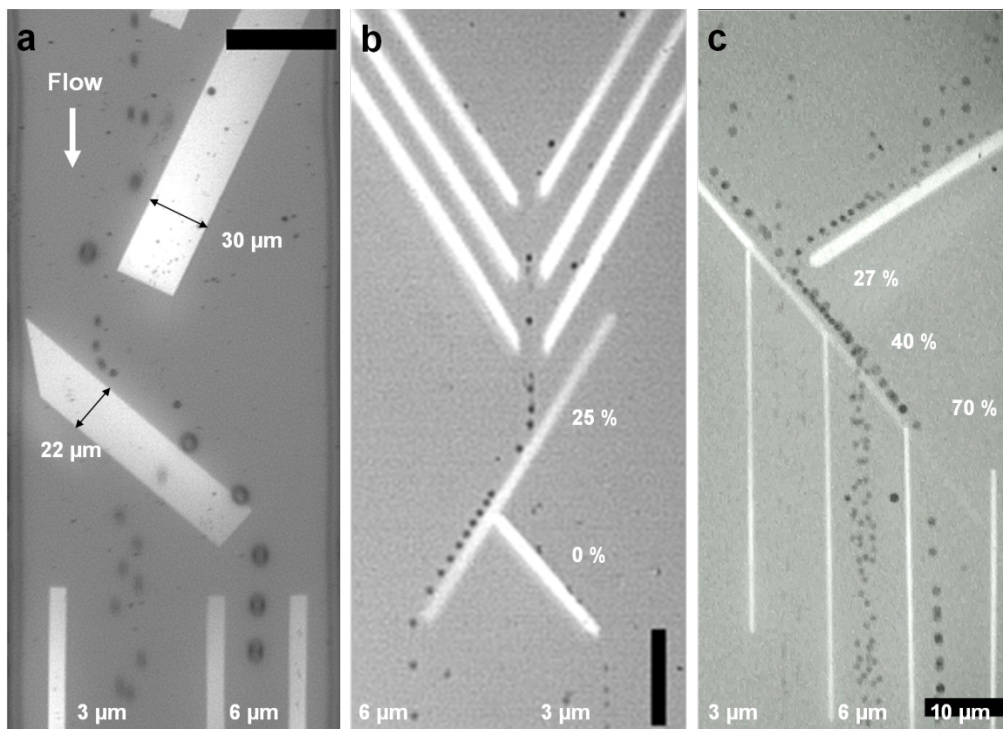


Figure 3-17: Separations of beads of various sizes by adjusting the DEP force using virtual electrodes of certain width and transparency. (a) Guiding and Separation of 6 μm and 3 μm beads into virtual microchannels at 100 KHz, 15 V (5 mS/m, 40x objective). An oblique virtual electrode of 22 μm width imposes a larger DEP force on 6 μm particles which were deflected along the electrode while 3 μm particles pass the virtual electrode with minor deflection. Scale bar: 50 μm . (b) Focussing and separation of 6 μm and 3 μm beads using an oblique virtual electrode of reduced light intensity (25 % transparency) to reduce the DEP force imposed on the 3 μm beads (100 KHz, 10V, 5mS/m, 10x objective). Scale bar: 100 μm . (c) Guiding of 10 μm , 6 μm and 3 μm particles towards a virtual electrode with an light intensity gradient (27 %, 40 %, 70 % transparency) to achieve size based sorting into virtual microchannels (50 KHz, 16V, 5 mS/m, 10x objective). Scale bar: 100 μm .

The results above indicate a good separation of differently sized beads; however, in the course of these experiments a significant limitation of the OET device became apparent which influenced the separation process. The effect is called mutual dielectrophoresis and is described in the next section. Briefly, the electric field in the OET device leads to the attraction of beads to each other, especially pronounced at higher bead concentrations (due to close distances) and voltages. An example is presented in Figure 3-18. Here, a time lapse shows a separation region for 10 μm beads triggered by a light intensity gradient. The large beads approach this region and pass the virtual electrode as the result of a low DEP force which was not able to guide the beads further along the electrode. However, mutual dielectrophoresis led to the accumulation of smaller beads around the 10 μm beads when being guided along the virtual electrode. This becomes obvious in the following image sequences of Figure 3-18. Once the virtual electrode was passed, the accumulated beads separated again with all ending up in the same virtual channel. Therefore, the separation efficiency is significantly reduced. This means, while the smallest beads can be sorted into one virtual channel, they partially end up in the other channels as load on bigger beads.

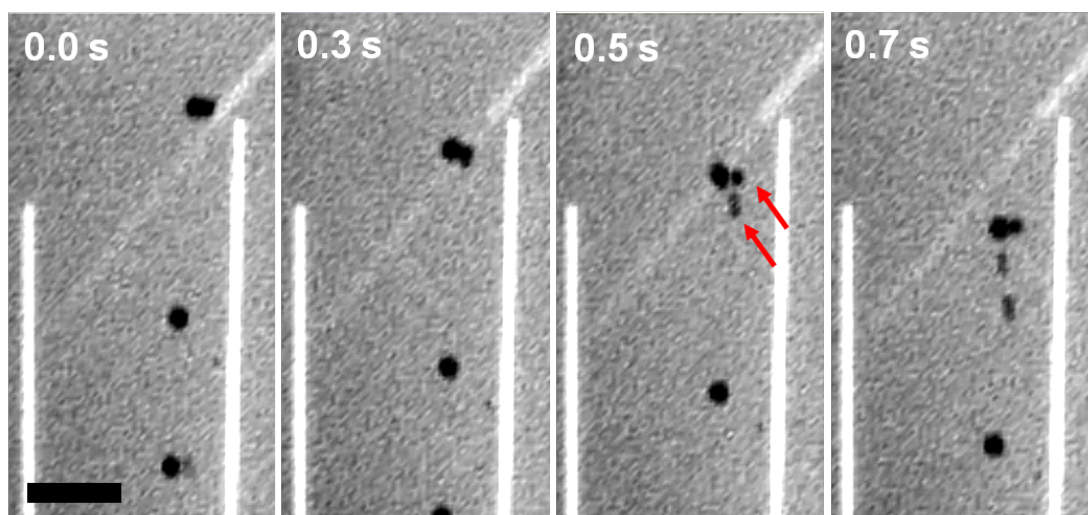


Figure 3-18: Time-lapse showing image sequences of a sorting experiment where smaller beads are loaded on larger beads due to mutual DEP. Scale bar is 50 μm . Red arrows point towards smaller beads which were loaded onto larger beads.

3.3.4. Limitations of the current OET device

The operation of the current OET device revealed several flaws associated with the electric field distribution in the liquid layer. The selective illumination to create a nonuniform electric field but also simply applying an AC signal to the device led to undesired particle interactions. These interactions occurred at the channel wall and in the bulk liquid between particles as the result of electrostatic interactions.

The aSi layer is not a perfect insulator in the dark state. At high voltages ($> 10\text{ V}$) a substantial electric field is created in the liquid even without selective illuminations due to voltage leakage beyond the aSi layer. The presence of a particle in the liquid layer can alter the leakage electric field and produces complex field distributions around it. A simulation in Figure 3-19a shows the electric field magnitude around an insulating 6 μm polystyrene bead subjected to a uniform electric field when an AC signal of 20 V at 100 KHz is applied to the OET device without illumination. A characteristic distribution of high and low field regions can be identified which becomes clear when comparing the electric field line distribution in the liquid (Figure 3-19b). The presence of an insulating bead leads to the distortion of the field lines creating low field regions at the poles and high field regions at the side of the bead. This non-uniformity induces mutual dielectrophoretic movements of beads nearby. As shown in Figure 3-19c, the DEP force vector field is directed away from the sides of the bead but towards the bead poles. If beads are in close proximity the induced dipole in the beads combined with mutual DEP force leads to bead – bead interactions (dipole-dipole interaction) which can result in the formation of chains. This effect is also known as pearl chaining⁸³ and

occurs when external uniform and non-uniform electric fields are applied. The latter one induced the bead aggregation in separation experiments described above.

In general, those particle interactions (at short distances), which resemble chain-like structures, are common observations when particles are exposed to an externally applied field. The presence of the particle in the field alters the field's spatial distribution. This creates new stable positions and configurations for interacting particles. The interaction of the particles is then dependent on their orientation and characterized by either attraction or repulsion forces. In acoustophoresis, it is the wave scattering on the particles surface that mediates particle interactions (see chapter 1.3.3). In dielectrophoresis, it is the altered electric field around the dielectric particle that causes attraction (pearl chaining) or repulsion phenomena. And in optical tweezing, it is the re-scattering of light by a particle that causes an interaction known as optical binding.²¹⁵

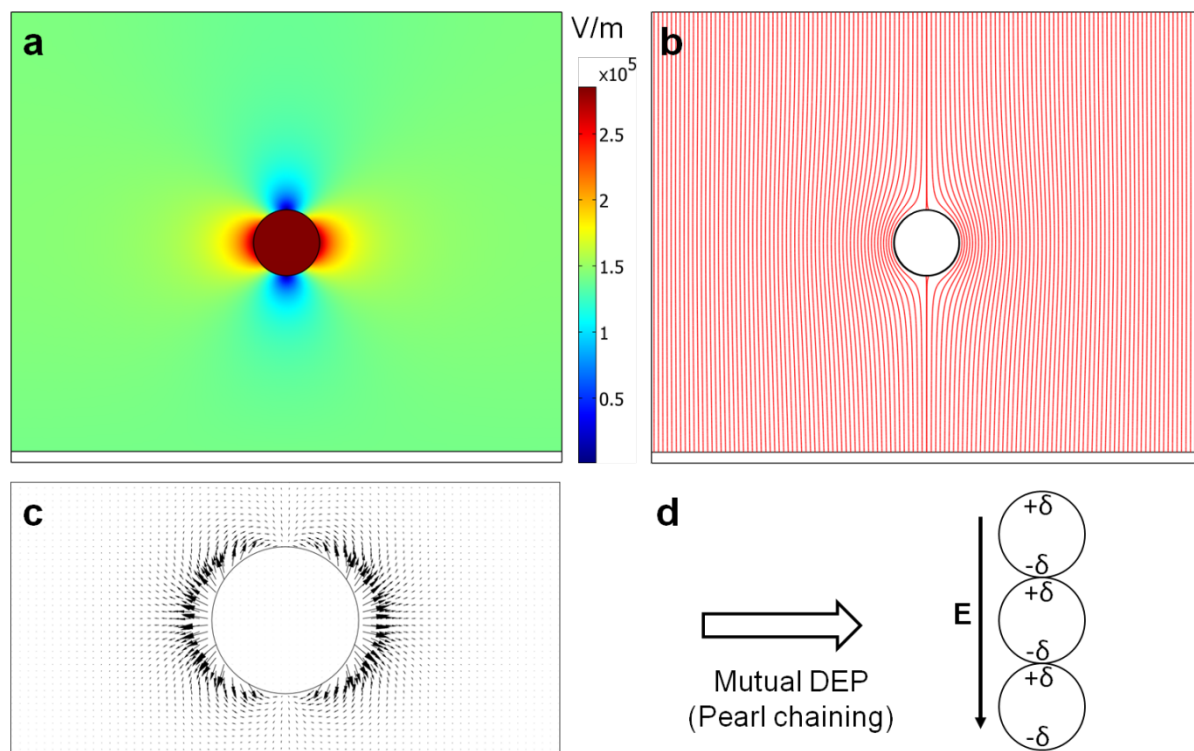


Figure 3-19: Electric field distribution in the presence of a particle (bead). (a) Electric field magnitude around an insulating 6 μm polystyrene bead subjected to uniform electric field (20 V, 100 KHz, 5 mS/m) when the aSi layer is not selectively illuminated (dark state). Colours in the scale bar and around the bead indicate electric field magnitude with blue being lower than red. (b) Corresponding representation of the electric field lines around the bead. For an insulating bead, the field bends around the particle. The bead is less polarisable than the surrounding medium. The results are lower field magnitudes at the poles of the bead compared to the sides. (c) The electric field distribution around the bead induces a DEP force on adjacent beads. This is called mutual DEP. The black arrows in the simulation represent the direction and magnitude of the DEP force imposed on an adjacent insulating bead. (d) The dipole within the bead induced by the electric field combined with mutual DEP leads to dipole-dipole-interactions between beads. This is also called pearl chaining because of beads lining up along the electric field lines.

The example in Figure 3-20 demonstrates the voltage leakage effect when an AC signal (20 V, 100 KHz) was applied to the chip without any illumination in a relatively static fluid. The top image in Figure 3-20 shows 6 μm beads randomly distributed in the bulk of the liquid layer when no AC signal was applied to the OET device. However, once the AC signal was switched on a new bead arrangement was observed accompanied with a sudden change in the amount of visible beads as well as their vertical position (out of focus) as the beads were now sitting on top of each other in the vertical electric field. When the AC signal was switched off afterwards (bottom image in Figure 3-20), the amount of beads visible increased again and beads were arranged in line style patterns. These observations were associated with the pearl chaining effect described above. Beads arranged vertically in form of a stack parallel to the fields lines. When the field was turn off, gentle fluid flow induced the bead movement which appeared as line arrangements. The alignment into a stack is dependent on the horizontal position of the adjacent beads.²¹⁶ At an angle of about 0° electrostatic repulsion takes place which can be expected based on the simulation in Figure 3-19a as result of the high field region on the lateral side of the bead. At higher angles of around 37° , as shown by Kang *et al.* for particles in a uniform field, electrostatic attraction takes place which promotes particle stacks.²¹⁶ In general, this effect is pronounced at high bead concentrations ($>10^6$ - 10^7 beads/ml) as the average distance between beads decreases while the electrostatic interaction increases with small distances (several micrometers) to up to 10^{-11} N²¹⁶ which is comparable to the DEP force induced upon illumination.

The results of this work demonstrated for the first time that OET is capable of manipulating particles at relatively high velocities. This required high electric field magnitudes to increase the DEP force and was achieved by reducing the gap between the photoconductor and the ITO electrode. However, it has to be noted that such shallow microchannels (15 μm) are not ideal when handling very large particle concentrations ($>10^7$ beads/ml). The combination of field leakage effects which produce pearl chaining and a high number of particles can cause large particle aggregates. This may results in clogging of the microchannel and could cause disturbances of the fluid flow which may interrupt the manipulation process. Moreover, the large surface area is prone to particle-wall interactions by unspecific bindings. It may be necessary to change the surface chemistry (e.g. coating with “lubricant” such as poly(ethyleneglycol)²¹⁷) to reduce these interactions and avoid clogging effects.

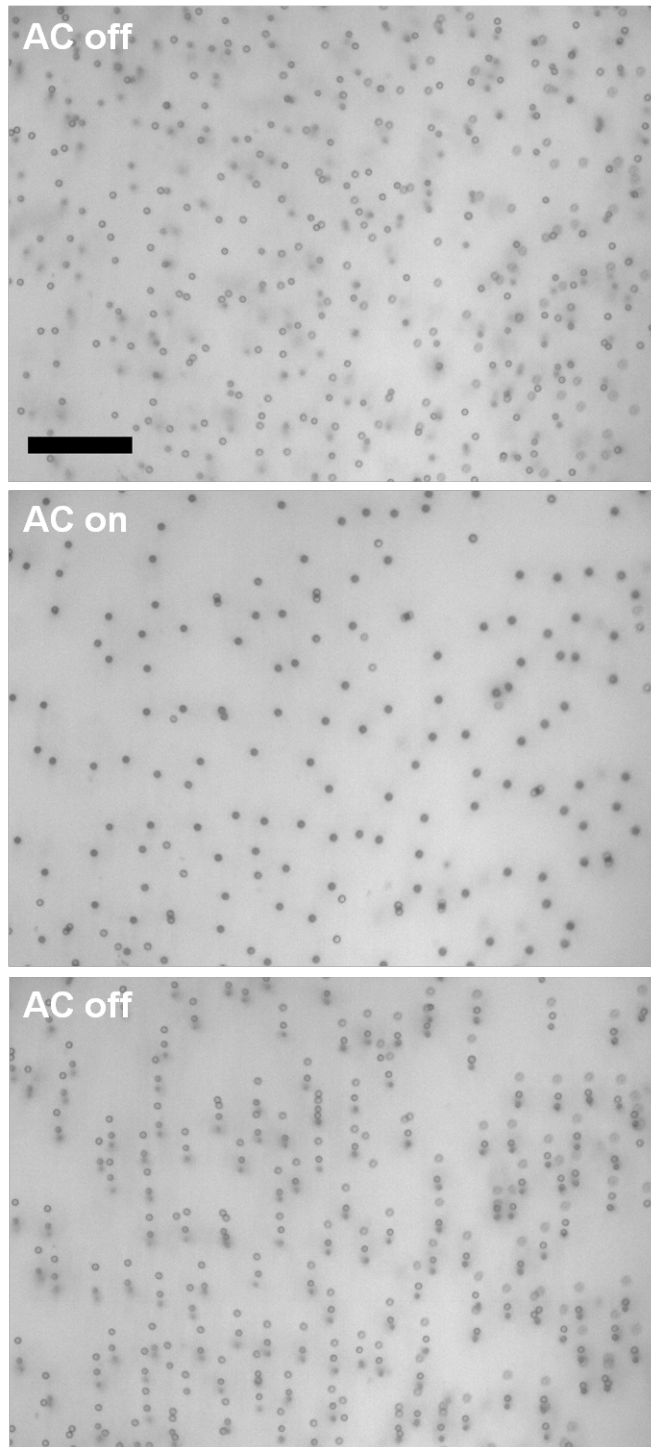


Figure 3-20: Voltage leakage effect induces the creation of an electric field in the liquid layer. This resulted in bead-bead interaction also known as pearl chaining. Top image shows randomly distributed 6 μm beads in the OET device without illumination and electric signal applied. The middle image demonstrates the stacking effect induced by the leakage field (no illumination). The bead concentration visually decreases as the beads were parallel aligned to the electric field lines. This becomes evident when the electric signal was switched off again and fluid flow driven separation occurred which revealed a line style bead arrangement.

Moreover, the voltage leakage triggers a significant bead motion under continuous flow in the microchannel at the wall – fluid interface. As mentioned earlier, SU8 is an insulating material and hence alters the field distribution of the leakage field. The channel walls in the microfluidic chip were not vertical but rather curved (see Figure 3-2d) which resulted in intense field regions at the edge of the SU8-aSi/ITO interface. The consequences of these high field regions are shown Figure 3-21 and 3-22.

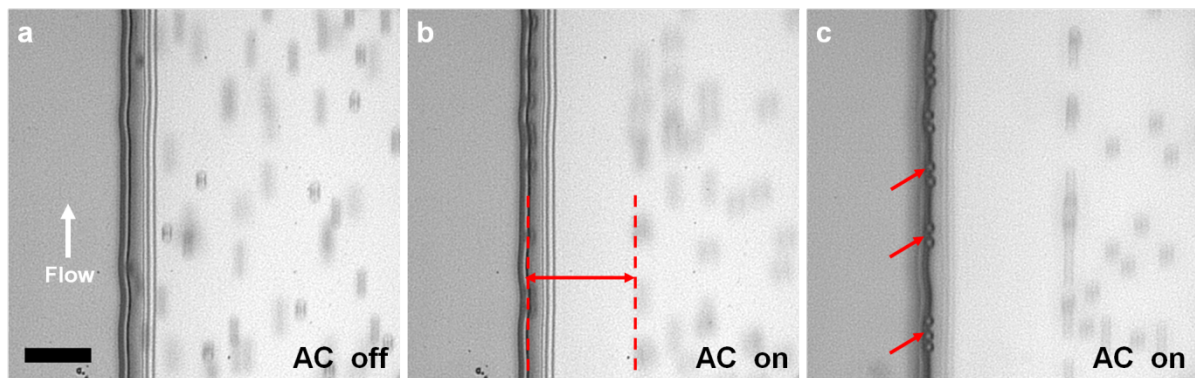


Figure 3-21: Influence of the leakage field (no illumination) on the bead distribution in the microchannel when a continuous flow was applied. (a) Distribution of 6 μm beads across the microchannel in absence of an AC signal. Voltage drop across the aSi layer in the dark state for an applied AC signal of 100 KHz at 20 V resulted in the displacement of beads towards (b) the microchannel centre and (c) the microchannel wall. The focal plane in (c) was change to improve the bead observation at the wall (Scale bar: 50 μm).

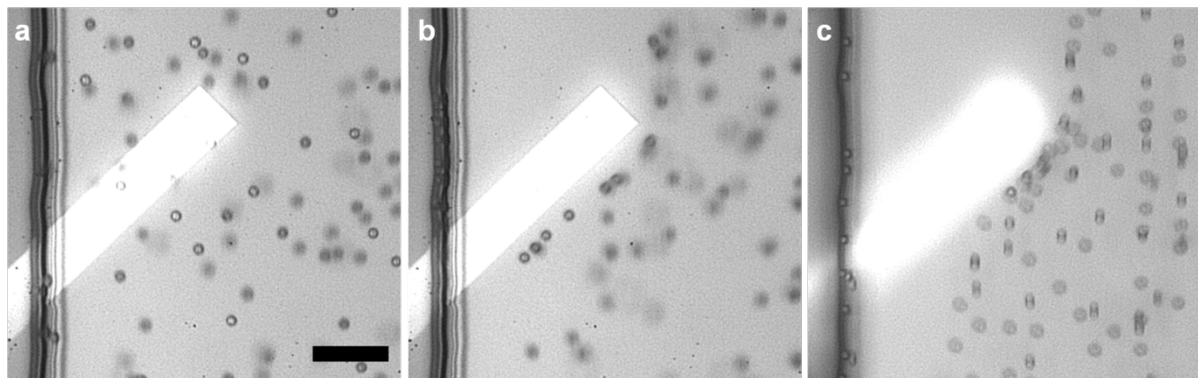


Figure 3-22: The curved microchannel wall acts as a shield preventing nearby beads from being manipulated by light induced DEP. (a) Absence of the AC field where beads were distributed randomly. (b) AC signal of 20 V at 100 KHz was applied leading to sufficient guiding of 6 μm along the virtual electrode. However, beads close to the channel wall (c) escaped the influence of the light induced DEP force due to the shielding effect of the insulating SU8 which resulted in bead motion toward the channel wall. Here, the focus was slightly changed for enhanced bead visibility by bringing the light pattern out of focus. (Scale bar 50 μm , flow from bottom to top).

In the absence of a leakage field (no AC signal applied, no illumination) beads were distributed across the channel (Figure 3-21a), however, once actuated with an AC signal (100 KHz, 20V, no illumination) bead motion and position was influenced by the leakage field. A region with beads being absent between the SU8/fluid interface and the bulk liquid was observed (Figure 3-21b). Also, an accumulation of beads at the channel wall could be

observed (Figure 3-21c). The insulating SU8 wall and the thin SU8 layer on the ITO and aSi electrodes as the result of the curved shape created a strong non-uniform leakage field region. Beads close to the wall were attracted to the SU8 because of a low field region, while beads further away from the wall (20 μm to 100 μm) were pushed towards the channel centre triggered by the high field region at the interface region. The projection of a virtual electrode to deflect beads from the wall was not helpful as seen in Figure 3-22. The curved SU8 wall acts as shield for nearby beads, which can escape the influence of the light induced DEP force. Moreover, the height of the beads within the microchannel changed due to the presence of the non-uniform field at the SU8-aSi/ITO interface. A DEP force acting towards lower field regions pushed beads in proximity to the wall either up or down towards the center region of the microchannel cross-section. In the Figures 3-21c and 3-22c the focus was changed from the photoconductor surface to the vertical channel center to show the height change of the beads along the channel wall.

The voltage leakage problem can be addressed by increasing the thickness of the aSi layer to achieve a higher voltage drop in the dark state. This strategy was considered in the OET device development, however, as shown in Chapter 2, the layer stability was significantly altered with a higher (1.5 μm) thickness resulting in poor adhesion and cracking of the aSi layer during the channel fabrication steps, eventually. Moreover, a thicker aSi layer may require increased optical power because of a relative high absorption coefficient within a 1 μm aSi which otherwise would not fully increase the photoconductivity throughout the layer.

An increased conductivity of the liquid medium might be used as alternative to increase the voltage drop across the aSi layer and avoid a leakage field. However, the device characterisation above revealed a significant reduction in the device performance with an increased conductivity and hence would slow down the throughput making particle manipulation and sampling under continuous flow inefficient.

The pearl chaining effect in the bulk liquid is difficult to suppress in the current device, however, the application of another force field may help to overcome particle-particle or particle-wall interactions. For instance, acoustic fields in form of standing pressure waves generated across the channel width can be used to push beads away from the channel wall due to the high pressure (see chapter 4). Moreover, a standing wave across the channel height may be used to align particle within a plane so that the relative particle orientation promotes electrostatic repulsion rather than attraction.

3.4. Conclusion

A novel fabrication method was introduced to integrate OET into a microfluidic chip. SU8 negative photoresist was sandwiched between two substrates by direct bonding of the top substrate to SU8 after spin coating. The advantages of this method are low bonding temperature, low stress induced by the bonding procedure, homogenous bonding area, stability to organic solvents for cleaning purposes and flexibility in creating microchannels of various heights. The bottleneck of the developed procedure and main disadvantage was the developing time which depends on microchannel dimensions and can take up to several days before a chip is fully fabricated and ready to use.

The OET device characterisation showed that the device performance can be tuned by controlling a range of parameters including the voltage signal, the conductivity of the liquid medium, the electrode gap, the virtual electrode size and transparency.

The flexibility of creating quickly virtual electrodes of arbitrary shape and intensity demonstrated useful microfluidic functions including particle focussing which can be combined with continuous subsequent particle separation steps.

However, the developed OET chips also revealed technical flaws which need to be solved to optimise particle handling, especially particle sorting. In particular, mutual DEP (pearl chaining) and undesired bead-wall interactions were identified as the result of a leakage field in the absence of light but an applied AC signal.

4. Acoustic tweezing using ultrasound standing waves

In this part of the thesis a concept for ultrasound standing wave based particle manipulation is presented. A SAW device with a broadband frequency response (slanted electrodes) was utilized for acoustic actuations. The transducer signal was coupled into a microchannel chip (superstrate) placed on the piezoelectric substrate to create an ultrasound standing wave at the resonance frequency. For the fundamental frequency, the one-dimensional standing wave is analysed in terms of acoustic energy density and pressure amplitude for different driving voltages. The shallow microchannel promoted acoustic streaming which appears as inner and outer boundary vortex rolls. The streaming velocity for small beads has been analysed showing an increase with increasing voltage applied to the SAW transducer. The broadband capability has been used to identify different resonance frequencies for different superstrates with changing microchannel dimensions. This functionality was then applied to pattern cells in the microchannel. The patterning time for different frequencies was characterized. Moreover, using just a single transducer, we demonstrated the separation of blood cells and parasite using different acoustic forces. Last but not least, a superposition principle was introduced where standing waves of different resonance frequency, excited by two transducers, were used for tuneable pressure distribution in the channel as well as for suppression of acoustic streaming to improve sorting of small particles and parasites. Combining this with an OET device enables the combination of acoustic fields and electric fields in a microfluidic chip as demonstrated in the following chapters.

4.1. Introduction

Microfluidics has brought forward several approaches for the manipulation of microscopic biological particles within microchannels. Different physical forces can be used, each having a particular set of advantages and limitations that make them suitable for different applications and different particles of interest, be they macromolecules or cells in suspension. Acoustic tweezing is particularly suited to the non-contact handling of microparticles within a microchannel^{116, 118, 123, 161, 173}. This can be achieved by attracting particles to acoustic nodes of a standing wave set up within the channel^{51, 110} which provides 3D control over the particles. As the pressure gradients extend throughout the channel the force acts on any particle within the channel and is governed by the particle's acoustic contrast which is a function of its density and compressibility.²¹⁸

The first applications of ultrasound standing waves in microfluidic compartments were demonstrated in the early 1980s by Weiser and Apfel, who studied mechanical properties of microparticles.²¹⁹ Since then, many concepts and strategies for microparticle trapping^{116, 117, 134, 136, 163, 220}, particle separation,^{120, 124, 171, 221, 222} mixing,^{189, 223} and transportation of particles and cells²²⁴ have been developed. Furthermore, approaches for bead based assays²²⁵, analysis of cellular activity²²⁶, the investigation of cell-cell interactions²²⁷ and separation of particles in biofluids¹²⁵ promise interesting applications.

BAW and SAW transducers are widely used for ultrasound based particle manipulations in microfluidics. For the latter one, it can be desirable to separate the acoustic transducer from the liquid/particles to be manipulated, so that the parts that come into contact with biological samples can be fabricated cost-effectively and easily disposed of. The concept of the 'superstrate', onto which the sample is placed, is an example of such a system.²²⁸ Acoustic waves generated by a SAW device are coupled into different superstrates, while the SAW device itself, usually fabricated in expensive single crystal piezoelectric wafers (e.g. LiNbO₃) is reused. The transmission of radio frequency radiation into a superstrate to move droplets has been reported first by Hodgson *et al.*(2009).²²⁸ Despite the fact that the longitudinal wave in the water layer is reflected between the interfaces of glass/water and lithium niobate/water^{228, 229}, there is still sufficient transmission of acoustic power into the superstrate to form a Lamb wave. This strategy has been successful in enabling a wide range of droplet manipulations on disposable superstrates.^{144, 155, 156} However, SAW based droplet manipulation on superstrates can be considered to be open microfluidics and therefore can be prone to contaminations.

Further microfluidics functions for particle manipulation have been shown for SAW transducers which were based on standing surface acoustic waves.^{118, 143, 159, 161, 162} Pairs of SAW transducers have been applied to create counter propagating surface waves of the same frequency resulting in constructive interference (standing surface acoustic waves, SSAW). The forces that result from pressure changes in the liquid have been used for different applications such as concentrating, trapping, and the continuous sorting of cells and particles. Usually, these devices utilize polydimethylsiloxane (PDMS) based microchannel chips bonded to the piezoelectric substrate. This requires precise alignment of the channel width relative to the pressure nodal planes between two SAW electrodes and can be challenging when the dimension of the channel are reduced to tens of micrometers.^{152, 230} PDMS is also associated with a high attenuation coefficient influencing the overall pressure amplitude of the acoustic field significantly.^{152, 231} Furthermore, the sample handling takes place on the piezoelectric material requiring cleaning, realigning and bonding after each usage or disposal of the expensive piezoelectric material.

To circumvent these fabrication issues, either channels can be etched into the piezoelectric substrate²³² or a complete decoupling of the particle manipulation from the piezoelectric surface into a superstrate with embedded microchannel can be performed while maintaining the benefits of a SAW transducer e.g. a compact planar device structure, broadband and high frequency response. Superstrates are used in this study and correspond to a typical transversal resonator design where the standing wave is the result of counter propagating waves reflected by the wall of a cavity. Uniquely it is shown that this approach requires just a single SAW device which couples the ultrasound signal into the superstrate. Here, a broadband slanted SAW transducer is used and we demonstrate the increased tolerance of misalignments between the microchannel and the acoustic field that this approach brings. This is a result of the microfluidic channel acting as a resonance cavity. The superstrate can be handled as a disposable glass/SU8/glass composite chip which combined with the simplified platform assembly allows quick and easy assembly of SAW devices for particle manipulations such as patterning and sorting. The outlined concept lays the foundation for combined use of electric fields and acoustic fields in a microfluidic chip, where the superstrate not only acts as acoustic resonator but also as DEP/OET device as shown later in this work (Chapter 5).

4.2. Materials and Methods

4.2.1. Slanted SAW device

A broadband interdigitated SAW transducer was used as ultrasound source to perform acoustophoretic particle manipulation. The fabrication process was shown in Chapter 2. The design of the transducer corresponded to a slanted electrode structure where the width of the electrode fingers changes along the aperture. The electrode width and pitch in relation to the piezoelectrical materials and its speed of sound define the frequency range.

4.2.2. Superstrate with embedded microchannel - fabrication

A detailed fabrication of the superstrate was described in Chapter 2. Briefly, a sandwich structure made of glass-photoresist-glass was used to create disposable composite microfluidic chips. The photoresist (SU8) acted as bonding agent to connect the glass substrates as well as the microchannel defining material.

4.2.3. SAW device and superstrate

The superstrate, shown in Figure 4-1a and 4-1b, contains a microchannel and was simply placed on the LiNbO_3 wafer in front of the SAW transducer where it was fixed using metal clamps (Figure 4-1c). A fixed volume of deionised water ($10 \mu\text{l}$) was injected between superstrate and piezoelectric wafer to provide an acoustic coupling layer. The LiNbO_3 wafer contained a pair of SAW transducer but was not diced into individual pieces. A good dicing result requires appropriate dicing tools which were not available. The wafers were very fragile and the use of a simple scribe can result in unwanted cracks which may influence the surface acoustic wave propagation. Moreover, the pair of SAW transducer was used simultaneously as shown in chapter 4.3.10.3.

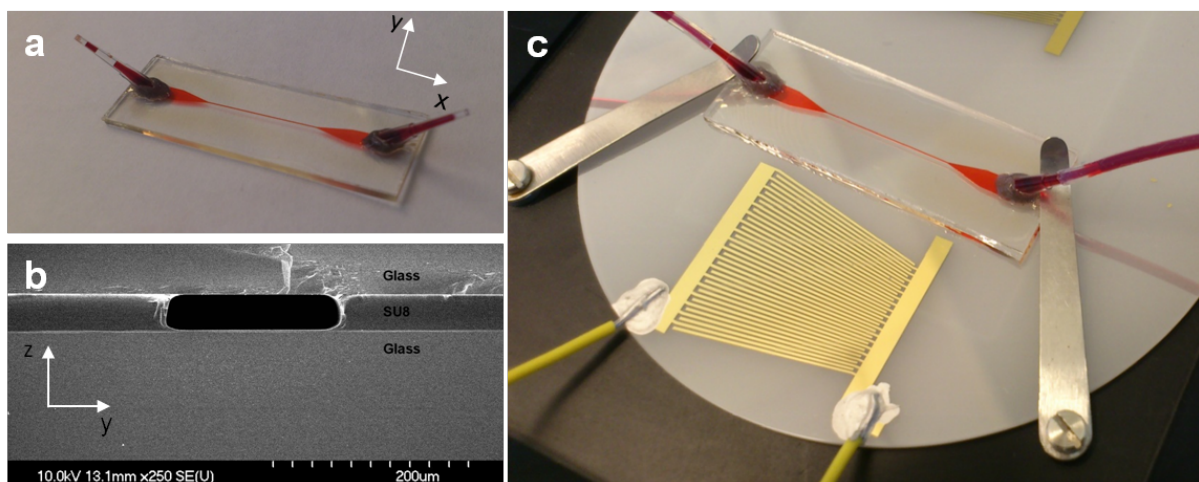


Figure 4-1: Superstrate with embedded microchannel (b) SEM cross section of microchannel. (c) Superstrate placed in front of a slanted SAW device on a piezoelectric wafer.

4.2.4. Acoustic energy densities and pressure amplitudes in the microchannel

The acoustic energy density and the pressure amplitude are difficult to predict by simulation models due to a complex acoustic interaction of all the components in the system. However, recently, a method to measure the local pressure amplitude and acoustic energy densities has been introduced by Barnkorb *et al.*¹¹⁰ Based on this approach we characterised the coupling efficiency from the SAW transducer into the superstrate by calculating acoustic energy densities and pressure amplitudes for varying input powers. This method is based on tracking the transverse path of beads in the microchannel experiencing an PAR force. For a one-dimensional plane standing wave the force on a particle is given by equation 1.20 (Chapter 1). In a static liquid of viscosity η , balancing the acoustophoretic force F_y^{rad} and Stokes drag force F_S (equation 1.1) leads to the differential equation,²³³

$$u = \frac{dy}{dt} = \frac{2\phi}{3\eta} k_y a^2 E_{ac} \sin(2k_y y). \quad (4.1)$$

The analytical expression for the transverse path of a particle undergoing acoustophoresis is then obtained by separating the variables y and t ,²³³

$$y(t) = \frac{1}{k_y} \arctan \left\{ \tan[k_y y(0)] \exp \left[\frac{4\phi}{9\eta} (k_y a)^2 E_{ac} t \right] \right\}. \quad (4.2)$$

The lateral movement of 3 μm beads were tracked, resulting in a curve of lateral position versus time. The theoretical description of the bead path was fitted to the tracked bead data points which then allowed the calculation of the acoustic energy density as E_{ac} being the fitting parameter. The pressure amplitude p_{ac} in the channel can then be calculated from equation 4.3.

$$p_{ac} = 2\sqrt{\rho_m c_m^2 E_{ac}} \quad (4.3)$$

Software called Tracker was used to perform tracking experiments for extracting the lateral path towards the pressure node (Figure 4-2). First, video files were imported to the software, followed by defining the scale of the image as well as the coordinate system. The point mass function in the software was then used to initialize the auto tracking of a bead of interest. An evolution rate, target size and scoring values were also defined to compensate changes in amount of pixel and intensity.

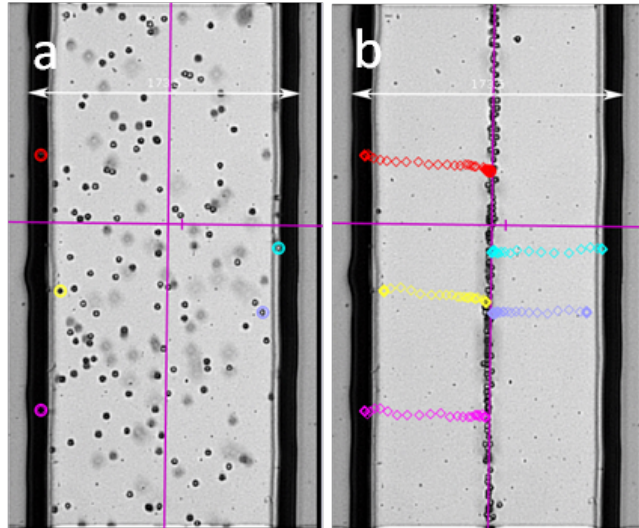


Figure 4-2: Tracking of 3 μm particles over time using video analysis software Tracker. (a) Dimensions and coordinate system were calibrated and defined. Beads of interest were marked and the auto tracking function was applied to monitor the bead position once acoustic actuation was on. (b) Beads were pushed towards the pressure node. The paths of individual beads were marked and can be seen by the different colour coding.

4.2.5. Acoustic streaming induced bead movement in microchannel

For particle sizes smaller than 2 μm acoustic streaming was observed. As a common effect in shallow channels, acoustic streaming is the result of viscous dissipation of acoustic energy near a solid boundary.¹¹⁴ In typical half-wave length resonators, the dissipation creates powerful vortices (Schlichting streaming) in the inner boundary layer which influences the fluid flow in the bulk producing outer-boundary layer streaming (Rayleigh streaming). Acoustic streaming results in a Stokes drag force on a spherical particle and can be expressed using equation 1.1. The velocities of 1 μm beads being moved by acoustic streaming were measured. As before the software Tracker was used to track the lateral movement in the vortices. In particular we measured the velocity of beads for a range of voltages applied to the SAW transducer. The extracted displacements in y direction were used to calculate the velocity and hence the force acting on the beads. The beads were injected into the chip and the streaming experiments were started after reaching a steady state in the channel without fluid flow. In Figure 4-3, a red track shows the lateral displacements of a 1 μm bead within a vortex flow generated upon ultrasound activation. The pressure nodal plane can be seen on the left hand side. It contained focussed 6 μm beads.

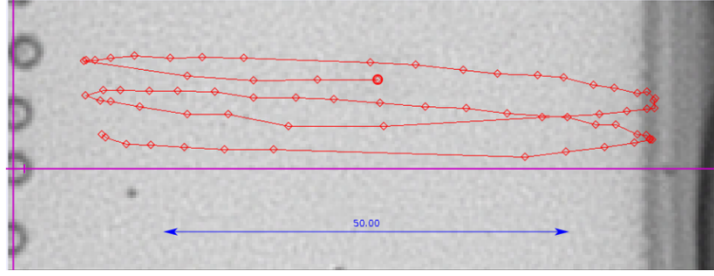


Figure 4-3: Tracking of 1 μm bead in vortex flow to determine streaming velocity for different applied voltages. Software Tracker was used to mark beads of interest and monitor position over time. The red path shows the circular motion of a 1 μm bead in the vortex flow. A coordinate system (violet) and image scale (blue line) were defined beforehand. The pressure nodal plane is shown on the left hand side of the image. It contains stationary 6 μm beads which were focussed upon ultrasound activation.

4.2.6. Model and simulations of pressure eigenmodes

Finite element method (FEM) numerical modelling (COMSOL Multiphysics v3.5, pressure acoustic module, COMSOL, UK) has been used to gain insight into the acoustic resonance of a liquid filled cavity like the microchannel in the superstrate. COMSOL was used for determining the eigenfrequencies of the superstrate as solutions to the Helmholtz equation for acoustic pressure fields which support transverse modes of half a wavelength with a pressure nodal plane in the centre of the microchannel. The pressure field p in a lossless medium is governed by the wave equation (equation 4.4) where ρ and c being the density of the material and the corresponding speed of sound.²³⁴

$$\frac{1}{\rho c^2} \frac{\partial^2 p}{\partial t^2} + \nabla \cdot \left(-\frac{\nabla p}{\rho} \right) = 0 \quad (4.4)$$

In a special case such as a simple time-harmonic wave, the wave equation is linear and has time-dependent coefficients so that the resulting pressure field is expected to be oscillating at the same frequency as the imposed excitation frequency. Then, one can assume that that the pressure field has the form:²³⁴

$$p = \text{Re}(p(x)e^{i\omega t}).$$

Using this assumption the time dependent wave equation transforms into the Helmholtz equation (equation 4.5) which is governed by the spatial dependency of the pressure field permitting the determination of the pressure distribution within a domain. COMSOL solves the Helmholtz equation in the frequency range of interest.²³⁴

$$\nabla \cdot \left(-\frac{\nabla p}{\rho} \right) - \frac{\omega^2 p}{c^2 \rho} = 0 \quad (4.5)$$

The pressure acoustic model in COMSOL requires that the computational mesh in the domain must resolve the wavelength. It is suggested to use at least 5 mesh elements per wavelength. Then the pressure modes can be determined by the Helmholtz equation with appropriate boundary conditions. Here, different conditions including a soft wall (equation 4.6), a hard wall (equation 4.7) and a lossy wall (equation 4.8) can be defined, with the latter one being approximated by using the specific impedance of the absorbing surface.²³⁴

$$p = 0, \quad (4.6)$$

$$\left(n \cdot \left(-\frac{\nabla p}{\rho} \right) \right) = 0 \quad (4.7)$$

$$\left(n \cdot \left(-\frac{\nabla p}{\rho} \right) \right) - \frac{i\omega p}{Z_s} = 0 \quad (4.8)$$

The specific impedance is given by:

$$Z_s = \rho c \frac{1+R_p}{1-R_p} \quad (4.9)$$

where R_p is the reflection coefficient (equation 1.26). The lossy wall was used to describe absorbing and damping boundaries. SU8 photoresist was used as a microchannel wall material. However, the reflection coefficient considering a SU8/water interface was only 40.9 % indicating significant attenuation at the channel wall. A hard wall boundary condition is usually applied when transmission of acoustic energy is low and incoming waves are mainly reflected which results in high pressure points but zero velocity at the interface. This kind of behaviour is often assumed in transversal resonator designs where materials like silicon are used to create microchannel features.¹¹⁰ The soft wall boundary conditions can be applied when an interface region is not able to sustain any pressure.²³⁵ Such interfaces can be an air-liquid boundary or a thin glass wall. Hammarström *et al.* modelled resonance modes of glass capillaries with thin walls ($\sim 200 \mu\text{m}$) using a soft wall boundary.¹³⁴

First, a simple 2D model depicting the fluidic domain of the microchannel was used to find resonance modes of the superstrate (Figure 4-4).

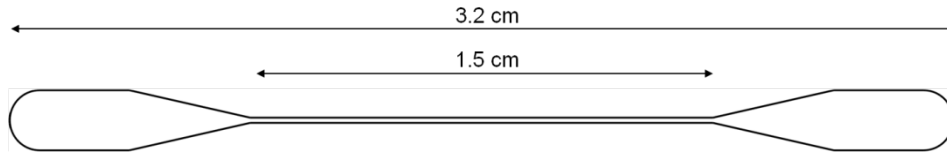


Figure 4-4: Fluidic domain of the microchannel in the superstrate used for simple 2D model.

In this simple 2D model, the centre plane of the fluidic domain was considered only, neglecting a vertical resonance mode which is justified by the height of the cavity ($35\ \mu\text{m}$) being ten times smaller than the wavelength ($\sim 360\ \mu\text{m}$ for the observed frequency range). Further assumptions were made by considering the channel to be of rectangular shape with straight walls. The width and length of the channel used in the model was $173\ \mu\text{m}$ and $15\ \text{mm}$, respectively. The speed of sound and density used for the fluidic domain was $1450\ \text{m/s}$ and $1000\ \text{kg/m}^3$, respectively. The 2D model was then extended introducing a solid domain surrounding the fluidic domain to ascertain how this improvement on the original very simplified model will affect the frequencies of the modes produced (Figure 4-5). The properties of SU8,²³⁶ density ($1200\ \text{kg/m}^3$) and speed of sound ($2880\ \text{m/s}$), were given to the solid domain representing the reflecting walls in the cavity of the superstrate. The outer superstrate interfaces were defined with boundary conditions (see above), with substrate dimensions of $15\ \text{mm}$ (width) and $40\ \text{mm}$ (length), while interior boundaries with the fluidic domain were given the continuity boundary conditions. The liquid domain position was centered relative to the solid domain.

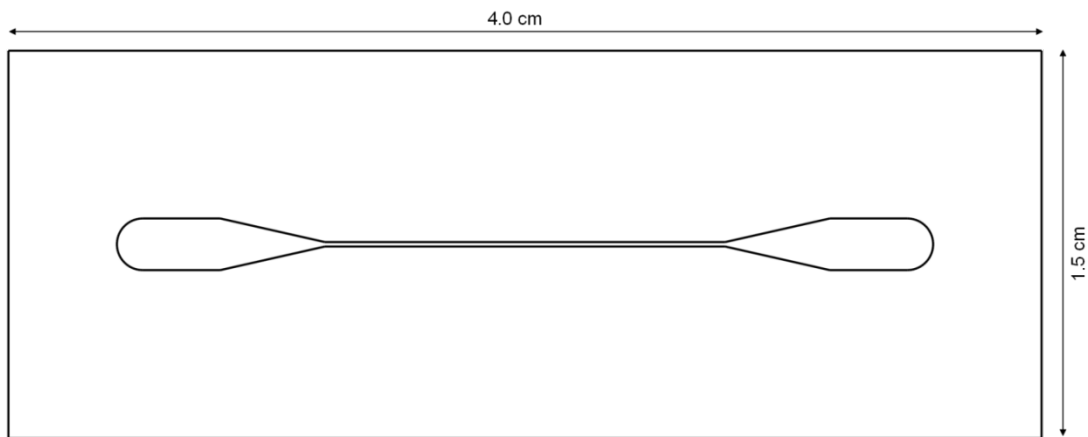


Figure 4-5: Extended 2D model containing solid domain (SU8) surrounding the fluidic domain.

The simple eigenfrequency analysis does not consider energy loss by acoustic attenuation or diffractions at boundaries and hence ignoring the acoustic interaction with the surroundings e.g. the coupling from the transducer to the superstrate. A 3D model of the superstrate containing all materials and their respective dimensions can be envisaged but

requires more computational power than is easily available and unless the complex system of materials, boundary assumptions and geometries are carefully considered may not result in a more physically accurate model. For instance, more comprehensive models have been described by Dual and Schwarz²³⁷ where the wave equation was combined with elastic equations (strain fields, stress fields, displacement fields) to consider deformations of solid boundaries and their influence on the liquid domain.

4.3. Results and Discussion

4.3.1. Device concept

A disposable composite superstrate (Figure 4-1a) with an embedded microchannel was used as the acoustic cavity for bead manipulation in a standing wave based on acoustic waves excited from a SAW device. This compares to conventional SAW based particle actuation in PDMS channels which require bonding and careful alignment relative to two SAW transducers. In a conventional SAW based manipulation platform (Figure 4-6a), the SAW travels along the piezoelectric substrate and enters the PDMS/LiNbO₃ interface where it partially couples as a bulk acoustic wave (BAW) at a certain angle into the PDMS before it reaches the microchannel and generates a surface standing wave from interference with a counter-propagating acoustic wave.¹⁵² In the concept presented here, the SAW travels along the LiNbO₃ substrate before it couples as a leaky Rayleigh wave into the fluid of the coupling layer (water) where it produces a longitudinal pressure wave (Figure 4-6b).²²⁹ The pressure wave is mainly reflected at the bottom glass substrate of the superstrate²²⁹, however, transmission of acoustic radiation as BAW into the glass itself takes place and radiates even further into a liquid above it.^{228, 238} In several studies it has been shown that droplets placed on a superstrate can be actuated to achieve fluid streaming and directed movement.^{144, 155, 156} In this study we make use of BAWs to create a standing waves in a microchannel embedded in a superstrate.

First, the fundamental frequency of the superstrate was analysed where the resonance modes support half a wavelength across the width of the microchannel. In addition to FEM modelling, experimental analysis by broadband transducers which enable scanning along a frequency range can be performed. The fundamental frequency is then used to characterise the coupling of acoustic energy into the superstrate. Later it is demonstrated that even higher harmonic resonances can be achieved and that the presented concept is able to provide some useful microfluidic functions.

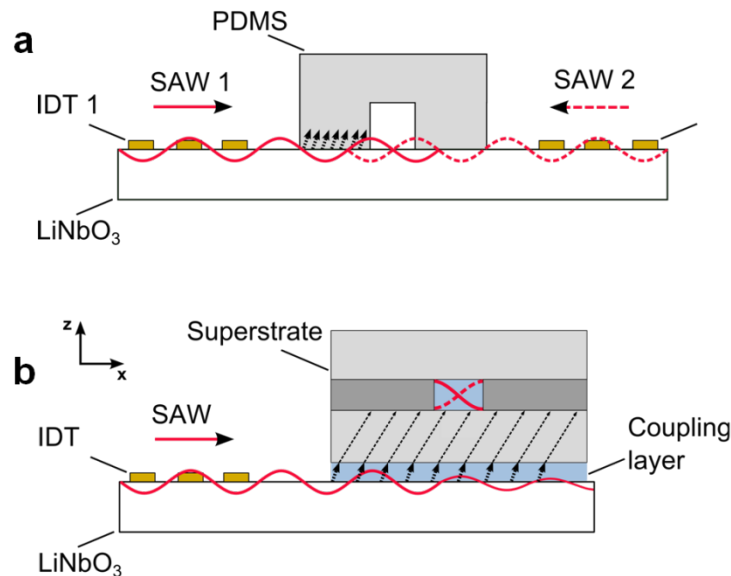


Figure 4-6: (a) Standing surface acoustic waves generated by a pair of identical SAW transducer exciting the same frequency. A PDMS channel is aligned and bonded with respect to the pressure landscape on the piezoelectric material. (b). Alternative concepts proposed in this study where a superstrate with embedded microchannel acts as transversal resonator. A single SAW transducer provides an ultrasound signal which is coupled into the superstrate creating standing waves upon resonance.

4.3.2. Modelling pressure eigenmodes in simplified microchannels

In an ideal system, the resonance frequency which supports half a wavelength of a pressure wave across the width of the microchannel can be approximated by considering the width of the cavity and the speed of sound in the fluid. For instance in this case, the resonance frequency would be 4.191 MHz (1450 m/s, 173 μm). However, in practice numerical methods can be helpful to predict resonance modes in more than one dimension more accurately as shown previously in studies by Hagsater *et al.* and Barnkob *et al.*^{110, 239} Therefore, to gain some qualitative insight in the resonance behaviour of a microchannel 2D models were implemented in the finite element analysis tool COMSOL Multiphysics. In particular, the Eigenmodes of a liquid filled cavity depicting the microchannel outline in the superstrate were analysed for different boundary conditions. A hard wall condition (equation 4.7) was applied which describes a boundary with indefinitely high acoustic impedance, where a reflected pressure wave undergoes a phase change while the displacement or velocity remains zero. This condition is often used for silicon or glass based resonator structures although transmission coefficients of up to 25% indicate a lossy wall behaviour. The transmission at a pure SU8 microchannel wall is expected to be higher with approximately 60% (calculated with equation 1.26), however, the superstrate is a composite structure and so deviations to this are likely. A soft wall condition was applied for comparison. The reflected wave undergoes no phase change because of the boundary

being assumed to be free and not able to sustain the pressure. The velocity is maximum at that point while the pressure is zero. The resonance behaviour of a thin-walled glass capillary attached to a BAW transducer has been modelled using a soft wall conditions.¹³⁴ Here, pressure nodal planes were located at the side walls of the capillary and in the bulk liquid while high pressure regions were confined to the bottom and top side. When the boundary is neither hard nor soft then part of the pressure wave is transmitted across the boundary which results in a reduced amplitude of the reflected wave. This case is likely to be the case for the superstrate and therefore a lossy wall condition with a specific impedance of 8.24 MPa s/m (calculated with equation 1.25) for the SU8 boundary was introduced.

In Figure 4-7, eigenmodes of the pressure field in the liquid domain for different boundary conditions are shown. For the hard and lossy wall boundary conditions several transverse modes supporting half a wavelength across the channel width were identified (Figure 4-7a and 4-7c). For instance at 4.192 MHz and 4.193 MHz maximum and minimum pressure regions were located along the channel wall, although the pressure distribution was not homogenous along the straight channel segment and the magnitude of the pressure can be assumed to be lower for the lossy wall. The pressure was close to zero in the straight channel entrance and exit regions and at 4.193 MHz in the centre of the microchannel. The existence of multiple modes has been observed earlier and the characteristic pressure distribution was experimentally verified and described as pinching region with acoustic forces being more confined at these points in a resonator structure.^{239, 240} In fact the number of these regions increases with increasing frequency of solutions to the Helmholtz equation. The close to zero pressure zone towards the end of the straight channel section may be associated with the channel design. The geometry of the channel can confine acoustic resonance to certain symmetrical regions without leaking into adjacent geometrically differing regions.²⁴⁰ In comparison, the soft wall condition resulted in resonance modes of half a wavelength with low and high pressure regions located in the liquid domain and zero pressure along the channel wall (Figure 4-7b). At 4.193 MHz a low and high pressure region spans along the straight channel with a single zero pressure zone in the center and across the channel width. The pinching region is now perpendicular to the channel length and the number increases with increasing frequency as shown for 4.208 MHz. Considering a pressure driven flow applied to the inlet, a particle with a positive acoustic contrast would move along the channel length in the case for a hard and lossy wall. The soft wall case would move particles along the channel wall parallel to the fluid flow and orthogonal to it at the pinching region. This may trap particles against the fluid flow when the PAR force overcomes the drag force.

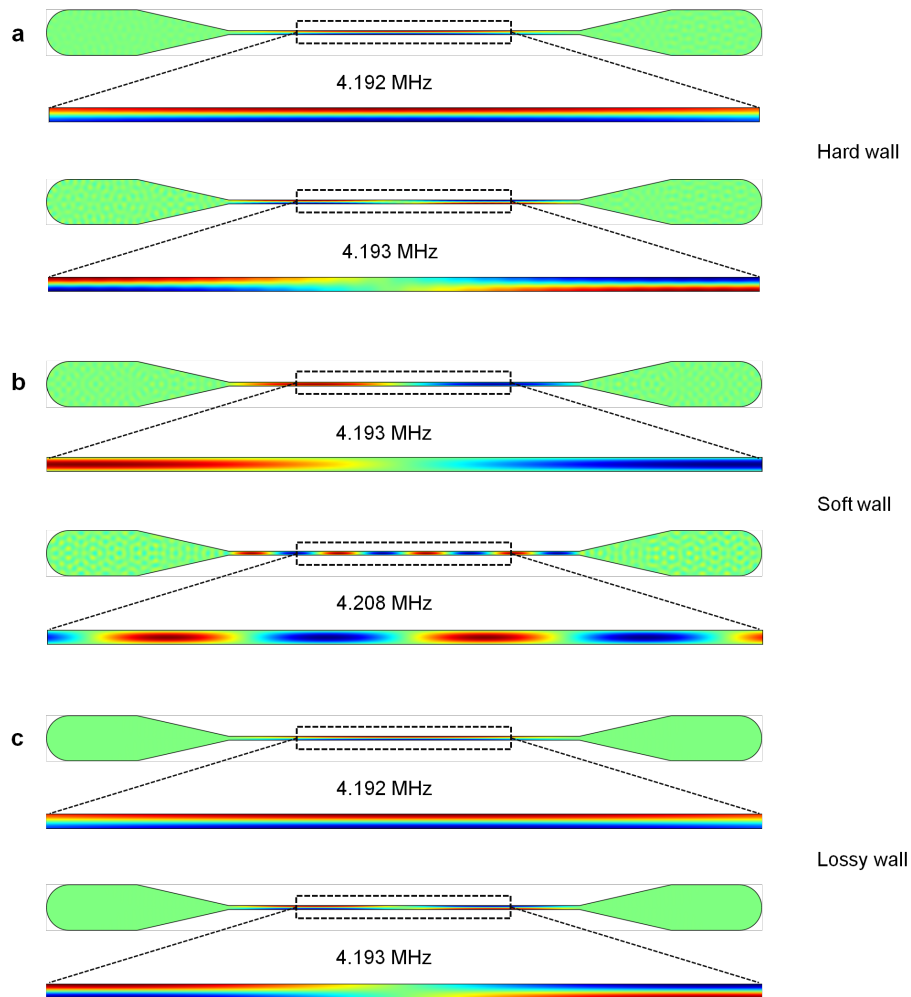


Figure 4-7: Eigenmodes of the pressure field in a simple liquid filled microchannel (green: zero, blue: negative, red: positive) as solutions to the Helmholtz equation with different boundary conditions where (a) depicts hard wall, (b) soft wall and (c) a lossy wall.

The model was modified to take some of the material properties of the channel walls in the superstrate into account. In this case the layer of SU8 was included. Usually, glass or silicon is used in transversal resonator designs while polymers are avoided due to acoustic losses and poor reflection properties which result from the increased elasticity and compressibility of polymers. The result of the eigenfrequency analysis for different boundary conditions is shown in the Figures 4-8 to 4-10. For hard and lossy wall conditions several eigenmodes supporting the half a wavelength criterion were found. However a significant shift to lower resonance frequencies compared to the first model was found. A decrease by slightly more than 100 KHz to 4.086 MHz and 4.088 MHz was found for a hard wall boundary, while the decrease for a lossy wall was by around 300 KHz to 3.902 MHz and 3.909 MHz. In both cases, the solid SU8 domain was characterised by sections of homogenous pressure distributions parallel to the straight channel of the liquid domain. When considering the top and bottom half of the SU8 layer, the existing pressure field resembles pressure waves with a phase difference of 180° . The interface between the solid and liquid domain confined high

and low pressure regions resulting in tight and loose pinching regions along the straight channel outline. A difference in the magnitude of the pressure can be expected for both the hard and lossy wall, however the resonance frequencies also differ.

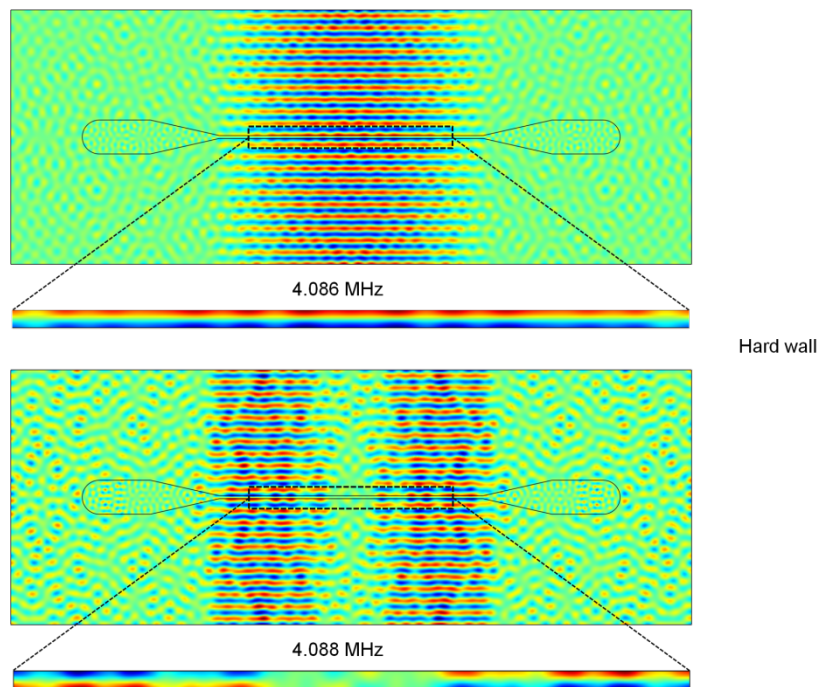


Figure 4-8: Eigenmodes of the pressure field in an extended 2D model including the SU8 as material surrounding the liquid filled microchannel. Eigenmodes are presented for hard wall (green: zero, blue: negative, red: positive).

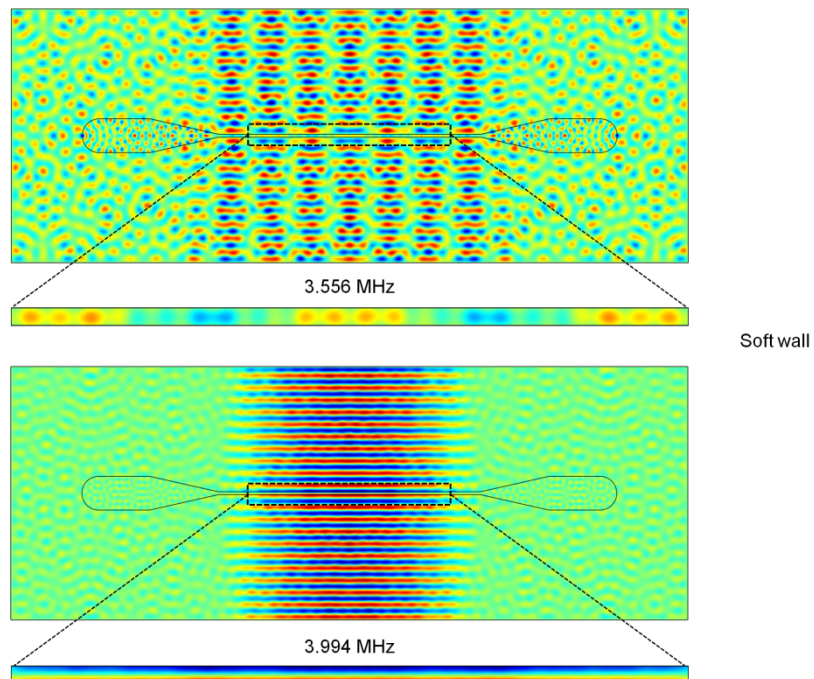


Figure 4-9: Eigenmodes of the pressure field in an extended 2D model including SU8 layer modelled as soft boundary.

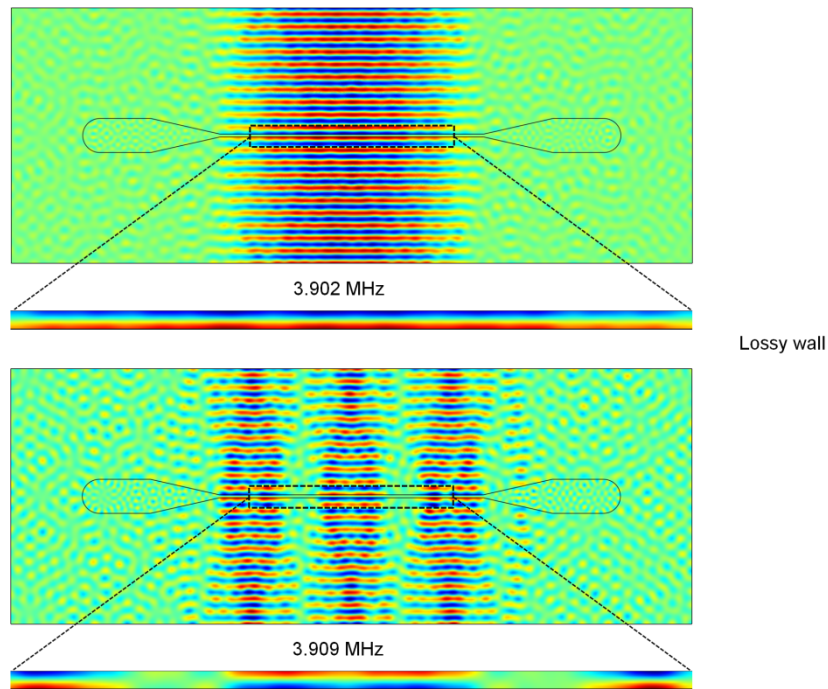


Figure 4-10: Eigenmodes of the pressure field in an extended 2D model including SU8 layer modelled as lossy boundary.

The soft wall case showed no support of half a wavelength across the channel width in the first model. The low and high pressure regions were found to be inside the liquid domain. Similar eigenmodes were also found for the extended model. An example at 3.556 MHz is shown in Figure 4-9. However, eigenmodes which support the half a wavelength criterion do also exist for a soft wall case as shown in Figure 4-9 at a frequency of 3.994 MHz. The outer boundaries of the SU8 layer parallel to the straight channel section were of zero pressure, but the top and bottom half showed a phase difference which combined with the symmetric arrangement of the microchannel resulted in confined low and high pressure regions along the straight channel sections.

These results indicate 2D effects and were considered with care due to missing levels of complexity in terms of the composite superstrate structure, channel cross-section geometries (see Figure 4-1b) and channel position within the superstrate (symmetry – antisymmetry). Nonetheless, even these simple simulations show that resonances differ significantly from idealized models when introducing materials other than glass or silicon into resonator structures.

4.3.3. SAW transducer design

An ultrasound source with a certain range of excitable frequencies can be helpful to investigate resonance modes of resonator structures. The frequency can be tuned by scanning through an available range until a resonance point is observed where a strong movement of particles towards minimal or maximal pressure points takes place.

In this study a SAW device based on slanted interdigitated finger electrodes was used (Figure 4-11a). The slanted device design was chosen to enable a broad frequency response in the lower Megahertz range. Alternatively, a chirped SAW transducer (Figure 1-15b) can also be used to achieve a broadband SAW excitation. This type of transducer is preferred when the position and the width of the aperture of the SAW beam should be constant for the range of frequencies. However, the device developed here creates narrow SAW beams at different positions along the aperture. The device consisted of 18 pairs of electrodes over an aperture of 2 cm deposited on a lithium niobate wafer. The frequency spectrum was measured using a network analyzer. The theoretical frequency band was within 3.5 MHz to 5.5 MHz considering the width and pitch of the electrodes. The spectrum analysis showed a fundamental frequency response between 3.7 MHz and 5.5 MHz (Figure 4-11b). However, SAW devices are well known for not operating only at fundamental but also harmonic frequencies. The slanted IDT showed harmonic responses of frequencies up to 21 MHz as seen in Figure 4-11b. The lowest, highest and the centre frequencies of the fundamental spectrum were visualized using an infrared camera. The piezoelectric substrate was coated with a water based jelly in front of the SAW device. The coupling of the SAW into the gel was associated with an increased attenuation of acoustic energy in form of heat which enhanced the imaging. The electrical signal was generated by a function generator and then increased by an amplifier before being fed into the SAW device. In Figure 4-11c the position of these frequencies along the aperture is shown. The narrow SAW beam travels along the substrate before radiating acoustic energy into the jelly which identifies the position of the excited frequency along the aperture of the SAW device. In Figure 4-11c the lowest fundamental frequency of the device was 3.7 MHz which produced a SAW beam on the outer right aperture side of the transducer. The centre frequency was determined to be 4.55 MHz and the lowest frequency was 5.5 MHz. The width of the of SAW beams were in the range of 2 mm to 3 mm according to infra red image analysis.

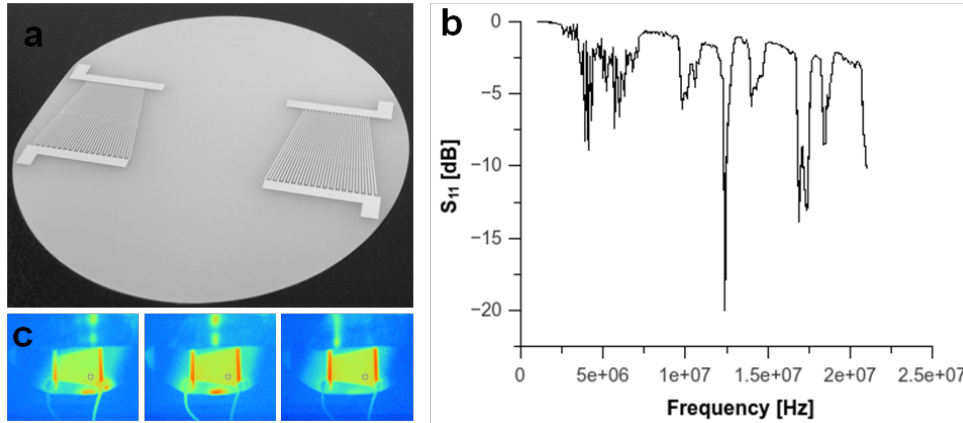


Figure 4-11: (a) SAW device with slanted interdigitated transducer design on LiNbO₃. (b) Broadband frequency response of SAW device. (c) Infrared images of transducer when actuated in the frequency bands with lowest frequency of 3.70MHz, centre frequency of 4.55MHz and highest fundamental frequency of 5.50MHz.

It has to be noted that the SAW device is not operating in a pure surface acoustic wave mode. The low frequency range (higher wavelength) creates radiation into the substrate in the form of bulk acoustic waves. The propagation of a mixture of bulk and surface acoustic waves is associated with radiation losses and leads to non-uniform amplitude profiles for different frequencies.²⁴¹ There are two kinds of losses due to BAW radiation.²⁴² One is associated with the propagation loss of the travelling SAW. This is also known as leaky SAW which continuously transmits energy as BAW into the substrate. The second one originates from the interdigitated electrodes which excite the leaky SAW and includes surface skimming BAW, which propagate close to the surface, and deep BAW radiated into the substrate. These BAWs decrease the excitation efficiency of the SAW.

The measured reflection coefficient (S_{11} -parameter) indicated that the power delivery over the frequency range was not homogenous (Figure 4-11b). Therefore, the coupling of acoustic energy into the superstrate can be expected to be dependent on the frequency. This arises due to impedance mismatches between the source (signal generator, 50 Ohm), the transmission line (coaxial cable) and the load (SAW transducer). The coupling from the signal generator to the SAW transducer may be improved by impedance matching circuits but that requires individual frequency specific designs and may be considered as an optimisation step in the future.

There are different strategies mentioned in the literature to suppress the attenuation of SAW (e.g. certain crystal cuts).²⁴³⁻²⁴⁵ However, a major reason for the mixture of bulk and surface acoustic waves in this work was due to the thickness of the piezoelectric wafer. The lower MHz frequencies range and corresponding acoustic wave length were in the order of 1 mm while the wafer was just 0.5 mm thick, producing travelling BAW in the substrate. It is

recommended to increase the thickness of the wafer to several times of the applied wavelength to improve SAW excitation¹⁵² or alternatively make use of a higher frequency range. Instead of 0.5 mm, a 3 mm thick wafer might be used to suppress bulk responses and benefit from a less leaky SAW with enhanced power transmission. Unfortunately, thick wafers would be expensive and hence were not available during the course of this study but nonetheless, the following experimental results show that the developed transducer can be used for acoustophoretic particle manipulation.

4.3.4. Acoustic actuation of the superstrate using a SAW transducer

The actuation of fluids on top of a superstrate using SAW devices has been shown in several studies which focused mainly on droplet actuation including mixing, merging or nebulisation.^{144, 155, 156} In this study a superstrate with integrated microchannel was utilized to enable particle and cell acoustophoresis.

The combination of a broadband transducer and a superstrate with embedded microchannel has some advantages compared to systems based on BAWs and systems based on SAWs in conjunction with PDMS microchannels. BAW transducers work in a narrow frequency range, often only at a single frequency defined by the thickness of the piezoelectric substrate. The arrangement of BAW devices has often a very bulky character (e.g. Manneberg *et.al.*²²⁴) and they are not environmentally friendly due to highly toxic contents such as lead oxide.²⁴⁶ It is surprising that PZT (lead zirconate titanate) based devices are still widely applied for transversal microfluidic resonators. Alternatively, SAW based acoustophoretic systems can be used but require the bonding of PDMS microchannels to the piezoelectric material.⁵³ As discussed earlier, this requires precise alignment and bonding relative to the pressure landscape on the surface.¹⁵⁹ It also necessitates cleaning after each sampling step to avoid contaminations and hence requires the removal of the PDMS chip followed by another cumbersome bonding step. However, the SAW approach provides a more planar arrangement compared to BAW transducers and enables easier fabrication of broadband devices using non hazardous materials.

Besides the established systems, one can think of a superstrate placed in front of a SAW device on the piezoelectric substrate, as shown in Figure 4-12a. This has the benefit of decoupling the sample handling from the piezoelectric wafer. By doing this, the superstrate can potentially be used as a disposable unit or it can incorporate more features such as additional force fields (e.g. electric field induced forces).

In Figure 4-12a, a superstrate with an embedded microchannel of $173 \pm 5 \mu\text{m}$ in width and a length of 1.5 cm was actuated at its fundamental resonance frequency. A standing wave was formed with a pressure nodal plane in the centre of the microchannel indicating a half a wavelength resonance. The resonance frequency was found by injecting a bead solution into the chip at a flow rate of $2 \mu\text{l}/\text{min}$ followed by adjusting the frequency along the aperture of the SAW transducer until an alignment of beads in the pressure node was observed. A strong focusing effect was found at a frequency of 4.138 MHz. A thermal image, shown in Figure 4-12b, revealed the position of this particular frequency within the aperture of the SAW device. In Figure 4-12a, the numbering indicates the different actuation regions shown in the insets. The first image depicts the area where the acoustic energy enters the microchannel sufficiently to impose an acoustic force to push approaching particles towards the pressure node. Further downstream, a stable particle alignment well centered in the channel was generated.

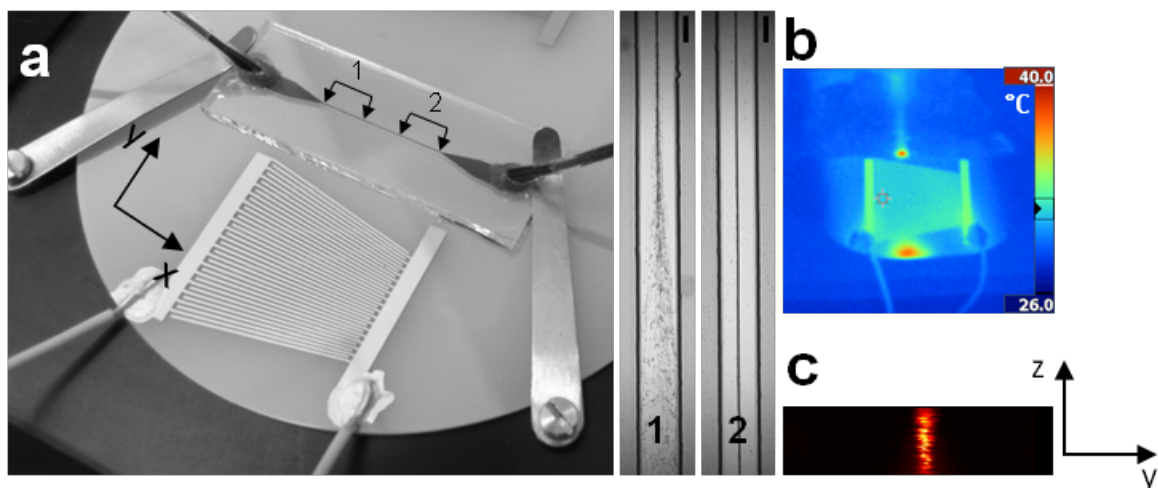


Figure 4-12: (a) Superstrate with microchannel placed on piezoelectric wafer. The marking on the superstrate correspond to the microscopic pictures (1,2) when the SAW transducer was actuated at the resonance frequency. The first image (1) shows the start of the acoustophoretic movement of $3 \mu\text{m}$ polystyrene beads towards the pressure node. Image 2 shows a stable stream of focussed beads further down the microchannel. Scale bar $100 \mu\text{m}$. (b) Infrared image of the SAW device when the resonance frequency of 4.138 MHz at 15 V was applied. (c) Image stack obtained from confocal microscopy showing the channel cross-section and the one-dimensional character of the standing wave.

The pressure field distribution inside the channel was analysed using a confocal microscope to get insight in to the nature of the wave. Individual images at different focal planes along the channel height ($\sim 35 \mu\text{m}$) were taken and assembled to a stack. These measurements were carried out under continuous flow and the result is shown in Figure 4-12c. The fluorescence labelled beads accumulated in the center plane revealing a one dimensional plane standing pressure wave. Therefore, the axial primary acoustic radiation force was dominating over a possible influence of the lateral acoustic force (equation 1.23). Previously,

it has been shown that a significant lateral force component was creating a three dimensional focusing effect with potential applications in flow cytometer.¹⁴⁶

The above example showed a single resonance but in fact several frequencies were identified which resulted in strong transverse modes. This is in agreement with the simple eigenfrequency analysis which suggested multiple modes. However, the identified resonance frequencies differ from this simple model but reflect the frequency shift indicated in the extended model where the SU8 layer was taken into account. In Figure 4-13(a-c) bead focusing in a static fluid for 4.179 MHz, 4.138 MHz and 4.096 MHz is shown (the lowest, fundamental frequency mode at 4.096 MHz was very close to that predicted by the extended simulation at 4.086 MHz).

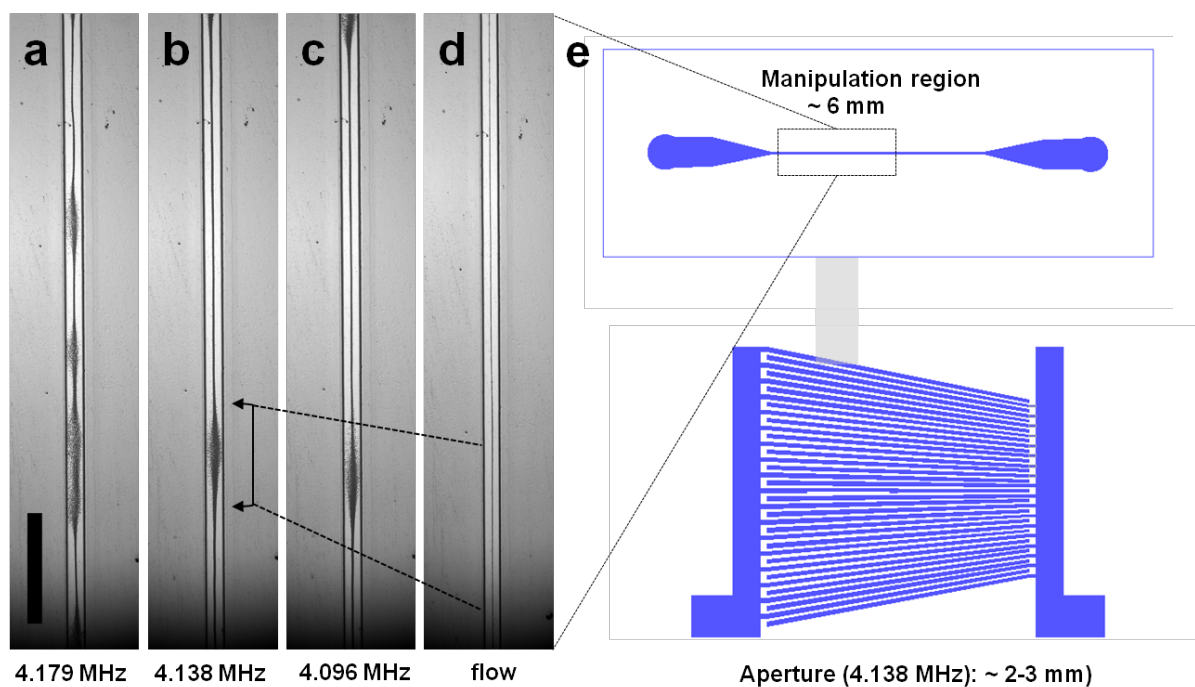


Figure 4-13: Experimentally observed resonance frequencies with strong transverse mode leading to alignment of beads in the pressure nodal plane. Images taken (a) 3 s and (b-c) 2 s after activating the SAW transducer (10 V) at the particular frequency shown. (d) Acoustic actuation at 4.138 MHz and 10 V under continuous flow (Scale bar: 1 mm). (e) Coupling of the initial incident narrow (~ 2 mm to 3 mm) SAW beam caused a wider acoustic manipulation region (~ 6 mm) along the channel length.

As already indicated by simulation in the form of tight and loose pinching regions, the pressure distribution inside the channel was non-uniform resulting in regions where beads were less tightly focussed. The variation in the focussing strength of beads along the channel is a common result typically seen only in a static fluid in acoustophoretic devices^{112, 224, 240} and to some extent related to the complex 3D interaction of the whole chip structure with the microchannel resonance. However, these irregularities were less evident when

applying a fluidic flow through the channel. The laminar flow kept the beads in the streamline once positioned in the pressure node by the PAR force (Figure 4-13d).

The structural interaction in the form of surface deformations was visualised to some extent by laser Doppler vibrometry measurements. Figure 4-14 shows the displacement induced by the excited SAW at 4.138 MHz (Figure 4-14a) on the LiNbO_3 substrate (Figure 4-14b) as well as the resulting deformation (of the bottom slide of the superstrate) across the width and the length of the microchannel in the superstrate (Figure 4-14c). The excited SAW travelled along the piezoelectric substrate as a narrow beam with relative homogenous surface displacement amplitudes in the range of hundreds of picometers and corresponding wavelength of 845 μm (close to the theoretical wavelength of 843 μm considering a speed of sound of 3488 m/s in y-direction on LiNbO_3). When the SAW was coupled to the superstrate, the laser of the vibrometer was focussed onto the bottom substrate to scan across the width and along the channel length. The displacement amplitudes were found to be located along the channel wall with zero displacements in the channel center. However, these surface deformations were not homogenous which compared well with the simulations of the pressure distribution inside the microchannel although the structural interactions were not considered in the model. The spatial correlation between pressure and displacements amplitudes has been shown in simulations by Dual and Schwarz.²³⁷ The study demonstrated that the resonance mode was influenced by all components of a system and that the standing pressure field in the liquid of a transversal resonator couples to structural deformations in the surrounding solid which can be described by stress, strain and displacements fields.

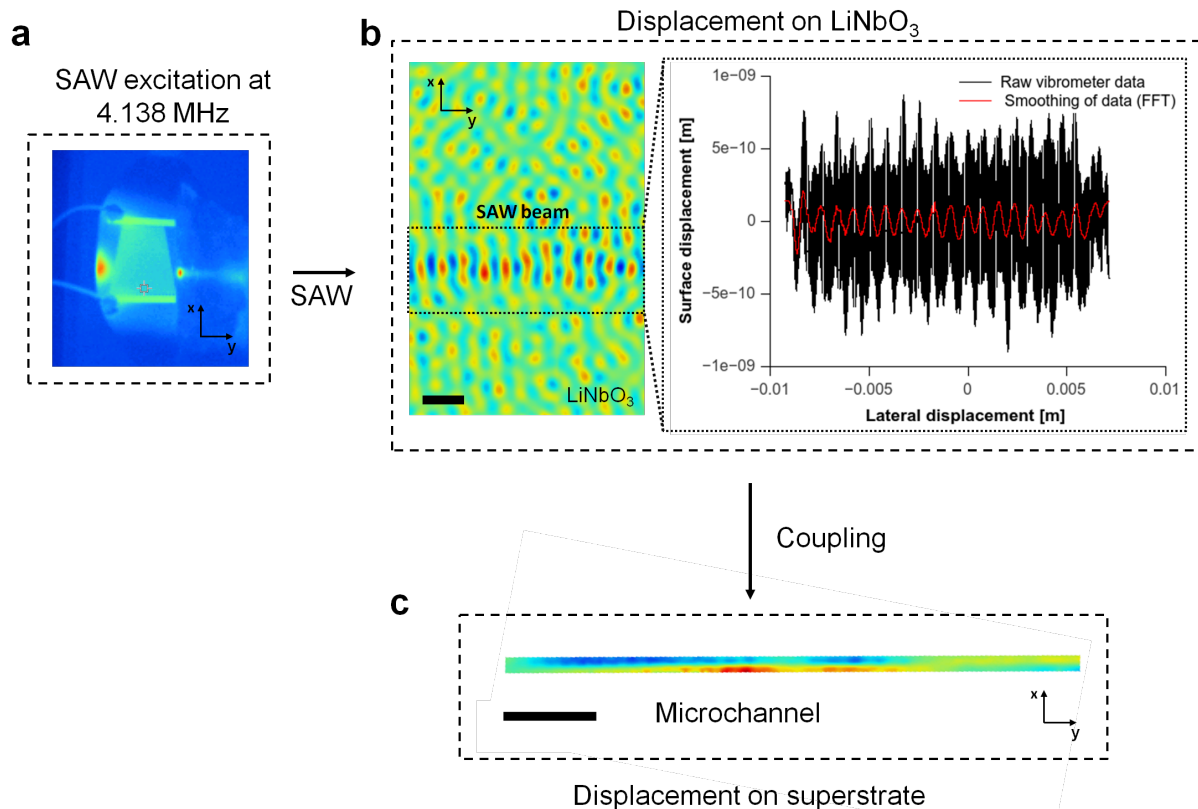


Figure 4-14: Visualisation of the surface displacements induced by a SAW on the LiNbO₃ substrate and the bottom glass slide of the superstrate within the microchannel region after coupling of the SAW. (a) SAW excitation at the resonance frequency of the superstrate visualised by thermal imaging. (b) Displacement on the surface of the LiNbO₃ along the SAW beam (Scale bar: 2 mm) and corresponding graph which shows the surface displacement amplitudes along the center of the SAW beam. (c) Surface displacement on the bottom substrate of the superstrate within the microchannel region (Scale bar: 1 mm). The color plots in (b) and (c) represent maximum (red), minimum (blue) and zero (green) displacements.

Furthermore, when slanted SAW transducers have previously been used to pattern particles, the manipulation region was limited by the aperture of the SAW beam for a particular frequency which varied in position along the width of the device.¹⁶² In comparison, the refraction of the narrow SAW beam into the coupling layer and subsequent refraction into the bottom slide of the superstrate led to the spreading of the acoustic field further along the channel length. For instance the aperture of the excited frequency of 4.138 MHz is 2 mm to 3 mm according to infrared images and vibrometer measurements but once coupled, a manipulation region spanning around 6 mm of the channel length was identified (Figure 4-14e).

Overall, the predicted resonance modes differed from the experimentally observed frequencies by up to 200 KHz. The deviation between these frequencies can be associated with the material used for creating the microchannel, a not perfectly symmetrical microchannel position, coupling effects and the non-ideal shape of the microchannel cross-section. In previous studies it was shown that vertical side walls in ideal rectangular

microchannels improve predictions for resonance frequencies¹¹⁰ and when using semi-rigid elastic boundaries with rounded shapes or even hard boundaries without vertical borders, the determination of resonances is complex and require more comprehensive models to achieve appropriate simulations.^{120, 153} Alternatively, resonance points can be investigated simply by the use of broadband transducers. Here, the benefit of exciting a range of frequencies is of advantage when using different channel geometries or materials. The slanted transducer design used may be applied to a range of superstrates made of polymers or polymer-glass substrates.

4.3.5. Characterisation of acoustic energy density and pressure amplitude

The acoustic energy coupled from the transducer into the fluid is hard to predict for acoustophoresis based systems.²¹⁸ Modelling the pressure distribution in the microfluidic cavity alone is not sufficient due to a complex interplay between the transducer, the resonator structure (superstrate) and any other layers connected to them which can cause damping of the acoustic energy.²⁴⁷ Moreover, the focussing experiments above have shown that the pressure distribution was not homogeneous evident by loose and tight pinching regions. Therefore, a method recently introduced by Barnkob *et al.*¹¹⁰, was used to characterize the acoustic energy density coupled into the superstrate when actuated at a resonance frequency. A frequency of 4.138 MHz was chosen based on the good and relative homogenous focussing results obtained earlier. As described in the experimental section, the bead's path, while experiencing the PAR force, was monitored over time and then fitted against the analytical expression (equation 4.2) with the acoustic energy density and wavelength as fitting parameters. In Figure 4-15a, an example of the lateral displacement of a 3 μm diameter bead is shown and compared with the fitted theoretical path. Curve fitting was performed using the least square method. From Figure 4-15a, it can be seen that the monitored path of the bead has the expected shape and values for the acoustic energy density can be extracted. The given example had an energy density of 203 J/m^3 . The fitted wavelength was 344 μm , where half of this wavelength was close to the width of the microchannel (173 μm). The velocity and the corresponding acoustic force experienced by the bead are shown in Figure 4-15b. In that example, a transducer voltage of 15 V was applied, a maximum bead velocity of 635 $\mu\text{m}/\text{s}$ and a force of 18 pN were determined.

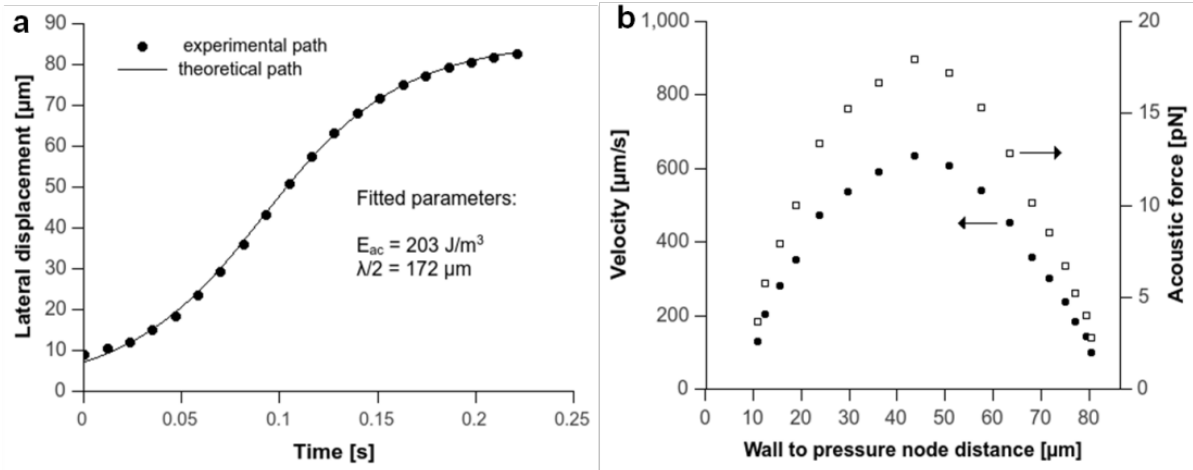


Figure 4-15: (a) Lateral displacement of 3 μm bead when SAW device was actuated with 15V at 4.138MHz (b) Calculated velocity and force based on lateral displacement of 3 μm bead using 15V at 4.138 MHz.

The acoustic energy densities were determined for a range of voltages from 5 V to 40 V. In Figure 4-16a the change in the acoustic energy density with increasing voltage is shown. Energy densities increased with an increase in the voltage applied to the transducer. The energy densities were in the range of 12 J/m^3 to 1143 J/m^3 . The corresponding pressure amplitudes (equation 4.3) were in the range of 0.3 MPa to 3.1 MPa. The pressure amplitude was proportional to the applied transducer voltage and the acoustic energy density scaled with the square of the pressure according to equation 4.3. The maximum axial component of the PAR force was in the range of 1 pN to 97 pN for 3 μm beads and the given set of voltages. The relatively large error bars may be explained by spatially varying pressure fields and increased structural interaction pronounced at higher pressure amplitudes which can interact with the microchannel resonance.

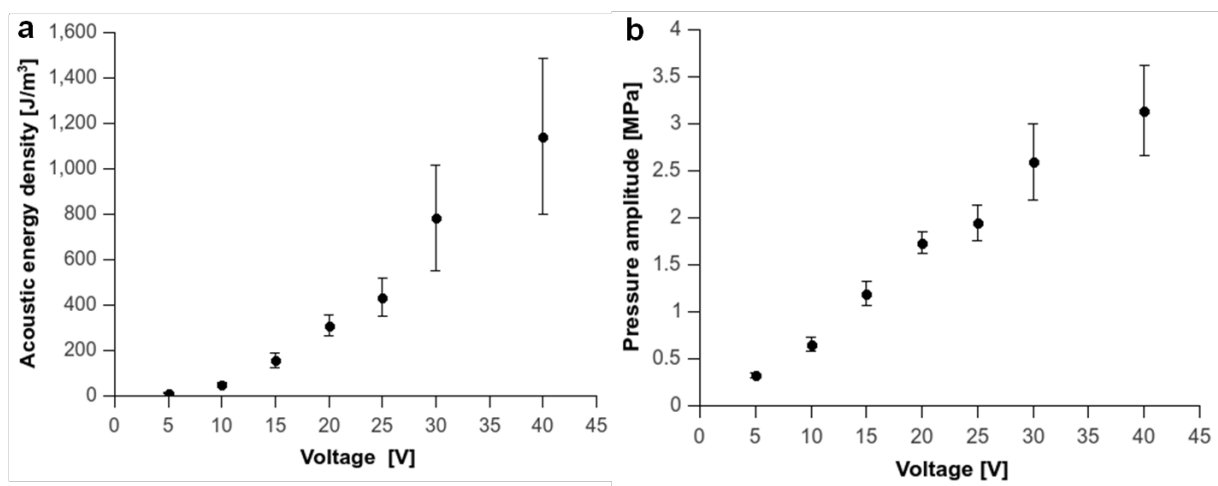


Figure 4-16: (a) Acoustic energy density determined from 3 μm bead tracking experiments using a set of voltages at 4.138 MHz. (b) Corresponding pressure amplitude.

In general, the acoustic force scales with the volume of spherical particles. This was monitored in additional experiments by investigating the lateral displacement of different bead sizes. In Figure 4-17a a frame sequence is shown where 3 μm , 6 μm , and 8 μm beads were focused using a voltage of 10 V at 4.138 MHz. A difference in the focusing time of these beads could be observed (Figure 4-17b). Hence the PAR force differed significantly (Figure 4-17c), despite the larger viscous force, larger beads were focused more quickly. The acoustic forces on 3 μm , 6 μm and 8 μm were 5 pN, 17 pN and 41 pN, respectively when 10 V at 4.138 MHz were applied to the transducer.

The individual size based bead displacement can be used to fractionate a heterogeneous sample. A good example for an acoustic separation platform has been shown by Petersson *et al.*¹²³ A mixture of 3 μm , 7 μm and 10 μm bead were fractionated into different outlets with separation efficiencies between 76 % and 96 %. However, a major problem which restricts further improvement in the separation efficiency is based on the initial position of beads before the PAR force induces movement towards the pressure node. Beads entering the channel are normally distributed in a certain volume resulting in different travelling distances towards the channel center. A pre-focusing step of beads when entering the microchannel can be a useful improvement. Later in the study a concept is proposed which enabled an acoustic pre-alignment of beads prior to separation triggered by the size dependent PAR force.

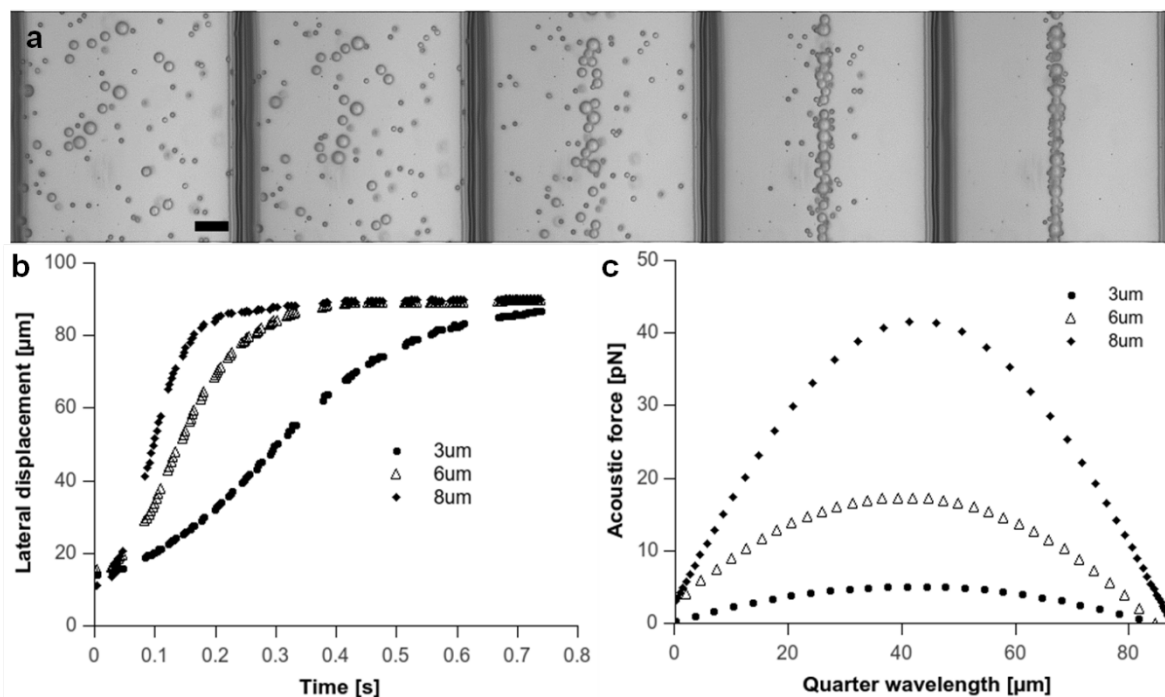


Figure 4-17: (a) Focusing of differently sized beads towards the pressure node using 10 V at 4.138 MHz. Scale bar is 25 μm . (b) Lateral displacements of various beads using 10 V at 4.138 MHz and (c) corresponding PAR force.

4.3.6. Acoustic streaming

In general, acoustic streaming is the flow produced by a force which is the result of a gradient in the time-averaged acoustic momentum-flux in the fluid.²⁴⁸ The viscous dissipation of acoustic energy into the boundary layer in the liquid along a solid boundary induces steady boundary layer vortices (inner boundary layer streaming). These again generate streaming vortices within the bulk of the fluid which is known as outer boundary layer streaming. It is especially pronounced in shallow microchannels and can be suppressed using high aspect ratio channels.¹¹⁵ For small particles, the drag which is induced due to acoustic streaming, can dominate over the PAR force. In our experiments, the influence of acoustic streaming was noticed when using bead sizes smaller than 2 μm . In Figure 4-18 a microchannel filled with 3 μm and 1 μm beads is shown. When a standing wave is created in the microchannel, 3 μm beads moved towards the pressure node but 1 μm stayed in the bulk of the fluid next to the nodal plane (Figure 4-18b). The motion of 1 μm was visualised in Figure 4-18c by frame overlays which resulted in streamlines of individual beads.

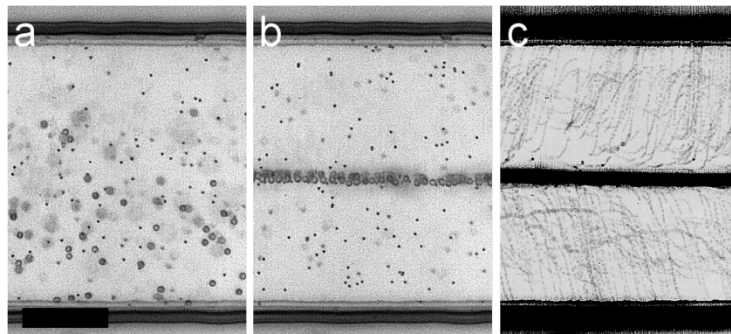


Figure 4-18: Acoustic streaming in microchannel (a) Channel filled with suspension of 1 μm and 3 μm beads. (b) Acoustic actuation leading to alignment of 3 μm bead in pressure node while 1 μm beads stay mainly in bulk vortex flow. (c) Frame overlay producing streamlines to visualize 1 μm bead movement in vortex flow. Scale bar 50 μm . Frequency 4.138 MHz.

The velocity of 1 μm diameter beads subjected to the bulk streaming flow was quantified by video analysis and tracking of the bead movement (see above). Figure 4-19a shows the displacement of a bead close to the bottom of a bulk streaming roll for an applied voltage of 40 V at 4.138 MHz. The curve shape represents the view when observing the elliptical bead motion from the top instead of the cross-section of the channel. The result is a sine-wave shaped curve where the peaks reflect the upward or downward motion within the vortex while the displacement in-between describes the lateral motion along one half of the microchannel width. Figure 4-19b shows the resulting velocity distribution considering the lateral displacement over time. The peak depicts the maximum velocity of approximately 1100 $\mu\text{m/s}$.

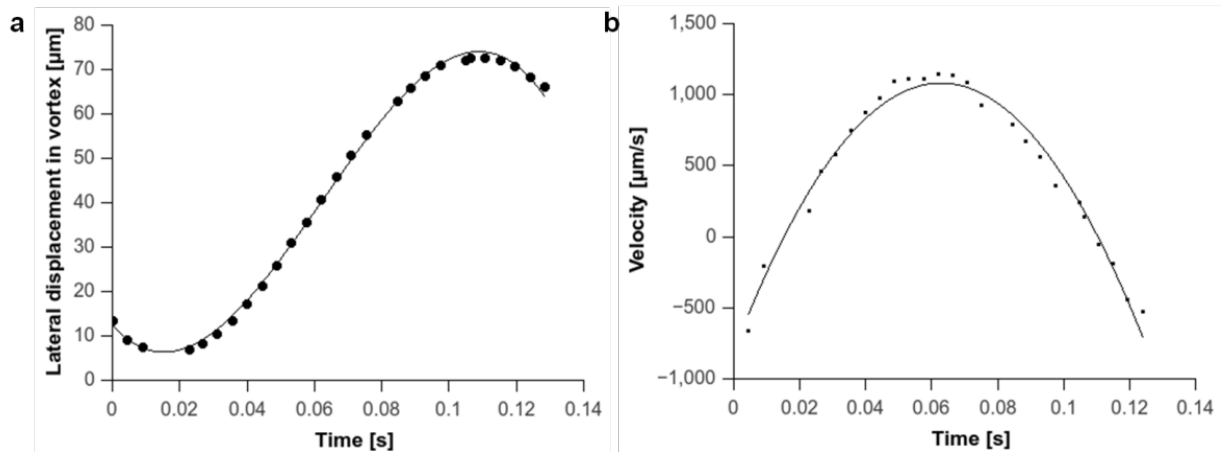


Figure 4-19: Example of the motion of 1 μm diameter beads in vortex flow. (a) Lateral displacement of bead over time in vortex flow when 40 V were applied (4.138 MHz) and (b) corresponding maximum bead velocity.

In a bulk vortex flow the fluid velocity decreases towards its centre which has been shown in simulations by Muller *et al.* where acoustic streaming was analysed in transversal resonator structures.¹¹⁵ Beads occupying positions closer to the vortex centre experience lower drag forces and move shorter lateral distances. In Figure 4-20a the lateral displacements of beads and the related velocities are shown when the chip was actuated with 40 V at 4.138 MHz. The velocity declined with decreasing lateral displacement corresponding to different streaming layers within the bulk vortex. When 40 V was applied the average velocity range was between 92 $\mu\text{m/s}$ and 885 $\mu\text{m/s}$. The maximum velocity was observed when the lateral bead movement took up almost half of the width of the microchannel or a quarter of the wavelength. This corresponds to a bead position close to the top or bottom of the substrate. The velocity of beads undergoing this kind of large displacement was determined for different applied voltages. From Figure 4-20b, it can be seen that the streaming velocity for 1 μm beads was controlled in the range of 28 $\mu\text{m/s}$ to 885 $\mu\text{m/s}$ when voltages of 5V to 40V were applied to the chip. This corresponded to drag forces of 0.2 pN to 8.3 pN. Acoustic streaming is usually an unwanted effect as it impedes the separation of particles. However, later in this chapter it is shown that acoustic streaming can be beneficial to separate different cell types.

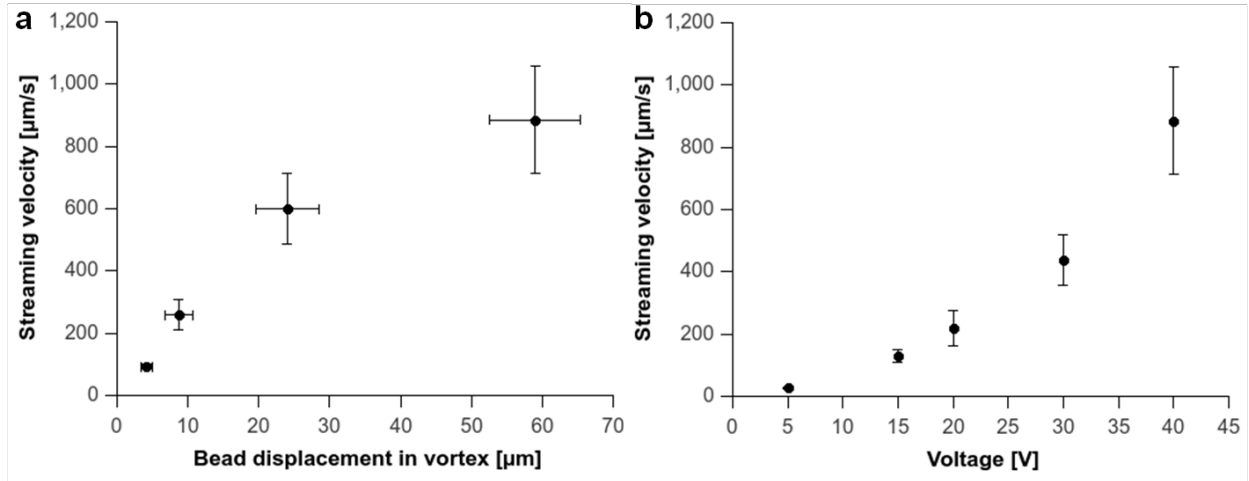


Figure 4-20: (a) Velocity of 1 μm beads depending on displacement in vortex flow (40V, 4.138 MHz). (b) Velocity of 1 μm bead for different voltages. Largest bead displacements were considered for velocity measurement (4.138 MHz).

4.3.7. Temperature change induced by coupling losses

The experiments above show that acoustic forces can be controlled by varying the applied voltage on the SAW transducer. The coupling process worked sufficiently well, however, as well as reflection and transmission of acoustic waves, energy absorption (losses) by all materials in the system takes place. The deformation (compression and rarefaction) of the material when an acoustic wave propagates through the bulk consumes energy in form of heat. The increase of the temperature alters the resonance point of a system as the speed of sound in a given material depends on its temperature. Therefore, heat generation should be considered in long-term acoustophoretic experiments and resonance frequencies may be adjusted accordingly to maintain the pressure amplitudes in the microchannel. The temperature increase might also affect the work with biological material such as cells or cellular components. At high temperature over 40°C biochemical processes inside of cells slow down and it may risk the cell viability.

The temperature increase after coupling of the SAW was measured with an infrared camera. However, the camera measured surface temperatures and could not be applied to measure the temperature inside the water filled microchannel of the superstrate. Therefore, the temperature readings were taken from a glass slide (to resemble the bottom part of the superstrate) placed on the piezoelectric wafer instead of the whole superstrate. The SAW was coupled into the glass slide via a water coupling layer which was reapplied every 5 minutes and the highest temperature values on the slide for a range of transducer voltages over a period of 30 minutes was monitored. The measurement results are shown in Figure 4-21 for voltages of 10 V to 40 V. A slight increase of the temperature over time was found for

all voltages. At 10 V and 20 V an increase during the 30 min period from 24.8° to 26.2° and 25.5° to 27.6° was observed. A more significant increase was found for 30 V and 40 V, where the temperature changed from 25.2° to 31.8° and 25.8° to 35.5°, respectively. However, the temperature was not homogeneously distributed across the whole glass slide. As mentioned, the reading just reflected the highest temperature points which were locally confined to the area where the approaching SAW couples into the glass slide. Nonetheless, for long-term acoustophoresis experiments, these results indicate that a resonance frequency adjustment may be necessary to account for the temperature change. On the other hand the temperature change should not affect the viability of biological samples. In practice when a continuous flow is applied to the microchannel a heat dissipation may take place due to heat absorption by the liquid combined with continuous fluid exchange. Alternatively, one might use thermal paste between a heat sink and the piezoelectric wafer to improve temperature conduction away from the system or introduce active cooling elements located close to the system.

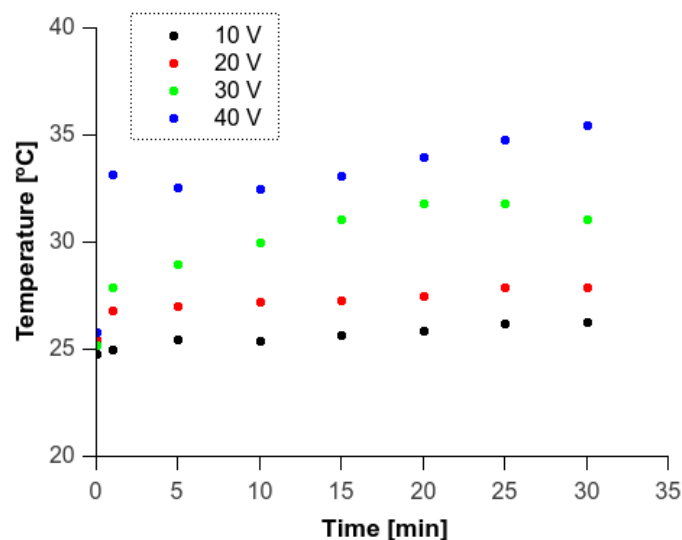


Figure 4-21: Temperature increase on top of the bottom glass substrate after coupling of the SAW (4.138 MHz) with different voltages applied to the transducer. Measurements were taken with an infrared camera.

4.3.8. Superstrate position

SAW devices for acoustophoretic particle manipulation have been used in combination with PDMS or glass channels bonded to the piezoelectric substrate.^{118, 153, 162, 230} This required very good control of the alignment of the channel relative to the SAW electrodes and the position of the pressure node on the surface of the piezoelectric substrate. In comparison, the approach presented here benefits from a reduced complexity of the assembly process. A precise alignment parallel to the surface acoustic wave front was not necessary. In fact, the superstrate could be misaligned relative to SAW electrodes by an angles up to 30° without

affecting the creation of a standing wave in the microchannel (Figure 4-22 a). It indicates that the coupling point of the SAW into the superstrate can be arbitrary chosen as long as the applied frequency matches the microchannel resonance. An position independent acoustic coupling into transversal resonator design was also found when using BAW transducer.⁵⁰

Furthermore, no change in the coupling was observed when actuating the superstrate at a distance of 1 cm away from the IDT. The average acoustic energy was around 46 J/m^3 in both cases which corresponded to a pressure amplitude of 0.63 MPa. This suggested that the propagation loss of the travelling SAW in form of BAW was negligible and that the magnitude of the coupled acoustic energy was dominated by coupling losses (heat, reflections) into the superstrate.

Overall, these features can be especially useful when lateral channel dimensions get in the range of tens of micrometers where aligning or positioning of PDMS devices gets cumbersome or when there is a need to reduce user related mishandling.

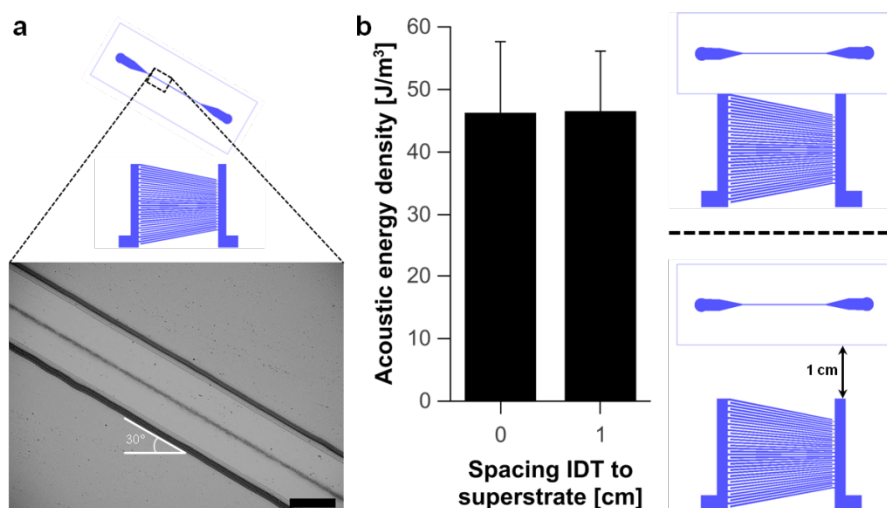


Figure 4-22: Reduced complexity in system assembly. (a) Superstrate can be misaligned by up to 30° without affecting the formation of the standing wave (Scale bar: $100 \mu\text{m}$). (b) Comparison of acoustic energy density of superstrate close to SAW device and at a distance of 1 cm (10 V at 4.138 MHz).

4.3.9. Tuneable pressure distribution

The slanted transducer design was suitable for finding the resonance point of the superstrate. The excited frequency was adjusted until a stable single pressure node in the center of the channel was achieved. This also means that a variation in the cavity width can be easily compensated for by a change in frequency. The SAW transducer worked for different fundamental frequencies defined by the electrode width and spacing which change along the aperture. However, beyond these frequencies the harmonic response of the

slanted electrodes offered additional frequency ranges (Figure 4-11b). This was used, besides a single pressure nodal plane, to obtain a tuneable pressure distribution by creating multinode arrangements based on higher harmonic responses of the superstrate (Figure 4-23a to Figure 4-23c).

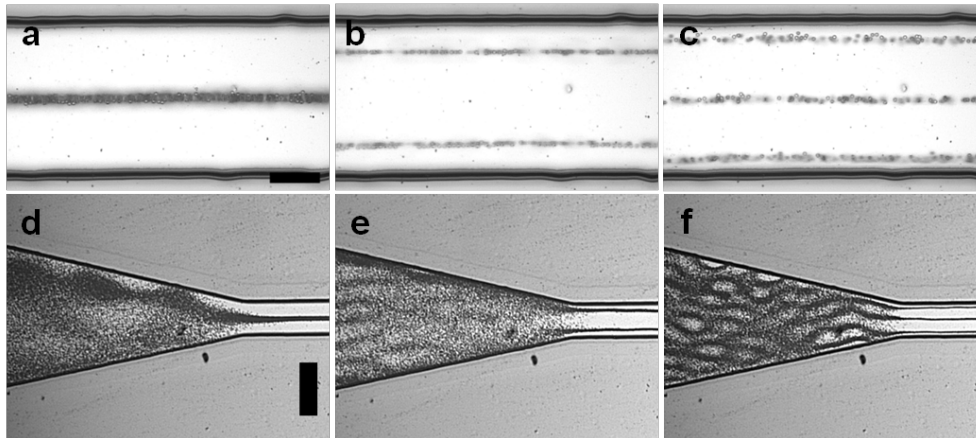


Figure 4-23: Multi pressure node arrangements in the microchannel using 3 μm beads. The frequency of SAW device was tuned to several resonance points of the superstrate, where (a) 4.138 MHz, (b) 8 MHz, (c) 12.514 MHz (10 V, Scale bar 50 μm), led to varying standing wave pattern confined to the straight channel section (d-f, scale bar 250 μm , static fluid).

The frequencies to realise 2 and 3 pressure nodes were found at 8 MHz and 12.514 MHz which corresponds to wavelengths of 188 μm and 119 μm . Measuring the node distances, values for the wavelength were found to be 181 μm and 116 μm which were close to the expected values. As mentioned before, a spreading of the acoustic wave coupled to the superstrate can be observed which limits the localized application of the PAR force. However, confinement can be achieved when using certain microchannel dimensions. A non-uniform channel with width differences changes the resonance frequency and localized acoustic fields can be obtained using special chip designs.²⁴⁰ The Figures 4-23d to Figures 4-23f show the confinement of the standing wave in the straight channel section for several resonance frequencies.

Moreover, different channel widths were tested to investigate the ability to tune the frequency towards the resonance point of a given superstrate. In Figure 4-24 channel widths of 280 μm and 350 μm were used and resonance frequencies yielding 2 and 4 pressure nodes were identified simply by scanning through the available frequency range of the SAW device. The 280 μm width channel responded at frequencies of 4.878 MHz and 9.807 MHz with multi pressure node arrangements which corresponded to theoretical wavelengths of 297 μm and 148 μm . The measured distances of the pressure nodes were 298 μm and 147 μm . The 350 μm channel showed a strong response at 3.791 MHz and 8.301 MHz which related to wavelengths of 391 μm and 177 μm . The measured wavelengths were 383 μm

and 175 μm . The fundamental frequencies of these superstrates were not applied due to a low frequency restriction. A wavelength of 560 μm and 760 μm would have been necessary which compares to frequencies of 2.589 MHz and 1.907 MHz.

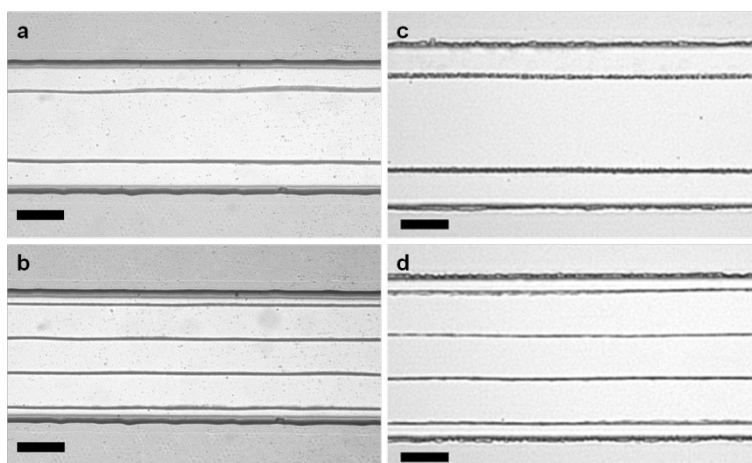


Figure 4-24: Adjustment of the SAW transducer frequency to match the resonance of different channel widths. For 280 μm channel width, the frequencies for (a) 2 and (b) 4 pressure nodal planes were found to be 4.878 MHz and 9.807 MHz, respectively (Scale bar: 100 μm). For a 350 μm channel width the frequency for (c) 2 and (d) 4 pressure nodes were 3.791 MHz and 8.301 MHz (Scale bar 100 μm).

4.3.10. Acoustic tweezing for dynamic particle manipulation

4.3.10.1. Cell patterning

The tuneable pressure landscape shown above can be used for the formation of cell patterns within enclosed microfluidic compartments. The control of the cell's position is of great interest in the area of cell biology and tissue engineering. Cell behaviour is influenced by the surroundings where factors like surface properties (chemically or mechanically structured) or adjacent cells (cell to cell signalling) create a microenvironment that stimulates processes including proliferation²⁴⁹ or differentiation.^{250,251} Although, there are cell patterning methods such as direct cell micro contact printing²⁵², optical laser guided micropatterning²⁵³ or surface mediated patterning induced by stamping techniques²⁵⁴, the approach here may offer a less complex and more cost effective way for dynamic cell patterning.

Fast cell patterning in a straight microfluidic channel was demonstrated for a range of resonance frequencies. Red blood cells (RBCs) were used to create linear cell bands of varying distances as shown in Figure 4-25. Four different resonance frequencies were applied under static flow conditions and the resulting node distances were determined. For the fundamental frequency the wall to node distance was $86 \pm 2 \mu\text{m}$. At higher harmonic actuation the distances between cell bands, the node to node pitches were varied depending

on the frequency from 89 μm (8 MHz, Figure 4-25b) over 57 μm (12.514 MHz, Figure 4-25c) to 36 μm (20.504 MHz, Figure 4-25d).

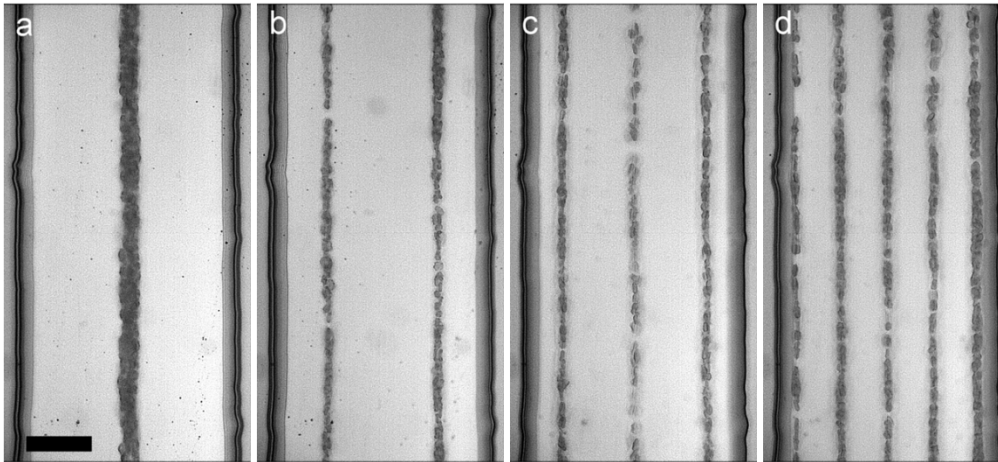


Figure 4-25: Patterning of red blood cells using a single SAW device with wide frequency range. (a) 4.138 MHz, (b) 8 MHz, (c) 12.514 MHz, (d) 20.504 MHz. The transducer was actuated with 10 V. The patterning was performed without fluid flow (Scale bar: 50 μm).

The time needed to focus cells into bands was dependent on the voltage and frequency applied to the transducer. In Figure 4-26 the time to create a stable cell alignment is plotted against the voltage for each frequency. The increase in the voltage from 5V to 20V decreased the patterning time from seconds and hundreds of milliseconds to less than a hundred milliseconds. One would expect shorter times for higher frequencies as the result of shorter travelling times, however, it has to be noted that the amplitude of the SAW excited by the transducer was not equal for the set of frequencies used, although the same voltages were applied. As described above, frequency dependent impedance mismatch between the signal generator and the SAW device alter the coupling efficiency.

The exposure to high pressure amplitudes might harm mammalian cells. It has been shown that the cell membrane itself can act as mechanical oscillator and that cavitation can take place with the result of sonoporation of the cell membrane.²⁵⁵ However, several studies have shown that the exposure time needs to be in the range of several seconds for pressure amplitudes larger than 0.1 MPa to create poration.²⁵⁶⁻²⁵⁸ In the experiments here, the exposure time to high pressure fluctuation was shorter than 1 s before the cells moved to low pressure regions. Moreover, lysis due to ultrasound standing waves has not been reported yet and studies investigating cell viability after exposure to pressure waves (pressure amplitudes of 1.23 MPa) suggested no impact on survival or functions of different cell types.¹²⁶

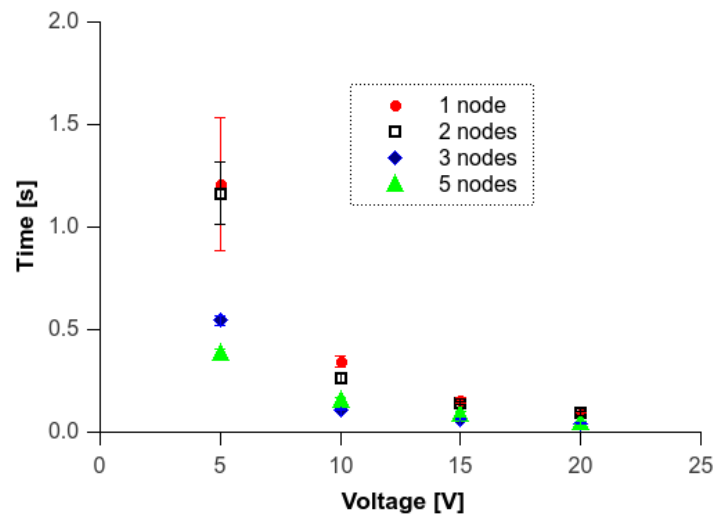


Figure 4-26: Red blood cell patterning time versus applied voltage for different resonance frequencies.

The frequency excited by a single SAW transducer can be easily switched to a different resonance point of the superstrate. The fact that harmonic frequencies were positioned at the same point along the aperture gave an additional ability to demonstrate dynamic cell patterning. In particular, a shift in the resonance frequency can be applied to induce merging (fusion) of cell bands aligned in individual pressure nodes. For instance, in Figure 5-27 red blood cells were first aligned into two pressure nodes. This was followed by applying the fundamental frequency and the fusion of these cell subgroups into a single pressure node within 1s after the frequency change. In Figure 5-28, the same was performed with higher harmonic responses. Here, 5 pressure nodes were first created and subsequently merged into two pressure nodes once the second harmonic frequency was applied.

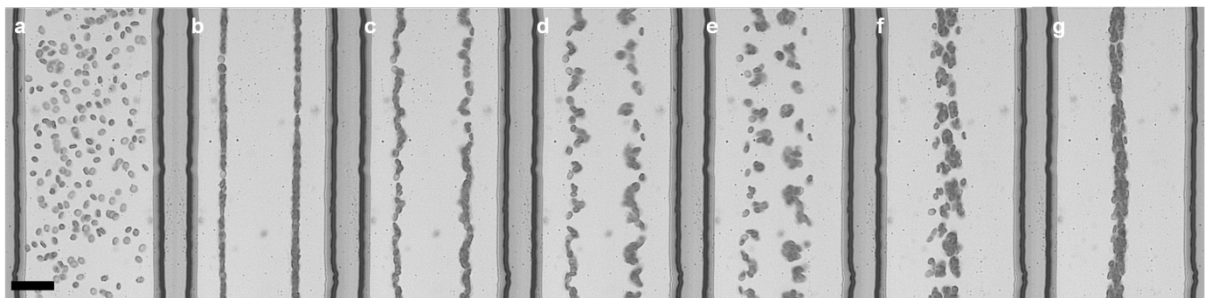


Figure 4-27: Fusion of patterned cells by switching between resonance frequencies. (a) RBCs in microchannel before acoustic actuation. (b) 8 MHz were applied to create 2 pressure nodes. (c-g) Switch to 4.138 MHz to merge cell pattern into single pressure node. No fluid flow (Scale bar: 50 μm).

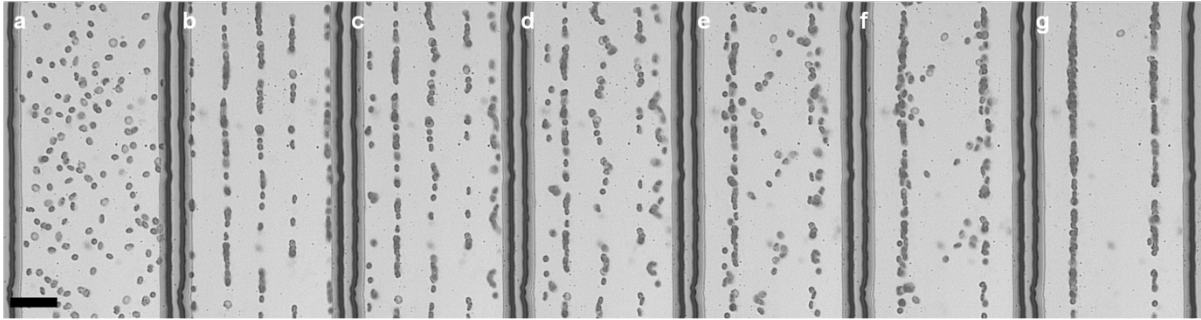


Figure 4-28: Fusion of patterned cells by switching between resonance frequencies. (a) RBCs in microchannel before acoustic actuation. (b) 20.514 MHz were applied to create 5 pressure nodes. (c-g) Switch to 8 MHz to merge cell pattern into two pressure nodes. No fluid flow (Scale bar: 50 μm).

These experiments simply demonstrated the capability of the system in terms of flexible standing wave patterns. Instead of using suspension cells such as blood cells, one could use adhesion cells in the future. Then the force fields in the superstrate can be used to first pattern the cell sample followed by holding the sample until adhesion to the surface is achieved. This of course requires the control of the temperature generated by the acoustic field to maintain viability of the cell sample. Subsequently, the superstrate could be perfused with cell culture medium to study proliferation or differentiation within a given microenvironment.

4.3.10.2. Separation of parasite from blood cells

In experiments with different bead sizes (Figure 4-17b) the scaling of the acoustic force has been demonstrated. However, beads of 1 μm in diameter followed vortex flows induced by acoustic streaming while larger beads moved towards the pressure minimum in the nodal plane due to a dominating PAR force. Although an unwanted effect sometimes in separation experiments of small particles, it can be used to achieve a displacement and fractionation of two previously homogeneously distributed particles kinds (e.g. 3 μm and 1 μm beads). Acoustic streaming is not only predominating for small spherical particle. A shape difference between particles can lead to a similar effect and was applied to separate bi-concave disc like RBCs from an elongated cone shaped parasite, called trypanosome.

Trypanosomes are unicellular flagellates with a length of 20-30 μm and a diameter of 2-3 μm . Due to a single flagellum that coils around them the parasite is able to move about with a corkscrew motion. Different species of trypanosomes are responsible for various conditions in bovines but also in humans with both African sleeping sickness, prevalent in sub Saharan Africa, and Chaga's disease, prevalent in South America, both being caused by forms of trypanosomes. The parasite is transmitted by different species of the tsetse fly with lethal outcome for human beings when left untreated. The parasite is a serious threat to more than 60 million²⁵⁹ people living in these areas but also potentially for people further

north when warmer climates promote spreading of the tsetse fly.²⁶⁰ The diagnosis of the disease requires first the detection of the parasite. However, the extremely low abundance of trypanosomes in blood samples (100 – 10,000 cells/ml)²⁶¹ or lymph fluid makes it extremely difficult to diagnosis the disease early. The most common diagnostic technique depends on sample analysis (e.g. blood smear) under a microscope which relies strongly on the training and expertise of the analyst.²⁶² Therefore, it is of great importance to develop enhanced techniques which enable the enrichment of the parasite for improved diagnosis of these diseases.

The acoustophoretic manipulation of trypanosomes during initial experiments revealed a oscillating motion of the parasite within a standing acoustic wave. In comparison, the biconcave RBCs moved towards a pressure node and stayed there. Hence, when a mixture of RBCs and trypanosomes were put into the channel a change in the total cell distribution was observed. For the RBCs the PAR force dominated and they travelled to the pressure node in the center of the channel. In contrast, trypanosomes were subjected to a dominating drag force induced by acoustic streaming that resulted in a spreading but also confining of the parasite along the halves of the microchannel (Figure 4-29a and Figure 4-29b).

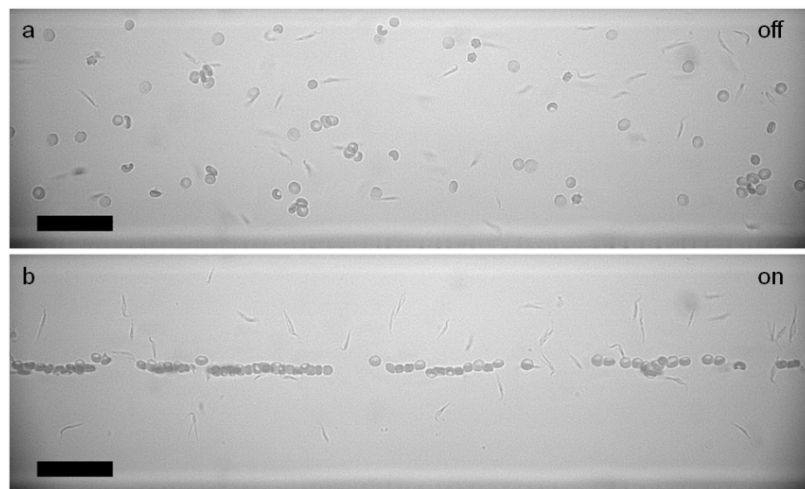


Figure 4-29: Displacement of RBCs and trypanosomes induced by acoustic forces. (a) RBCs and trypanosomes were randomly distributed in the microchannel channel (no acoustic actuation). (b) Channel is acoustically excited (30 V) producing a standing pressure wave with single pressure node. Blood cells were pushed toward the pressure node by primary acoustic radiation force. Trypanosomes experienced a drag force induced by acoustic streaming (Scale bar: 50 μm).

It has to be noted that the parasite is motile and could have actively moved out of the pressure node. However, control experiments with heat inactivated non-motile parasites (heat shock, 2 x for 10 s at 95°) led to the same result which indicates that a size/shape difference of the parasite compared to the biconcave RBCs was responsible for this phenomenon.

The findings can be used as a strategy to design a microfluidic chip that enables continuous separation of the parasite from a blood sample. This is of considerable interest for disease diagnosis; as low levels of parasitemia can mean that only one parasite among billions of RBCs exist. Hence a combination of streaming and PAR forces while a pressure driven flow injects a blood sample into a microfluidic device can be applied to induce a displacement between these cell types which then may be utilized to guide them into different channel outlets.

In Figure 4-30, a schematic of a microchannel superstrate with two inlets and outlets and the SAW device is shown. This setup was used to separate trypanosomes from blood cells by utilizing the difference in the acoustic forces. The two inlet channels were used to inject the sample and a buffer with slightly different flow rates. Buffer sample was injected with a flow rate of 0.4 $\mu\text{l}/\text{min}$ and the sample with 0.2 $\mu\text{l}/\text{min}$ resulting in an initial hydrodynamic focusing of the sample along the channel wall closest to the SAW transducer at the inlet junction (Figure 4-30i). Without acoustic actuation the sample left the channel at outlet 1 (Figure 4-30ii, off). When acoustically actuated the hydrodynamically focused sample was switched to the laminar stream of the buffer due to the presence of a pressure node in the channel centre. The change in the position caused the sample to leave the channel via outlet 2 (lower hydrodynamic resistance, Figure 4-30ii, on). The switching time, from outlet 1 to 2 was approximately 300ms for an applied voltage of 40 V.

The need for the initial sample focusing close to the channel wall becomes clear when looking at Figure 4-30iii. Here, blood cells and trypanosomes are shown when the channel was acoustically excited. Blood cells were aligned in the pressure node while trypanosomes were mainly confined to one side of the channel in the acoustic streaming rolls. This kind of displacement between these cell types was then used to achieve a fractionation at the outlet junction.

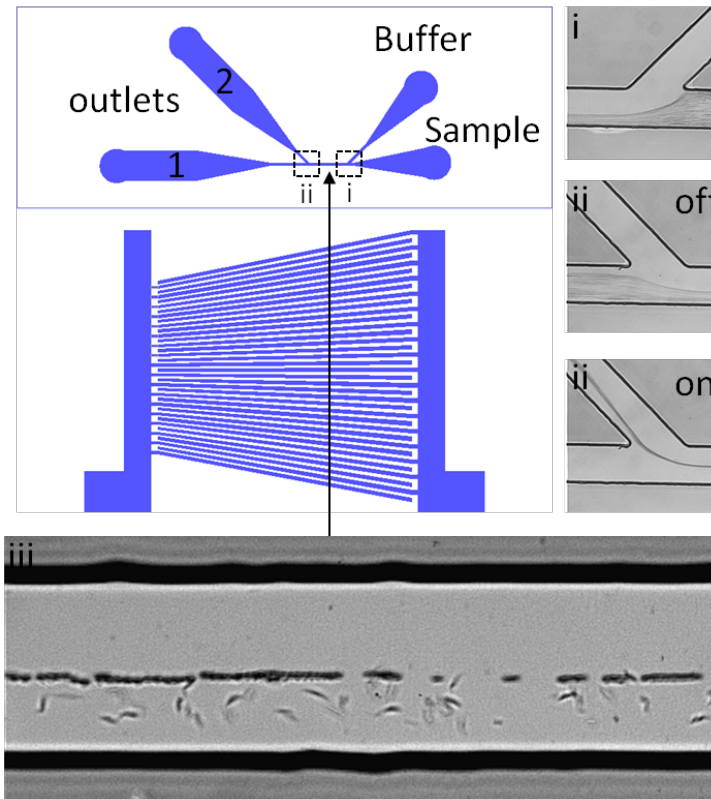


Figure 4-30: Setup for separation of trypanosomes from a blood sample based on acoustic streaming induced displacement. (i) Sample was hydrodynamically focussed to achieve initial sample flow along the channel wall. (ii) Without acoustic actuation, the sample was leaving via outlet 1. Acoustic actuation switched the sample into the laminar stream of the buffer which resulted in the sample leaving via outlet 2. Switching time was about 300 ms for 4.138MHz and 40V. (iii) Trypanosomes and red blood cell displacement under flow in straight channel section. Flow rates are 0.2 $\mu\text{l}/\text{min}$ and 0.4 $\mu\text{l}/\text{min}$ for sample and buffer inlet, respectively.

The situation at the outlet junction can be seen in Figure 4-31. The RBCs from the centre of the channel exit through outlet 2 (with a few trypanosomes), whilst the majority of trypanosomes exit through outlet 1. This kind of continuous enrichment process where the large background noise in terms of a high amount of red blood cells was reduced can be used to aid an easier detection of the parasite.

While this approach is very promising, some issues related to the flow rate need to be optimised to improve the setup. The volume throughput was relatively low owing to the utilisation of acoustic streaming. The pressure applied to the syringe pump had to be reduced so that vortex rolls can be set up in the channel and time for displacement between the parasite and blood was given. To overcome this limitation, a blood sample can be spread over several individual devices or a superstrate with several channels can be designed. This is also in favour with problems arising from blood settling in the tubing. A parallel approach would be able to compensate changes in concentrations due to settling of the sample over time. The low flow rate also caused problems with collecting sample at the outlets. The

hydrodynamic pressure was too low to generate an appropriate volume without concentration change in a short time scale (<5min). This made quantification of the separation efficiency unreliable and only the qualitative result can be presented here.

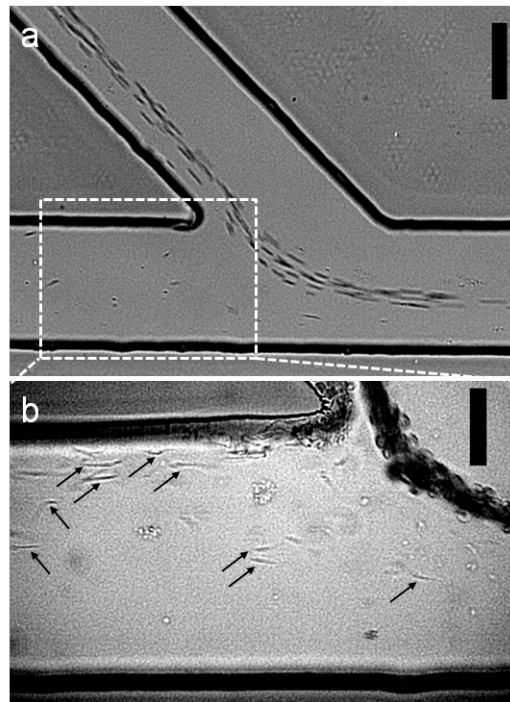


Figure 4-31: (a) Separation of the parasite from a blood sample at the microfluidic junction (Scale bar: 100 μm). (b) Close up of junction showing separation of both cell types into different outlets. Arrows show positions of trypanosomes (Scale bar: 50 μm). Flow rates are 0.2 $\mu\text{l}/\text{min}$ and 0.4 $\mu\text{l}/\text{min}$ for sample and buffer inlet, respectively.

An alternative configuration is shown in Figure 4-32. A simple straight channel configuration was used to show a separation effect induced by red blood cell retention against the flow. The non-uniform nature of the standing wave with increasing amplitude was utilized. Instead of a pure one-dimensional wave, at high amplitudes (>50 V) hot-spot regions in the channel were observed where trapping of cells occurred. This indicates a more complex pressure distribution in the channel with two-dimensional character. For instance, in chapter 1 the lateral component (equation 1.23) of the primary acoustic radiation force was introduced. The force becomes significant with large lateral velocity gradients and can be used to hold particles at stable positions within the pressure nodal plane.¹¹¹

Here, the effect of axial and lateral primary acoustic radiation force combined with secondary forces induced the aggregation of red blood cells. Smaller particles or in this case the parasite experienced the drag force induced by the applied flow as well as due to acoustic streaming. In Figure 4-32b, focusing of blood and parasite sample at a lower voltage (30 V) is shown. This simply led to focusing of blood cells and displacement of parasites by acoustic streaming along the channel while flowing towards the outlet. An increase in

amplitude to 60 V produced a trapping site of blood cells (Figure 4-32c). Over time, the cell clump size increased, while trypanosomes subjected to the drag forces mainly passed the trapping point which led to separation of these two cell types. It has to be noted that due to interparticle forces some trypanosomes were trapped in the blood cell clump. However, in general the drag force was high enough to overcome this attraction when passing the trapping site.

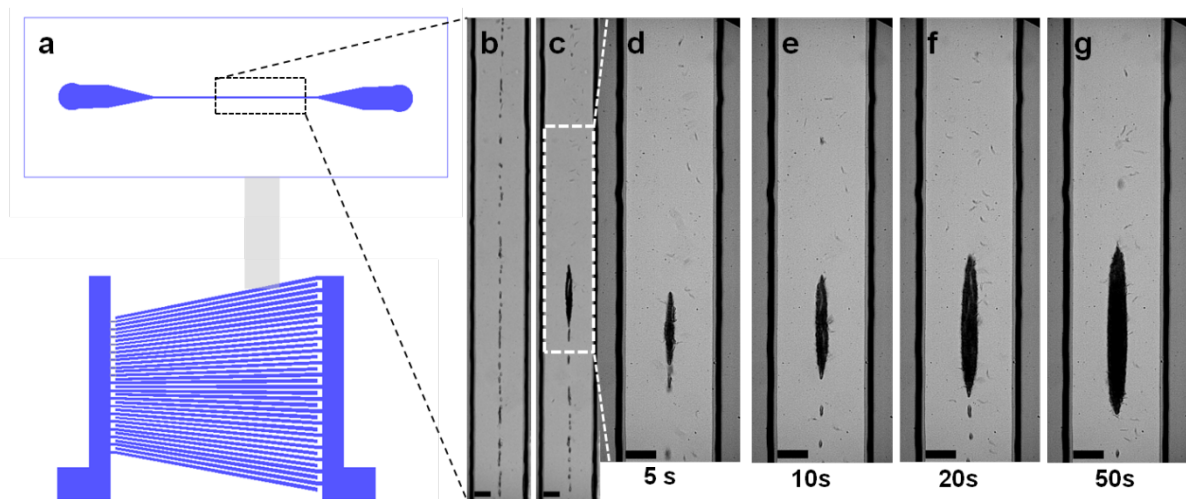


Figure 4-32: Separation of parasite from blood sample in straight channel using the PAR force to trap blood cells while trypanosomes subjected to acoustic streaming flow along the channel. (a) Schematic of the setup containing superstrate, SAW device and actuation area. (b) Sample acoustically focused by applying 30 V at 4.138 MHz. (c) Increased voltage (60 V) created a hot spot where blood cells aggregated and were trapped against the flow while trypanosomes followed fluid flow along the channel as well as the flow pattern of the vortex rolls. (d-g) Zoom into the trapping site which shows increasing blood cell aggregation over time. The trypanosomes pass the blood cell aggregate and get separated. Flow direction from bottom to top. Flow rate 0.4 $\mu\text{l}/\text{min}$. Scale bar: 50 μm

This approach simplified the separation setup significantly. The straight channel required only one pressure driven flow connection. A restriction in throughput again, rested on the acoustic streaming effect which required lower flow rates to be influential on the displacement between the cell types. Furthermore, an advantage would be a widening of the channel width or the application of parallel channels. This helps to improve sample throughput and sample spreading without blocking the microchannel.

The high voltage applied raises the temperature and can cause death to the parasite. When simple visual detection only is required the approach is still useful. However, when the species needs to be identified, a subsequent culturing step of the trypanosomes is necessary and in this case active cooling (e.g. by peltier elements) might be used to keep the temperature stable over time.

4.3.10.3. Dual resonance frequency excitation using a transducer pair

The application of just a single SAW transducer was one of the advantages of the superstrate concept. It was also shown that the pressure distribution can be varied by switching to a different higher harmonic resonance of the superstrate to create multi pressure nodal planes at the same position in the microchannel. Instead of a rapid switching between these states, one can think of a smooth transition from one to the other where the pressure node positions can be controlled across the width of the channel. This can be achieved by introducing a second SAW transducer to induce a superposition of two standing waves. For instance, this can include a superposition of the fundamental frequency and the first harmonic frequency where the pressure distribution in the channel is then modulated by a change in the amplitude of one of the applied frequencies. The concept can be visualised by the interference of two plane pressure waves of a different frequency and amplitude (Equation 4.10). In Figure 4-33 the resulting constructive interference of a fundamental and 1st harmonic frequency is shown where the graph limits depict one half of a microchannel with channel wall (left) and centre (right). The resulting pressure distribution as the sum of the fundamental and 1st harmonic pressures is plotted against one half of the microchannel for an increasing pressure amplitude of the fundamental frequency (Figure 4-33 a –d). It can be seen that the pressure nodal plane of the interference moves towards the centre of the microchannel with increasing amplitude of the fundamental frequency.

$$\begin{aligned} p &= p_{ac1} \sin(\omega_1 t - k_1 y) + p_{ac2} \sin(\omega_2 t - k_2 y) \\ &= p_{ac1} p_{ac2} \cos\left(\frac{\omega_1 - \omega_2}{2} t + \frac{k_1 y - k_2 y}{2}\right) \sin\left(\frac{\omega_1 + \omega_2}{2} t + \frac{k_1 y + k_2 y}{2}\right) \end{aligned} \quad (4.10)$$

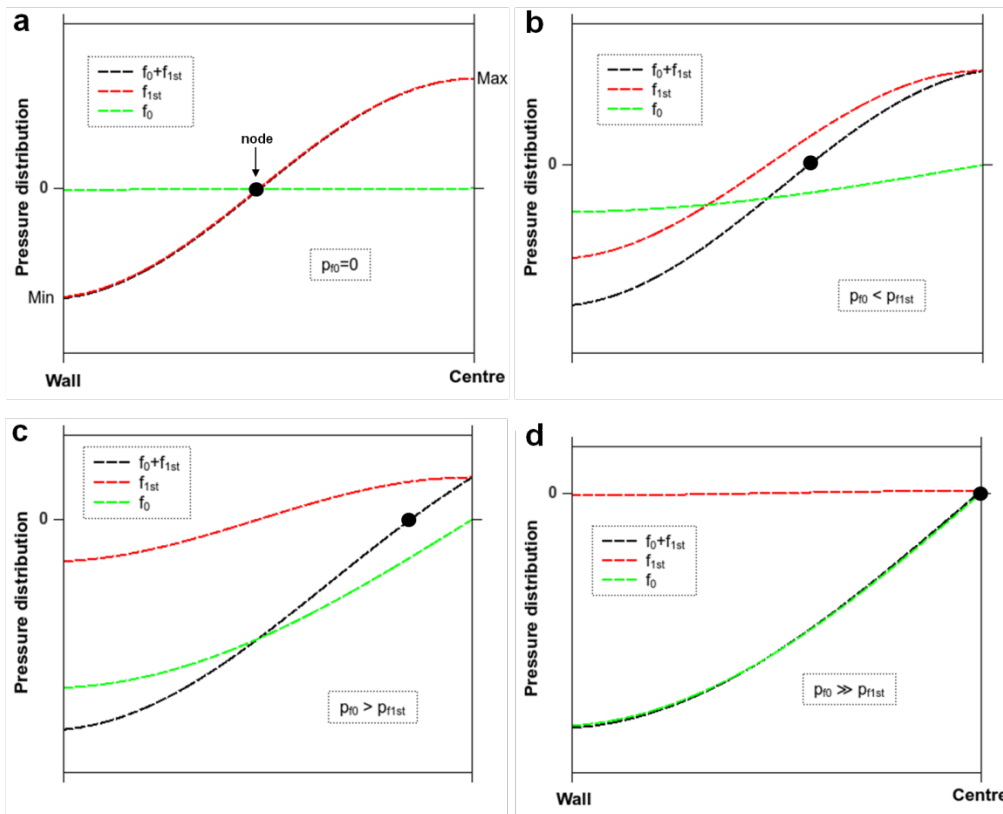


Figure 4-33: Interference of pressure waves (fundamental and 1st harmonic) and modulation of pressure node position by pressure amplitude control of the fundamental frequency. (a-d) The amplitude of the 1st harmonic is constant while the pressure amplitude of the fundamental frequency increases until a pressure node in the channel centre is formed.

In Figure 4-34a a schematic is shown to clarify the principle of superposition of standing waves with two SAW transducers. A superstrate with straight microchannel was placed between two identical SAW electrodes. One electrode was excited with the 1st harmonic frequency leading to two pressure nodal planes located close to the channel walls. The second SAW device was fed with the fundamental frequency to create a single pressure node in the centre of the microchannel. First, the 1st harmonic frequency was dominating and aligned beads along two nodes (Figure 4-34 b). A fixed amplitude of 20 V for the 1st harmonic was applied while the second SAW device was actuated at the fundamental frequency with an amplitude of 1 V. Under these conditions the influence of the fundamental frequency was negligible. However, a slight increase in the amplitude applied to the 2nd SAW device shifted the two pressure nodal planes further away from the channel walls (Figure 4-34c). Subsequently, a continuous increase of the amplitude as shown in Figure 4-34d to Figure 4-34e, resulted in particle translation towards the centre of the microchannel. At that point, the fundamental frequency dominated over the 1st harmonic. In Figure 4-35, the lateral displacement as a function of the applied voltage is shown with a voltage range of 1 to 25 V.

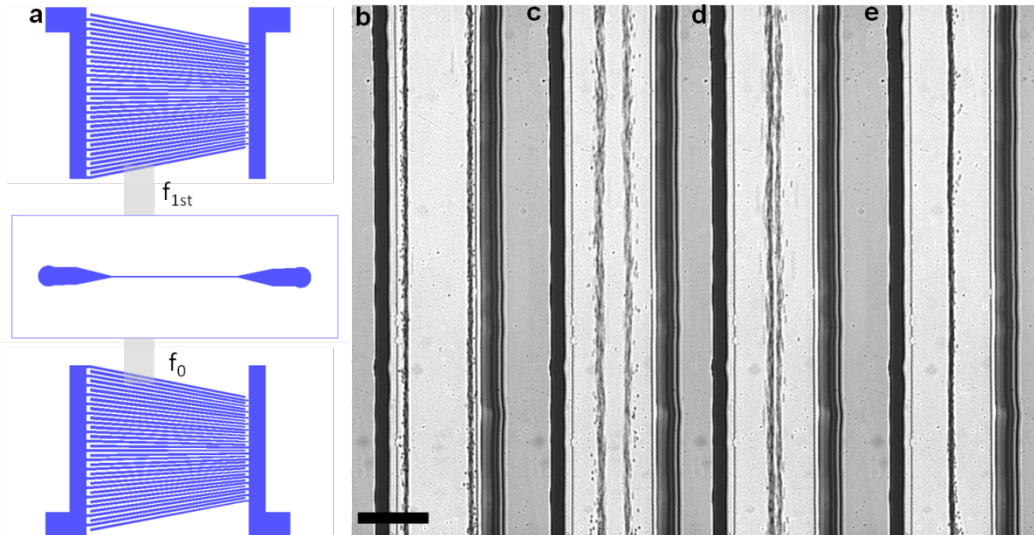


Figure 4-34: (a) Schematic showing the principle of superposition of two standing waves. In this case the fundamental frequency f_0 was superimposed to the 1st harmonic. (b-e) Image sequence is shown starting with 1st harmonic frequency (8 MHz, 20 V where 2 pressure nodes were created and then the pressure distribution was altered by superimposing the fundamental frequency (4.138 MHz, 1 V – 25 V) which led to merging of the separated bead (3 μm) streams. Flow rate applied was 2 $\mu\text{l}/\text{min}$ (Scale bar: 100 μm).

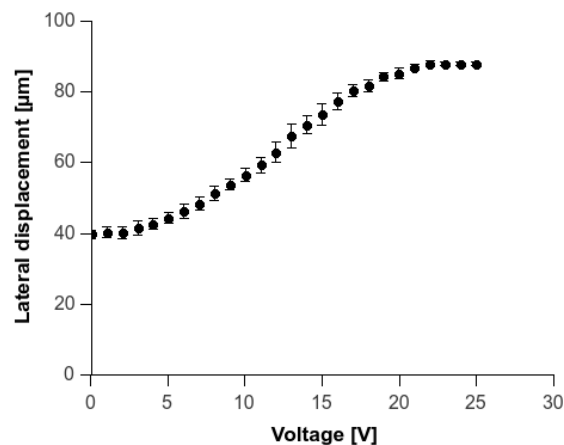


Figure 4-35: Lateral displacement of bead streams aligned in two pressure nodes when 1st harmonic (8 MHz, 20V) was applied and the fundamental frequency (4.138 MHz) was superimposed. Voltage range corresponds to fundamental frequency. The displacement at 3 different positions along the stream is plotted.

Interestingly, a local low amplitude spot in the pressure distribution along a channel section caused a denting effect (Figure 4-36). Such loose pinching regions were shown for the fundamental frequency in Figure 4-13. However, at this particular position the superimposed fundamental frequency dominated over the 1st harmonic in this region, leading to a short merging effect of two bead streams before a dividing took place again. The amplitude was in the range of 1 V to 8 V for the fundamental frequency.

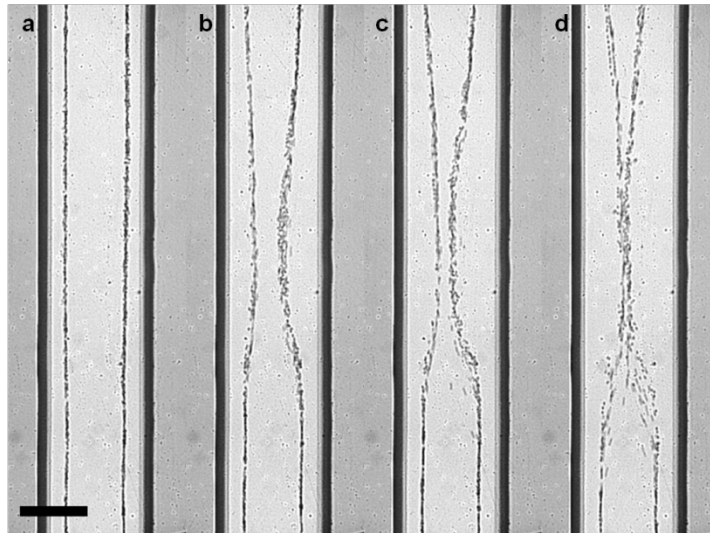


Figure 4-36: Superposition of fundamental frequency (8 MHz, 20 V) and 1st harmonic (4.138 MHz, 8 V) around a loose pinching region where the pressure amplitude for the 1st harmonic is low. This led to a localised denting effect when the fundamental frequency was superimposed (Scale bar 100 μm).

4.3.10.4. Sorting using the principle of superposition

The acoustophoretic movement of particles towards points of minimal or maximal pressure changes has been used for the separation of particles in heterogeneous mixtures.^{53, 263} While a difference in the sign of the acoustic contrast factor between two kinds of particles is of advantage for the separation, as the translation is towards pressure antinodes and nodes, most separation problems involve particles with the same sign in the contrast factor but different magnitudes of forces arising from acoustic actuation. For instance, a mixture of different sized polymer beads ($> 2\mu\text{m}$) with positive acoustic contrast experience a PAR force which scales with the radius of the particles. Peterson *et al.*¹²³ used this principle to achieve a good fractionation of 4 different bead sizes and many more studies utilized the difference in the travelling time towards a pressure node for particle separation.^{118, 140, 171, 173, 264} In all of these studies, the sample was hydrodynamically focused prior to the acoustic actuation to trigger the separation. The initial focusing step is an essential part for this process. The particles in the mixture should have the same starting position before being acoustically stimulated otherwise the difference in the force and therefore the travelling time may not lead to an optimal separation process (compare with Figure 4-17b). The use of several laminar streams with different flow rates is the most common approach to create this kind of prepositioning. However, the focussing result is often not tight but rather like a particle band as in several studies mentioned above. A solution to this issue can be the aforementioned principle of standing wave superposition.

In Figure 4-37a a schematic of a separation setup is shown where the formation of two standing waves was used to create a sample preposition followed by separation within a microchannel. In particular, a superstrate with two inlets, one for buffer and one for the sample was fabricated to inject a particle suspension (3 μm and 6 μm beads) which was first hydrodynamically focused by a buffer stream (Figure 4-37ai). Two SAW devices were applied, one for the generation of the fundamental resonance and one for the 2nd harmonic of the superstrate. The latter one induced three pressure nodal planes in the microchannel and caused a tight alignment of the injected beads along the channel wall. In Figure 4-37aii the transition from the hydrodynamically pre-focussed sample to acoustic focussing is shown. Compared to Figure 4-37ai, it is clear that acoustic pre-focussing resulted in a tighter particle alignment and therefore better prepositioning for a subsequent separation process.

The feasibility of this concept was demonstrated by separating 3 μm and 6 μm beads. With just a single SAW device excited at the 2nd harmonic, the particle mix exited the chip via the outer outlets (Figure 4-37aiii). For both bead sizes, the PAR force dominated over the acoustic streaming induced drag force. As shown in Figure 4-37aii, the sample was pre-focussed using the 2nd harmonic frequency (12.514 MHz, 20 V) and then the fundamental frequency (4.138 MHz, 8 V) was activated and its amplitude was tuned (increased) to initialize the separation process. In Figure 4-37b, the lateral displacement of 6 μm beads towards the centre node is shown while the smaller 3 μm beads remained in the outer pressure node created by the 2nd harmonic. Further down the microchannel at the outlet junction, 6 μm beads exit the chip via the centre outlet while 3 μm bead left via the outer outlets (Figure 4-37c).

An optimization of the system and goal for future work could involve the removal of the initial hydrodynamic focussing step. Instead of using several inlet channels, one single channel in conjunction with a multi transducer system could be applied. In particular, an injected particle sample can be first focussed using the 1st harmonic frequency which would result in two pressure nodal planes. This is then followed by the activation of the 2nd harmonic and fundamental frequency with two additional SAW transducers further down the channel to trigger the separation.

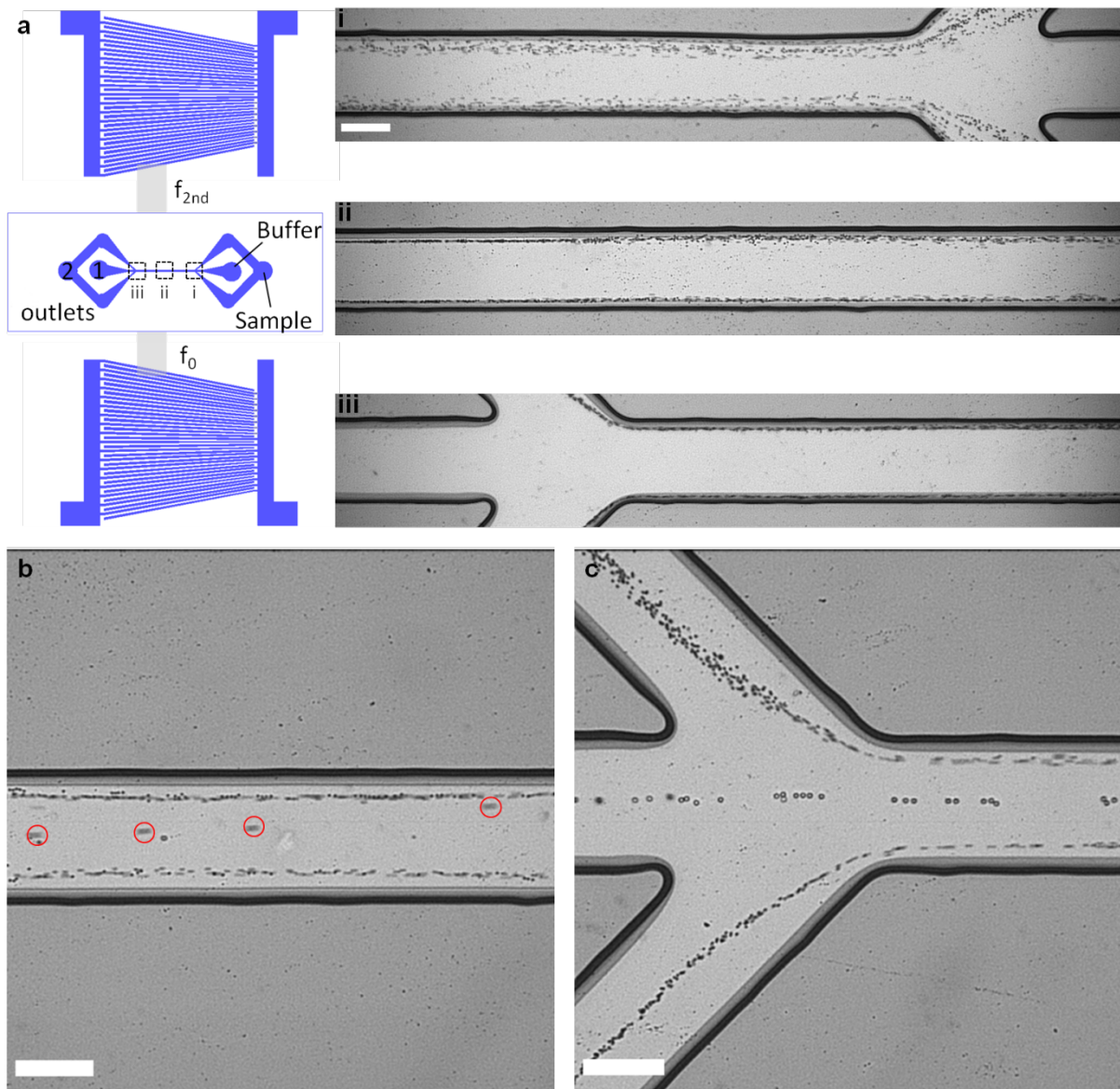


Figure 4-37: Superposition fundamental f_0 and f_{2nd} harmonic frequency for particle pre-focussing and sorting. (a) Schematic of SAW electrodes with superstrate in-between, as well as microchannel images at 3 positions along the channel, with (i) showing the inlet junction where a bead sample was hydrodynamically focussed using the center buffer inlet. (ii) Shows the transition from hydrodynamically to stronger acoustically focussed bead streams using a frequency of 12.514 MHz (20 V). (iii) Outlet junction and exit of bead streams via outer outlets. (b) Superstrate was actuated with two resonance frequencies to achieve superposition of standing waves (4.138 MHz, 8 V; 12.514 MHz, 20 V). Image shows separation of previously focussed 6 μm and 3 μm beads. The fundamental frequency was tuned to an amplitude which enabled the translation of 6 μm beads towards the centre pressure node. The red circle marks several 6 μm beads moving towards the centre node. (c) Image shows the situation at the outlet junction after superimposing to standing waves for bead separation. 6 μm beads exit via the centre outlet while 3 μm beads, still being focussed exit via the outer channel outlets. The applied flow rate was 3 $\mu\text{l}/\text{min}$ and 1 $\mu\text{l}/\text{min}$ for the buffer inlet and the sample inlet, respectively (Scale bars: 100 μm).

During experiments with higher resonance frequencies a suppression of the acoustically induced streaming effect on smaller particles was observed. The bulk streaming rolls which typically arose when the chip was activated at the fundamental frequency were significantly reduced when the 2nd harmonic was applied to the chip. This was partially explained by the fact the PAR force scales with the frequency while the size of the inner boundary streaming rolls which drive the bulk fluid reduce hence pronouncing the influence of the primary acoustic radiation force on small particles.

In combination with the superposition principle, this feature was used to separate small particles from larger ones. As mentioned above, particles smaller than $< 2 \mu\text{m}$ undergo motions induced by vortex flows in the bulk of the fluid while larger ones move to the pressure nodes. This led to a fractionation between these two particle sizes and can be used for continuous separation. However, further improvement of the separation efficiency is complicated; as the streaming rolls occupy the bulk fluid next to the pressure nodes which means the position of the small particles cannot be controlled accurately. At an outlet junction, such as in Figure 4-37c, small particles close to the pressure nodes are likely to exit via the same outlet as larger particles due to inefficient displacement. To circumvent this particular issue a concept such as that shown in Figure 4-38a may be used. Again, the superposition of two standing waves (f_0 and $f_{2\text{nd}}$) was utilized to separate $1 \mu\text{m}$ and $3 \mu\text{m}$ beads. For the fundamental frequency, $3 \mu\text{m}$ beads accumulated in the pressure node, while $1 \mu\text{m}$ beads were subjected to the vortex and occupied the bulk next to the pressure nodal plane (Figure 4-38b, middle). However, when the 2nd harmonic frequency was applied, the pitch between the pressure nodes showed only a minor vortex induced displacement of $1 \mu\text{m}$ beads (Figure 4-38b, middle). When both frequencies were applied to create the superposition effect, the bulk streaming was still reduced (Figure 4-38b, bottom) and $3 \mu\text{m}$ particles accumulated in the centre node while $1 \mu\text{m}$ particles were found in all of the 3 pressure nodes. For the case shown in Figure 4-38b (bottom), the 2nd harmonic was applied first, followed by the fundamental frequency. The amplitude of the latter one was increased until the bigger beads moved towards the centre node, while $1 \mu\text{m}$ beads stayed in the outer pressure nodes.

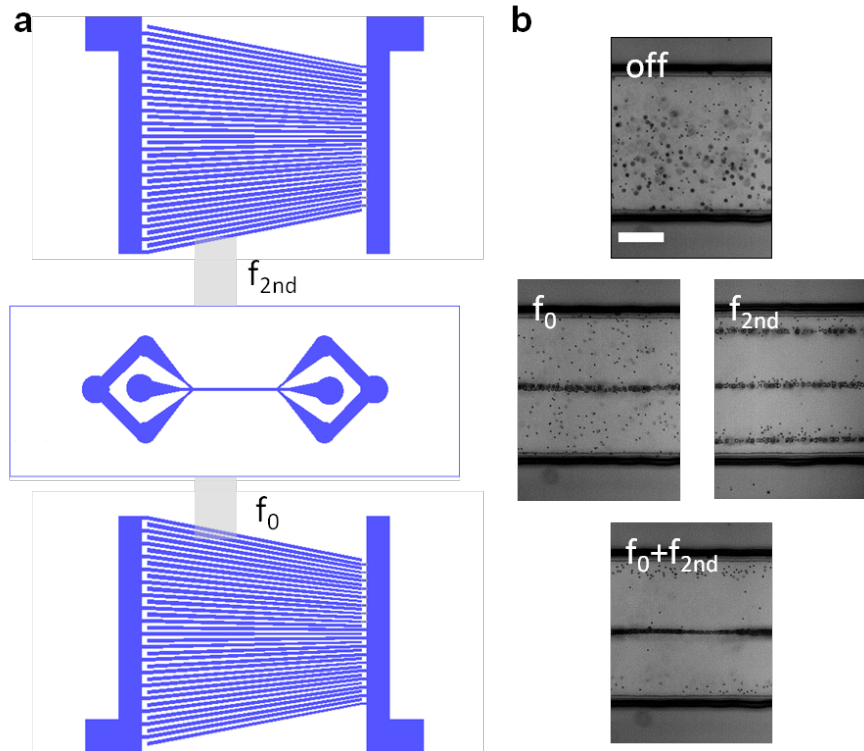


Figure 4-38. Superposition of fundamental f_0 and 2nd harmonic resonance frequency f_{2nd} to suppress acoustic streaming induce particle displacement. (a) Schematic of SAW transducers showing approximated position of wave propagation into the superstrate. (b) Situation in microchannel filled with 1 μm and 3 μm diameter beads when the fundamental frequency f_0 (4.138MHz, 20 V), 2nd harmonic f_{2nd} (12.514MHz, 30 V) and both f_0 and f_{2nd} were applied to the transducer (Scale bar: 50 μm , static fluid).

The concept was then applied for continuous separation. A bead mixture of $0.89 \cdot 10^7$ beads/ml and $0.17 \cdot 10^7$ beads/ml of 1 μm and 3 μm beads, respectively, was used which gave an initial ratio of 83.9 % and 16.1 %. In Figure 4-39a and b, images of the microchannel outlet junction are shown. Figure 4-39a shows the state when the 2nd harmonic (12.514 MHz, 20V) only was applied, the bead mixture exits via the outer channels. However, the superposition of the fundamental frequency (4.138 MHz, 10V) caused the lateral movement of 3 μm beads towards the centre node and the exit of these beads via the center channel while the smaller 1 μm beads remained close to the pressure nodes along the channel wall (Figure 4-39b). Here, the applied amplitude was tuned by visual feedback until the separation could be seen clearly. To quantify the separation, samples were taken from different outlets and bead counts were performed using a haemocytometer. In Figure 4-39c and 4-39d, the ratios of the beads in outlet 1 (center channel) and outlet 2 (outer channels) are presented. The total amount of 3 μm beads in outlet 1 and outlet 2 were 97.50% and 0.14%, respectively, while 1 μm beads were found to be 2.5% and 99.86 % in outlet 1 and outlet 2.

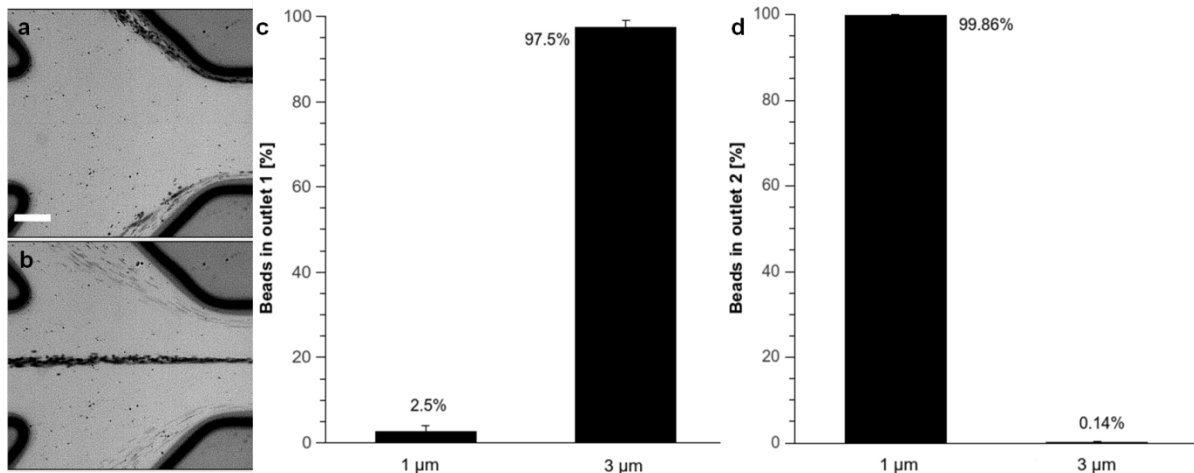


Figure 4-39: Sorting of 1 μm and 3 μm beads using the principle of superimposing the 2nd harmonic frequency to suppress acoustic streaming induced displacement. (a) 2nd harmonic frequency (12.514 MHz, 20 V) was applied leading to pre-focussing of injected sample along pressure nodes close to channel wall. All beads exit chip via outlet 2. (b) Superimposing the fundamental resonance frequency (4.138MHz, 10 V) resulted in lateral movement of 3 μm beads towards the pressure node in the centre of the channel. 1 μm beads exit via outlet 2 while 3 μm beads left via outlet 1 (Scale bar: 50 μm). Flow rates for buffer and bead sample were 4.5 $\mu\text{l}/\text{min}$ and 2.1 $\mu\text{l}/\text{ml}$, respectively. (c) Bead concentration in outlet 1 and (d) outlet 2 for sorting experiment. Initial bead concentrations were 83.9 % and 16.1 % for 1 μm and 3 μm beads, respectively. The data shown in (c) and (d) was obtained from bead count analysis in a haemocytometer (see chapter 2.4.1).

The method was also applied to enable the separation of trypanosomes from a blood sample. As described above, the streaming induced drag was dominant for the parasite leading to a random displacement adjacent to the pressure nodal plane. In Figure 4-40a the result of acoustic actuation at the fundamental frequency and the position of individual parasites in the vortex flow is shown. However, when the 2nd harmonic mode was excited on the SAW device the streaming flow was significantly reduced and the parasites could be found close to the pressure nodes in proximity to the red blood cells (Figure 4-40b).

Consequently, a parasite sample was spiked in to a blood sample and then injected into the chip. An initial ratio of 97.2% (169 $\cdot 10^6$ cells/ml) and 2.8 % (4.7 $\cdot 10^6$ cells/ml) for blood cells and trypanosomes, respectively was used for these experiments. In Figure 4-41a, an image of the experiment is shown where the sample was subjected to the 2nd harmonic mode. The blood cells and trypanosomes left the chip via the outer channels. When the fundamental frequency was superimposed and the amplitude was increased until a strong focussing of blood cells could be observed, samples were collected and analysed for parasite content in the outer outlets (outlet 2) and the inner outlet channel (outlet 1). In Figure 4-41b, an image is shown where blood cells were aligned in the centre channel close to the outlet junction, while trypanosomes followed the flow along the outer pressure nodes to exit the chip via the side channels.

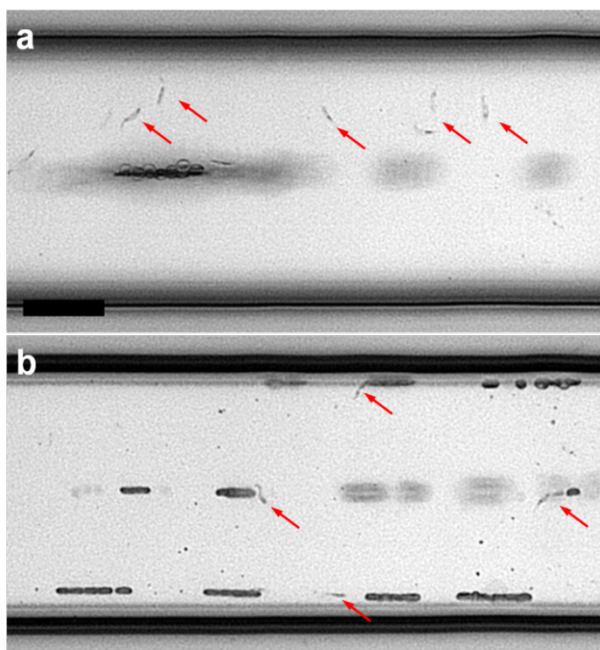


Figure 4-40: (a) Fundamental frequency (4.138 MHz, 25V) applied to the superstrate induced alignment of blood cells in the pressure node, while the parasite underwent acoustic streaming induced vortex motion. (b) 2nd harmonic frequency (12.514 MHz, 25V) was applied, followed by the alignment of blood cells and parasites in pressure nodes. No vortex induced parasite movement was observed. Experiment conducted without external flow applied. The red arrows mark position of parasites (Scale bar: 50 μ m).

The analysis of the collected samples was carried out with a haemocytometer. It was noticed that the sample settled in the tubing quite quickly (4 min to 8 min) and a significant change in the cell concentration over time was observed. This means that the initial ratio was altered over time during the experiments. Therefore the absolute values are given in table 1. Nonetheless, the visual control and the analysis of the collected sample prove the feasibility of this strategy. Based on the analysis of the cell counts an average ratio of 99.1% and 0.9% in outlet 1 and 8.8% and 91.2% in outlet 2 for blood cells and parasite, respectively, was determined (Figure 4-41c and 4-41d). These results show that the majority of the blood cells exited via the centre channel while the majority of the parasites exited the side channels.

Table 4-1: Cell count analysis from samples collected from different outlets for 4 experiments. It has to be noted that due to the settling of the cells in the tubing the initial ratio of $169 \cdot 10^6$ cells/ml blood cells to $4.7 \cdot 10^6$ cells/ml trypanosomes was altered over the course of each experiment. Therefore the absolute cell counts are given in the table.

Tests	Outlet 1 [cells/ μ l]		Outlet 2 [cells/ μ l]	
	Blood	Trypanosomes	Blood	Trypanosomes
1	41285	125	344	1438
2	41591	265	333	1520
3	14857	88	14	2125
4	22019	447.3	13	1625

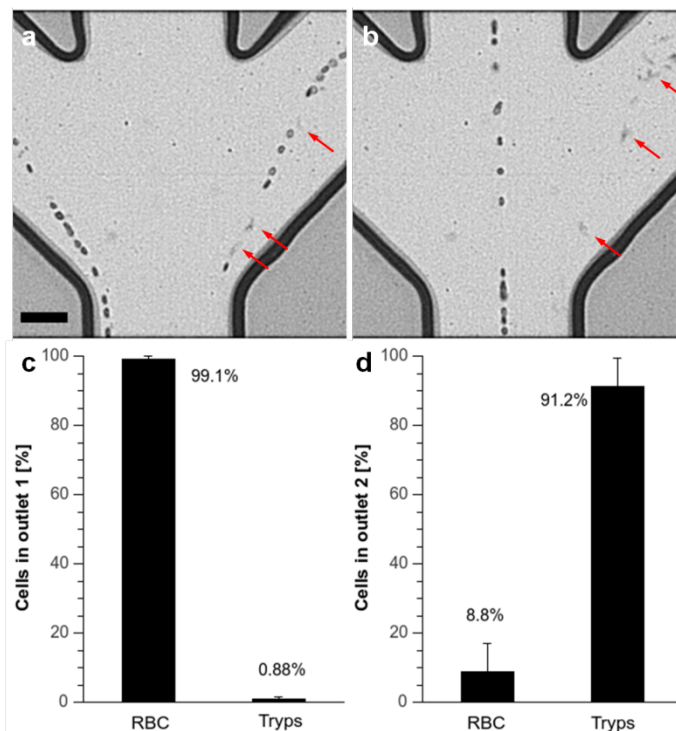


Figure 4-41: Sorting of trypanosomes and red blood cells using the principle of superimposition. (a) 2nd harmonic frequency (12.514 MHz, 20 V) was applied leading to pre-focussing of injected sample along pressure nodes close to the channel wall. Trypanosomes and blood cells exit chip via outlet 2. Red arrows mark position of parasites. (b) Superimposing of the fundamental resonance frequency (4.138MHz, 15 V) resulted in the movement of blood cells towards the pressure node in the centre of the channel. Blood cells exit channel via outlet 2, while trypanosomes exit via outlet 1 (Scale bar: 50 μ m). Flow rates for buffer and blood sample were 6 μ l/min and 3 μ l/ml, respectively. (c) Cell concentrations in outlet 1 and (d) outlet 2 for sorting experiment. Initial cell concentrations were 97.2 % ($169 \cdot 10^6$ cells/ml) and 2.8 % ($4.7 \cdot 10^6$ cells/ml) for blood cells and trypanosomes, respectively. The data shown in (c) and (d) correspond to the data in table 4-1 and represents the analysis of cell counts performed in a haemocytometer after sample collection at the outlets.

4.4. Conclusion

A new strategy for acoustophoretic particle manipulation was developed, characterized and used for cell and particle manipulation. In particular, the system consisted of a superstrate with an embedded microchannel as a transversal resonator structure to induce a plane standing wave. Acoustic waves within a tuneable frequency range were excited by a slanted SAW transducer. The characterisation of the system showed that the acoustic energy coupled from a single transducer to a superstrate was sufficient for particle manipulation using different acoustic forces, namely PAR force and acoustically induced streaming. In comparison with previously reported systems based on surface acoustic waves, a simplified system assembly was demonstrated avoiding cumbersome aligning and bonding procedures, while keeping the benefits of surface acoustic wave device such as a planar device structure, broadband and high frequency capabilities.

The practicability of a slanted broadband electrode was shown by tuning the frequency applied to the transducer to several resonance points of different superstrates. This resulted in flexible pressure distributions within the microchannel and was used for dynamic patterning of cells and particles. Furthermore, the acoustic streaming induced displacement between blood cells and the blood born parasite trypanosomes was identified and a separation concept based on a single SAW device and two superstrate designs was demonstrated. A combination of two SAW devices was used to superimpose two standing waves by applying different resonance frequencies to the electrodes. This can be used to change the position of the pressure nodal planes, to enable a pre-focussing of particles prior to the triggering of sorting and to reduce the effect of acoustic streaming in the channel. The latter one was used to successfully separate different sized particles as well as cell mixtures with high efficiencies. In summary, a novel concept for particle manipulation on a disposable superstrate was developed which may find application in the field of acoustofluidic miniaturized analysis systems. Moreover, it set the basis for an integration of optoelectronic and acoustic tweezing into a microfluidic chip (see Chapter 5).

5. Combined use of optoelectronic and acoustic tweezing

This chapter demonstrates the combined use of optoelectronic and acoustic tweezing in microfluidics. OET chips served as superstrates and were placed onto the piezoelectric wafer to be acoustically excited at resonance frequencies by the SAW transducer. Virtual electrode arrangements as well as flexible pressure node distributions were applied for both, very localized and far-reaching particle manipulation. DEP and acoustic forces enabled controlled particle trapping, aggregation and fusion of particle streams under continuous flow. A sequential use of both fields enabled concentration of particles towards pressure nodes followed by precise particle guiding into channel outlets, virtual channels or adjacent pressure nodes to achieve sorting and fractionation of mixtures.

5.1. Introduction

The arbitrary handling of microparticles in microfluidic compartments can be achieved by non-inertial force fields arising from focused laser beams or magnetic, electric and acoustic fields. In chapter 1.1 and 1.4 examples of micromanipulation systems utilizing such force fields were given and relative benefits were discussed. Ideally, a platform that can perform many different functions within the micro scale is desirable but until now none of the introduced platforms is able to fulfil all requirements. The shortcomings are associated with a lack of fine control where particles can be individually selected and then independently handled or the ability to perform manipulations on a large number of particles over a wide area of the chip. Many systems also lack the control of particles in all 3 dimensions and sometimes particles need to be labelled to be able to control them or certain medium conditions have to be established before any manipulation is feasible. For instance, magnetic tweezers require that the particle of interest is magnetic for efficient handling. This is often achieved by modifying particles of interest with tiny magnetic objects. In contrast, methods using DEP require a dielectric particle to be suspended in a medium of relatively low conductivity to generate sufficient DEP forces. And acoustic field based approaches often lack the fine control that enables individual addressing of particles. Therefore, strategies are needed that enable the combination of methods making use of individual benefits to compensate for these disadvantages.

The previous chapters introduced the integration of OET into a robust microfluidic chip and applied the chip concept in the form of a superstrate that acts as transversal resonator to confine acoustic fields. Particle manipulations were demonstrated individually by non-uniform electric fields and acoustic standing waves. In this chapter dielectrophoretic and acoustophoretic manipulations were combined to demonstrate versatile particle handling characterized by a flexible but well localised applied DEP force and a long-range PAR force. While this was the first time that OET was combined with another non-inertial force field, the combined use of DEP and acoustophoresis has been shown before. Wiklund *et al.* showed for the first time that fixed metal electrodes integrated into a silicon resonator chip allowed enhanced particle handling such as trapping, concentrating, merging and fusion of particle groups.¹⁸⁹ Later, Ravula *et al.* demonstrated that the acoustic field can be used as pre-concentrator of particles before a fixed electrode array refines the particle position into a single stream.²⁶⁵ Both studies revealed that localised force fields induced by electric fields and far reaching acoustic fields were of great benefit. It is assumed that the principle of OET extends the level of control when DEP and acoustophoresis are used together which is based on the fact that electric fields can be selectively as well as dynamically patterned and tuned. In this part of the thesis it was shown that the use of both force fields enabled concentration of particles towards pressure nodes followed by precise particle guiding into channel outlets, virtual channels or adjacent pressure nodes to achieve sorting and fractionation of mixtures.

5.2. Materials and Methods

The main details of the materials used and the setup were already described in chapter 2 to 4 which included fabrication details of the ultrasound transducer and the OET chip. In this chapter OET chips and the SAW device were used together. Figure 5-1 shows an assembled system consisting of an OET chip (superstrate) with a straight microchannel placed onto the piezoelectric substrate underneath a microscope objective. Besides straight channel superstrates, different channel designs including channels with several inlets and outlets of varying width were used while the channel height was approximately 15 μm in all cases. The experiments were all conducted under continuous flow. PS beads suspended in a 5mS/m conductivity solution were injected into the OET chips using a syringe pump and the manipulation by acoustic and electric fields were monitored by cameras attached to the microscope. The OET chip was directly connected to a signal generator (TG5011, TTI, UK) to apply voltages in the range of 15 V to 20 V at frequencies of 50 KHz and 100 KHz. The ultrasound transducer was connected to an amplifier and signal generator and the frequency of the excited SAW was tuned to the resonance frequencies of the OET chips. Video recordings of bead manipulation experiments were analysed using ImageJ (v1.47) to extract the velocities of manipulated beads under various conditions.

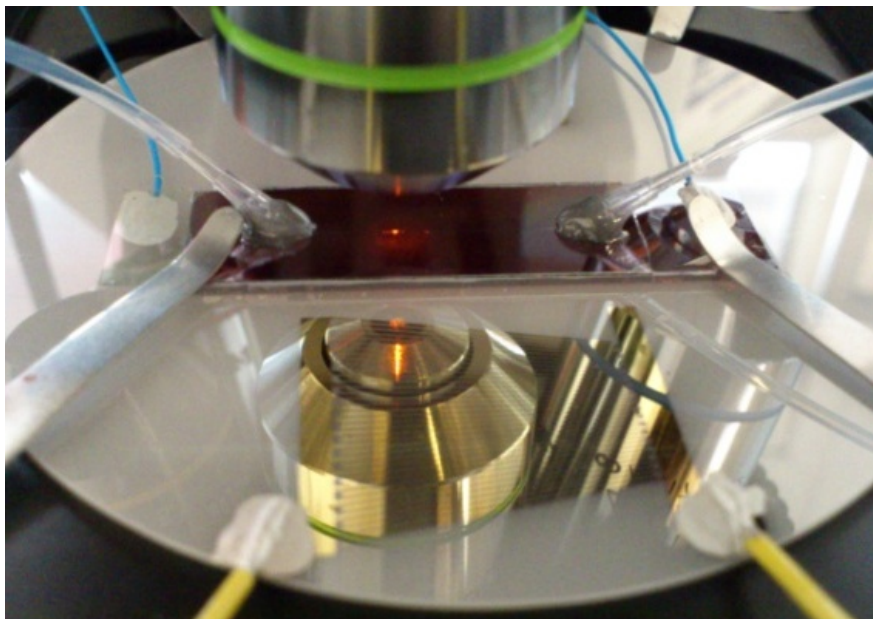


Figure 5-1: Assembled setup on the microscope stage showing OET chip (superstrate) placed onto the piezoelectric wafer close to the SAW transducer.

5.3. Results and Discussion

In chapters 3 and 4 the individual use of OET and acoustic tweezing was demonstrated. In this chapter the combined use of a light induced DEP force and the PAR force is shown and was found to have the advantage that particles within a microchannel can be addressed locally and over a wide area along the microchannel utilizing the particle's electrical and mechanical properties. Especially the use of virtual electrodes generated at arbitrary positions provided a very versatile approach which compensated for the relatively inflexible application of pressure gradients within standing wave fields. Although, the results in chapter 4 demonstrated tuneable pressure node distribution and the literature shows array like pressure landscape for single particle control¹⁴³, the acoustic field arrangement is limited to the transducer or resonator design. In the following sections, a sequential use of DEP and acoustic forces was used to enable a range of complex particle manipulation such as sorting, guiding and merging of particles streams under continuous flow. However, before this, some issues regarding the leakage of the electric field are briefly discussed.

5.3.1. Influence on leakage field on particle-particle interactions

In chapter 3 the influence on the leakage field induced by an applied AC signal was shown. A significant voltage drop into the microchannel was observed despite no selective illumination leading to electric fields that influenced particle movements and positioning along the channel wall and in the bulk liquid. The field disturbance around particles induced pearl chaining while the insulating channel wall created a non-uniform field which attracted or repelled particles depending on their initial position and polarisability.

As suggested before, the bead wall interaction can be reduced by applying a standing pressure wave across the channel. The pressure amplitude has to be tuned until the PAR force dominates over the attractive force imposed by the electric field distribution around the particles and the channel wall. In Figure 5-2a, an example is shown where a OET chip was electrically and acoustically actuated using an AC signal of 100 KHz at 20 V and the first harmonic resonance at 8 MHz and 10 V. The 3 μm beads were injected under continuous flow followed by application of the electric signal but no illumination. Afterwards the standing acoustic wave was created. It can be seen that beads were able to align along the pressure nodes. However, beads close to the channel wall were dominated by the electric leakage field induced attraction. The pressure amplitude had to be tuned by increasing the applied voltage to the SAW device to 15 V before the influence of the leakage field was overcome. Due to persisting leakage fields, this kind of tuning had to be carried out for each

experiment. This makes the combined application slightly complicated because the non-uniform character of the pressure along the channel length (see chapter 4) and the frequency dependant coupling of acoustic energy from the SAW device. Hence, depending on the manipulation position along the channel and the applied resonance frequency a fine adjustment was necessary to enable an improved particle manipulation.

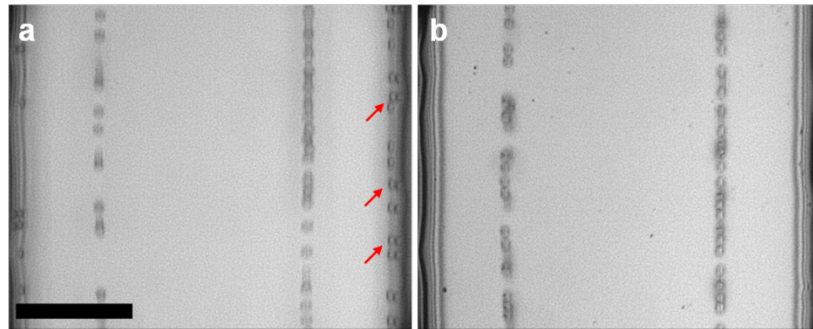


Figure 5-2: Influence of leakage field and acoustic field on particle ($3\ \mu\text{m}$ beads) interaction with channel wall. (a) OET chip acoustically (8 MHz, 10 V) and electrically (100 KHz, 20V) actuated to demonstrate dominating particle-wall interaction induced by a leakage field. (b) OET chip acoustically (8 MHz, 15 V) and electrically (100 KHz, 10V) actuated but this time tuned to the point where the PAR force overcame particle wall interactions (Scale bar: $50\ \mu\text{m}$; flow rate: $0.5\ \mu\text{l}/\text{min}$).

A significant influence of the leakage field could also be observed within the pressure nodal plane. The bead ($3\ \mu\text{m}$) alignment in the OET chip within a single pressure node without electric signal applied is shown in Figure 5-3a. The beads were focused under continuous flow into a band that was around three bead sizes ($9\ \mu\text{m}$) wide. The leakage field, however, resulted in a bead rearrangement mainly along the channel height which is shown in Figure 5-3b. The electric field distorted around the beads and the induce polarization triggered a dipole-dipole interaction between them. The pearl chaining effect within the nodal plane then created a fine single bead wide stream along the channel length. This effect was accompanied by the secondary acoustic radiation force which arises at close distances between particles in the pressure node and was attractive for particles aligned perpendicular to the direction of wave propagation. This meant that pearl chains where not only created along the channel height but also along the channel length as long as the bead concentration within the pressure node was high enough. However, here one needs to consider that the disturbed electric field around the bead normally causes a repelling effect that is acting perpendicular to the electric field line direction. This is likely to prevent real physical contact between the beads but indicates that the secondary acoustic radiation force partially dominated and brought beads in the same plane within the pressure node closer together. Nonetheless, beads subjected to delayed lateral movement may face an electric and acoustic barrier due to the tight bead alignment in the pressure node. This is shown in Figure 5-3b, where beads were rejected from entering the pressure node. The primary

acoustic radiation force forced beads towards the channel center but a negative DEP effect arising from beads in the same plane within the pressure node as well as a repulsion in form of the secondary radiation force that acted parallel to the wave direction impeded further movement keeping those beads in an equilibrium balanced by the sum of several forces.

In general, these results showed that when a combined application of OET and acoustic tweezing is envisaged, several effects need to be considered and adjustments of the force fields have to be carried out to minimize unwanted effects. Although, none of these issues can be fully solved, the following sections demonstrate a range of manipulation schemes which may become useful once the leakage fields and particle-particle interactions can be better controlled.

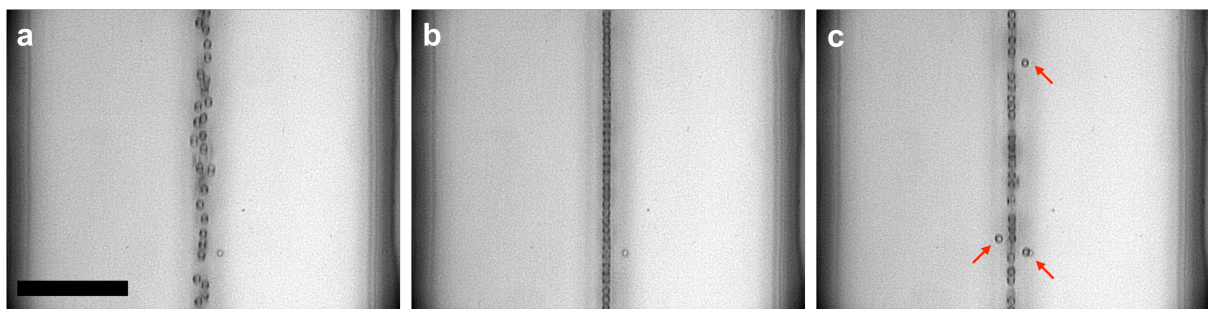


Figure 5-3: Influence of leakage field and acoustic field on particle ($3\ \mu\text{m}$ beads) alignment in pressure node. (a) Acoustic actuation at fundamental frequency using 20 V. (b) Electrical signal (100 KHz, 20 V) applied to OET chip while being acoustically actuated (no illumination). The resulting leakage field promoted partially tighter bead focusing due to pearl chaining. (c) Same conditions as (b), however, some beads were repelled by electric interactions arising from tight bead stream and potentially due to secondary acoustic radiation forces in the pressure node. Red arrows mark the beads which were not able to enter the central bead stream due to an electric and acoustic barrier (Scale bar: $50\ \mu\text{m}$; flow rate: $0.5\ \mu\text{l}/\text{min}$).

5.3.2. Dynamic sorting into channel outlets using virtual electrodes

The sequential use of acoustic tweezing and OET can be used to achieve a quick particle positioning followed by a local and dynamic control. An application might involve the concentration of a particle sample within a pressure nodal plane and a subsequent guiding or sorting of particles into desired regions (e.g. outlet) of the microchannel network. This can be easily achieved by patterning electric fields, while acoustic standing wave approaches with transversal resonator concept have limited lateral control of pressure node positions. For instance, selective guiding of a concentrated particle stream into specific outlet channels would require a change in the phase or wavelength of the travelling wave to switch the position of the pressure node. However, the transversal resonator concept requires specific resonance frequencies to generate a standing wave and no change in the phase upon reflection of the wave at the boundary takes place which fixes the position of the pressure

nodes. Instead, the generation of moving light patterns to generate non-uniform electric fields as guiding pathways can provide a viable route for dispensing particles into desired microchannel outlets. An example is shown in Figure 5-4, where 6 μm beads were manipulated by sequential use of acoustic and electric fields in a microchannel and at a microchannel junction with three outlets. First, the randomly distributed beads were acoustically concentrated into a single pressure node located in the center of the microchannel using the fundamental resonance of the chip (Figure 5-4a). The laminar fluid flow directed the beads along the channel and into a central channel outlet. By projecting a virtual electrode into the outlet junction a dynamic switch was created that enabled routing of the concentrated particle stream into the side outlet (Figure 5-4b and c). The time to switch the particles direction into the side outlet after change of the virtual electrode configuration was 10 ms while the applied voltage was increased for increased flow rates (Figure 5-4d). As mentioned beforehand, the pressure amplitude was tuned to overcome bead-wall interactions. The bead sample was acoustically focussed within the channel inlet area; however, the manipulation of the beads by virtual electrodes was in absence of a significant acoustic field, so that the deflection of the beads was mainly the result of a net force arising from the drag force and the negative DEP force.

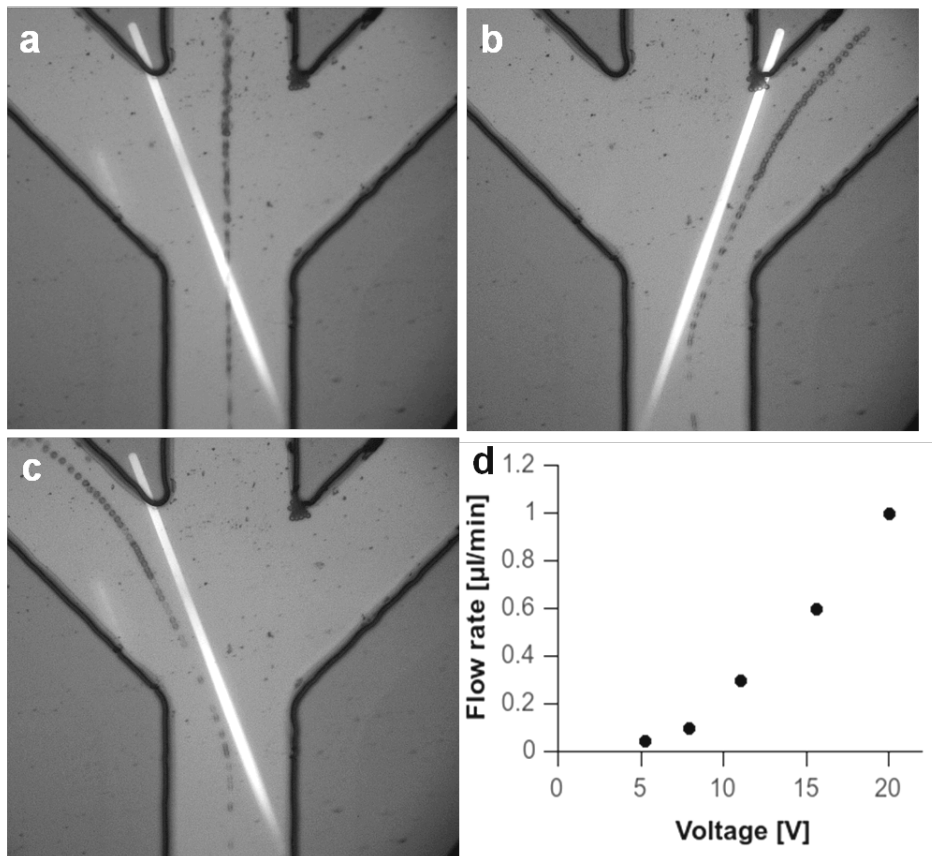


Figure 5-4: Deflection of particles (6 μm beads) into channel outlets using dynamic virtual electrode arrangements that deflect particles to a desired outlet (flow from bottom to top). (a) Acoustic actuation (4.138 MHz, 15 V) focused particles along the channel center followed by the particles exiting via the central outlet. (b-c) Additional application of virtual electrode (70° , 15 μm width, 50 KHz) provided dynamic particle switching into the side outlets. (Scale bar: 100 μm , solution conductivity 5mS/m, 20 x objectives). (d) Voltage needed to switch particles to side outlets when different flow rates were used.

In Chapter 3 it was demonstrated that the DEP force can be adjusted by parameters such as voltage signal or the transparency of the virtual electrode which enabled particle size selective handling. By adjusting the voltage carefully, a mixture of two bead types can also be fractionated into different outlets. An example is shown in Figure 5-5 where 3 μm and 6 μm beads were first concentrated in the pressure node and then size selectively guided into different outlet channels by activating a virtual electrode and tuning the DEP force by adjusting the voltage signal until the 6 μm beads were routed along the virtual electrode while 3 μm beads passed the electrode to enter the central outlet channel.

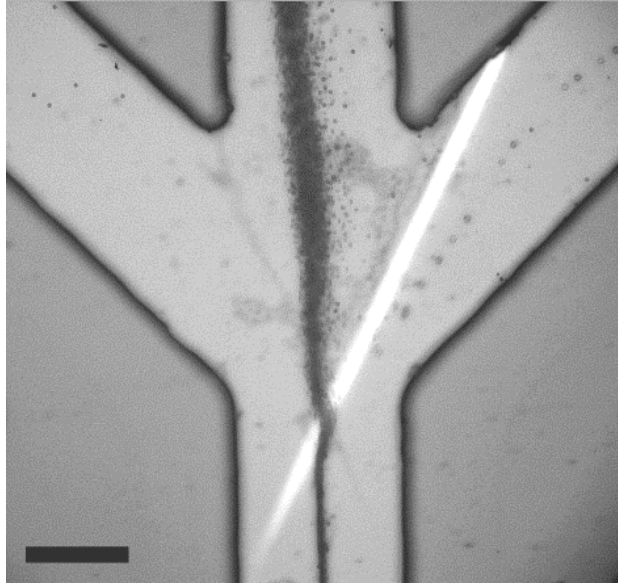


Figure 5-5: Sorting different sized particles into outlets using the PAR and DEP force combined with hydrodynamic force (flow from bottom to top). Bead mixture consisting of 6 μm and 3 μm were first concentrated within a pressure node by applying the fundamental frequency (4.138MHz, 15 V) followed by tuning the size dependent DEP force (50 KHz, 16 V) to enable size selective guiding of 6 μm bead into a side outlet. (Scale bar: 100 μm , 5mS/m, 20x objective, 0.5 $\mu\text{l}/\text{min}$).

5.3.3. Acoustic sorting supported by virtual electrodes

The PAR force scales with the radius of a particle. A size difference between particles in a mixture can be exploited for fractionation when the particles have similar mechanical properties. The time-dependent lateral movement of particles along a pressure gradient has been used in several studies^{118, 123} to sort particles into different channels. The position of the standing wave within these systems and the flow rate should be well controlled to make sure the different sized particle reach a lateral position that leads them into different channels otherwise mixing into the same pressure node takes place again. Furthermore, before a separation is initiated it is of advantage to have the particle mixture within a similar lateral position to assure a similar distance to the pressure node. This is usually achieved using a sheath flow which focuses the mixture beforehand. However, one can replace this by making use of virtual electrodes and their free rearrangement within a microchannel to achieve sorting into virtual channels prior to particle concentration and alignment into similar lateral positions. The use of localised virtual electrodes supports a very localised use of acoustic fields to perform sorting in simple straight microfluidic channels.

The acoustic sorting of particles with the help of virtual electrodes is demonstrated in Figure 5-6.

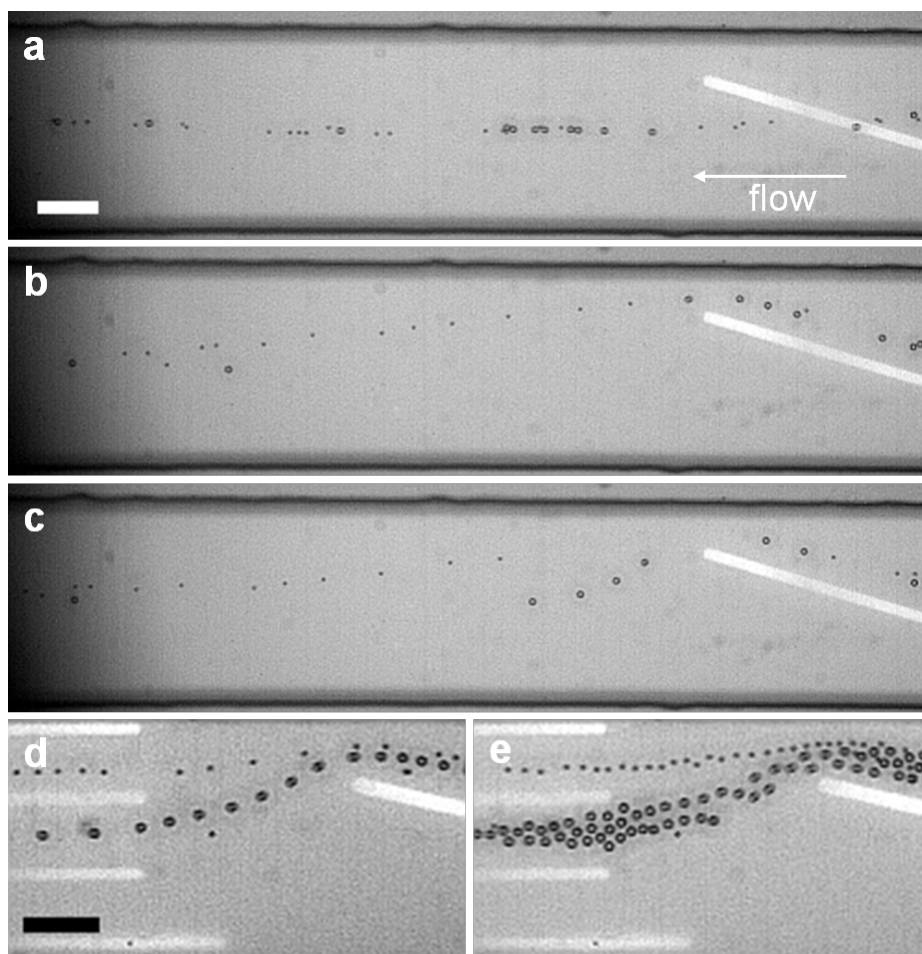


Figure 5-6: Acoustic sorting of 3 μm and 6 μm beads supported by virtual electrodes (flow from right to left). (a) The bead mixture was acoustically (4.138 MHz, 5 V) focused into a single pressure node in the channel center. An oblique virtual electrode (75°) was projected into the channel crossing the pressure nodal plane. (b) The activation of the electrode (15 V, 100 KHz) deflected the beads along the length of the electrode and therefore out of the pressure nodal plane. (c) Once the influence of the virtual electrode was overcome, the PAR force pushed particles back to the pressure node. The movement towards the channel center was size dependent due to the PAR force scaling with the radius of the particle and lead to varying displacement times between the bead sizes. This difference was used to sort the bead mixture into virtually defined channels using (d) low (10^5 beads/ml) and (e) high (10^5 beads/ml) bead concentrations (Scale bars: 50 μm , flow rate: 0.5 $\mu\text{l}/\text{min}$, 5mS/m).

A mixture of 3 μm and 6 μm PS beads were injected into a straight microchannel of the OET chip. First, the mixture was concentrated within a single pressure node in the center of the microchannel using the fundamental resonance of the chip (4.138 MHz, 5 V; Figure 5-6a). Second, an oblique virtual electrode was projected into the microchannel crossing the pressure node at an angle of 15° . The activation of the electrode (100 KHz, 15 V) induced a negative DEP force that together with the drag force overcame the PAR force and resulted in a net movement of the particles along the virtual electrode and against the pressure gradient set up by the standing wave (Figure 5-6b). From Figure 5-6b it can be seen that the applied electric field generated a strong DEP force which pushed particles away from the electrode edge and hence dominated over the PAR force. This deflection process brings the particle

mixture into a similar initial position prior to the start of the separation. The downstream end of the virtual electrode was approximately positioned an eighth wavelength distance from the channel wall where the peak of the PAR force distribution was situated. When the deflected particle stream passed the electrode and the influence of the DEP force, the PAR force combined with the drag force resulted in a restoring force towards the pressure node. The time-dependent displacement from an initial starting point towards the pressure node can then be used to achieve a separation between the two particle types (Figure 5-6c). In this case, a sorting into virtual channels defined by virtual electrodes that impede further lateral movement was carried out. In Figure 5-6d and 5-6e, the sorting process with different bead concentrations (10^5 beads/ml and 10^6 beads/ml) is shown. The separation into the channels was achieved within 200 μm of a straight physical microchannel section once the oblique virtual electrode was passed. This showed that OET can be used to augment the acoustic force in very localised manner.

However, as discussed beforehand, the influence of a leakage field limits the separation due to mutual dielectrophoresis and wall-particle interactions. Both can be reduced by applying a standing wave across the channel height and width. Although, no standing wave was generated across the height of the microchannel, from Figure 5-6e it is clear that particles within the same plane repel each other due to strong field regions that exist at each particle side as the consequence of the leakage field. The shallow microchannel reduced the pearl chaining length but aggregations along the channel height were still present. Furthermore, a secondary acoustic radiation force (Bjerknes force) can lead to particle aggregation within the pressure plane when particles align perpendicular to the wave propagation (see section 1.3.3). However, during these experiments such acoustic induced particle-particle interaction was not observed which indicates that the dipole-dipole repulsive interaction dominated. Particle-wall interactions can be overcome by the standing wave field across the width but to optimize this sorting process one would also need to introduce a second SAW device that runs at the vertical channel resonance. Another interesting observation was made when monitoring the deflection of the particle mixture along the oblique virtual electrode. Initially, the deflection was the initiator of the separation but also served as prepositioning of the particles into similar lateral positions. However, the deflection led already to a slight displacement which can be seen in the Figures 5-6d and 5-6e. The smaller 3 μm beads were further repelled from the edge of the electrode than the 6 μm beads. This was partially attributed to the leakage field that acted along the whole microchannel length and the initial acoustic focusing step to concentrate particles in the channel center. The 6 μm particles were focussed much faster into the pressure node creating an electrically and acoustically

repelling barrier that partially accumulated the 3 μm beads at the outer areas within the pressure node. However, when the particle stream approached the oblique electrode, the deflection of beads against the pressure gradient was also size dependent with the smaller ones easier to repel by negative DEP and secondary acoustic radiation forces than the bigger beads.

5.3.4. Particle handling in multipressure nodal planes using virtual electrodes

The advantage of a broadband SAW transducer was presented in chapter 4 and included the creation of a tuneable pressure landscape by changing the frequency towards higher harmonic resonances of the channel within the superstrate. The multipressure nodal planes can be used to spread a concentrated sample across the channel width instead of dense packaging into a single node at the fundamental frequency which might lead to clogging or unwanted resonance changes as a result of wave refraction at the particle aggregate. Moreover, several particles streams might be used to handle subgroups of particles modified with biological surface compounds (e.g. antibodies) that react with solution molecules or capture analytes of interest (e.g. antigens) in a sample liquid (e.g. blood plasma). This may enable multiplexed assay processes (e.g. bead based assays) where screening for several biomarkers can take place in an automated and high-throughput fashion. The combined use of OET and acoustic tweezing has the potential to be helpful in creating such bead based assays. The PAR may serve as a rail which defines the global bead positions in multipressure nodes while locally defined electric fields can be supportive for signal readout by trapping particles temporally or initiating reactions of subgroups to enable for instance an agglutination test with subsequent sorting of bead aggregates.

The possibility of such concepts was shown by using an OET chip that enabled multipressure node creation combined with the SAW transducer. In particular, a 270 μm wide channel was chosen and when acoustically excited at the resonance frequencies of 4.782 MHz and 10.002 MHz two and four pressure nodal planes across the channel were generated (Figure 5-7). By projecting virtual electrodes onto the photoconductor surface several operations, depending on the electrode arrangement were achieved. A simple manipulation action can involve the deflection of a particle stream within a pressure node into an adjacent particle carrying pressure node. Figure 5-8 shows a node merging process triggered by an oblique virtual electrode (70° , 20 μm wide) under continuous flow. The applied negative DEP force was tuned to overcome the pressure gradient within the nodal spaces to switch the 3 μm particles towards the neighbouring node. Figure 5-8 (a-e) shows

the sequence starting from the activation of the electrode and the break-up of the particle stream by deflecting the beads until merging with the adjacent particle stream takes place.

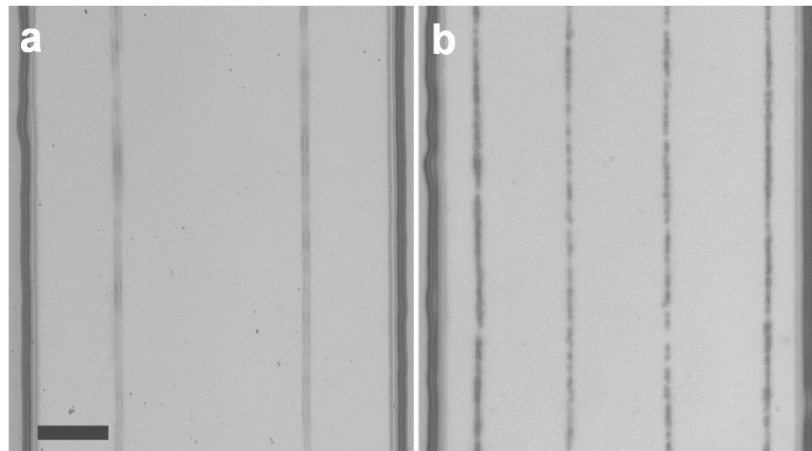


Figure 5-7: A 270 μm wide microchannel in an OET chip acoustically excited at the resonance frequencies of (a) 4.782 MHz and (b) 10.002 MHz (Scale bar: 50 μm).

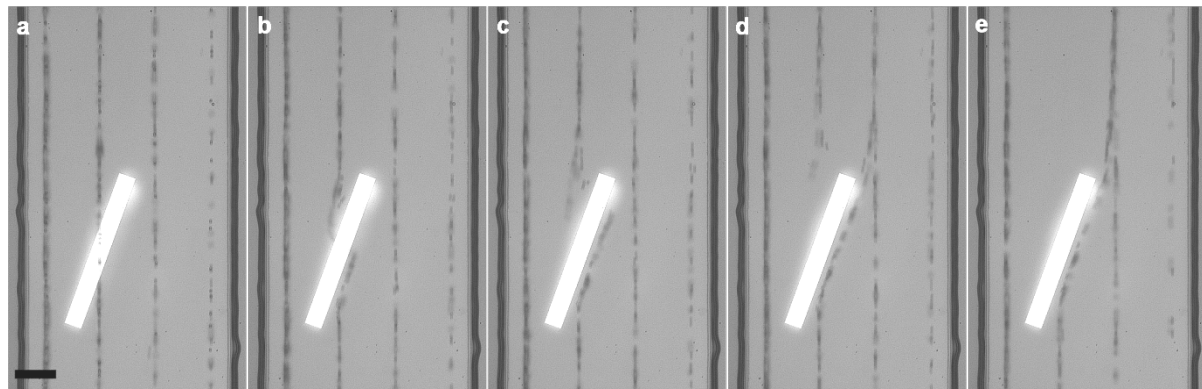


Figure 5-8: A sequence of continuous bead (3 μm) manipulation using OET and acoustic tweezing. Beads focused into 4 streams by the PAR force at 10.002 MHz at 20 V followed by virtual electrode activation (100 KHz, 20 V) to partially merge two streams by deflecting beads along the edge of the electrode due to negative DEP (Scale bar: 50 μm , flow rate: 0.5 $\mu\text{l}/\text{min}$, medium conductivity: 5 ms/m, 20x objective.).

A virtual electrode perpendicular to the flow direction can be used to trap particles when the DEP force overcomes the drag from the fluid flow as shown in chapter 3. The combination with an acoustic standing wave with the non-uniform field enables well localised particle aggregates. In Figure 5-9 a standing wave with four pressure nodal planes and a 25 μm wide virtual electrode were set-up across the microchannel. When an AC signal was applied to the OET chip (100 KHz, 20 V), 3 μm beads focused in the pressure nodes were trapped at the edge of the electrode followed by an aggregation over time. While the DEP force component acted against the drag force in the flow direction, the PAR force was directed perpendicular to the flow direction and so confined the particles in the pressure node leading to small aggregates rather linear particle arrangements.

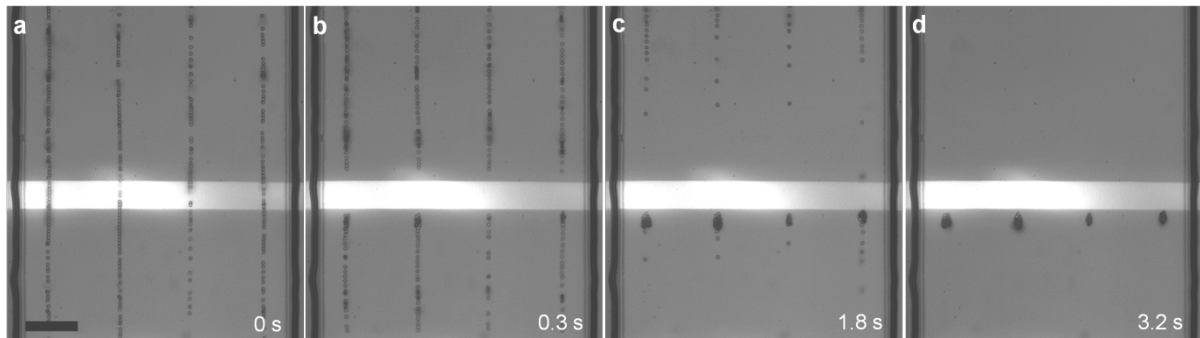


Figure 5-9: Manipulation sequence of 3 μm beads by acoustic and optoelectronic tweezing under continuous flow (flow from bottom to top). The OET chip was first acoustically actuated using the 3rd harmonic resonance frequency (10.003 MHz, 5 V) followed by activation of the virtual electrode (50 KHz, 10V) to trap particles in front of the virtual electrode (25 μm wide) within the pressure node. (a) OET off, ultrasound on. (b-d) Activated electrode led to accumulation of particles over time while being confined to the pressure node (Scale bar: 50 μm , flow rate: 0.1 $\mu\text{l}/\text{min}$, 20x objective, 5 mS/m)

The versatile projection of images and hence the patterning of electric fields can be exploited for more complex manipulation schemes which can be dynamically changed and adapted to specific requirements. Instead of creating a single trapping site as shown in Figure 5-9, multiple sites can be created on the fly to enable array-type profiles within sections of the microchannel. An example is presented in Figure 5-10 where u-shaped virtual pockets were designed to collect beads in the pressure node under continuous flow (Figure 5-10b). Once the electric field (100 KHz, 20 V) was activated, beads aggregated within a second in these pockets and were stably hold against the fluid flow. The virtual pockets could be used to replace mechanical traps in microfluidic channels which are typical used in live cell arrays to study the drug response in cells and cellular heterogeneity.²⁶⁶ The benefit of using virtual traps are the easiness of defining trap sizes (according to cell size or cell numbers) and the ability to easily release cells (if non-adherent) from the trapping sites by altering the field strength or the light pattern. However, the electric field strength should be chosen with care to avoid harming the cells (e.g. electroporation).

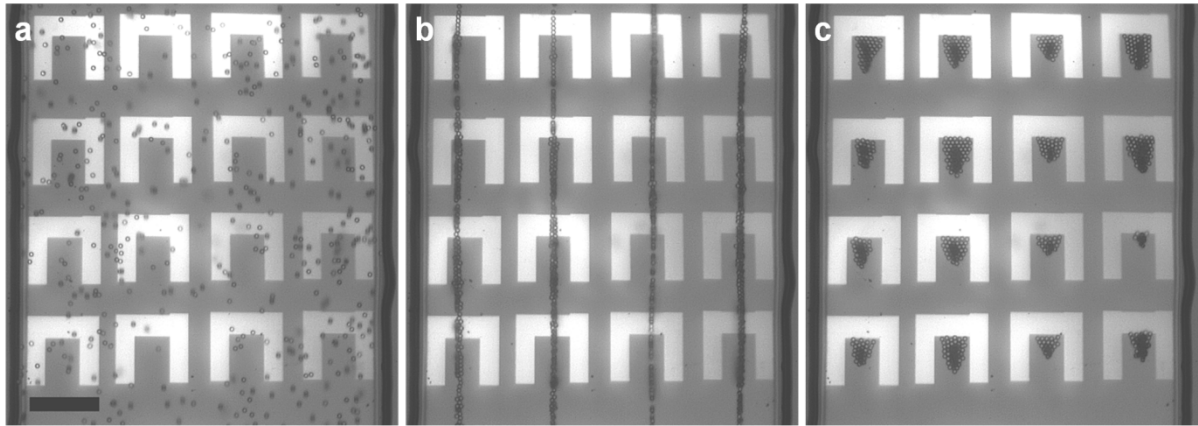


Figure 5-10: Virtual trapping sites defined by virtual electrodes for array-like capturing of 3 μm beads focussed in pressure nodes under continuous flow (flow from bottom to top). (a) Beads flowing through the microchannel. No actuation. (b) Acoustic actuation at 3rd harmonic resonance (15 V, 10.003 MHz), followed by (c) activation of OET (100 KHz, 20 V, 20x objective) to create trapping sites on demand (Scale bar: 50 μm , flow rate: 0.25 $\mu\text{l}/\text{min}$, 20x objective).

The individual control of acoustic and DEP force relative to the drag force can also be used for a sequential manipulation scheme of trapping and fusion of particle groups under continuous flow. This is demonstrated in Figure 5-11. The beads were first focussed into pressure nodes (Figure 5-11a) followed by trapping and aggregation along an oblique virtual electrode (Figure 5-11b). The DEP force and PAR force were tuned to overcome the drag force imposed on the bead with the PAR force acting as restoring force into the pressure nodes that combined with the virtual electrode angle of 30° were able to hold the particle aggregate. However, the trapping site was released by switching off the PAR force while using the negative DEP force along the angled electrode combined with the fluid drag as guiding pathway to merge particle aggregates at a trapping site at the end of the electrode within 2s. When reactivating the acoustic actuation, the merged particle clump moved back into a single pressure node.

The sequential manipulation scheme might be of interest for the area of tissue engineering in microfluidics²⁶⁷ to study the process of vascularisation in the presence of different cell types. A range of different cell types (instead of beads), each in a particular pressure node, could be merged together to form cell aggregates. The number of cell types, the concentration of the cells in each pressure node as well as the final aggregate size could be controlled using the set of externally applied forces. This is followed by seeding the aggregate into a specific location on the chip or as shown above, trapping the aggregate in virtual pockets, and investigate the cellular development.

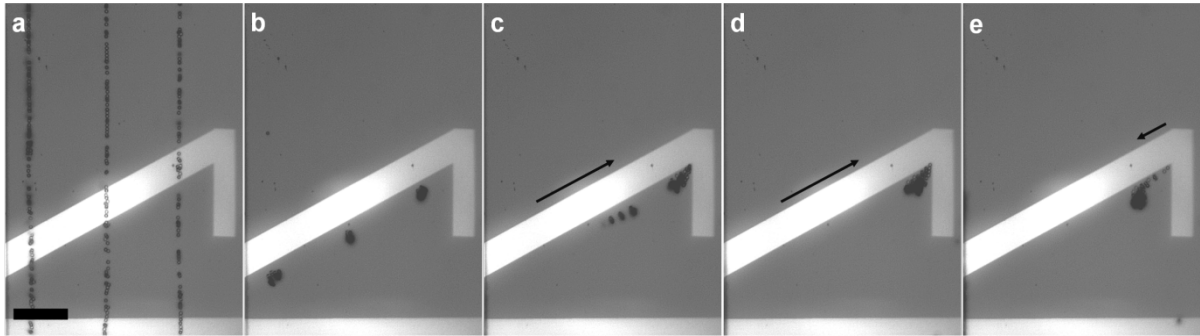


Figure 5-11: Trapping and fusion of bead aggregates along a virtual electrode (30° , $25\ \mu\text{m}$ wide) under continuous flow (flow from bottom to top). (a) Acoustic actuation using the 3rd harmonic resonance frequency (10.003 MHz, 15 V). (b) Activation of OET (17 V, 100 KHz, 20x objective) induced bead aggregation in front of the virtual electrode. (c-d) Bead aggregates released from trap after switching off acoustic actuation followed by flow induced movement along electrode which led to fusion of bead agglomerations. (e) Activation of ultrasound induced movement of fused beads back into pressure node (Scale bar: $50\ \mu\text{m}$, flow rate: $0.1\ \mu\text{l}/\text{min}$, 20x objective).

Finally, a virtual electrode was used to enable a size selective sorting of beads into a particular pressure node under continuous flow. A bead mixture containing $3\ \mu\text{m}$ beads and $6\ \mu\text{m}$ beads were hydrodynamically focussed along one side of the channel (Figure 5-12a). This was followed by applying the first harmonic resonance frequency to create a concentrated particle stream along one pressure node (Figure 5-12b). The mixture was then fractionated by activation of the oblique virtual electrode (45° , $18\ \mu\text{m}$ width) which imposed a negative DEP force onto the $6\ \mu\text{m}$ beads to overcome the PAR force and guided the beads out of the pressure plane against the pressure gradient into the adjacent pressure node (Figure 5-12c). The $3\ \mu\text{m}$ beads passed over the virtual electrode with minimal deflection as the DEP force on them is smaller and so were dominated by the drag force and remained focussed in the initial pressure node.

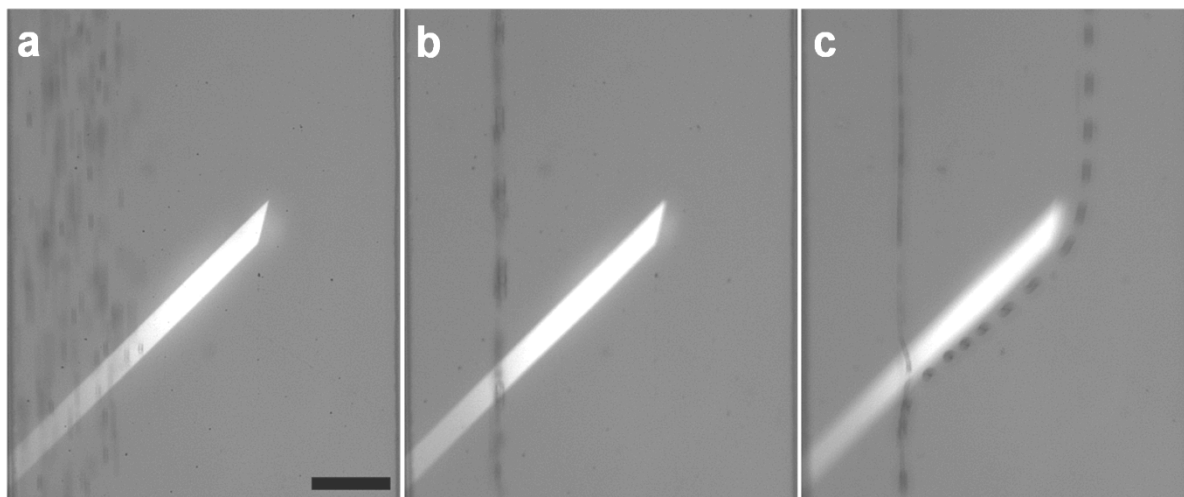


Figure 5-12: Sorting of particles into pressure node using a virtual electrode. (a) A bead mixture (3 μm and 6 μm suspended in 5 mS/m solution) was hydrodynamically focussed along one side of the channel before (b) concentrated into a pressure node created by applying the first harmonic frequency (4.782 MHz, 20V) to the OET chip with a 270 μm channel width. (c) An activated oblique virtual electrode (45°, 18 μm width, 100 KHz, 25 V, 20x objective) was used to guide 6 μm beads into the adjacent pressure node (Scale bar 50 μm , flow rate: 0.5 $\mu\text{l}/\text{min}$).

5.4. Conclusion

The combined use of OET and acoustic tweezing provides the advantage of performing localized as well as more global particle manipulation. Virtual electrodes can be applied selectively to small microchannel sections while acoustic standing wave fields stretch along the channel length when using a simple resonator design. It was demonstrated that acoustic standing wave fields were well suited to rapidly concentrate particle samples into fixed pressure nodal planes before being addressed by virtual electrodes in the form of selective sorting and guiding into channel outlets, pressure nodes or trapping and merging of particle aggregates. The application of local virtual electrodes within a microchannel section can be exploited to support a localised use of the PAR force as shown by sorting of different sized beads into virtual channels.

The experiments also revealed that particle-particle interactions arising from leakage fields, patterned electric fields and acoustic standing wave fields influence manipulation processes including particle focussing and sorting. A strategy to reduce such unwanted interactions may involve the increase in the photoconductor thickness and the introduction of an additional SAW transducer. This might reduce the amount of the field leaking into the liquid layer as well as pearl chaining effects when beads are focussed into one horizontal plane.

6. Cell lysis through the combination of electric and acoustic fields

In this chapter electric and acoustic fields are applied to perform cell lysis in a microfluidic environment. The developed platform where a surface acoustic wave transducer is combined with an OET chip can be used for continuous cell lysis with high efficiencies of > 99 %. We characterize the lysis time for cells exposed to light pulses and show that concentrating cells using pressure nodal planes in the microchannel is beneficial to improve the overall cell lysis rate. Furthermore, the OET chip can be used as a standalone system to perform true single cell lysis. Small beam spot sizes down to 2.5 μm are used to selectively lyse target cells in a dense population of cells. We also demonstrate that single cell lysis can be performed in physiological buffer with cells in suspensions or adhered to the surface of the photoconductor.

6.1. Introduction

6.1.1. Cell lysis in microfluidics

Cell lysis describes the break down of the cellular integrity. It is an essential part of sample preparation processes where intracellular molecules such as DNA, proteins or metabolites need to be released for analysis purposes. Significant effort has been applied to sensing of analytes of interest in miniaturized systems but only little is focused on integrated sample preparation steps including cell lysis. So far, in the literature microfluidics based lysis strategies are mainly based on mechanical, chemical and electrical techniques. In general, the use of microfluidic concepts has a number of promising capabilities for biological analysis. The benefits are the ability to handle very small quantities of samples and reagents, and to perform separations and detection with high resolution and sensitivity, as well as low cost, minimized chances of contamination, short analysis times and small footprints of the analytical device.^{7, 268, 269}

Mechanical lysis strategies utilized different techniques including using an ultrasound transducer or laser to create cavitation bubbles. The oscillation or sudden collapse of microbubbles create shear forces which are able to rupture the membrane of cells nearby.²⁷⁰⁻²⁷³ Alternatively, micro or nanostructures with sharp edges can be used to shear

the membrane knife-like when cells pass them due to pressure driven flow. Lysis can also be achieved by crushing cells by pressure driven membrane actuation which leads to compression, deformation and finally splitting of the cell membrane.^{274, 275}

Chemical lysis in microfluidics has been shown by applying ionic and non-ionic detergents like Triton X or SDS which disrupt the cell membrane by solubilising proteins and lipids.²⁷⁶ Laminar streams of cell sample and lytic agent can be used to trigger lysis by diffusion between the stream and along the channel length while a continuous process can be maintained.²⁷⁷ Alternatively cells can be trapped in microchannel containing hydrogel or pockets followed by perfusion with a lytic agent to induce lysis.²⁷⁸

One of the most flexible approaches is based on electrically stimulated lysis. Here strong electric fields can be used to alter the permeability of the cell membrane (more details in the next section). The concepts to integrate electrodes for lysis in microfluidics are manifold and can be adapted to special needs like lysis of large populations or even single cells. Here, microelectrode designs to localize electric field exposure or large conductive substrates can be utilized to fulfil certain requirements.²⁷⁹⁻²⁸¹. The electrical signals used are usually pulsed DC or AC fields with magnitudes of $1 \cdot 10^3$ V/cm to $1 \cdot 10^4$ V/cm. The flexible nature arises not only because of the way electrodes can be integrated into the microfluidic chip, electrodes could also be applied for a range of electrokinetic effects like dielectrophoresis, electrophoresis or electroosmosis to manipulate samples in form of separation, mixing and fractionation.

6.1.2. Electroporation of the cell membrane

Under physiological conditions the cell membrane is a good permeation barrier for ions and molecules. However, as mentioned above, the permeability can be modified using different techniques which can lead to a release of intracellular components. One of the most interesting techniques to achieve a change in the permeation is based on electric fields and is generally described as electroporation. A cell exposed to an intense external electric field experiences a change in the electrical properties of the membrane. In particular, exceeding the dielectric strength of the cell membrane due to an applied field, causes dramatic increase in the specific membrane conductivity and is accompanied with the creation of pores in the membrane.²⁸² The process is called electroporation and includes the following essential features.²⁸³ An electrical pulse is applied to a cell followed by charging of the lipid bilayer. This leads to rapid, localized structural rearrangements within the membrane and can produce water-filled membrane structures. The resulting perforation increases the ionic and molecular transport across the membrane. The natural

transmembrane potential $\Delta\varphi$ of a cell in physiological conditions is approximately $\sim 60\text{mV}$.²⁸² An applied electric field causes an accumulation of intra- and extracellular charges. While the interior of the cell is at an equipotential, the charge distribution at the membrane interface generates a potential much larger than that (Figure 6-1).

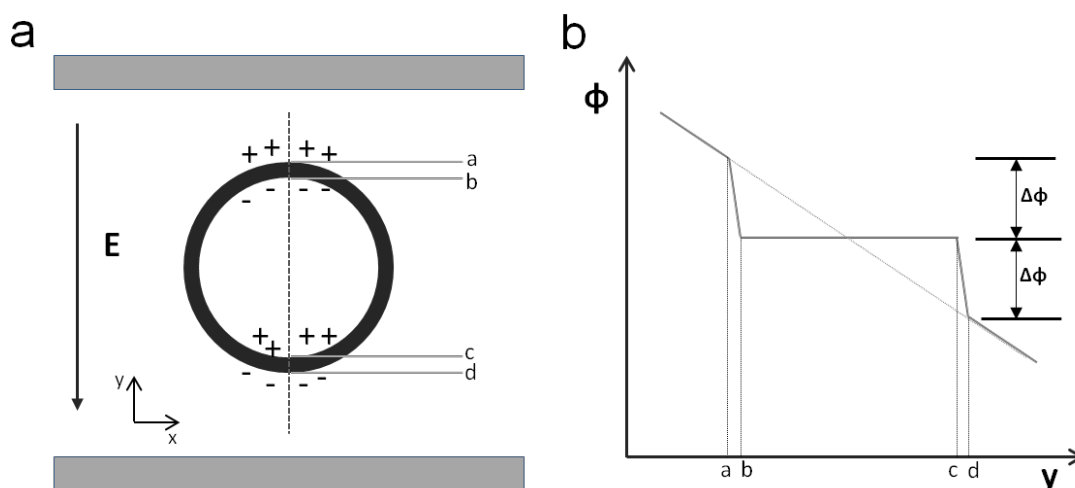


Figure 6-1: (a) Schematic of a cell exposed to an external electric field applied between two parallel electrodes and (b) corresponding potential along the y-axis of the cell highlighting the voltage drop across the membrane.

Depending on the cell type, shape and size the imposed electric field can result in reversible and irreversible pore formation. Reversible behaviour is often observed for $\Delta\varphi < 1\text{V}$, while irreversible damage takes place for voltage drops of $\Delta\varphi \gg 1\text{V}$.²⁸⁴ A schematic of the occurring potential change between two electrodes in the presence of a cell is shown in Figure 6-1. The transmembrane potential $\Delta\varphi$ of cell of radius r due to an external field E can be described as²⁸⁴

$$\Delta\varphi = 1.5rE\cos\theta \quad (6.1)$$

where θ is the angle between the site on the cell membrane where $\Delta\varphi$ is measured. Experiments on planar lipid bilayers have shown that electroporation is a stochastic phenomenon.²⁸⁵ There is a critical transmembrane potential $\Delta\varphi$ at which the probability for pore formation becomes large.²⁸⁶ The formation of pores is a fast process and occurs in time scales of nanoseconds to microseconds^{283, 287} and recovery of the membrane by resealing processes is possible but depending on the applied electric field pulse and amplitude. The time for membrane recovery is on a time scale of seconds.²⁸⁸ However, extended exposure to high electric fields leads to irreversible electroporation. Here, increased pore density and

size can cause rupture of portions of the membrane as well as chemical imbalances promote increased molecular transport across these perforations which results in cell lysis.²⁸⁵ Colloid osmotic pressure as the result of poreformation can cause swelling of cells up to mechanical loads where membrane rupture occurs.

Electropermeabilization is often used to describe the molecular transport across the electroperforated membrane. But it has to be noted that more processes are involved. One of the main driving forces is diffusion, but during an electrical pulse localized electrophoresis and electro-osmosis dominate.²⁸³ For instance, diffusion plays a major role in the transport of small molecules.²⁸⁹ Electrophoresis effects are responsible for the transport of macromolecules like DNA.²⁹⁰ In general, electropermeabilization has broad applications. The advantage of cell membrane recovery after a electric stimulation is used for transfection experiments like localised gene therapy^{291, 292}, drug delivery²⁹³ or loading of dyes or tracer²⁹⁴ into cells.

6.1.3. Light induced electric fields for lysis and electroporation

A few studies reported the use of light induced electroporation and lysis and should be mentioned within the scope of this thesis. An ITO substrate and a photoconductor based on amorphous silicon were used in all of these studies. Valley *et al.* showed electroporation of Hela cells in a batch-like microfluidic OET chip.¹⁰⁴ A 5 s pulse (field strength of 1.5 kV/cm) at 100 KHz was used to reversibly porate cells and trigger the uptake of propidium iodide. The study also showed that cell viability could be maintained when cells were exposed to field strength in the range of 1.4 kV/cm to 2.3 kV/cm. A device for batch mode and continuous lysis of cells has been shown by Lin *et al.*^{105, 192} Lysis of single fibroblast cells was demonstrated by applying an ac signal of 20 KHz with an amplitude of 9 V during batch mode actuation. An optical power of 155 kW/cm² combined with an illumination area of > 60 μm (~ 4 times the size of the cell and hence although only one cell is lysed at a time this is not single cell precision as near neighbours, were there any, would also have been lysed) resulted in lysis efficiencies of 100 %. A continuous approach was shown by using an OET chip with SU8 microchannel. A 60 μm SU8 layer was spincoated onto the ITO glass substrate, exposed and developed to set the channel structure. The photoconductor substrate was placed on top of the SU8 channel and epoxy was used to seal the chip around the substrate edges. The microchannel consisted of 3 inlets and one outlet channel. Fibroblast cell were injected by a syringe pump and hydrodynamically focussed with sample flow rates of 0.3 $\mu\text{l}/\text{min}$. A light pattern of 150 μm length was projected onto the photoconductor to induce lysis in fibroblast cells. The exposure time necessary to induce lysis was found to be 250 ms, corresponding to cell velocities of 585 $\mu\text{m}/\text{s}$. A lysis rate of

93.8 % (45 out of 48 cells) was achieved when an optical power of 11 W/cm² and an amplitude of 10 V were used (no information given about frequency). Last but not least, a novel lysis approach has been shown by Kremer *et al.*¹⁰⁶ In a conventional OET chip, enrichment of white blood cells and trypanosomes by lysis of red blood cells was demonstrated. For frequencies lower than 20 KHz and an amplitude of 15 V, differences in the transmembrane potential which come about due to the difference in the cells shapes triggered the lysis process.

6.2. Material and Methods

6.2.1. SAW transducer and OET chip - setup

In this work lysis experiments were performed in an OET chip consisting of a straight microchannel which was placed on the piezoelectric substrate next to the SAW transducer to enable electric and acoustic actuation (Figure 6-2a). The OET chip was actuated with an AC signal of 5 V to 20 V at 25 KHz, while the SAW transducer was driven at the fundamental frequency at higher harmonics of the OET chip with an applied voltage of 20 V. The lysis of cells was performed under continuous flow and static fluid conditions. For the continuous lysis experiments an electrode gap of 15 µm were used (Figure 6-2b), while the single cell lysis experiments were performed in an OET chip with a gap of 35 µm. The Olympus microscope (BX53) equipped with an Orca Flash4.0 CMOS-camera (Hamamatsu, Japan) was used for monitoring the lysis experiments. PowerPoint was used to create fixed and dynamic image patterns for virtual electrodes. A range of control experiments were performed to quantify cell lysis under influence of the acoustic field and the leaked electric field without selective illumination of the photoconductor. Furthermore, efficiency of pure light induced lysis was compared with combined electric and acoustic actuation of blood samples.

6.2.2. Cells and sample preparation

Human blood samples were provided by the blood transfusion service and stored at 4°C prior usage. Jurkat cells were cultured in RPMI growth media containing 10 % serum, at 37 °C (5 % CO₂). Jurkat and blood cells were washed one time in PBS, followed by three washing steps in a buffer solution made of 8 % sucrose, 0.3% glucose and 3 mM Hepes (pH 7.4) at 1500 rpm for 5 mins. This buffer gives a solution with osmotic pressure of 310 mOsm and a conductivity of 10 mS/m. For the experiments in PBS buffer, blood cells were washed one time in PBS and then resuspended. For the single cell lysis and batch experiments blood samples were manually injected using a pipette. MCF 7 cells were cultured in cell media, DMEM, containing 10 % serum, 4.5 g/l Glucose, L-Glutamine, Penicillin and

Streptomycin. After injection of the MCF 7 cells, the OET chip was placed in a petri dish and incubated over night at 37 °C (5 % CO₂). For continuous lysis experiments blood samples were injected using a syringe pump (NE-1000, New Era Pump Systems, USA. Continuous lysis experiments were carried out at 5 µl/min and volumes of 10 µl were sampled shortly after injection and then used to quantify cell concentrations in a haemocytometer (Neubauer, Marienfeld, Germany).

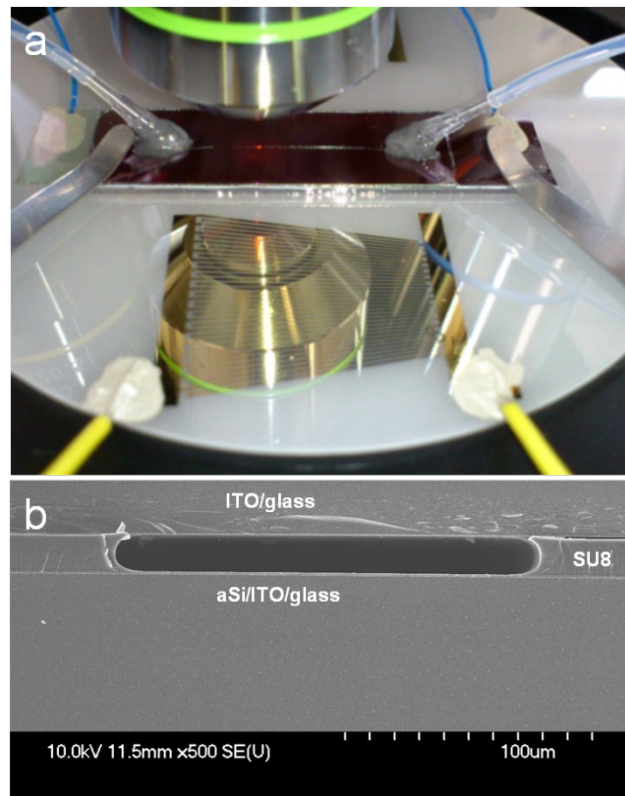


Figure 6-2: (a) SAW transducer with OET chip clamped on piezoelectric wafer for combined acoustic and electrical actuation. (b) Cross-section of OET channel chip showing sandwiched SU8 3025 between ITO/glass and aSi/ITO/glass substrates to produce a 15 µm spacer.

6.2.3. Image analysis and modelling of transmembrane potentials

ImageJ was used to quantify the lysis time. The frames of video sequences were converted to gray scale images. The threshold function was used to convert all frames into binary images highlighting cells as dark spots and defining the background as white. Cells, as region of interests were marked by drawing an outline. Finally, the average pixel intensity was monitored using the time versus intensity plot function to quantify cell lysis times. Simulations for electric field strength and transmembrane potentials in RBCs were performed using COMSOL (3.5) software. A 2D cross section model of the OET chips (15

μm and $35 \mu\text{m}$) and a single-shelled blood cell were used to simulate electric fields and transmembrane potentials. Table 6-1 and 6-2 show the parameters which were used for the models. The 20x and 40x objectives were used for the continuous and single cell lysis experiments, respectively.

Table 6-1: Parameter used in the model for continuous lysis experiments.

Channel height	5 – 300 μm	Conductivity aSi (light state)	$8.5 \cdot 10^{-4} \text{ S/m}$
Frequency	25 kHz	Permittivity of aSi	14
Amplitude	5 V, 10 V, 20 V	Cell membrane thickness	7 nm
Conductivity cell suspension	0.01 S/m	Conductivity cell membrane	$1 \cdot 10^{-6} \text{ S/m}$
Permittivity cell suspension	79	Permittivity cell membrane	12.5
Thickness amorphous silicon	1 μm	Conductivity cytosol	0.8 S/m
Conductivity aSi (dark state)	$1.1 \cdot 10^{-5} \text{ S/m}$	Permittivity cytosol	60

Table 6-2: Parameter used in the model for single cell lysis experiments.

Channel height	25 - 300 μm	Conductivity aSi (light state)	$1.4 \cdot 10^{-3} \text{ S/m}$
Frequency	25 kHz	Permittivity of aSi	14
Amplitude	20 V	Cell membrane thickness	7 nm
Conductivity cell suspension	0.01 S/m, 1.4 S/m	Conductivity cell membrane	$1 \cdot 10^{-6} \text{ S/m}$
Permittivity cell suspension	79	Permittivity cell membrane	12.5
Thickness amorphous silicon	1 μm	Conductivity cytosol	0.8 S/m
Conductivity aSi (dark state)	$1.8 \cdot 10^{-5} \text{ S/m}$	Permittivity cytosol	60

6.3. Results and Discussion

6.3.1. Electric field characterisation in OET chip for continuous lysis

The pore formation in cellular membranes is dependent on the electric field strength in the sample liquid and the resulting voltage drop across the cell membrane. A certain threshold value is necessary to induce irreversible damage and cell lysis. Below this threshold the applied electric field strength may result in electroporation with recovery of the cell membrane. For cell lysis, the field strength is in the range of 1 kV/cm to 10 kV/cm. An analytical model developed in COMSOL was used to investigate the electric field in the OET chip for a frequency of 25 KHz. The influence of the liquid gap between the photoconductor and ITO electrode and the illumination length of the virtual electrodes were modelled to characterize the device response. The latter is especially of importance for microfluidic cell lysis. OET is mainly used to create nonuniform electric fields using small localized illumination patterns. Here, the field strength changes significantly between the electrodes which is favourable for dielectrophoretic manipulation. We modelled the influence of the size of the virtual electrode produced by the light pattern. In Figure 6-3a and 6-3b, a comparison of a small (2.5 μm) and wide (50 μm) light pattern in a 15 μm high microchannel is shown. The electric field strength changes exponentially along the liquid gap between the electrodes for 2.5 μm light pattern. The intensity of the field is high (12 kV/cm) close to surface of the photoconductor but drops to values >2 kV/cm in a few micrometers. However, this situation changes when the light pattern size is increased (Figure 6-3b). The field intensity at the edge stays highly nonuniform but in the centre of the light pattern a homogenous field is obtained. In Figure 6-3c the influence of the change in the illumination length is shown. The nonuniformity of the field along the microchannel height disappears for increasing light patterns and converges to a constant value (7 kV/cm). This result is important considering that a cell suspension occupies the whole volume when pumped through the microchannel.

Furthermore, the dependency of the electric field strength for a change in the vertical microchannel dimensions was investigated. A wide illumination pattern and alterations in the distance between the ITO electrode and the photoconductor from 5 μm to 300 μm was considered. In Figure 6-3d, it can be seen, that the intensity across the channel height drops sharply within 50 μm and leads to values smaller than 1 kV/cm for lateral channel dimensions higher than 100 μm and 200 μm for voltages of 10 V and 20 V, respectively. A low conductivity solution of 10 mS/m was used in this simulation. However, it has to be mentioned, that increasing the liquid conductivity results in further decrease of the electric field strength as more voltage drops across the photoconductor. In Figure 6-4, the change of the field intensity for increasing liquid conductivity is simulated for a microchannel with 15

μm and $100\ \mu\text{m}$ gap. For low medium conductivities ($< 100\ \text{mS/m}$) the vertical channel dimensions influence the field intensity significantly and limit the application of high field strengths. Therefore, shallow microchannels should be used to be able to adjust the field values according to the needs. For the experiments aiming to do continuous cell lysis, the protocol for SU8 channels of heights down to $15\ \mu\text{m}$ was applied.

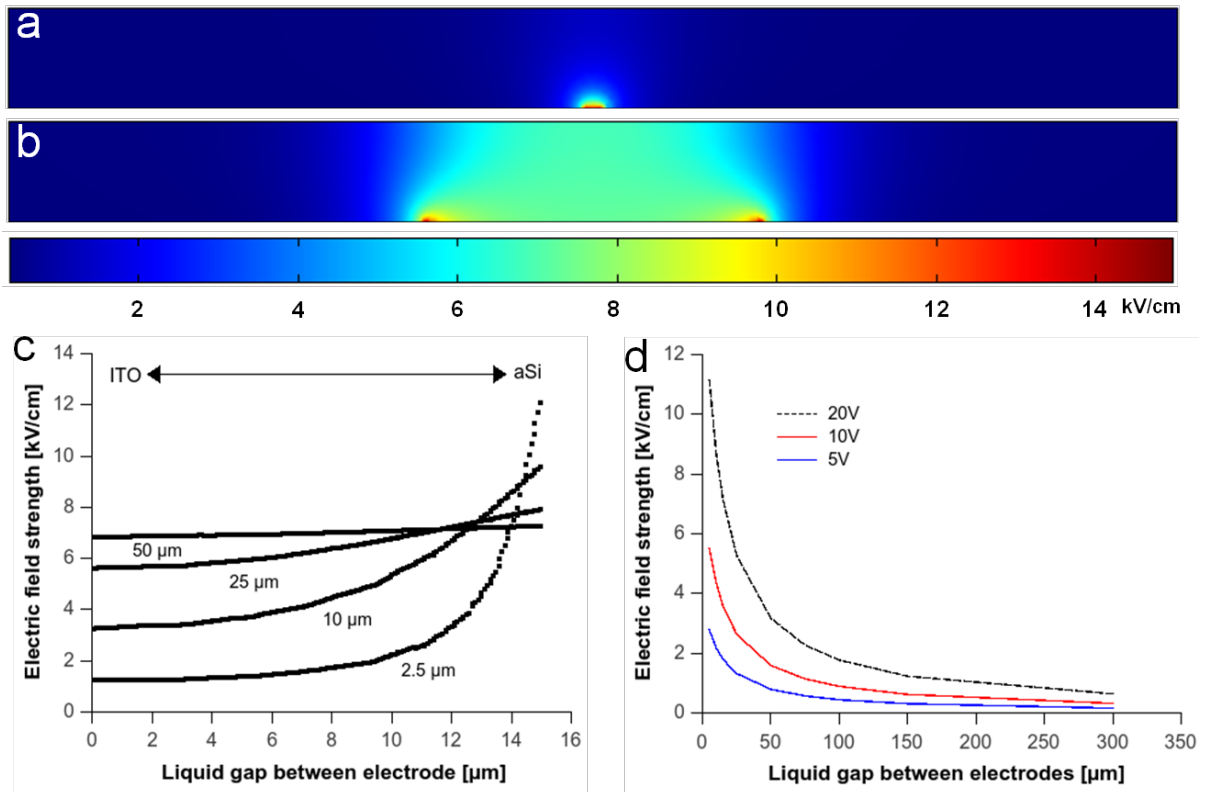


Figure 6-3: (a-b) Intensity of the electric field across a $15\ \mu\text{m}$ liquid gap for short ($2.5\ \mu\text{m}$) and wide ($50\ \mu\text{m}$) photoconductor illuminations (20V , $25\ \text{KHz}$, $10\ \text{mS/m}$). (c) Electric field strength across a $15\ \mu\text{m}$ liquid gap for different illumination lengths ($25\ \text{KHz}$, $20\ \text{V}$, $10\ \text{mS/m}$) determined from the center of the light pattern. (d) Electric field strength versus liquid gap within the OET chip for a range of voltages when a wide field illumination ($> 50\ \mu\text{m}$) is applied at $25\ \text{KHz}$, $10\ \text{mS/m}$.

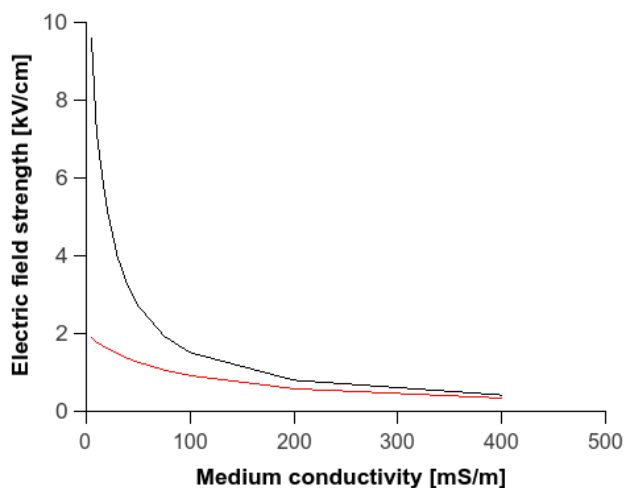


Figure 6-4: Electric field strength versus medium conductivity for a 15 μm (black line) and 100 μm (red line) thick microchannel illuminated with a wide light pattern (25 KHz, 20V).

6.3.2. Modelling the transmembrane voltage in OET

A cell exposed to an external electric field of a certain field strength experience a change in the transmembrane potential. The accumulation of intra- and extracellular charges increases the electrical conductivity of the cell membrane. Under physiological conditions the transmembrane potential is approximately $\sim 60\text{mV}$. However, strong electric fields produce voltage drops across the membrane of several volts. Depending on the cell type, shape and size, changes in the transmembrane potential can cause reversible electroporation of the bilipid layer. The induced accumulation of charges at the interfaces leads to compression pressures which initiate pore formation. When the field intensity is increased even further, it is understood that irreversible chemical modification by ionization occurs which leads to a dielectric breakdown. This destroys the cell and results in lysis. The average transmembrane potential do create irreversible pore formation is $\sim 1\text{ V}$).²⁸²

We used a single-shell model to investigate the transmembrane potential of a cell exposed to a field in the OET chip. The physical values for permittivity and conductivity of the cell membrane and the cell interior can be found in table 6-1. A membrane thickness of 7 nm was used for the simulations. In Figure 6-5a, the voltage change in the presence of a cell is shown. In this case, the cell is centred in the volume of the liquid gap of a 15 μm high microchannel. The voltage drop across the membrane is determined along the cross-section centre of the cell. In Figure 6-5b the potential change along the channel height for an AC signal of 20V and 25 kHz (10mS/m) and a wide illumination pattern is shown. Under these conditions the electric field strength is 6.2 kV/cm and induces a transmembrane potential of 1.7 V. This is well above the mentioned average threshold of 1 V and therefore, this chip

configuration should be suitable for cell lysis. However, it has to be noted that the microchannel height as well as the position of the cell and the illumination pattern influence the transmembrane potential. An increase in a few tenth of micrometer in the liquid gap between the electrodes reduces the voltage drop significantly for a cell centered in the volume (Figure 6-6a). For instance, the transmembrane potential in a 100 μm high microchannel is only 420 mV. Furthermore, the use of illumination patterns of a few micrometer produce very nonuniform electric fields with high field intensities close to the surface of the photoconductor and decrease sharply across the channel height compared to wide patterns. The transmembrane potential of a cell with changing vertical position relative to the photoconductor surface in a 15 μm high microchannel was determined. In Figure 6-6b, the case of 2.5 μm and 50 μm wide illumination pattern are shown. Due to high electric field strength in the volume of the chip, a wide pattern can induce a sufficient membrane potential, regardless of the position of the cell. However, the position of the cell becomes important when the light pattern is reduced to a couple of micrometer. The potential drops below 1 V for distances $> 3 \mu\text{m}$ relative to the surface.

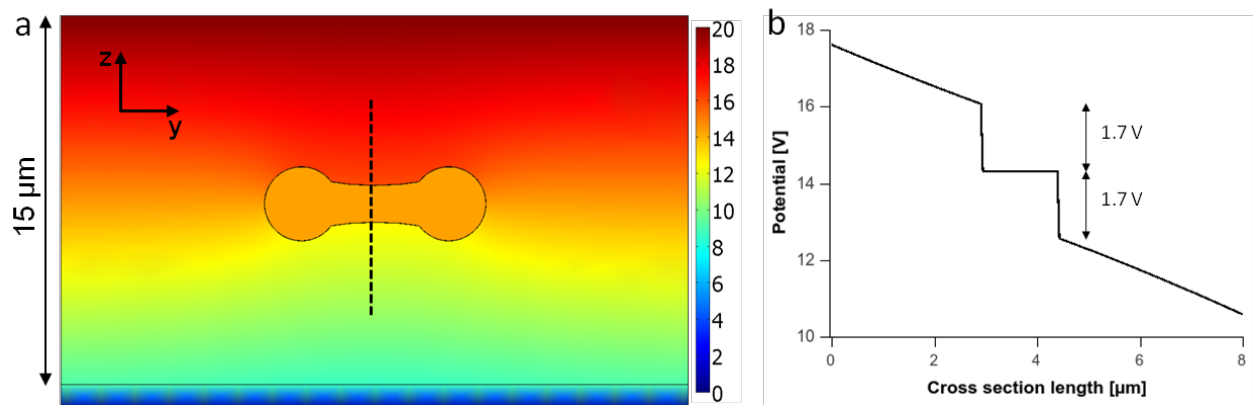


Figure 6-5: (a) Simulated potential plot (in V) of 15 μm high microchannel in the presence of a red blood cell for 20 V, 25 KHz, 10mS/m. (b) Cross section plot through the centre of a red blood cell (indicated in Figure 6-5a as dotted line) showing voltage drop of 1.7 V across the membrane (20 V, 25 KHz, 10 mS/m).

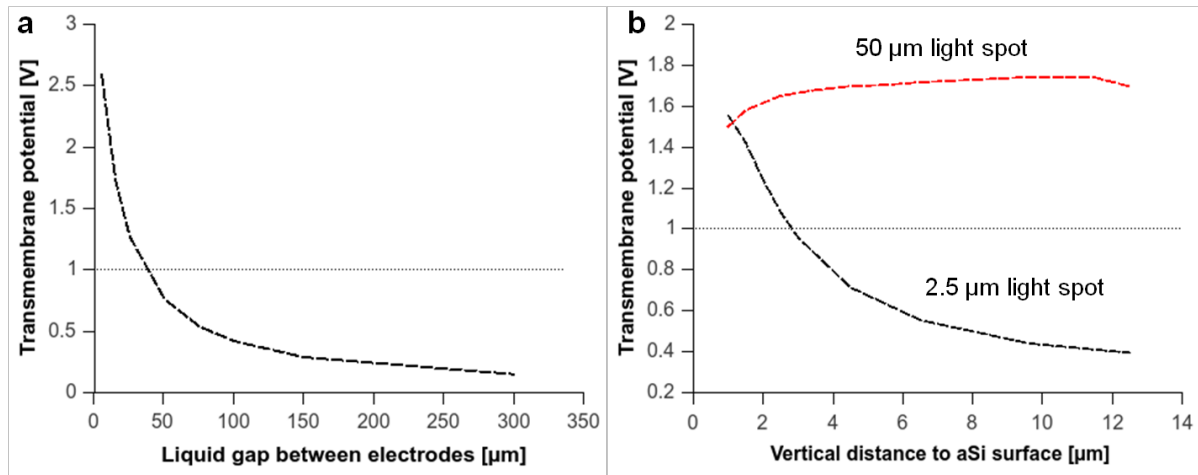


Figure 6-6: (a) Simulated transmembrane potential for a cell centred in a microchannel with changing vertical dimensions (Illumination pattern: 50 μm , 20 V, 25 KHz, 10 mS/m. (b) Influence of a 2.5 μm light spot and the vertical cell position on the transmembrane potential compared with a 50 μm light spot. Dotted line represents the threshold voltage for irreversible pore formation.

6.3.3. Cell lysis under static conditions to investigate time scales

A continuous exposure of blood cells to light induced electric fields of appropriate magnitude leads to irreversible electroporation of the membrane. Using a conventional OET chip where spacer made of double sided tape between the electrodes is about 100 μm , it is possible to achieve lysis. In Figure 6-7(a-c) a wide illumination pattern is applied to a suspension of red blood cells in a typical buffer solution of 10 mS/m. However, the lysis efficiency is dependent on the position of the cell. It has been shown that cells floating above the surface experience lower electric field strength without being lysed.¹⁰⁶ Furthermore, a negative DEP force can act on cells causing them to escape from high electric field regions leading to unsuccessful lysis. Therefore a settling time needs to be considered (5 mins) before treating the sample. This increases the handling time and lowers the throughput, despite wide light patterns which are able to cover hundred of cells. A continuous approach with shallow microchannels to create high field strengths across the microchannel height is therefore desirable to apply. First, it was shown that floating cells can be lysed in an OET chip of narrow vertical dimensions. Second, the average lysis time and efficiency for blood cells after exposure to light pulses of 10 ms, 100 ms and 500 ms as well as different amplitudes was determined. These experiments were conducted under static condition for an easier observation of the lysis process over time. This approach is reasonable due to the fact that wide illumination patterns in narrow microchannel produce relative homogenous field strengths within the lysis area and therefore transmembrane potentials are fairly independent of the cell position

relative to the photoconductor surface. In contrast, small light pattern induce larger electric field gradients strongly pronounced along the edge of a light pattern.

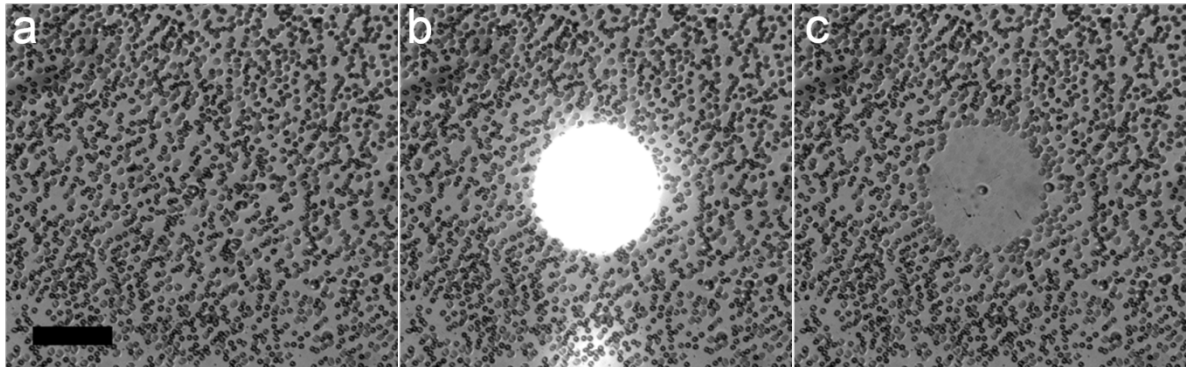


Figure 6-7: Conventional OET device made by double sided tape creating a liquid gap of about 100 μm between the electrodes. (a) Homogeneous distribution of red blood cells settled on the photoconductor (b) Light spot and a electric signal of 20 V at 25 KHz was applied. (c) Lysis was achieved after ~ 60 s of exposure to the electric field. Scale bar: 100 μm

To verify the ability of lysis of cells floating above the surface, blood cells were injected into the chip and a low flow rate with cell velocities of ~ 10 $\mu\text{m/s}$ was applied. Instead of a constant exposure which would restrict cell observation a light pulse of 100 ms was applied and the cells were monitored over time. In Figure 6-8 a sequence of frames is shown where two red blood cells flowing along the microchannel before exposure to the light induced electric field. After the pulse a change in the contrast of the cell could be observed, indicating the formation of pores and release of haemoglobin. However, considering the experimental condition (25 kHz, 10 mS/m), a negative DEP force can cause lifting of cells towards the top electrode, and shifting them out focus giving the impression of a changing contrast. To make sure lysis is observed, the focus was changed towards a higher plane. A change in the plane could not be observed which indicates that the field in the centre of the light pattern is rather uniform.

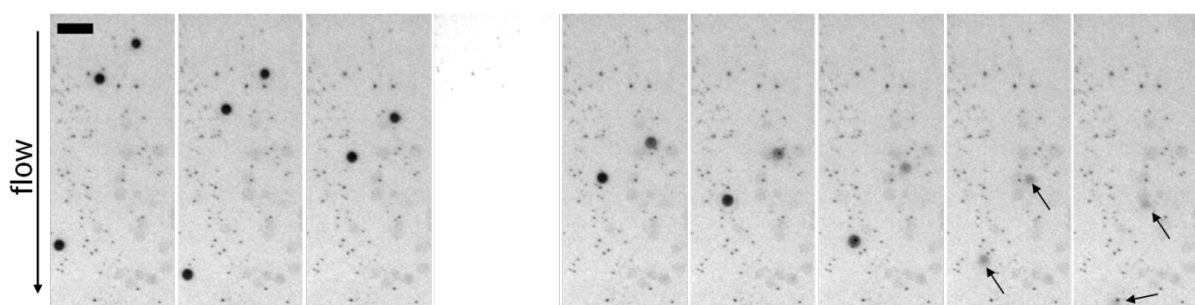


Figure 6-8: Lysis of red blood cells floating above the surface. Lysis was triggered by 100 ms light pulse and an applied electrical signal of 25 KHz and 10 V in 10 mS/m conductivity buffer

Based on these result we investigated the lysis time of red blood cell lysis depending on a light pulse generated by the data projector. The results gave guidance for the continuous

lysis approach where the exposure time depends on the applied flow rate. To quantify the lysis time videos were recorded and analysed using ImageJ. First, the video frame sequences were converted to gray scale images. Then, the threshold function was used to convert all frames into binary images highlighting cells as dark spots and defining the background as white (Figure 6-9). Here, a cell was considered as lysed when the mean pixel intensity of the image area defined by the cell differs less than 8% from the mean background intensity. The threshold value was set according to this definition and a cell, as region of interest (ROI), were marked by drawing an outline. Finally, the average pixel intensity in the ROI is monitored using the time versus intensity plot function to quantify cell lysis times.

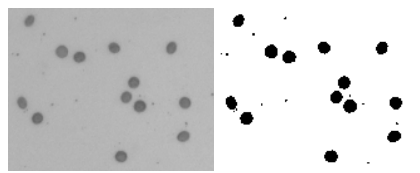


Figure 6-9: Converting of greyscale image to binary image by threshold functions in ImageJ.

An example of the intensity versus time plot is shown for two target cells in Figure 6-10. A 100 ms light pulse at 25 kHz, 20 V was applied to trigger the formation of pores and induce lysis. The pulse was recognized as a sudden intensity change in the plot after 2.3 s. To compare the pixel intensity change with the actual image of the cells (original image and thresholded), snapshots for particular time points are shown. Only after a significant change in the average pixel intensity (defined by the threshold), which was associate with the lysis of the cell, the progress of lysis over time was monitored and after approximately 9.4 s since the start of monitoring, it can be clearly seen that cells are hardly indistinguishable and complete lysis was achieved. Between the time points a and b in Figure 6-10 no difference was made despite intensity differences in the original image. This was because of the threshold being set to a higher value to assure only significant changes in the cell's pixel intensity can be associated with irreversible lysis in the end. For instance, the time points b and c showed significant differences in the pixel intensities however, time point c was still not considered as being lysed due to the threshold settings. If the cell's intensity would not change further than seen in time point c, the cell cannot be considered as lysed but rather being reversible porated with recovering of the membrane.

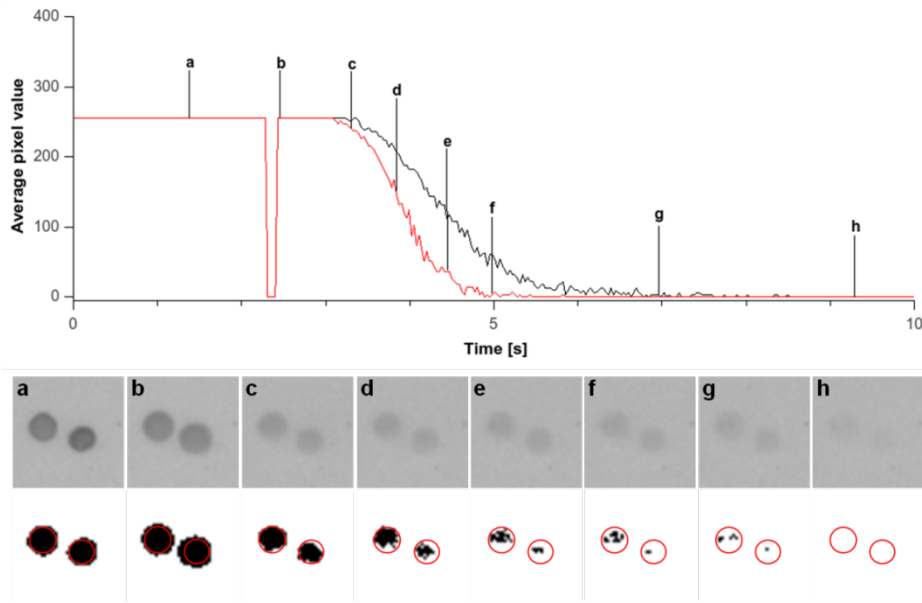


Figure 6-10: Example for time versus intensity plot monitored for two red blood cells after a 100 ms light pulse at 25 KHz, 20 V in 10 mS/m buffer. Sequence below graph shows lysis stages according to numbering in graph for original images and threshold image.

Besides 100 ms pulses, 10 ms and 500 ms pulses were used to investigate the influence of shortened and prolonged exposure to high electric field strengths. Figure 6-11a shows an example plot with typical time ranges for the applied pulses. It can be seen that an increased exposure led to a decrease in the lysis time. However, despite different pulse times, 100% lysis was achieved in all cases. The time for lysis showed significant deviations for 10 ms (10 s) and 100 ms (7 s) pulses. On one hand this could be due to the fact that the population of cells was heterogeneous. The age of the blood cells deviates in a sample. A blood cell has a life span in the body of ~ 120 days. During that time its durability decreases due to repeated large deformations when circulating through microvessels.²⁹⁵ The vertical positions of the cell should not affect the electric field strength when using wide light patterns (see above). But cells close to the edge of the virtual electrode can experience electric fields which are significant higher. Another important reason was found when the light pulse generated by the projector was analysed. For instance, during a 10 ms pulse, the illumination area was not constant. Cells in the target area were actually exposed for times > 10 ms. Figure 6-12 shows an example of 10 ms light pulse for an illumination area of $1 \cdot 10^5 \mu\text{m}^2$.

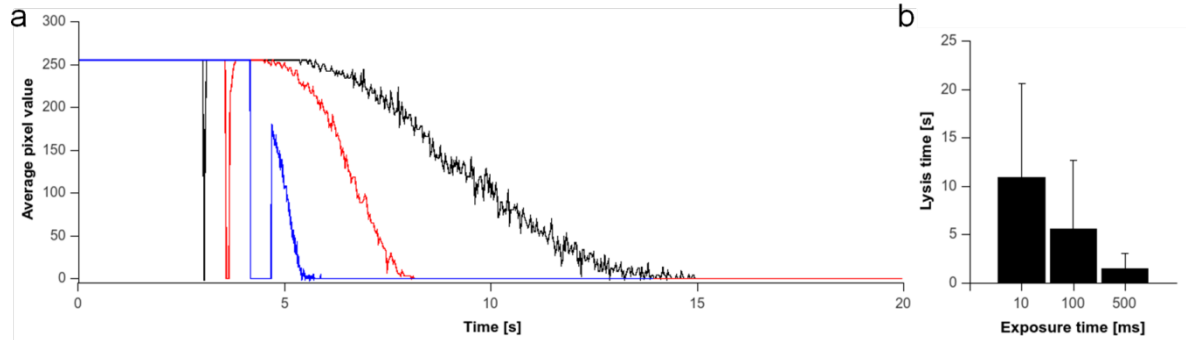


Figure 6-11: Lysis time of red blood cells for different exposure times. (a) Example pixel intensity versus time plot for 10 ms (black), 100 ms (red) and 500 ms (blue) pulse at 20 V, 25 KHz in 10 mS/m buffer. (b) Average lysis time of red blood cells for different exposure times at 25 KHz, 20 V, 10 mS/m.

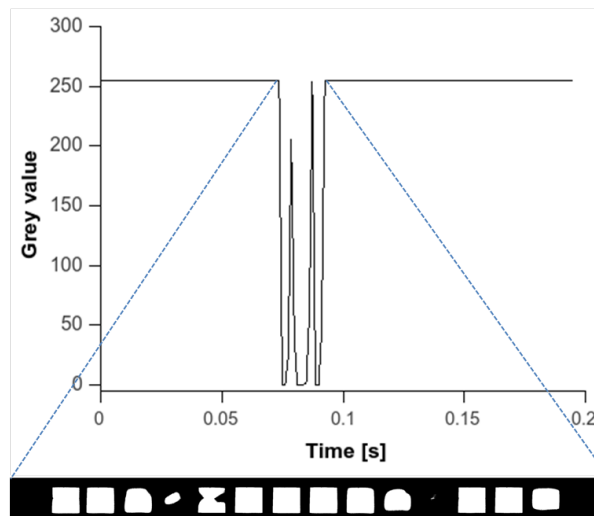


Figure 6-12: Light pulse time of 10 ms and the corresponding illumination area was not homogenous over time.

In general, the lysis time can be improved with an increased exposure to the electric field. When a 500 ms pulse was applied the average cells lysis time was 1.1 s. But in several cases, the lysis was complete within the pulse length and lysis time was set to 0.5 s. This indicates that a further increase in the exposure time was not necessary under these conditions as complete lysis will be achieved within the duration of the pulse. Only an increase in the amplitude to elevate the transmembrane potential might improve the lysis time. The physical difference in the cell after different exposure times can be related to the pore formation process. The density and size of the pores can be increased with an extended exposure as well as irreversible changes in the membrane.²⁹⁶ As mentioned in the beginning, during the pulse mechanism such as electrophoresis or electro-osmosis dominate the movement of molecules through the cell membrane.²⁸³ Hence, longer pulses enhance the molecular transport and can decrease the lysis time.

The influence of the amplitude was investigated by applying voltages of 5 V and 10 V to the cell samples. Exposure times of 10 ms, 100 ms and 500 ms were used again and lysis times

were determined. For a voltage of 5 V it was found that lysis was not complete independent of the used exposure durations. In Figure 6-13 an example plot is given where the pixel intensity was monitored after applying a 100 ms pulse with applied voltages of 5 V and 20 V. A contrast and shape change can be observed for an amplitude of 5 V. However, compared to experiments using 20 V amplitudes, the average pixel intensity kept constant over time because of the threshold settings. The cell is not considered as being lysed. When a voltage of 10 V was applied instead, complete lysis was observed for all exposure times. The difference in the lysis times compared to the previous experiment (at 20 V) was found to be marginal and within the deviation. The incomplete lysis when applying a voltage of 5 V can be explained by reversible electroporation. The external electric field for 5 V amplitude showed an induced transmembrane potential of 440 mV (simulated) when the cell was centred in the middle of the channel. This was well below the average breakdown value, but apparently, enough for poration of the membrane. It can be assumed that a further increase in the exposure time results in lysis, eventually. The observed change in the cell was based on colloid osmotic haemolysis which leads to molecular transport across the membrane after increasing the permeability by electroporation. However, the membrane can recover under these conditions by resealing of the formed pores. The transport of molecules is stopped and no further change occurs. Nevertheless, in these experiments the shape of the cells seemed to be irreversibly altered. The water influx increased the cell volume while transforming from a biconcave to a spherical shape could be observed.

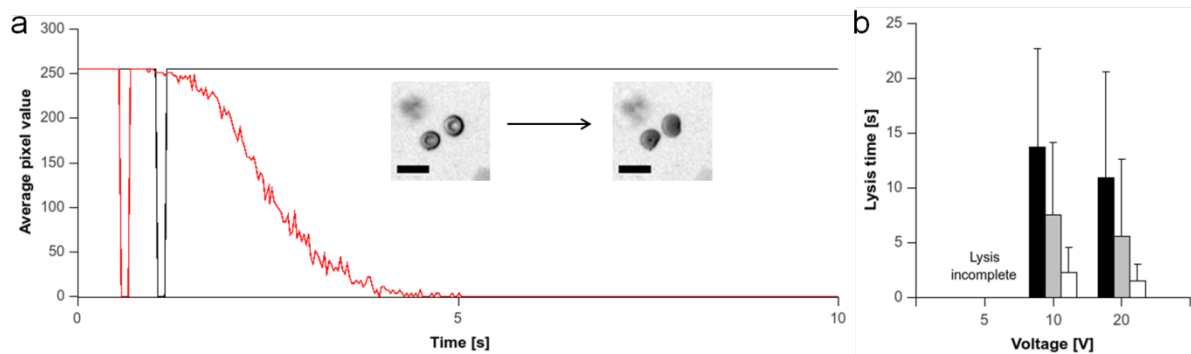


Figure 6-13: Lysis time of RBC for different voltages and exposure times. (a) Example pixel intensity versus time plot for 100 ms pulses with applied voltage of 5 V (black) and 20 V (red). Inset shows RBCs after 5 V, 100 ms exposure. Lysis was not complete, indicating reversible electroporation. (b) Lysis times for different applied voltages and corresponding exposure times of 10 ms (black bar), 100 ms (grey bar) 500 ms (white bar). A frequency of 25 KHz was used.

Figure 6-14 depicts this transformation. A high resolution image sequence of red blood cells treated with a light pulse is shown. The typical bi-concave discoid shape of an erythrocyte is the result of an interaction between the membrane and the cytoskeleton. The cytoskeleton consists of a two-dimensional protein network called spectrin. The contact between the

network and the membrane is realised by transmembrane and peripheral proteins. A disruption of these connection points results in morphological changes.²⁹⁵ Electroporation of the membrane seemed to affect this interaction even at lower transmembrane voltages.

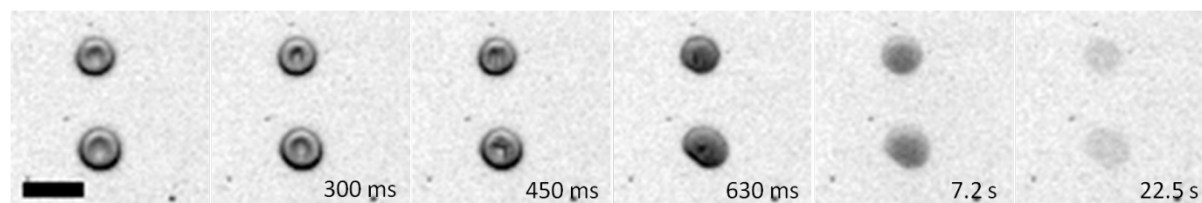


Figure 6-14: Change of red blood cell morphology after light pulse (25 KHz, 20 V, 10 ms pulse). Scale bar is 10 μm .

When the voltage was increased to 10 V, 100 % lysis was achieved. Simulations showed a transmembrane voltage of 880 mV when the cell was centred in the middle of the channel. This value was lower than the average transmembrane potential for irreversible electroporation. However, the timescale of the pulse combined with the elevated transmembrane potential seemed to be the reason for lysis when compared to the results using 5 V amplitude. The dielectric strength of the cell membrane depends both on the amplitude and on the length of the applied electric field.²⁸² Also, in this static case, the cell was closer to the photoconductor surface than depicted in Figure 6-5a due to cell settling. When a distance of 100 nm was considered the potential across the membrane increased to 1.03 V. This value agreed with the obtained results regarding lysis efficiency, but does not explain the marginal difference in the lysis times towards an amplitude of 20 V. A possible explanation can be given when comparing these results with studies on planar bilipid layers where the membrane life time has been investigated depending on the induced transmembrane voltage.^{297 298} Here, the membrane life time was defined as time before a significant current change across the membrane was measured. This was associated with the rupture of the membrane as a whole. In these experiments it has been shown that there was linear behaviour between the transmembrane voltage and the membrane life time in the range of 300 mV to 700 mV. However, a further increase in the membrane voltage resulted in no significant decrease in the membrane life time. This could suggest that a saturation of membrane ruptures or pore formation was reached for a particular transmembrane voltage. Only an increase in pulse duration changes lysis times like it is seen in Figure 6-13b and this can be associated with increased molecular transport mechanism across the membrane and the growth of pores.

6.3.4. Jurkat cell lysis compared to red blood cell.

Red blood cells are fairly small and unique in shape compared to other mammalian cells in suspension. For instance, white blood cells have a spherical shape and the radius ranges from 10 μm to 20 μm depending on the type. The size of the cell determines the induced transmembrane potential. According to equation 6.1, the transmembrane potential is proportional to the radius of the cell. Lysis experiments with Jurkat cells were conducted and lysis times were compared with the one obtained for red blood cells. Jurkat cells are human immortalized line of T lymphocyte cells and are about 10 μm to 12 μm in diameter.

A 10 ms light pulse was used and an electrical signal of 20 V at 25 KHz was applied to the OET chip. The progress of lysis was monitored as before, however compared to red blood cells, the lysis time quantification was based on subjective assessment. This approach seems inappropriate but considering the modality of the lysis process a fairly precise value can be given. In Figure 6-15a an image sequence of the lysis progress in a pair of Jurkat cells is shown. Compared to red blood cells, the contrast change due to the release of intracellular molecules was negligible. A more obvious sign which signalled complete lysis was given by sudden structural changes. In Figure 6-15a, 1.3 s after the light pulse, a rupture of the Jurkat cell membrane could be observed which resulted in an immediate release of the intracellular components. The sudden rupture can be explained by the increased colloid osmotic swelling after pore formation. The DEP buffer was osmotically balanced, however if pore formation occurs water can enter the cell which leads to swelling. This can be prevented by using suspension molecules (e.g. tetrasaccharide) bigger than the pore size²⁹⁹, but in this case the swelling reached a critical point where the strain on the membrane was too high causing a prompt rupture. Lysis of Jurkat cells was achieved within 1 s to 2 s, while red blood cells lysed in > 10 s after a 10 ms pulse. The difference might be explained by the size difference which leads to a transmembrane potential (see equation 6.1) of 4.5 V for Jurkat cells compared to 2.6 V for RBCs. However, the mechanical properties of these cells should be considered as well. Red blood cells undergo large deformations when travelling through capillaries in the human body. The membrane and the underlying cytoskeleton are evolved to handle mechanical stress. Despite pore formation, shape change and colloid osmotic swelling in red blood cells, no sudden membrane rupture was observed. Nonetheless, these findings could be used to develop a selective electroporation or lysis process by adjusting the electrical parameters. The response (poration, viability) of different cell types upon exposure to the electric field can be investigated (reversible – irreversible poration) and conditions identified where one particular cell type will be lysed or significantly more electroporated. On one hand this can

then be applied to enrich a particular cell type in a bulk sample by the lysis of other cell types. On the other hand, selective poration (reversible) could be used for the treatment of a particular cell type with chemicals (e.g. DNA, drugs). This might be of interest for drug therapy or environmental studies within mixed populations.

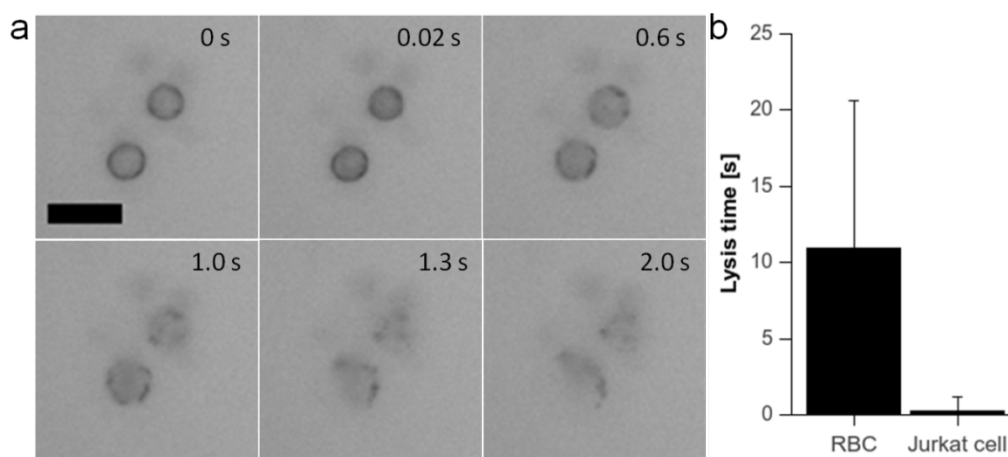


Figure 6-15: (a) Sequence of induced lysis in Jurkat cells after a 10 ms light pulse at 25 KHz, 20 V. Scale bar: 20 μm . (b) Comparison of lysis times between red blood cells and Jurkat cells using a 10 ms light pulse at 25 KHz and 20 V.

6.3.5. Continuous lysis of red blood cells

Analysis of lysis times for red blood cell has shown that short light pulses (10 ms) at 25 kHz and 10 V to 20 V were sufficient for complete cell lysis. Based on the results a continuous approach was implemented where a flow rate of 5 $\mu\text{l}/\text{min}$ was applied to the shallow microchannel chip. Instead of a light pulse, a continuous light pattern with a length of 580 μm and a width wider than the microchannel width was projected onto the photoconductor. Measurements of the cell velocity under the applied flow rate revealed speeds of ~ 20 mm/s, which is around half of the average speed of red blood cells in the human body. This gives an exposure time of ~ 30 ms when passing a 580 μm long light pattern sufficient to induce irreversible electroporation. The lysis process was combined with ultrasound actuation to create a concentrated stream of cells in the centre of the microchannel. The influence of the standing wave on the lysis efficiency was investigated and compared to lysis when only light induced electric fields were applied. Control experiments were conducted to investigate potential influence of shear stress due to high flow rates, acoustic pressure amplitude and electrical signal applied to the ITO and photoconductor without light illumination. Moreover, the determined cell concentrations after electrical, acoustical or combined actuation were compared to cell concentrations obtained from subsequent controls where the sample were just pumped through the channel without actuation. The sampling process was

performed within 2 minutes after injection of the blood cells. The settling time of blood cells in the tubing was quick resulting in decreased cell concentrations. Figure 6-16 shows the time window where sampling could be performed to assure a reliable quantification of the lysis efficiency.

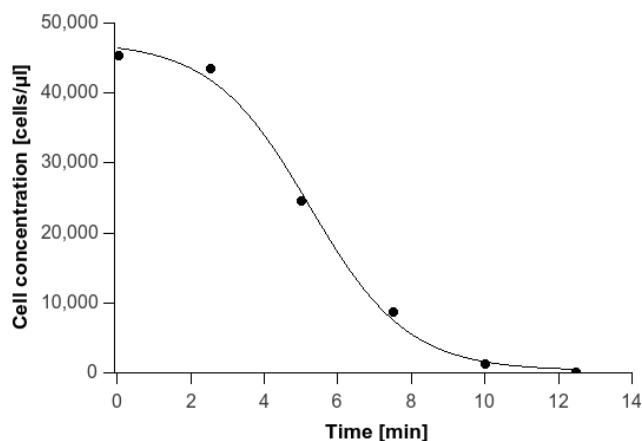


Figure 6-16: Blood cell concentration change over time due to settling of cells in tubing. Sampling time for quantification of cell concentrations was set to 2 min.

A standing pressure wave was used to focus and concentrate blood cells along the channel length. A surface acoustic wave transducer with a broad frequency response was applied to couple the ultrasound signal into the OET chip. The frequency and amplitude were tuned until a strong resonance could be observed that translated blood cells towards the pressure node of the standing wave. A frequency of 4.138 MHz resulted in a one-dimensional alignment of cells in the centre of the microchannel (Figure 6-17a and b). The voltage applied to the SAW device was 20 V, producing a pressure amplitude high enough to translate cells towards the pressure node within 2 mm for a flow rate of 5 $\mu\text{l}/\text{min}$ (Figure 6-17c). The temperature increase due to acoustic actuation was measured with an IR camera on the surface of a blank photoconductor substrate. The temperature rise within 10 minutes were in the range of 2°C to 3°C from initial room temperature values of 23°C to 25°C. The real temperature change inside the microfluidics channel might be lower than measured under static conditions. The heat exchange with the moving fluid may reduce the overall temperature increase.

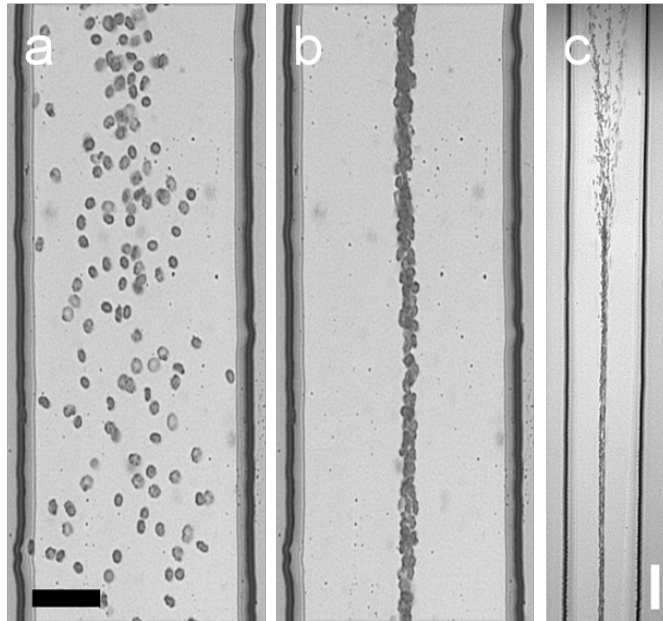


Figure 6-17: Focussing of blood cells towards the pressure node for a frequency of 4.138 MHz and an applied voltage of 20 V. (a) No flow, cells randomly distributed, and acoustics off. Scale bar: 50 μm . (b) Acoustic actuation pushed cells towards the pressure node by the PAR force. (c) Focussing under flow (flow from top to bottom), 5 $\mu\text{l}/\text{min}$, and aligning of sample within 2 mm for 4.138 MHz, 20 V. Scale bar: 100 μm .

When particles or cells of a certain radius ($r \geq \sim 2 \mu\text{m}$) experience the PAR force, acoustophoretic movement is directed towards the pressure node or antinode depending on the density and the compressibility of the object relative to the liquid medium. The sign of the force is characterized by the acoustic contrast factor and for the lysis experiments, a change in the mechanical properties of red blood cells can be expected and hence reaction towards the PAR force needs to be considered. To investigate this issue, combined acoustic and electric actuation experiments under static conditions were conducted. In Figure 6-18 a sequence of acoustically triggered cell alignment and electrically triggered cell lysis is shown. First, cells were randomly distributed in the microchannel (Figure 6-18a). After activation of the SAW transducer, cells were focussed and lined up along the centre of the channel due to the PAR and interparticle forces (Bjerknes force). This was followed by a 100 ms light pulse directed towards a pair of cells in the centre of the channel (Figure 6-18c) to induce electrical lysis. Note, the proximity of the cell pair as result of the Bjerknes force in the standing wave may have promoted a fusion of the cell's membranes, also called electro/fusion, after the pulse. The image in Figure 6-18d might give the impression of a single cell. However, the light pulse induced electroporation and a sudden loss of cell's contrast due to water influx could be observed. Furthermore, the damage of the cellular integrity altered the mechanical properties in terms of density and compressibility which affected the responses towards the PAR force. In particular, a sign change in the acoustic contrast factor was observed switching the acoustic force direction away from the pressure

node towards the antinode. Figure 6-18e and 6-18f show the movement of the irreversibly lysed cell aggregate from the centre to the microchannel wall. The influx of water into cell, because of extra/intracellular concentration gradient, changes the density dramatically and results in an empty aggregate of lipid molecules. These move towards the pressure antinode which shows similarity to previous reported results where lipid microemboli were separated from blood using the difference in the acoustic contrast factor.¹²¹ For future applications, this kind of displacement between lysed and viable cells could be useful for sample preparation steps. For instance separation of membrane debris can be applied to purify a sample or when membrane compositions of specific cells are of interest, selective lysis followed by fractionation might ease the extraction process.

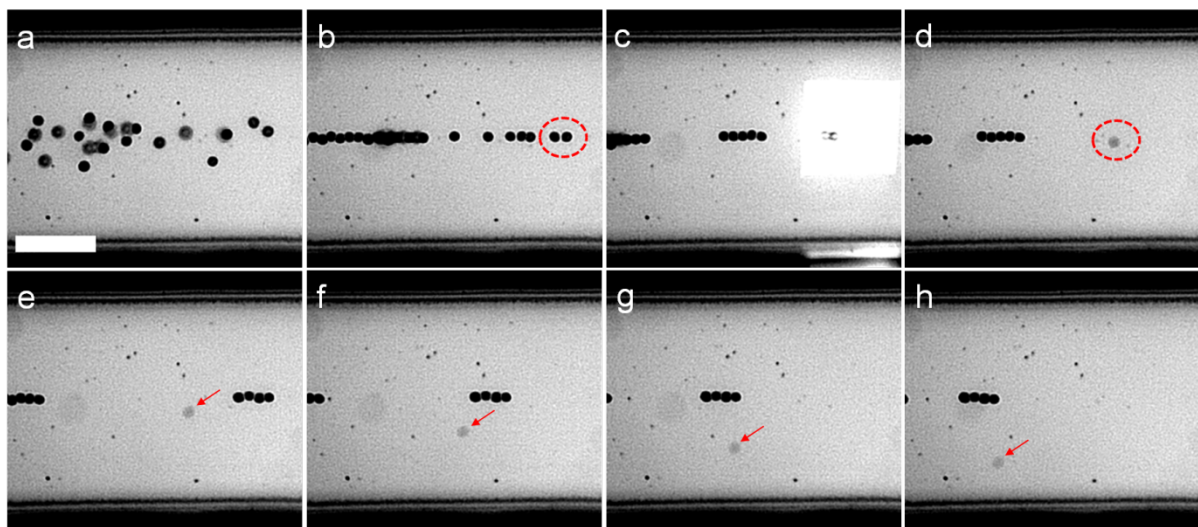


Figure 6-18: Change in acoustic contrast factor due to lysis of red blood cell. (a) RBCs in microchannel. (b) Acoustic actuation forced cells into pressure node (Target cells marked in red circle). (c) A light pulse created an electric field for localised cell lysis. (d) Lysis process induced in cells and change in intracellular and mechanical properties (density). (e-h) Cells started to move towards pressure anti-node due to sign change in acoustic contrast factor. Scale bar 50 μm .

While the PAR forces pushes particles towards pressure minima or maxima, a dielectrophoretic force exerted on particles or cells in a nonuniform electric fields results in dielectrophoresis towards high or low electric field strength. The direction of the DEP force is dependent on the Clausius-Mossotti factor which describes the polarisability of a particle or cell relative to the liquid medium. The magnitude of the factor is frequency dependent and can become zero at the cross over frequency, where no DEP force is experienced by the cell. For the conditions used in the studies (10 mS/m, buffer conductivity), the cross over frequency of a red blood cell is approximately 95 KHz (calculated using single shell model and electric properties of erythrocytes, adapted from⁸⁶). The frequency of the ac signal for the lysis experiments was 25 kHz. Therefore blood cells would experience a negative DEP force acting towards low electric field strength. The electric field induced by the light pattern

in the microchannel was fairly uniform across the channel height. However, at the light pattern edge a strong non-uniformity was obtained. This can result in a dielectrophoretic response of red blood cells when approaching the illuminated area in the microchannel.

The Figure 6-19 shows the influence of the forces acting on the cell in the microchannel. The PAR and DEP force act mainly perpendicular to the hydrodynamic force. However, lateral components of the negative DEP force at the light spot edge can oppose acoustic and hydrodynamic forces. The latter one as well as the PAR force should dominate over the DEP force to avoid trapping of cells at the electrode edge and to ensure a stable stream of cells. In Figure 6-19a the electric field was switched off and cells experienced only PAR and drag forces which led to focussing effect along the channel center. However, when the electric field was switched on, a low flow rate and high cell concentration ($>10^7$ cells/ml) can lead to a cumulative dielectrophoretic response followed by aggregations at the electrode edge due to negative DEP force while a strong PAR force supports the accumulation (Figure 6-19b). In Figure 6-19c, the negative DEP force was dominating over the acoustic and hydrodynamic force which led to a lateral displacement of the focused cell stream. Furthermore, the vertical component of the DEP force can lift cells away from the photoconductor surface towards low electric field strength. In Figure 6-19c, it can be seen that the acoustically focused cells disappear after passing the light pattern. This was mainly due to the DEP force and not due to lysis which might be assumed due to a contrast change such as observed earlier. The cell sample simply moved out of focus. This should be considered when using smaller light patterns of strong non-uniformity and larger photoconductor to ITO electrode distances. To overcome these problems high flow rates and shallow microchannels were used within this work.

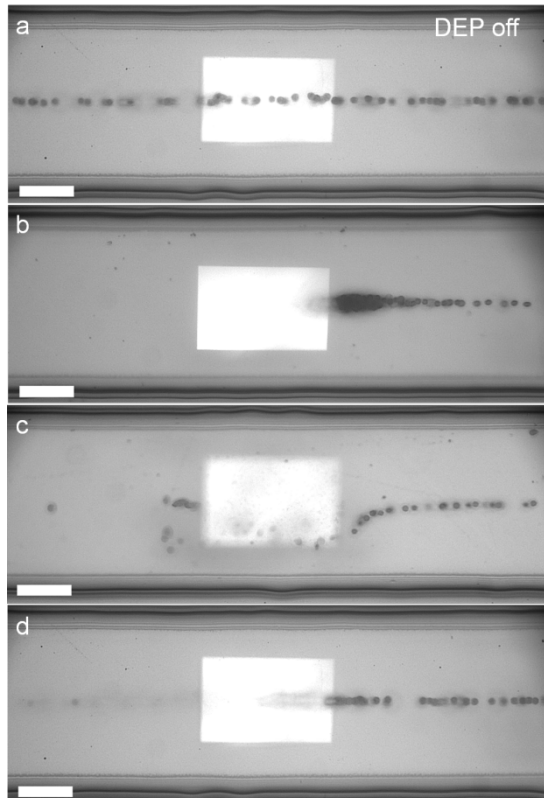


Figure 6-19: Focussed blood cells undergo dielectrophoretic movement when passing the illuminated region. (a) Electric field was switched off and cells experienced PAR and stokes drag force. (b) At 25 KHz (20 V, 10 mS/m) negative DEP force was dominating over stokes drag force leading to trapping of blood cells at the light pattern edge. (c) Negative DEP force dominated over PAR and drag force which led to lateral displacement of cells. (d) DEP force pushed red blood cells towards the channel top (cells out of focus). Lysis was induced but not completed when light pattern was passed by cells. Scale bar: 50 μm . Flow from right to left.

Figure 6-21 shows the results for the continuous lysis of red blood cells. The total cell counts are shown in table 6-3. The first experiments have been conducted with cell concentrations up to $17 \cdot 10^6$ cells/ml. The influence of the PAR force and the applied voltage (20 V, no light) on the cell count were investigated as well as the effect of forces like the shear force on the cell morphology after pumping the sample through the channel. In Figure 6-20a, a cell sample after injection into the OET chip and collection at the outlet without electrical or acoustic actuation is shown. The red blood cells showed a typical binconcave or donut-like shape while only very little membrane debris could be observed. This indicates that shear forces in the narrow channel were below mechanical stress levels which otherwise can lead to cell rupture. But it has to be noted that blood cells, especially erythrocytes, have a remarkable deformability. Their intrinsic structural properties are evolved to handle large mechanical deformations.

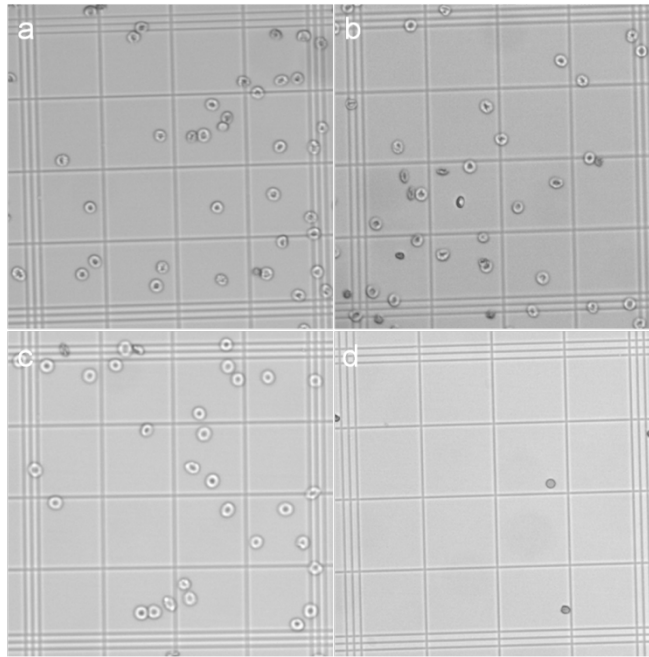


Figure 6-20: Collected blood samples after (a) pumping through the channel without acoustic or electric actuation, (b) after applying an ac signal of 25 KHz and 20 V, (c) after acoustic actuation at 20 V, and 4.138 MHz and (d) after optoelectrical actuation at 25 KHz, 20V.

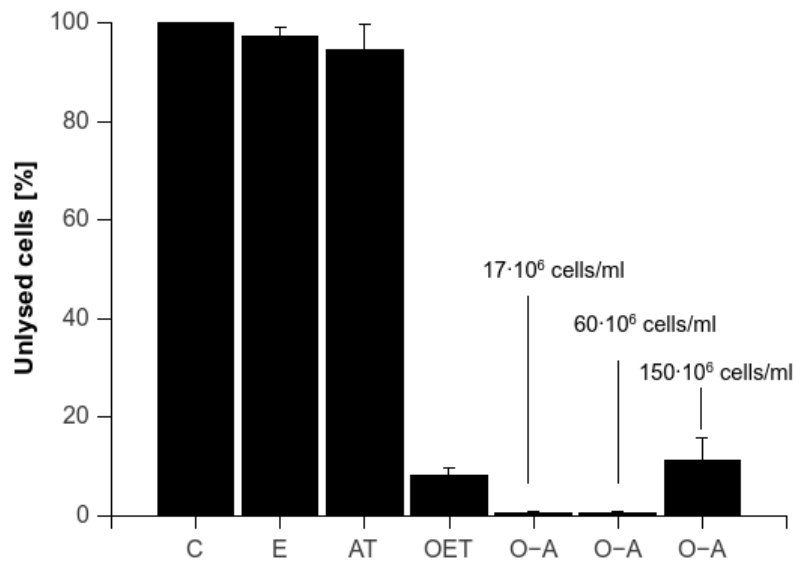


Figure 6-21: Lysis efficiency under continuous flow (5 μ l/min) in 15 μ m high channel with 30 ms exposure times when lysis was triggered by optically induced electric fields. C – Control (control run, no actuation, conducted after every actuation run), E – power on (20 V, 25 KHz), no light, no sound, AT – acoustic actuation on (20 V, 4.138 MHz), OET – light induced electric field (20 V, 25 KHz) only, O-A – acoustic and electric actuation for cell concentrations of 17·10⁶ cells/ml, 60·10⁶ cells/ml, 150·10⁶ cells/ml. The lysis efficiency was obtained from cell count analysis in a haemocytometer after injecting cells into the microchannel and collecting samples from the outlet.

When high voltages were applied (10-20 V) to the OET chip, a voltage leakage effect could be observed leading to electric field generation in the liquid despite no selective illumination. The influence on cell count and cell morphology was investigated and compared to the control runs without actuation. A slight decrease by 3% in the cell count was obtained.

Comparing the cell morphology with the control run, some differences in the shape could be observed (Figure 6-20b). The majority of the cells showed the expected shape; however, shrunk and deformed cells were spotted. The reason for this was not clear but the leakage electric field might create non-uniform fields at the outlet and inlet holes drilled in the ITO slide which could lead to electroporation and then lysis. However, the difference to the control run was very low and despite morphological changes of cells, which were treated as not lysed, the overall effect considering the amount of cell can be neglected.

When the chip was acoustically actuated to induce sample concentration in the channel centre a slight decrease by 5.5 % in the cell count compared to the control was obtained. However, the cell morphology showed no difference to the control runs (Figure 6-20c). Cell lysis using ultrasound has been shown before, but required cavitation effects induced by contrast agents.³⁰⁰ Lysis due to ultrasound standing waves was not reported yet and studies investigating cell viability after exposure to standing waves (pressure amplitudes of 1.23 MPa) suggested no impact on survival or functions of different cell types.¹²⁶ The pressure amplitude in this study was slightly higher and new findings have shown that mechanical energy from ultrasound waves can be translated into cell membrane oscillations.²⁵⁵ An additional mechanical stress beside shear forces could be the reason for the difference in the cell concentration. Nevertheless, there is no significant change in the cell concentration or shape which suggests a negligible influence by acoustic actuation. However, later in this work we investigate a potential sonoporation effect which can support the obtained results.

Single OET actuation followed the control experiments. A substantial difference compared to the previous result could be seen. Using cell concentrations of $17 \cdot 10^6$ cells/ml a decrease by 92 % in the cell count was achieved. Also, morphological changes of the collected samples were obvious. Transitions from biconcave geometries to spherical shapes were visible (Figure 6-20d). This was a typical sign for electroporated blood cells in the experiments mentioned above. The results show that the light induced electric field is triggering lysis and 30 ms exposure times under continuous flow was sufficient for a high yield.

Table 6-3: Total cell count of lysis experiments for different actuation modes. A control run for each test was performed and included the cell count of cells pumped through the chip without actuation except of the pressure driven flow.

Tests	Actuation mode	Control
	E	
1	16,950,00	17,297,500
2	16,900,00	17,150,000
3	16,125,00	17,005,000
	AT	
1	10,400,000	11,700,000
2	11,400,000	11,500,000
3	8,220,000	8,610,000
	OET	
1	1,290,000	17,297,500
2	1,315,000	17,150,000
3	1,680,000	17,005,000
	O-A	
1	100,000	18,805,000
2	25,000	15,400,000
3	90,000	17,125,000
4	145, 000	17,125,000
5	230,000	61,038,000
6	490,000	60,965,000
7	430,000	57,375,000
8	17,125,000	155,125,000
9	10,345,000	144,625,000
10	24,400,000	151,700,000

OET triggered lysis was then combined with acoustically tweezing to concentrate samples in a single stream. Compared with single OET actuation, the lysis efficiency could be improved

to values of > 99 %. Even a 3 fold increase to $60 \cdot 10^6$ cells/ml showed lysis efficiencies of > 99%. Only a further increase to $150 \cdot 10^6$ cells/ml led to a drop to 89 %. The improvement to almost 100 % cell lysis is clearly associated with the acoustic actuation and potential reason for this could be discussed as follows.

The difference in the lysis efficiency between single OET and combined OET and AT actuation can be explained by leakage effects when high voltages were applied between the electrodes. As indicated in previous chapters, in an ideal OET device the voltage drops across the photoconductor in the dark state and only upon illumination an electric field is produced in the liquid between the electrodes. However, in practice that is not the case. A leakage electric field was present even in absence of illumination when a frequency of 20 V at 25 kHz was applied. The produced field influenced the distribution of cells in the channel. In Figure 6-22a, the cell distribution before and after applying the electric signal is shown. It can be seen that a significant amount of cells migrated towards the channel wall when the voltage was switched on despite no illumination. The curved channel wall of the fabricated chips (Figure 6-22b) acted as insulator leading to an electric field disturbance (non-uniformity) that promoted cell-wall interaction due to lower electric field strength in proximity to the channel boundaries. The same effect was observed for a selectively illuminated channel (whole channel width). Cells that were lined up at the channel wall escaped from the lysis inducing field which resulted in reduced lysis efficiency of 92 % compared with combined actuation where the sample was concentrated along the pressure node.

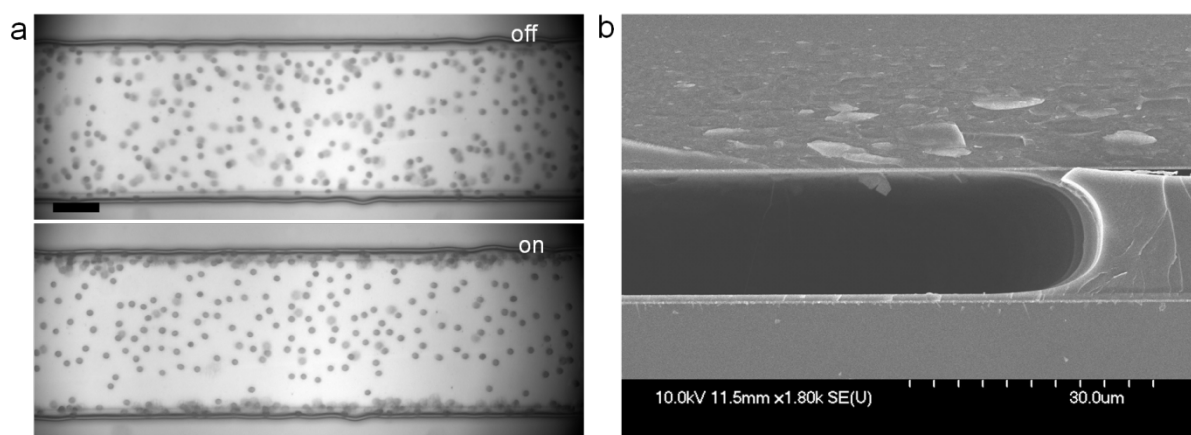


Figure 6-22: (a) Accumulation of red blood cells at the channel wall under a low flow rate when 20 V were applied at 25 KHz without light or acoustic actuation. Red blood cells moved toward insulating SU8 wall where electric field strength was lower creating a dielectrophoretic effect due to voltage leakage into the liquid despite no illumination. The photoconductor was not a perfect insulator in its dark state, especially at high voltage a significant voltage dropped across the liquid is observed (b) This led to non-uniform electric fields along the channel wall due to a curved channel wall which acted as insulator.

The observed improvement in red blood cell lysis can also be associated with pore formation due to exposure of high acoustic pressure amplitudes. Normally, the cavitation activity of microbubbles mediates the permeability of membranes in an ultrasound field. The steady pulsation or a rapid collapse of microbubbles in close proximity to tissues or cells causes membrane ruptures which can be used to deliver molecules into the cells. However, even in the absence of microbubble cavitations, it was hypothesised that intracellular cavitation can occur.²⁵⁵ This means the membrane itself acts as an oscillator. Fluctuations in the acoustic pressure are translated towards the bilipid layer inducing cycles of expansion and contraction. An acoustic negative pressure can overcome the molecular attraction forces between lipid monolayers and pulling them apart, while a positive pressure pushes them back together. Large monolayer stretching might lead to rupture while membrane protein stimulation or damage might promote pore formation.²⁵⁵ In several studies, ultrasound standing waves were utilised for the delivery of molecules across the membrane and the described mechanism might be involved in the change of the membrane permeability. For instance, Khanna *et al.* showed the release of haemoglobin from red blood cell after treating cells in the presence of a contrast agent³⁰¹. In their half-wavelength device poration was mainly achieved due to cavitation effects produced by microbubbles, but the study noted that cells were stressed when travelling towards the pressure nodal plane (0.83 MPa to 1.96 MPa). In the absence of contrast agent retroviral transduction of Human erythroleukemia cells within an ultrasound standing wave was reported by Lee *et al.*³⁰² Here, acoustic microstreaming and possibly sonoporation improved the gene delivery into the cells. Rodamporn *et al.* reported high transfection efficiencies of a DNA plasmid when HeLa cells were exposed to high pressure amplitudes (19.5 MPa) while moving towards the pressure nodal plane. Microstreaming streaming effects around the cells, while trapped in pressure minima, causing viscous shearing were given as a possible explanation for membrane poration. Also, cell migration time towards the pressure nodal plane was 5 s exposing the cell to many cycles of fluctuating pressure. Another contrast agent free system based on ultrasound standing waves in a half-wave length capillary device was used by Carugo and Ankrett *et al.* to deliver pharmaceutical agents and fluorescence labelled dextran into cardiomyoblast cells.^{256, 257} Pressures of 0.11 MPa to 1.39 MPa were applied and intracellular cavitations were considered as possible mechanism for membrane poration.

To investigate a potential sonoporation effect due to high acoustic pressure amplitudes or acoustic streaming effects we conducted control experiments with Jurkat cells and erythrocytes incubated in a 3 kDa FITC-dextran solution which would enter the cell and show up as a fluorescent image if poration was present. PBS buffer and DEP buffer solutions with

0.5 mg/ml FITC-dextran in a blood cell suspension of $15 \cdot 10^6$ cells/ml and Jurkat cell suspension $5 \cdot 10^6$ cells/ml were prepared. The samples were injected into the chip with a flow rate of 5 μ l/min. The SAW device was actuated with amplitude of 20 V and a frequency of 4.138 MHz to focus cells into the pressure node. Samples were collected at the outlet and FITC-dextran uptake was measured direct and after a washing step in the corresponding buffer solution using a fluorescence microscope. Cell samples were also incubated for 30 min in 0.5 mg/ml FITC-dextran to investigate uptake without external stimulation. Figure 6-23 shows a bright field image and the corresponding fluorescence image of sample measured direct after acoustic treatment. An uptake of the fluorescence labelled dextran was not observed. Each sample, Jurkat cell and red blood cells in PBS or DEP buffer, showed an absence of a fluorescence signal indicating that the applied pressure amplitude is not powerful enough or the time being exposed to cycles of positive and negative acoustic pressure is too short to induce pore formation. Control experiments with cells only incubated in the dye solution showed no uptake, assuring that no unspecific signal is detected.

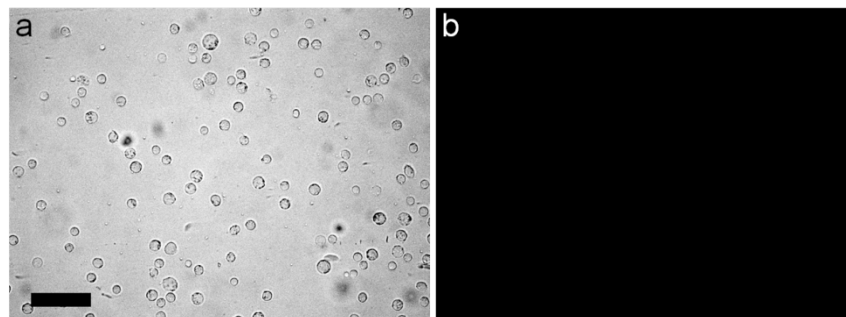


Figure 6-23: Jurkat cells sampled after acoustic actuation at 20 V, 4.138 MHz in 0.5 mg/ml of 3 kDa FITC-dextran DEP-buffer solution. (a) Bright field image (b) Fluorescence imaging (excitation at 495 nm) measured direct after sampling. Scale bar: 50 μ m.

Comparing the results with studies in the literature, the exposure time rather than the pressure amplitude seems to be the reason why no dextran uptake could be observed. Work by Carugo *et al.*, Ankrett *et al.* and Krasovitski *et al.* used pressure amplitude in the range of 0.11 MPa to 1.93 MPa. The system here was able to produce amplitudes in the range of one MPa (based on experiments in Chapter 4) for an applied voltage of 20 V which should be sufficient to induce permeabilization. However, considering the exposure time mentioned in the literature, a significant difference to this work was apparent. Carugo *et al.*, Ankrett *et al.* and Krasovitski *et al.* used exposure times of 5 s and 30 s. Rodamporn *et al.* exposed cell samples for 5 s to 15 s to pressure amplitudes of up 19.5 MPa. The approach in this work used flow rate of 5 μ l/min in a narrow channel, leading to cell velocities of \sim 2 cm/s. The acoustic pressure in this system was not applied along the whole channel length of 2.5 cm

but only around ~ 0.6 cm resulting in an exposure time of ~ 300 ms. Despite a frequency of several MHz with cycle times in the μs - ns range, membrane rupture or sonoporation seems to be dependent on exposure times in the range of seconds. Moreover, ultrasound standing wave actuation involves pressure distributions with minimal pressure change in the nodal plane. Only one study²⁵⁸ where standing waves were used gives details about the actual time of exposure to positive and negative pressure fluctuations. This is the travelling time till the pressure node is reached. Once the cell sample is in the nodal plane, only shear forces induced by acoustic micro streaming might influence the membrane permeability. Acoustic streaming can be neglected in our system due to high flow rates in the microchannel.

In summary, these results can give a possible explanation for the fact that no dextran uptake could be observed. However, it also needs to be considered that despite short exposure times, mechanical deformation can be induced without rupture or pore formation. Pore formation with pore sizes smaller than the dextran molecules may occur which leads to size exclusions. A combined acoustic and electrical stimulation of the membrane could improve the overall lysis efficiency but more investigations should be done to study the influence of a potential sonoporation effect on a subsequent electrical stimulation. A possible experiment to get a better insight could involve acoustic cell focusing followed by a light induced electroporation under static conditions. Variations in the pressure amplitude while keeping the optical intensity and electric field strength constant might give indications for promoting lysis effect by pre acoustic actuation. In particular, the influence of acoustic streaming could be studied by comparing the lysis time for steadily applied high and low acoustic pressures after a light pulse. Shear stress due to acoustic streaming rolls next to a pressure node in a half-wave length device can be a promoter for cell lysis under static and low flow rate conditions. Furthermore, a microchannel with increased lateral dimensions and a transducer for lower frequency might be utilized to increase the exposure time. Cell samples will be exposed to high pressure changes while travelling towards the pressure node. Once in the pressure node, the acoustic actuation is switched off to stop acoustic streaming. A light pulse is then applied to cells in the centre of the channel. This is followed by monitoring the lysis time where the results are considered in relation to exposure time and amplitude.

At higher cell concentrations the lysis efficiency dropped. This could be attributed to a denser packing of cells in the pressure node which can result in electric shielding of cells by surrounding cells. An improvement could be made by increasing the exposure time or amplitude. We tested the effect of an increased exposure time applied to a dense package of cells. First, we trapped cells at low flow rates by negative DEP at the electrode edge to

generate an aggregation (Figure 6-24 a). Secondly, the trapped cells were released to enter the illuminated region (Figure 6-24b) and then the electric field was switch on again to induce cell lysis (Figure 6-24c-d). It can be seen that lysis of densely packed cells is feasible. In this case the exposure time was ~ 7 s.

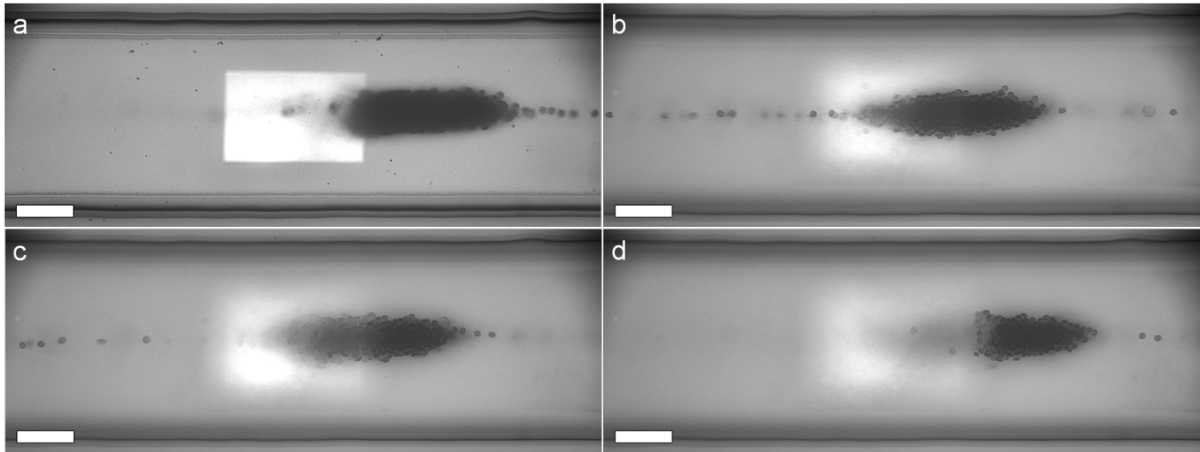


Figure 6-24: Lysis of densely packed cells using an increased exposure time. (a) Cells were trapped at electrode edge due to negative DEP force (20V, 25 KHz). (b) Applied voltage was switched off to release cells and allow movement towards the illuminated area.(c) 2 s after the electric signal (20 V, 25 KHz) was switched on again. (d) 7 s after lysis was induced (Scale bar 50 μ m). The focus in the images (b-d) was changed towards a higher plane to observe the lysis process as negative DEP pushed the cells upwards.

An alternative for handling large cell concentrations without reducing the throughput could be the distribution of cells over several pressure nodes. Figure 6-25 shows two cases when the OET chip was actuated at higher resonance frequencies. At 8 MHz and 12.514 MHz, two and three pressure nodes were created in the microchannel. This would lead to less dense streams and can be used to optimize the lysis process. In Figure 6-19b it was shown that high cell concentrations can cause a cumulative dielectrophoretic response and aggregation at hard edged electrode pattern. It can be of advantage to introduce a graded pattern that for instance changes in light intensity and hence reduces the DEP force acting on the cells. This would promote a sleeker entrance into exposure regions of high electric field strength to induce lysis.

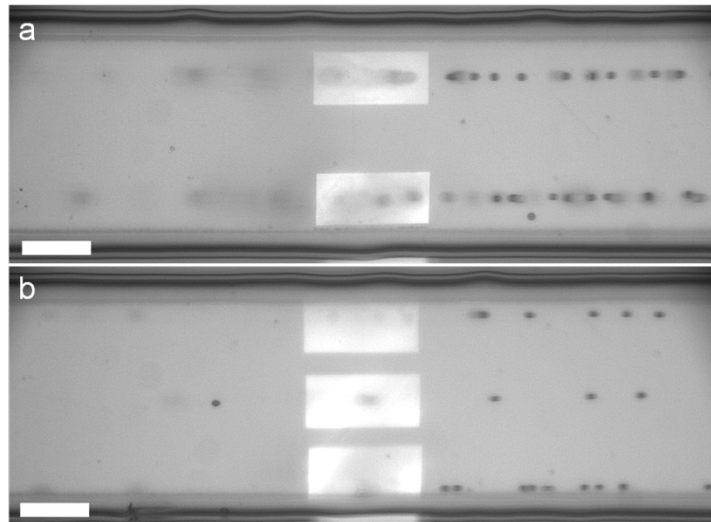


Figure 6-25: Alternative configuration to optimize lysis of high cell concentrations based on multiple pressure nodes. (a) Two pressure nodes at 8 MHz, (b) three pressure nodes at 12.541 MHz (Scale bar 50 μm). Distribution of high cell concentrations over several pressure nodes might help to prevent dense cell aggregates and therefore electric shielding by surrounding cells.

6.3.6. Single Cell lysis

The selective lysis of single cells is one of the major bottlenecks in the analysis of rare cells or targeted populations in complex biological samples such as blood or biopsies, and more especially so in miniaturized systems.^{266, 269, 303, 304} Whilst there have been advances in sequencing,³⁰⁵ expression profiling³⁰⁶ and metabolite analysis³⁰⁷ at the single cell level, new techniques for single cell lysis are still challenging. Microfluidic lysis strategies are primarily based on mechanical,³⁰⁸ chemical³⁰⁹ and electric³¹⁰ strategies, with a particular focus on bulk sample treatment rather than targeted single cell lysis. Electrical methods that aim at single cell lysis require exceptionally good control of the position of the microelectrodes relative to the cell of interest to trigger lysis³¹¹⁻³¹³. Optical techniques, usually based on intense laser excitation (kW), are thought to arise as a consequence of the creation of a plasma by energy absorption in the liquid, followed by the emission of a shockwave and a cavitation event, resulting in a mechanical event close to the cell of interest (although cavitation bubbles create wider lysing areas and damaging zones^{314, 315}). Other, alternative methods, involving either chemical gradients^{309, 316} or acoustic forces^{272, 273}, result in responses that are widely distributed in space, leading to limited specificities in a dense or confluent population of cells.

In previous studies, it has been shown that OET is a useful tool to perform single cell electroporation and lysis under specific conditions using beam spots in the range of 20 μm to 80 μm .^{104, 105} The advantage compared to conventional metal electrodes is that the electric field is optically induced which provides a highly flexible approach in terms of the position of the electric field as well as the size of the virtual electrodes. Transportation of the target cell

towards a lysis area is not necessary. The electric field produced at the area of interest on the photoconductor. Furthermore, device design, electrode fabrication and integration into a microfluidics chip are more complex when using metal electrodes compared to the optoelectronic tweezers approach. The device presented here was a simple sandwich structure of two parallel electrodes bonded together using a photoresist. The working area where lysis is performed can easily be increased and an automated lysis process might be feasible. It has to be noted that single cell lysis has been performed in a previous study by applying OET. A focused light beam of tens of micrometer diameter was able to induce single cell lysis when using a high optical power of 10^5W/cm^2 .¹⁰⁵ Here, a simple data projector producing optical powers of 1W/cm^2 was sufficient for precise single lysis despite reduced light spot sizes.

The increased accuracy and reduced optical intensities used in this study are possible through the integration of a microfluidic channel with the OET device which has the effect of decreasing the distance between the top and bottom electrodes. This reduction of the distance between the electrodes was of significant advantage for the creation of high electric field strength. When the beam spot was reduced to a few micrometers the field was highly non-uniform with high magnitudes well defined close to the surface of the photoconductor. The electric field in the device was investigated performing a 2D simulation using COMSOL. Figure 6-26a shows the simulated electric field contours created by a $2.5 \mu\text{m}$ light spot. Magnitudes of up to 16kV/cm for an applied voltage of 20V and frequency of 25kHz in a low conductivity medium (10mS/m) can be achieved. The FWHM of the area of higher electric field created by the $2.5 \mu\text{m}$ optical spot in the liquid just above the photoconductor was $4.6 \mu\text{m}$ (Figure 6-26b). It shows that the device concept can precisely control the electrical fields with the optical pattern. In the presence of a cell the electrical field lines were disturbed so that some pass through the cell and some were diverted around the cell.¹⁰⁶ The model used depicts the shape, size and properties of a red blood cell; and a substantial potential difference at the membrane interface was induced once subjected to the electric field (Figure 6-27a). In particular, the voltage drop across the membrane produced by a $2.5 \mu\text{m}$ spot was approximately 2.1V under the given conditions (Figure 6-27b). However, the induced transmembrane potential was dependent on the lateral dimensions between the electrodes. An increased electrode distance, while keeping a constant beam spot size, resulted in a reduced voltage drop across the membrane. In Figure 6-27c, this influence was modelled for a set of voltages applied to the electrodes. For a small light spot of a few micrometers, the distance between the electrodes became important, especially when working with low applied voltages.

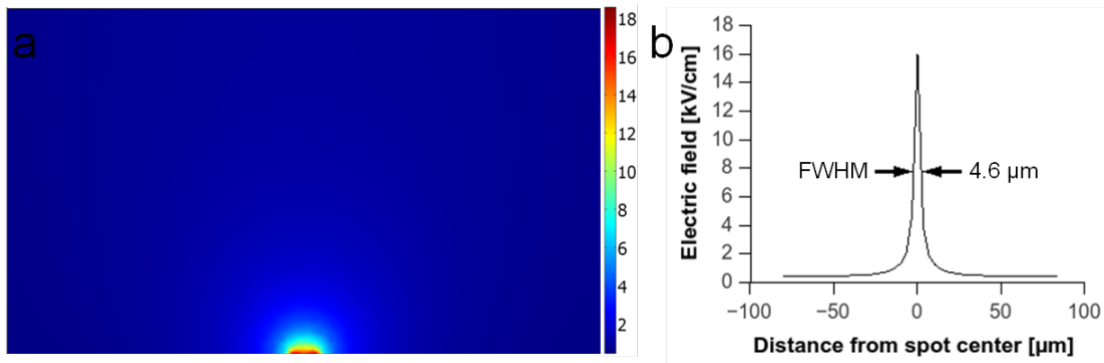


Figure 6-26: (a) Simulated non-uniform electric field (kV/cm) created by a 2.5 μm spot in microchannel with 35 μm distance between ITO electrode and photoconductor when a voltage signal of 20 V and 25 KHz is applied. (b) Corresponding FWHM of the area of higher electric field created by the 2.5 μm light spot. Measurement was taken at 100 nm above the photoconductor surface.

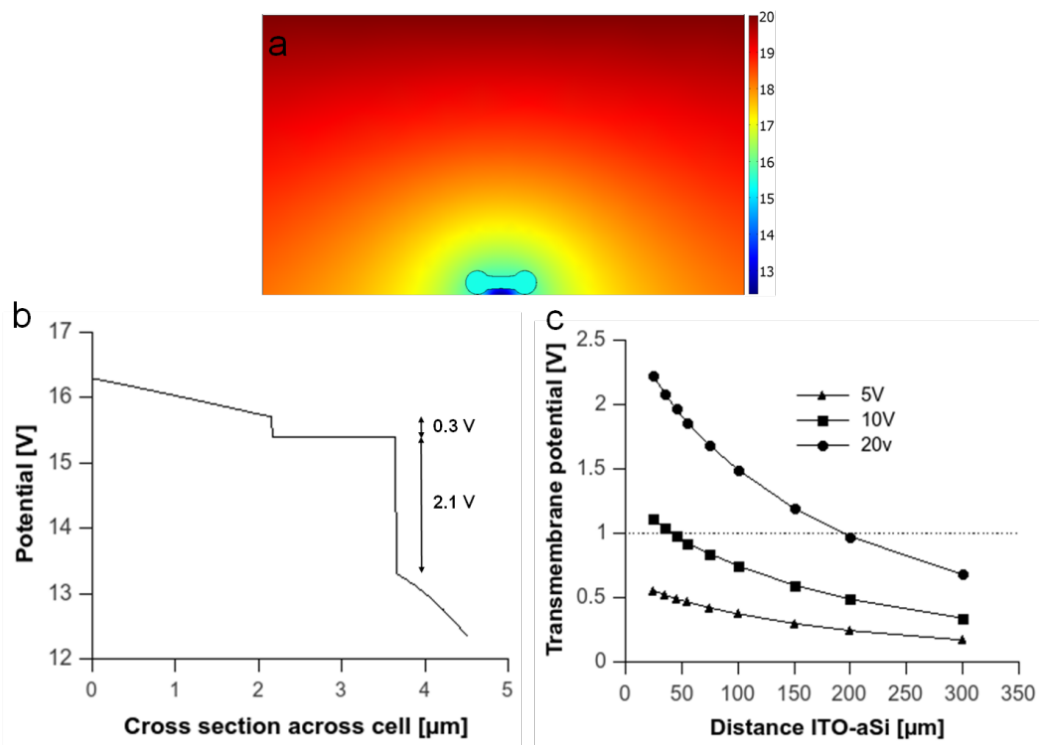


Figure 6-27: (a) Simulated potential distribution in the presence of a red blood cell (V) for 20 V and 25 KHz. (b) Cross section potential plot through the center of the red blood cell showing voltage drop of 0.3 V and 2.1 V across the furthest and closest membrane site relative to the photoconductor surface for 20 V, 25 KHz. (c) Transmembrane potential for different voltages and changing electrode distances (25 KHz). Simulations considered a low conductivity buffer of 10 mS/m.

This work showed for the first time, that the beam spot can be reduced to a size smaller than the target cell without losing the ability to induce lysis. In Figure 6-28(a-d) a red blood cell suspended in low conductivity buffer (10 mS/m) was targeted with a beam spot size of 2.5 μm . An AC signal of 20 V and 25 kHz was applied to the OET chip. The simulated field strength under these conditions was about 16 kV/cm. A vertical distance of the cell to the photoconductor surface of 800 nm at the furthest place and 100 nm at the closest was considered due to the biconcave shape of a red blood cell. The voltage across the

membrane at the centre point of the cell with the furthest distance from the surface was determined. The transmembrane potential was 2.1 V according to the model. When the beam spot was placed on the centre of the cell, the field was activated and complete lysis was achieved within 20 s to 50 s with 100 % lysis efficiency. Surprisingly, no dielectrophoretic movement of cells were observed when the smallest light spot was applied. Under similar conditions negative dielectrophoretic force is often experienced by cells, resulting in movements towards low electric field strengths. Only after increasing the spot size to 5 μm x 5 μm did the cell tend to align with the electric field lines, a movement associated with an induced electrical dipole within the cell aligning with the applied electrical field. However, lysis was still achieved and an increase in the pattern size of up to 45 μm was carried to investigate the influence on the time for lysis (Figure 6-28e). A significant reduction in the lysis time was observed with minimum time of around 1 s for beam spot sizes >14 μm . Although the simulation clearly showed that the smaller 2.5 μm diameter optical spot produced a large enough transmembrane potential to lyse the cell, the larger the light spot is the more electron-hole pairs are created within the semiconductor decreasing its impedance and hence increasing the electrical field within the liquid layer of the OET device. This results in a faster electrical lysis of cells if a larger optical pattern is used. The use of bigger beam spot sizes was beneficial for faster lysis. However, it has to be emphasised that the precision given by the smallest spot size is of importance for true single cell lysis.

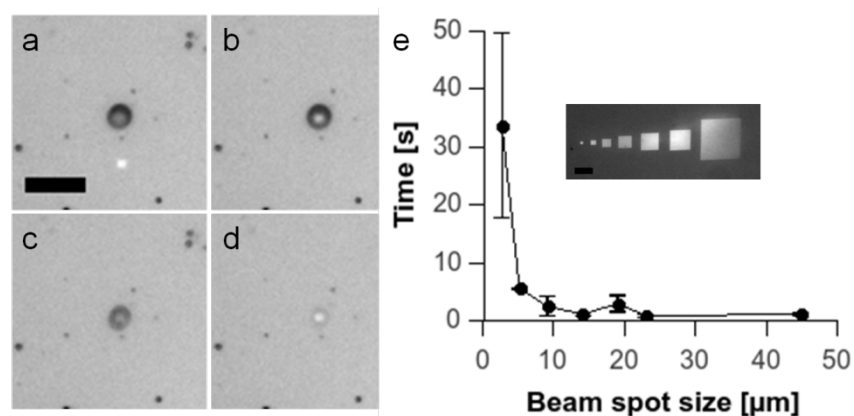


Figure 6-28: Single cell lysis using 2.5 μm light pattern at 25 KHz and 20 V in 10 ms buffer solution. (a) 2.5 μm beam spot close to RBC. (b) Beam spot was focused on the centre of the cell and a voltage of 20 V was applied. (c) Cell after 14 s. (d) Lysis complete after 20 s. (e) Cell lysis times for a range of beam spot sizes. Scale bars: 20 μm .

The example above shows the spatial control of the electric field and lysis of a single cell in a much diluted sample. Single cell lysis has been shown before in a sparse cell population. Here, however, it was demonstrated that the developed system was precise enough to target a cell surrounded by many other close cells. In Figure 6-29(a-f), two cells were selected for lysis. These cells were in the proximity of others and even in contact with its

neighbours. The results obtained under these conditions revealed that lysis was induced only in the targeted cells. The adjacent cells were unaffected by the well localized electric field. The model was used to look at the transmembrane potential for a cell with changing positions relative to the beam spot. A shift in the vertical or horizontal position of the cells is accompanied with a decrease in the transmembrane potential. A distance of less than two microns between the cell and the center of the light spot reduces the voltage drop across the membrane to values below 1 V (Figure 6-29 g). The model was in agreement with the experimental observation. This means adjacent cells experience a transmembrane potential which was not sufficient for a dielectric breakdown and shows that this approach was highly selective and efficient towards lysis of targeted cells.

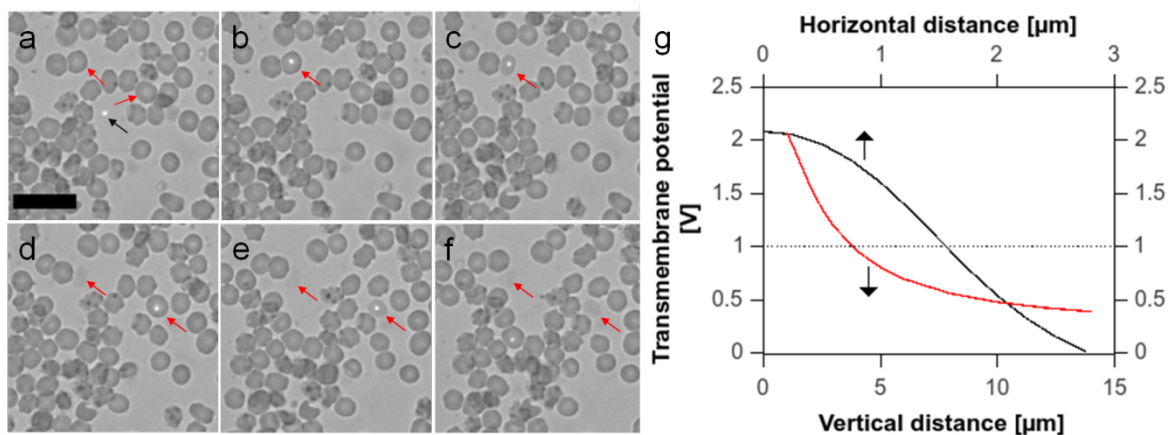


Figure 6-29: Single cell lysis at 25 KHz and 20 V in 10 mS/m buffer solution. (a) 2.5 μm beam spot (marked by black arrow) was used for selective lysis of target cells (red arrow). (b) Beam spot was focused on the center of first target cell and a voltage of 20 V was applied. (c) First target cell after 20 s of electric field exposure. (d) After 35 s, second target cell lysis was started. (e) 27 s after inducing lysis in second target cell. (f) 50 s after inducing lysis in second target cell. (g) Simulated change in transmembrane potential with increasing vertical and horizontal distance of the cell to the light spot center (25 kHz, 20 V, 10 mS/m). Scale bar: 20 μm.

The conditions for cell lysis were optimized for the operation of the OET chip. This means a low conductivity buffer was usually used to create an electric field in the sample solution. When the buffer solution was highly conductive (> 1 S/m), the applied voltage drops mostly across the photoconductor while the field in the sample solution was weak. Therefore conductivity was usually chosen so that the impedance of the liquid layer lies between the dark and light conductivity of the photoconductor. In Figure 6-30a, a comparison of the field produced by 2.5 μm beam spot in low and high conductivity buffer is shown. The field strength in a high conductivity buffer was two magnitudes lower. This suggested that the potential across the cell membrane induced by the weak field in the solution was not sufficient for lysis. However, considering the cell membrane as a good insulator, a close distance between cell and photoconductor could change the impedance at the interface of photoconductor/liquid significantly. The impedance change on electrodes due to adhesion of

cells, proliferation or migration and their detection has been successfully demonstrated by techniques like ECIS (Electrical cell-substrate impedance sensing).^{317, 318} Hence, the transmembrane potential of the biconcave blood cell was modelled dependent on the vertical distance between it and the photoconductor. The closest distance to the electrode was 5 nm and the furthest was 640 nm referring to the edge of the red blood cell (see Figure 6-30c). The results of the model showed that the transmembrane potential was well below the average threshold voltage of 1 V for distances of > 100 nm (Figure 6-30b). However, a significant change can be observed when reducing the distance to tens of nanometers. An increase in the potential of an order of one magnitude was obtained for gaps < 10 nm. Even cell to substrate contact can be considered. Previous studies have shown that buffer solution with high ionic strength reduce electro static repulsion and promote molecular contact to surfaces.³¹⁹ Furthermore, the model showed a significant potential change in the liquid underneath the cell. The reason for this might be associated with the impedance of the cell membrane, which may dominate at close distances, producing a well localized low conductivity region between the cell and the photoconductor which can result in an increased voltage drop and field strength at the interface. This effect may have allowed the lysis of cells suspended in PBS buffer (Figure 6-31).

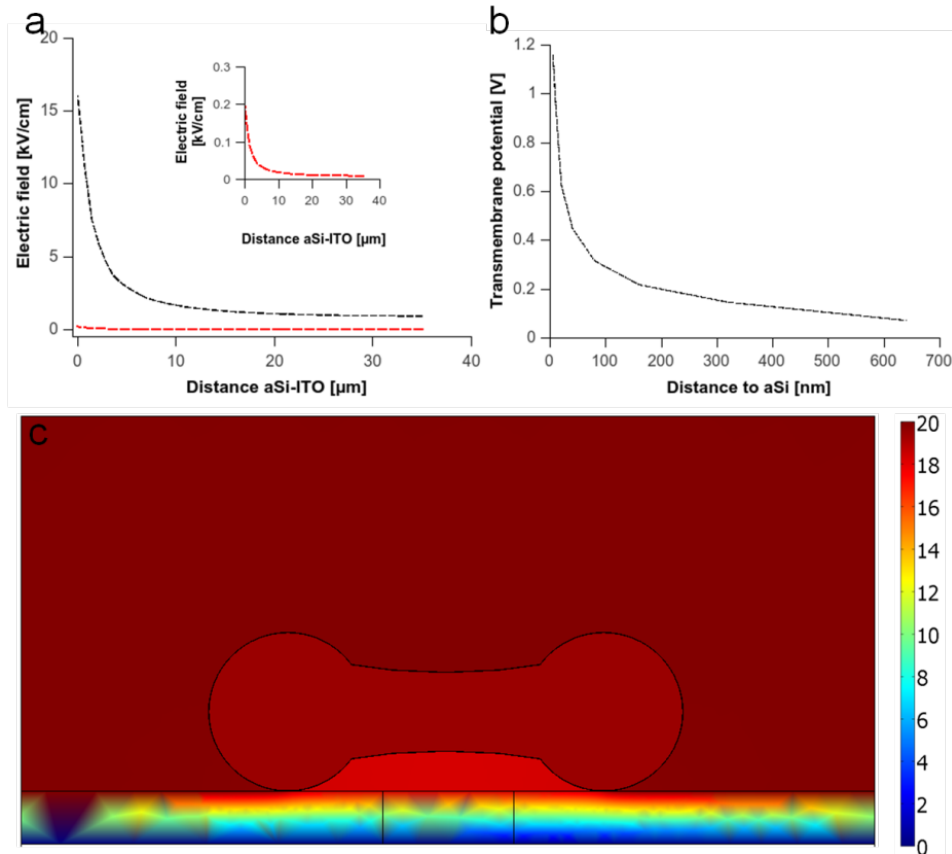


Figure 6-30: (a) Comparison of simulated electric field strength created by a 2.5 μm beam spot in low (10 mS/m, black curve) and high (PBS, 1.4 S/m, red curve) conductivity buffer. Inset shows detailed view of red curve. (b) Modelled transmembrane voltage of a red blood cell in PBS buffer. The distance between the cell and the photoconductor surface was varied between 5 nm and 640 nm. (c) Potential plot of a red blood cell with 5 nm distance to the photoconductor at the closest (edge of red blood cell).

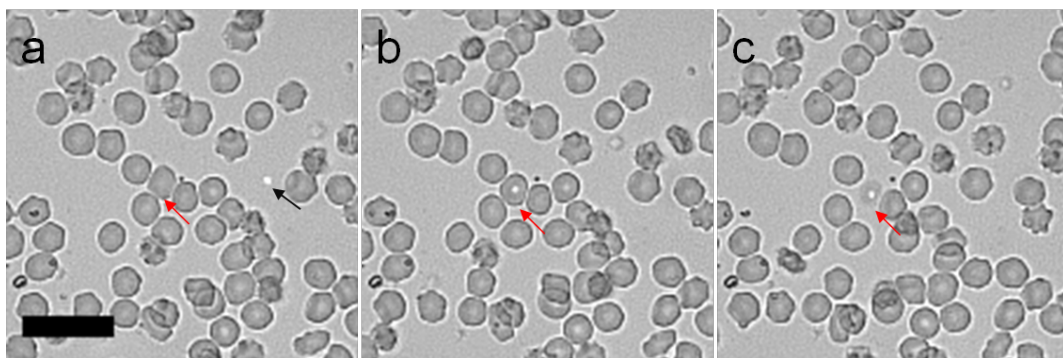


Figure 6-31: Single cell lysis at 25 KHz and 20 V in PBS buffer. (a) 2.5 μm beam spot (marked by black arrow) is used for selective lysis of target cell (red arrow). (b) Beam spot was focused on the centre of cell and a voltage of 20 V was applied. (c) Lysis complete after 25 s. Scale bars: 25 μm .

A 2.5 μm diameter beam spot was used to target cells while applying a frequency of 25 kHz and a voltage of 20 V. As the model predicted, under these condition it was possible to successfully lyse red blood cells. The time for lysis was between 25 and 55s; and lysis was

achieved for any selected target cells. The Figure 6-31 shows an example of targeted red blood cell in a dense sample. Irreversible pore formation causes release of intracellular components. Red blood cells are well suited for observing the loss of the cellular integrity because of high concentration of haemoglobin (350g/L) which produces a strong contrast relative to the surroundings. In Figure 6-31, the targeted cell lost contrast and faded away over time leaving the empty membrane or “ghost” of the cell.

Furthermore, while suspension cells like circulating cancer cells or white blood cells are interesting targets for single cell studies, the majority of the mammalian cells form tissues (in vivo) or grow on surfaces (in vitro). If adherent cells need to be transferred into an analytical device by suspending them first, the activation of signalling pathway related to the environmental change can lead to perturbation of biological processes and might influence the experimental outcome.³²⁰ Therefore, a planar substrate where cells are attached prior to lysis can improve the control of the sampling process. The amorphous silicon in this work has a thin natural oxide layer on its surface so that the cells can be grown on this glass like surface which is a very well understood environment for them. The first demonstration of lysis of adherent cell lines with light patterned electrical fields was shown in this work. A breast cancer cell line (MCF 7) sample was injected into the chip and incubated over night. The photoconductor was covered with clusters of cells immersed in cell culture medium (~ 0.95 mS/m). A 5.5 μm diameter optical spot was used to verify if lysis can be achieved. In Figure 6-32 (a-b) a large cluster of cells was lysed within 80s. Moreover, selective lysis can be easily applied. In Figure 6-32 (d-g), a MCF 7 cell in the center of a cluster is shown and lysed within 35s.

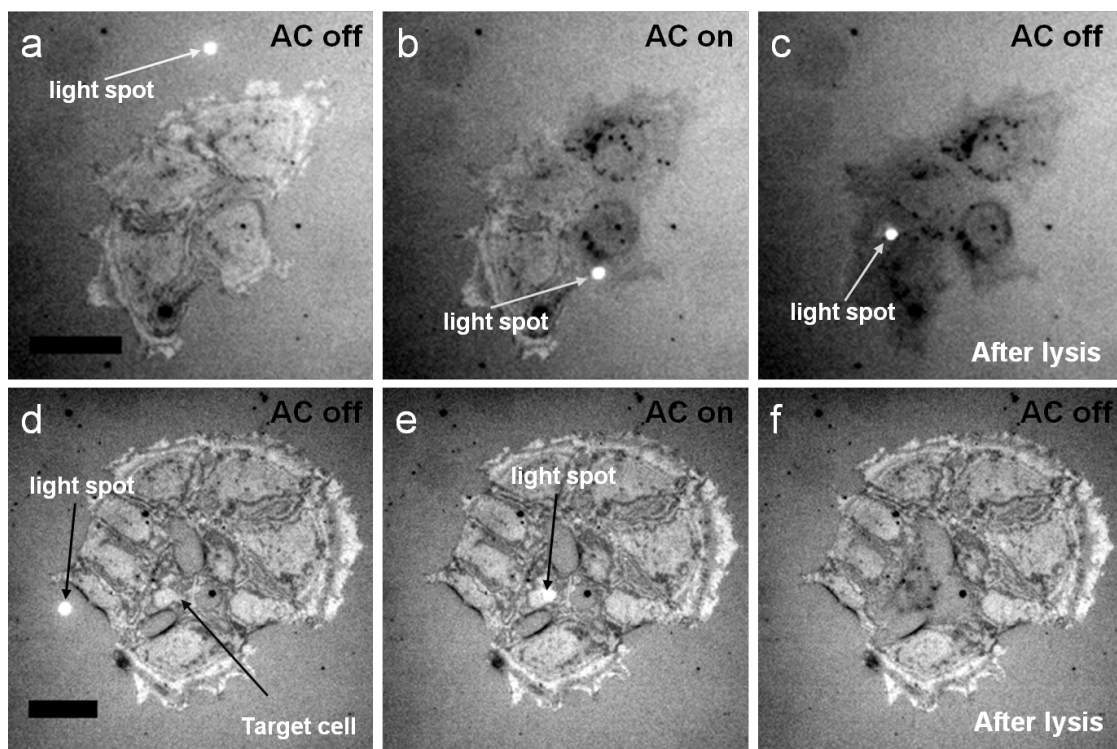


Figure 6-32: MCF7 cells adhered to the surface of the photoconductor and immersed in cell culture medium inside the OET chip. (a-c) A 5.5 μm light beam spot was used to achieve lysis of a cluster of cells within 80 s (25 KHz, 20 V). (d-g) A cell in the centre of a cell cluster was targeted and lysis was induced using 20 V at 25 KHz. Lysis was achieved after 35 s (Scale bars: 30 μm).

6.4. Conclusion

This work demonstrates the application of acoustic and electric fields in a microfluidic chip for cell lysis. A flexible approach was outlined which can be used for experiments in batch and continuous mode (e.g. cells flowing through the device). A surface acoustic wave device was combined with an optoelectronic tweezer chip to acoustically control cell sample position and optically trigger lysis. Short light pulses in a millisecond range were used to induce irreversible damage of the cell membrane. An ultrasound standing wave with a pressure amplitude of ~ 1.73 MPa was applied to create a focused stream of cells in the centre of the microchannel. The combination of acoustic and electric actuation has shown to improve the lysis process significantly with efficiencies close to 100% for blood cell concentrations of up to $60 \cdot 10^6$ cells/ml. Improvements of the continuous lysis process can be made by the use of higher resonance frequencies to create cell distributions over multi pressure nodes or exposure times may be increased to process more dense cell samples.

A true single cell lysis approach was demonstrated using just the OET chip. Small light spot sizes of up to 2.5 μm were applied to create well localized electric fields with magnitudes high enough to induce irreversible electroporation. This configuration was used to

demonstrate targeted single cell lysis in a dense sample without lysis of adjacent cells. Furthermore, we have shown that this technique is applicable to high conductivity buffers (PBS) and cell culture media which is of advantage as cells can be treated under conditions closer to the physiological state. Suspension cells and cells adhered to the photoconductor were lysed on single cell level.

This work has shown an improvement compared to work by Lin et al¹⁹². Optimisation of the concept included the reduction of the channel height, combination with acoustophoretic cell alignment while optical power and applied voltage were kept in the same magnitude. Higher sample throughputs as well as lysis of denser cell samples with efficiencies of > 99% have been achieved. Moreover, an improvement was made compared to previous work focusing on light induced single cell lysis.¹⁰⁵ Under physiological conditions single cell lysis could be achieved using smaller beam spots and significantly less optical power. We believe that these findings are beneficial in the field of on chip cell lysis and single cell analysis.

However, this work also indicated that potentially non-invasive cell manipulations using the OET chip need careful investigation. The efficient handling of cells under continuous flow (e.g. sorting) requires an appropriate increase in the DEP force to overcome the influence of the drag force. This, however, also requires the increase of the electric field strength which may induce an unwanted electroporation effect in cells of interest. Therefore, it is recommended to perform cell viability studies after cell manipulations with light induced electric fields in the OET chip.

7. Microbubble actuation in microfluidics using optoelectronic tweezing and surface acoustic wave transducer

Contrast agents or microbubbles (MBs), for enhanced ultrasound imaging were recently found to be potentially useful as carriers for drugs and the controlled release of them at specific cell targets in the human body. The activation of these gas-filled microbubbles which leads to their oscillation and collapse is triggered by ultrasound (insonation). The mechanism and factors responsible for an efficient delivery of chemicals into a cell after MB stimulation is the focus of current studies, however, a lack in available technologies which enable the in vitro individual control of microbubbles and their insonation complicate the detailed characterisation of the underlying process. In this study we introduced a concept for the individual control of microbubbles. An optoelectronic tweezing device was applied to selectively trap and move microbubbles using optically induced electric fields. In combination with an ultrasound transducer microbubbles were insonified. This concept may be used in conjunction with adherent cells or tissues attached to the optoelectronic tweezer device to accelerate the study of membrane alteration and drug delivery mediated by MB actuation.

7.1. Introduction

Acoustic contrast agents or microbubble (MBS) are gas filled particles with sizes of 1 – 10 μm . When injected into the body, they are usually used in ultrasound based diagnostics where they act as echo-enhancer for improved imaging of organs and vessels. The difference between the acoustic impedance of organic tissues in the body and the gas in the MB results in backscattering of the ultrasound signal at these interfaces. The reflection of an incident sound wave at a particular point in the body where MBs are accumulated is received by a transducer and used to create a contrast-improved image. The reflectivity is proportional to the size and the concentration of the gas-filled particle.³²¹ Compared to body tissue, MBs are several thousand times more reflective.

MBs are able to resonate when subjected to certain ultrasound signals. The resonance frequency is dependent on the size and lies within 2 – 15 MHz. In an acoustic field, the

insonified MB undergoes volumetric oscillation due to their compressibility which is characterised by rapid expanding and contracting in response to the fluctuating pressure amplitude. The oscillation of MBs can be visualized but requires extremely high frame rates in the range of several million frames per second.³²² However, besides oscillation there are more MB interactions with ultrasound. The PAR force can lead to lateral microbubble translation,³²³ fluid motion can occur in the form of microstreaming³²⁴ due to pressure changes around oscillating MBs, or, depending on the exposure time and the ultrasound signal, MBs can be selectively destroyed. For instance, at low acoustic powers the gradual escape of gas from microbubbles can occur.³²⁵ At high acoustic powers a large size variation in the MB can cause a sudden impulsion known as inertial cavitation and an asymmetric microbubble collapse is able to produce directed fluid jets.³²⁶

In general, the structure of a MB consists of a shell of 1 nm to 200 nm thick and a gas filled core. The shell defines the mechanical properties of the MB and the diffusion process of the gas. Materials for the shell can be proteins (e.g. albumin), surfactants (e.g. ploysorbate), lipids (e.g. di-acyl-phospholipds), polymers (e.g. polyvinylalcohol) or polyelectrolyte multilayer. Bio-inspired shells based on phospholipids are one of the most interesting components for MB development due to their biocompatibility, low surface tension and their ability to self-assemble. The gas core can consist of a single gas or a combination of gases (e.g. air, perfluorocarbon, sulphur hexafluoride). Preferable gases are used which have a low permeability through the shell as well as low solubility in blood and serum.

The above described MB responses to insonation have gained much attention because of its potential therapeutic effects. MBs could be used as delivery systems for carrying therapeutic drugs which can be released on demand exploiting an ultrasound triggered process to induce MB destruction. There are different approaches to attach, incorporate or encapsulate drugs in combination with MBs. The approach usually depends on the chemistry of the MB and the strategy of how to deliver the drug specifically to a certain region in the body. Drugs can be attached to the outer shell, inserted into the shell material or loaded inside of the MB. A brief overview of lipid based MBs is given in Figure 7-1. For instance, site specific drug delivery can be obtained using ligands (antibodies, peptides) coupled (via avidin-biotin) to the surface of the shell which target receptors in selected tissues or cells (Figure 7-1 A). Alternatively, the charge on the surface of the shell can be used to attach oppositely charged molecules by electrostatic interaction. An example is the highly negatively charged backbone of DNA or RNA molecules which can be attached to cationic (positively charged) phospholipids (Figure 7-1 B). Moreover, the hydrophobic nature of a shell made of lipids is ideal for the incorporation of lipophilic drugs which naturally partition into it during the self-

assembly process of the microbubble (Figure 7-1 C). To overcome the limited surface area, the lipid monolayer can be thickened using an additional oil layer suitable for concentrating more lipophilic drugs into the MB (Figure 7-1 D). Instead of using the surface shell area and the shell volume for drug loading, the whole internal volume of liposome attached to MBs can be exploited as drug carrier (Figure 7-1 E). Alternatively, the MB can be incorporated into a drug loaded liposome to increase the amount of the delivered drug (Figure 7-1 F).

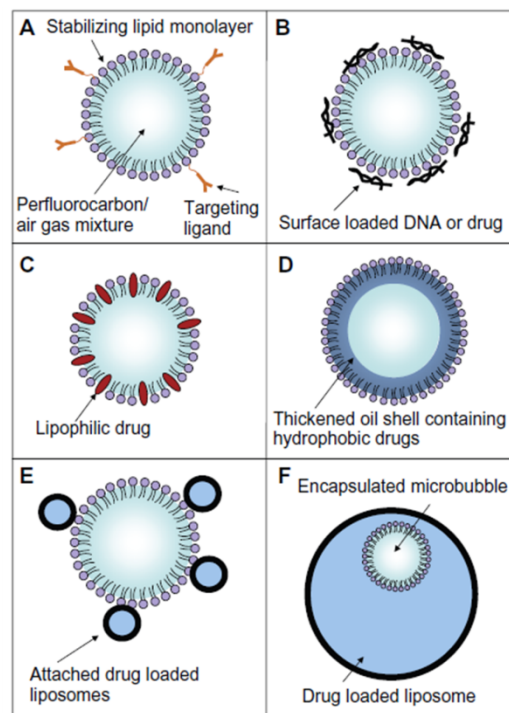


Figure 7-1: Schematic of microbubble based drug carrier systems. (A) A MB design with lipid monolayer shell which stabilises a gas mixture core. The shell can also be modified with ligands (antibodies, peptides) to enable targeted microbubble accumulation at desired tissues (B) MB as carrier of drugs or DNA on the shell surface by electrostatic interaction. (C) Integration of lipophilic drugs into the shell of MBs. (D) Incorporation of hydrophobic drugs in a thickened oil shell. (E) Attachment of drug-filled liposomes on the MB surface. Ultrasound exposure causing mechanical oscillation of the MB disrupts the liposomes. (F) Incorporation of drugs and MB in liposome. Stimulation with ultrasound ruptures MB and liposome. Schematic and description from Ibsen et al.³²²

Microbubble destructions by ultrasound results in the release of energy in the form of inertial cavitation shockwaves, microjets, micro streaming and their associated high shear flows. In the presence of tissue or cells, these events can cause transient or irreversible damage to biological matter. For instance, shockwaves due to MB collapse as well as microjets are able to create ruptures in the cell membrane, a process known as sonoporation.^{327, 328} This has been used for gene (attached to MB) delivery to targeted tissue³²⁹ or drug transport across the blood-brain barrier³³⁰. Liposomes attached to the MB or with incorporated MBs undergo the same rupture event just as cell membranes do. The actuation of the MB leads to a rapid release of drugs loaded in the liposomes.^{331, 332} Microstreaming created by MBs loaded with

lytic agents has been used to remove blood clots from vessels (thrombolysis).^{333, 334} Blood clots consist of platelets and fibrin. The insonation of MBs nearby enabled the alteration of the fibrin network and allowed an improved transport and penetration of lytic agents to dissolve blood clots.

The detailed study of MB responses (oscillation, destruction) to ultrasound parameters (frequency, power) and their impacts on cells and the release of drugs, genes or proteins require novel manipulation techniques. The efficient insonation of a MB can only be achieved when the behaviour of the MB in the ultrasound field is properly characterised.³³⁵ While experimental system for bulk MB investigations have been developed³³⁶⁻³³⁸ the availability of systems for individual MB handling and actuation is very limited. The disadvantage of bulk methods originates from the problem of polydispersed samples which cause signal averaging or masking. For instance Emmer *et al.* showed that recorded responses of subpopulations of MB can be masked by other subpopulations.³³⁷ Specifically, it was found that small MB have a low contribution in the total acoustic scattering, since a small amount of larger bubbles dominate the fundamental frequency response. Moreover, the coating of a MB has a significant influence on the MB response to an acoustic pressure as it dampens the vibration and thereby the resonance frequency of the MB.³³⁹ But recent studies have shown that phospholipid coatings were not equal or homogenous in MB samples.³³⁵

Currently, only a negligible amount of studies focused on single bubble characterization.³⁴⁰⁻
³⁴² One major problem associated with these studies is the lack of methods to easily isolate a MB from a population. The common techniques to obtain single bubbles are based on high sample dilutions, the use of capillary tubes or flow focusing. These methods have been shown to be useful, but it is also evident that they require cumbersome preparation steps, fragile equipment or external forces with limited spatial control. In addition, none of the mentioned methods considers the introduction of cells for in vitro cell-MB interaction studies. Only a few studies investigated the sonoporation event based on single bubble cavitation in proximity to a cell.^{185, 343, 344} In two studies, MBs were produced and individual MBs were controlled by applying laser technologies. In detail, a focused pulsed laser beam is applied to a solution. The laser energy is absorbed in the liquid and the MB results either from an explosive vaporization or due to the formation of a plasma (optical breakdown) and the associated shockwave³⁴⁵. The pulsating MB can then be controlled using the PAR force induced by laser-photoacoustic tweezing or applying optical traps by laser induced gradient forces (optical tweezers). However, these studies focused on the cavitation effect of simple air bubbles which differ significantly from therapeutic MB or contrast agents. So far, to best

of our knowledge, only one study showed single bubble-cell interaction using a clinical relevant contrast agent (Optison, UK).¹⁸⁵ The bubble was controlled with an optical trap and the membrane damage in a cell monolayer was observed after bubble cavitation.

The literature overview clearly shows a limited range of systems to study and characterise MBs. Many systems focus solely on the MB characteristics in bulk samples with minor attention to single bubble investigations and have limited relevance to biological applications. So far, only laser based methods seem to be able to fulfil the need to control single bubbles to investigate their influence on cells upon insonation. However, sophisticated laser systems are expensive and difficult to use which dampens the research output in this field.

In this part of the thesis a less complex, cheaper and an easier to use system is proposed which may help to accelerate the research on MB for characterisation purposes and therapeutic applications. We demonstrate the selective handling of MBs as well as the arbitrary arrangement of MBs of different sizes using light induced electric field gradients. The insonation of MBs was achieved using a surface acoustic wave (SAW) device. The acoustic signal was coupled into the optoelectronic chip and the bubble behaviour observed over time. In this study we use the contrast agent SonoVue (Bracco, UK) to demonstrate selective bubble handling. The main clinical purpose for SonoVue is for improved diagnostic imaging of liver tissues to identify lesions. These microbubbles consist of a phospholipid monolayer shell and a core filled with sulphur hexafluoride (SF_6). SF_6 is a non-toxic, colourless and odour-less gas with a high dielectric strength. It is heavier than air and shows poor solubility in water. The structure and properties of SonoVue represent one of the most promising for MB mediated drug delivery, they are approved for clinical use and are therefore used as model particle for dielectrophoretic and acoustic manipulation in this research.

7.2. Materials and Methods

ITO and amorphous silicon coated glass slides were used as bottom and top electrodes to enable dielectrophoretic manipulation of the MB in the optoelectronic chip (see chapter 2 for fabrication details). A couple of changes to the manipulation system were made to optimise MB observation and light induced electrical movement. These included the change of the electrode configuration as shown in the schematic in Figure 7-2c. The microbubble density was lower than that of the buffer suspension resulting in a buoyancy force acting on the MBs and their rise towards the top electrode substrate. To achieve an improved dielectrophoretic control, the photoconductor site was switched, however, that also necessitated a change in the bright field illumination settings. Previously, illumination was obtained from a top light source but the aSi layer blocked most of the light leading to a poor visibility in the manipulation area. Therefore, a more powerful bottom illumination had to be used which then necessitated a modification of the piezoelectric substrate. Here, a lithium niobate wafer polished from both sides was used to obtain a transparent transducer allowing light transmission to the optoelectronic chip above (Figure 7-2a). The projection path of virtual electrodes was unchanged. Instead of using SU8 photoresist to structure the microfluidic chamber, double-sided PET tape (3M UK PLC, UK) was used to produce a manipulation volume of 25 mm x 10 mm x 0.1 mm (L x W x H).

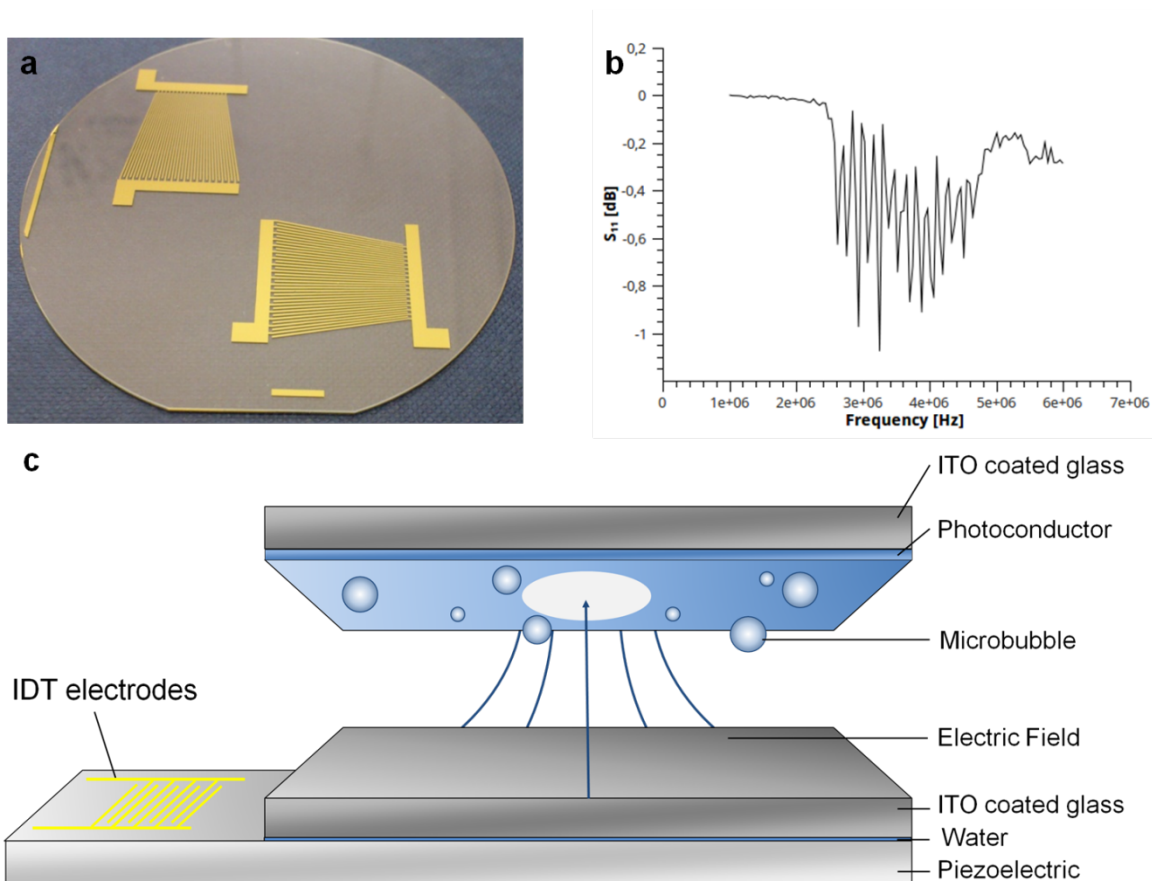


Figure 7-2: (a) Transparent piezoelectric substrate (Lithium niobate) with slanted interdigitated electrodes (IDT, SAW device). (b) Frequency spectrum for SAW device in x-propagation direction. (c) Schematic of the setup showing SAW device and OET chip filled with microbubbles. Here, the photoconductor was used as top substrate compared to the previous setup where it was on the bottom.

SonoVue (Bracco Suisse SA, Switzerland) MBs were purchased as a kit including a vial containing 25 mg of lyophilised sulphur hexafluoride (SF_6) powder and a pre-filled syringe with a 5 ml sodium chloride solution. The salt solution is usually used to dissolve the powder, however DEP buffer (10 mS/m) was used, which was transferred to the vial followed by 20 seconds of shaking to mix all contents. MB samples were withdrawn into a syringe and then manually injected into the optoelectronic chip after further 1:10 dilution in DEP buffer.

The optoelectronic chip was connected to a function generator and a voltage signal of 70 KHz and 10 V was applied. The SAW device was actuated at a frequency of 2.8 MHz. The frequency spectrum of the SAW device is shown in Figure 6-2b. The bandwidth lies within the spectrum which is commonly used for medical ultrasound applications. Microbubbles were exposed to a pressure wave caused by an amplitude of 60 V applied to the SAW device in burst mode using a 12 cycle sine wave with a pulse repetition frequency of 300 ms. Note, the slanted SAW device deposited on the transparent piezoelectric wafer was designed for the frequency range of 3.5 MHz to 5.5 MHz. However, the network analysis

showed frequency responses down to 2.6 MHz. A frequency of 2.8 MHz was chosen because of a good MB response.

To quantify the pressure amplitude in the optoelectronic chip a fibre-optic hydrophone (Precision Acoustics, UK) was used. The 10 μm (diameter) fibre sensor was placed in the microfluidics chamber between the electrodes substrates and the acoustic response was measured after applying 2.8 MHz and 60 V to the SAW device. The maximum pressure amplitude obtained was 100 kPa.

The dielectric response of MBs of different sizes was modelled using a MatLab script and the parameters shown in table 7-1. In detail, we modelled the real part of the Clausius-Mossotti factor to investigate the sign of the dielectric force on the MB when subjected to non-uniform electric fields. We assumed a homogenous particle with an effective conductivity given by the sum of its bulk and surface conductivity. The conductivity of SF6 is dependent on the temperature and no values were found for ambient temperatures. However, used as a dielectric gas for insulator purposes it has similar conductivity values to air (20°C). Therefore, the bulk electric conductivity value of air was used as an approximation (see results, Figure 7-4). The electric field strength was modelled (2D model) using Comsol (v3.5, Comsol Ltd., UK). The chip thickness (100 μm), light pattern of 10 μm length, the medium conductivity (10 mS/m), the applied voltage of 10 V and the frequency of 70 KHz were used in the model to simulate the electric field. The conductivity of amorphous silicon in dark and light state were set to $1.8 \cdot 10^{-5}$ S/m and $1.4 \cdot 10^{-3}$ S/m in the model corresponding to the use of a 40x objective (see results, Figure 7-6).

Table 7-1: Parameter used to model Clausius-Mossotti factor for various sized MB.

Permittivity of media	79
Permittivity of SF ₆	1.0024
Conductivity of media [S/m]	0.01
Bulk conductivity of SF ₆ [S/m] ³⁴⁶	$3 \cdot 10^{-15}$
Surface conductivity [S/m]	$1 \cdot 10^{-9}$
MB sizes [μm]	0.25 – 10.00
Frequency [Hz]	10 000 – 1000 000

The velocity of MBs of various sizes trapped in a ring pattern was quantified by analysing recorded video sequences. The inner and outer diameters of the ring pattern were 23 μm and 33 μm . MBs experienced a negative dielectrophoretic force when 70 KHz were applied to the optoelectronic chip. The ring pattern with trapped MB was moved (keyboard controlled) with constant speed to record the path over time. The speed was adjusted to the maximal trapping force (before the bubble escaped the trap) when 10 V were applied to the chip. The videos were analysed using the video analysis tool Tracker (v4.84, Douglas Brown, USA)

MBs were trapped in the ring pattern during insonation. The size changes while constantly insonified were recorded and ImageJ (v1.47, USA) was applied to extract the diameter of MB over time.

7.3. Results and Discussion

MBs modified with drugs or ligands are promising tools for theranostic applications. Originally used for ultrasound based imaging due to their scattering properties, new MB-ultrasound interactions were found to be excellent mechanism to deliver molecules to target cells or induce controlled tissue alteration. The characterisation of insonified MB and the potential influence on cells and tissue requires new examination methods with flexibility in terms of MB handling (single or multiple), insonation parameters (frequency, pressure amplitude), microfluidic scalability and ability for working with biological matter (cells, tissue).

In previous chapters, a combined platform, which brings together optoelectronic and acoustic tweezing was introduced and now applied to comply with the need of new strategies for enhanced MB manipulation. To allow for MB insonation, a transparent lithium niobate substrate containing a surface acoustic wave (SAW) device was used. As can be seen from Figure 7-2b, the frequency response of the SAW device was tuneable within a frequency band from 2.6 MHz to 4.8 MHz which is of importance as medical ultrasound devices work in this particular range or even higher up to 15 MHz. MBs were contained in the microfluidic environment of an optoelectronic chip placed on the SAW device substrate. The ultrasound signal was coupled from the substrate to the chip via a water coupling layer (Figure 7-2c). The microfluidic volume was simply created by a spacer between the electrodes of the optoelectronic chip. In this case double sided tape with a thickness of 100 μm was used. The MB sample was then manually injected with the aid of capillary forces.

The MB samples used consisted of phospholipid shells with a sulphur hexafluoride (SF_6) gas core and were provided by SonoVue. The sample contained bubbles sizes from 1 - 10 μm with mean diameter of 2 – 3 μm . The rather nonuniformity showed that the creation of uniformly sized MB samples is still challenging although novel strategies based microfluidic approaches³⁴⁷ seem to be a promising route. Even with a homogenous sample, once transferred into a different environment, maintaining a constant MB size is technically challenging. When suspended in a liquid, MBs can grow, shrink or coalesce in response to physico-chemical alteration of the environment.³⁴⁸ The hydrostatic or acoustic pressure as well as the surface tension between the liquid-gas interfaces causes a static diffusion of gas from the core of the MB into the liquid. Small MBs are more susceptible to these influences and dissolve quickly once injected, into the blood flow, for example.³³⁹ The reason for this is the increased excess pressure (difference between internal and external pressure) within the MB which is generated to balance the surface tension. This leads to an increase in the partial pressure (pressure of the gas in a certain volume) inside the MB compared with the partial pressure in the surrounding liquid. The resulting steep concentration gradient

increases the diffusion and therefore the dissolving of the MBs over time. The shell material is of importance as it reduces the surface tension between the gas/liquid interface and acts as a permeation barrier. During the experiments using SonoVue, a static diffusion and the associated size change was not observed within an hour after injection into the microfluidic compartment. Figure 7-3 shows a microscopic image of SonoVue MBs in the optoelectronic chip. MBs were suspended in low conductivity medium (10 mS/m) and injected into the optoelectronic device. It can be seen that the sample is not uniform but contained MB sizes from 1 to 10 μm .

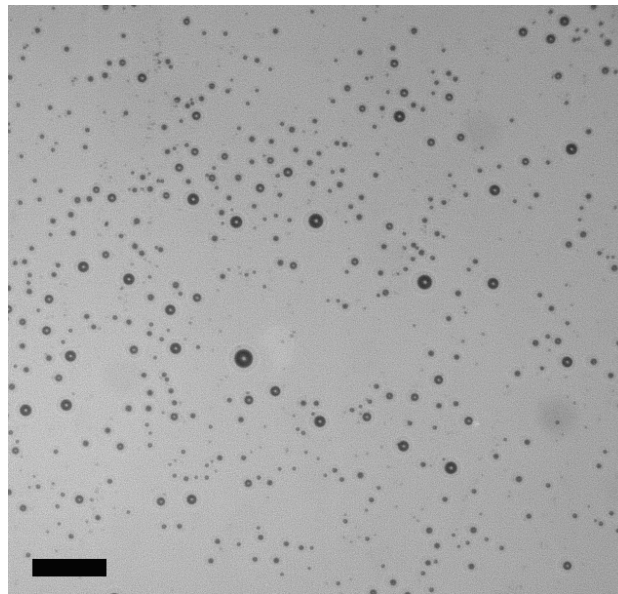


Figure 7-3: SonoVue microbubbles for drug delivery. Image depicts the non-uniformity when working with microbubble samples. Scale bar: 50 μm .

The size distribution can be considered as a general issue when dealing with MBs. But as well as the size, the coating and the environment are significant factors which influence the MB's response to an acoustic pressure. Therefore, it is desirable to investigate the optimal insonation parameters for particular conditions. To do so, selective addressing and isolation of MBs is necessary. The usage of the dielectrophoretic force (DEP force) in a nonuniform electric field seems to be a promising route as it allows for precise targeting of single and multiple MBs. The dielectrophoretic response of a MB depends on its electrical properties which are a function of the applied frequency as well as the medium properties and is described by the CM factor. When a MB is subjected to a non-uniform electric field any induced dipole inside the MB would interact with the external applied field. This would result in a net force which is either towards high or low electric field strength. The SonoVue MB core contained SF_6 which is a gas of high dielectric strength. Therefore, it can be assumed that the MB acts as an excellent insulator with low polarisability compared to the surrounding medium and experiences a negative dielectrophoretic force. The CM factor was modelled for

different sized MBs for a frequency range of 10 KHz to 1 MHz considering a medium (DEP buffer) conductivity of 10 mS/m. Figure 7-4 shows the real part of the Clausius-Mosotti factor. As expected, the sign of the factor is negative under the given condition over a long frequency range for a relatively large MB size distribution. The CM factor increases with decreasing MB radius showing the growing influence of the MB surface conductivity imposed by the medium conductivity. Even MBs in submicrometer range experienced a negative dielectrophoretic force according to the model. However a surprising result was found when a decrease in the medium conductivity (modelled) as well as MB size (<200 nm) changed the sign of the DEP force as the less polarisable medium and the surface conductance dominated. Therefore, trapping, isolating and translating MBs from a sub-population by light patterns using OET might be conceived.

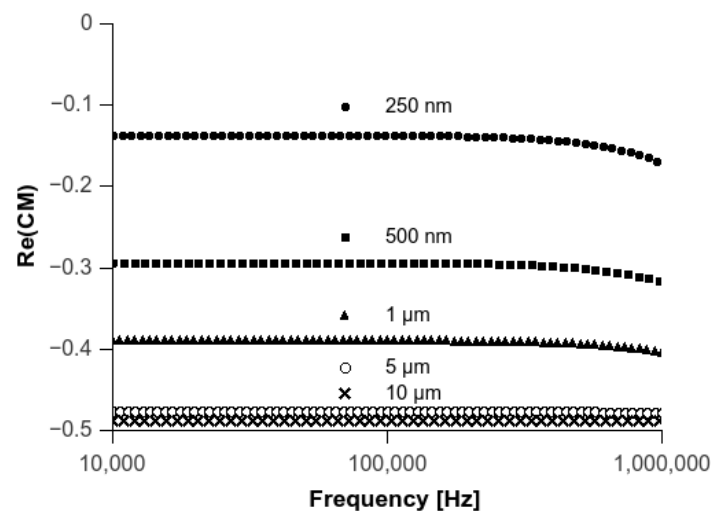


Figure 7-4: Simulated real part of the Clausius-Mosotti factor for various MB diameters (0.25 - 10 μm) in DEP buffer (10mS/m).

For MB actuation, a ring pattern was used to selectively trap and isolate MBs from a population. The pattern is ideal as it allows to trap a MB inside the ring while no other MBs can enter because of the negative DEP force. In Figure 7-5, ∇E^2 was modelled for a ring trap and the direction of the DEP force acting on a MB is represented as black arrows. As can be seen from the simulation, the DEP force is partially directed towards the centre of the ring trap. This results in a stable MB trap and is used for individual MB handling. The inner and outer diameters of the ring were 23 μm and 33 μm, respectively. The dimensions were arbitrary chosen and one advantage of OET is in being able to create patterns on the fly to suit a particular case. For instance, the ring pattern's size can be decreased when the population of MB is very dense or increased to trap several MBs.

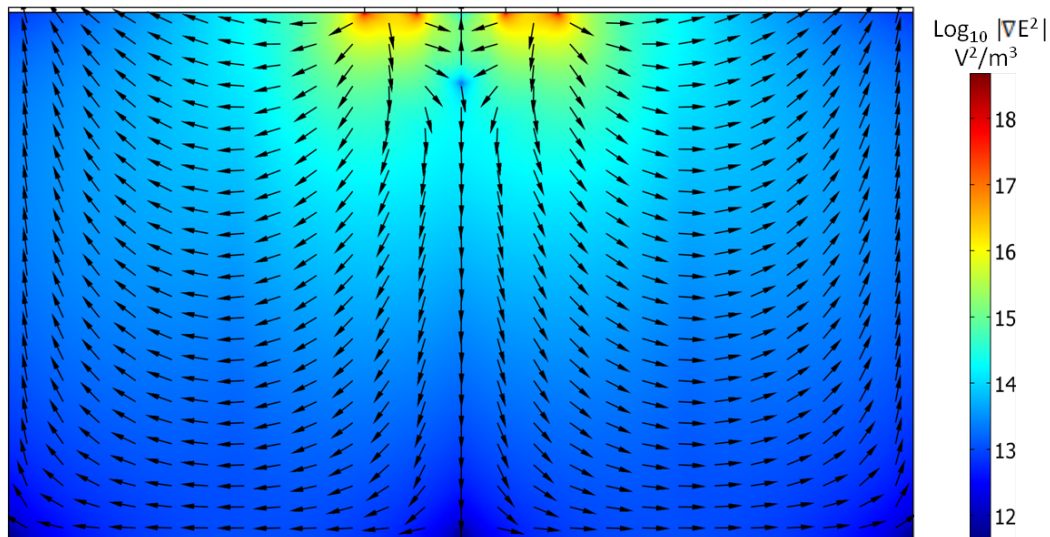


Figure 7-5: Simulated ∇E^2 for a ring trap. Scale bar shows the magnitude of the gradient of the electric field squared and the black arrows show the direction of the DEP force for an insulating MB. A negative DEP force points away from high field regions. However, the use of a ring trap results in the DEP force pointing towards the centre of the ring. Hence, the result is a stable MB trap which can be used to select and move single MBs.

In Figure 7-6 we demonstrated a sequence of single MB manipulations where the diameter of the MB was $7 \mu\text{m}$. First, a MB was targeted (Figure 7-6a) and the light pattern was moved (keyboard controlled) to encircle the MB in the absence of an applied electric field (Figure 7-6b). When the MB was targeted, a frequency of 70 KHz and voltage of 10 V was applied to create a stable trap. This was followed by a horizontal and vertical movement of the ring pattern to isolate the MB (Figure 7-6c-d).

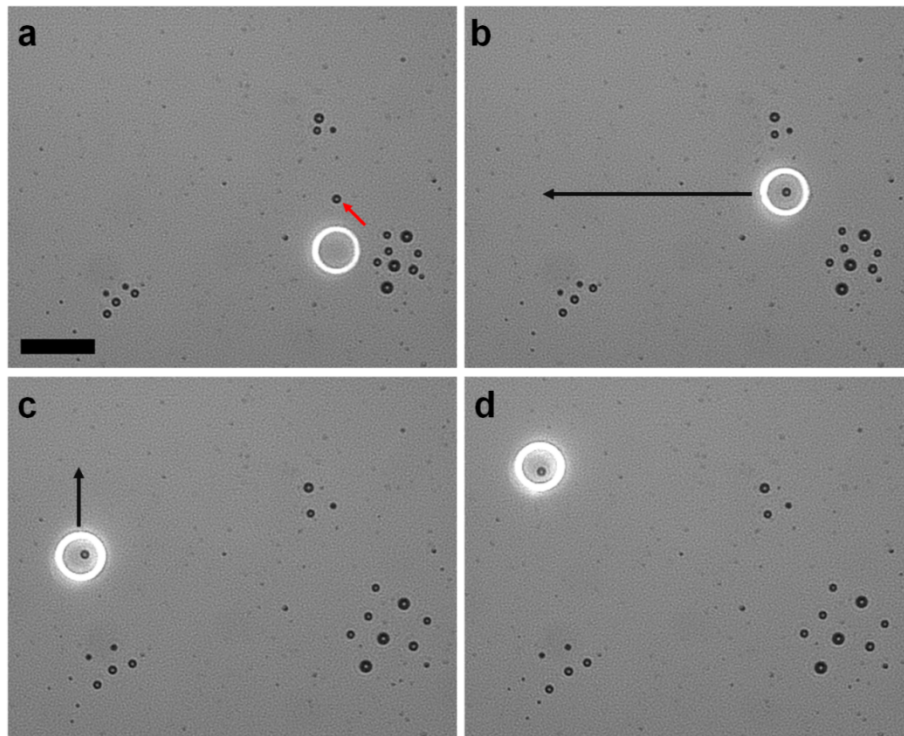


Figure 7-6: (a-d) Selective trapping and moving of 7 μm microbubble using a light induced dielectrophoretic trap at 70 KHz and 10 V. Scale bar: 50 μm .

During these experiments, the influence of the electric field on the MB appearance was visually monitored. Electroporation is likely to cause damage to the phospholipid layer as it is seen in experiments with cells when threshold electric field is applied to the sample. Under the given conditions (70 KHz, 10 V), no change in the MB morphology was observed when trapped and transported by light induced dielectrophoresis. The exposure times to the electric field were in the range of 5-10 minutes. The electric field strength in the liquid was modelled and is shown in Figure 7-7a. The field strength was higher close to the surface of the photoconductor and decreased rapidly towards the bulk liquid (Figure 7-7c). The highest field strength was close to the inner and outer edge of the projected ring pattern with values of 5.6 kV/cm and 7.4 kV/cm (10 nm above the aSi layer) respectively (Figure 7-7b).

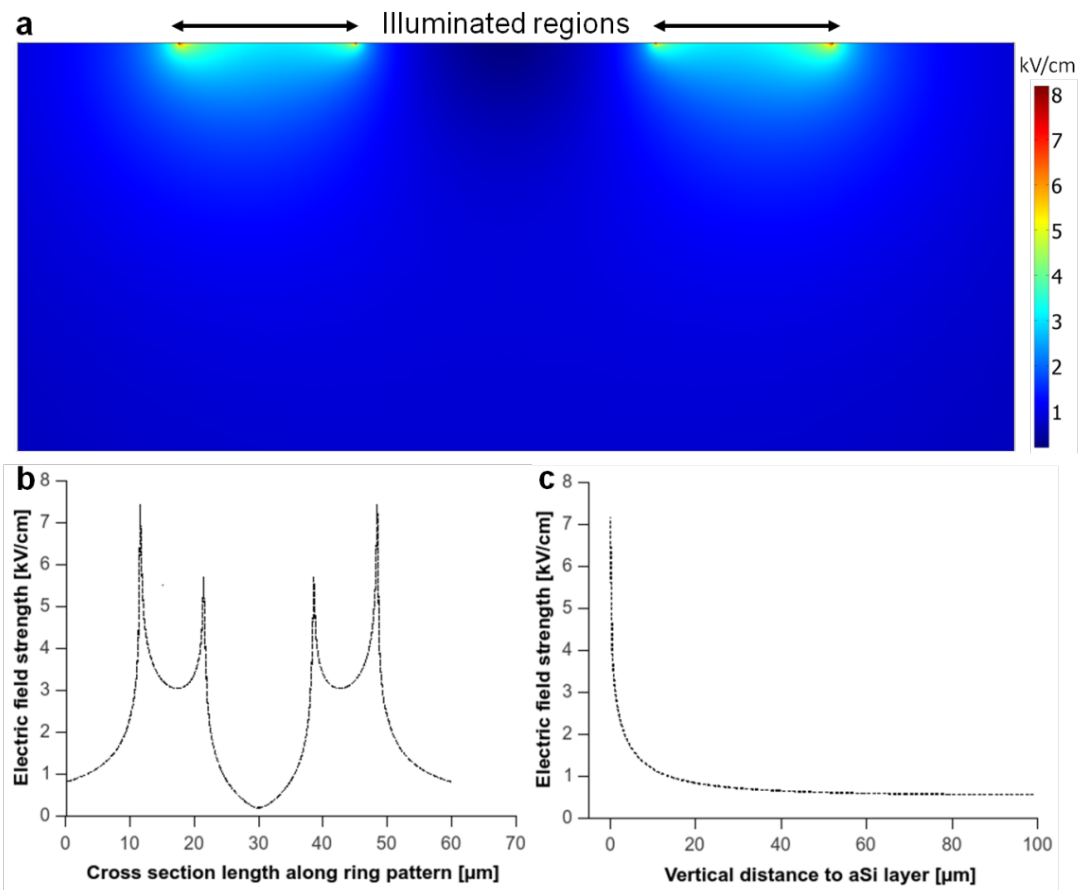


Figure 7-7: 2D cross section model of the electric field strength distribution when a ring pattern illumination was used with 70 KHz and 10 V applied to the OET chip. The colours represent the electric field strength in kV/cm. (b) Cross section plot of the electric field strength along the ring pattern 10 nm above the aSi layer. Peak values of 7.4 kV/cm and 5.6 kV/cm correspond to outer and inner edge of the ring pattern. (c) Decay of the electric field at the outer edge of the ring pattern with increasing distance to the aSi layer.

The maximum velocity of transported particles was of interest to get insight into the times needed to perform manipulation tasks. Therefore, several MB of different sizes were trapped in the ring pattern at 70 KHz and 10 V, followed by linear movements of the trap. The velocity was increased to a maximum value close to the point where the MB escaped from the trap. Figure 7-8 shows the velocities for MBs of sizes from 2.7 μm to 7.1 μm . The measured velocities for this size range were 2.5 $\mu\text{m/s}$ to 11 $\mu\text{m/s}$ corresponding to forces of 0.06 pN to 0.73 pN.

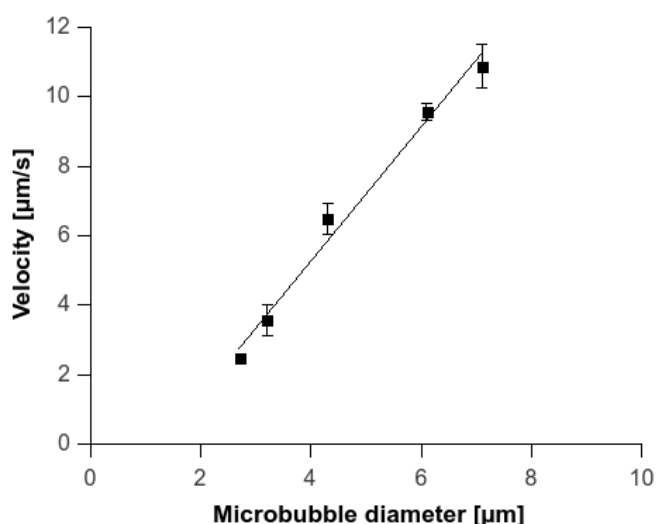


Figure 7-8: Velocities of various sizes of microbubbles when trapped and moved in ring pattern applying 10 V and 70 KHz.

Subsequently, MB insonation was investigated by coupling an acoustic signal from the SAW device into the optoelectronic chip. MBs respond to an alternating pressure field by volume oscillation. The magnitude of the pressure defines whether the oscillation is linear or nonlinear.³³⁹ When low acoustic pressures are applied (up to 100 KPa), the radius of the MB oscillates linearly in relation to the amplitude of the pressure field.³⁴⁹ High pressure amplitudes instead result in nonlinear oscillations of the MB, where the contracting (compression) phase differs from the expanding phase. The oscillation behaviour can be observed but a high speed camera (several MHz) would have been necessary but was not available during this study. Therefore, we focused on bubble behaviour on longer time scales and started with the coupling of the ultrasound into the chip. In Figure 7-9 a MB sample in the OET device before (a) and after (b) acoustic actuation can be seen. Here, the ultrasound signal (2.8 MHz, 50V) was applied for several seconds.

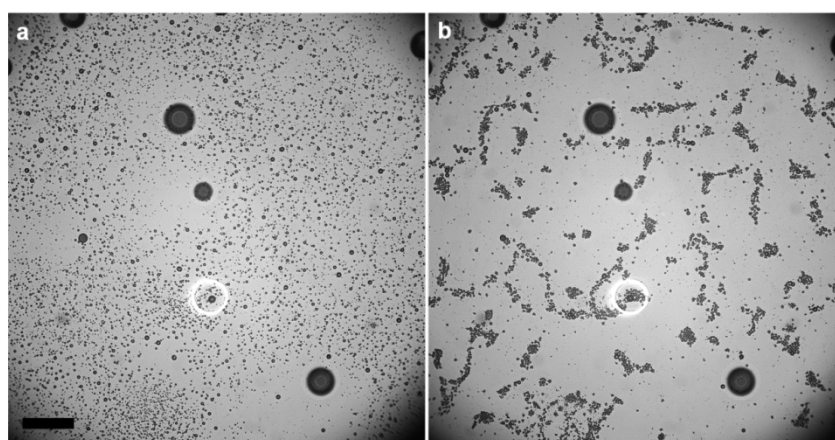


Figure 7-9: Microscopic images show inhomogeneous acoustic pressure distribution. (a) Chip filled with microbubble suspension. (b) Accumulation of microbubble in local pressure maxima after coupling of ultrasound into the chip at 2.8 MHz and 50 V. Scale bar: 100 μm.

An instantaneous movement of MBs was observed once the SAW device was activated. The surface acoustic wave was coupled into the microfluidic chamber creating a rather complex pressure distribution as a result of wave reflections at interfaces along the device boundary, similar to standing waves. This generated a rapid translation of MBs, driven by the PAR force, towards areas of maximal pressure changes. However, such a MB movement was unwanted in the device and a pulsed ultrasound signal, as is used in most ultrasound studies, was applied to study the MB behaviour without lateral movement. In detail we applied a sine wave signal (2.8 MHz, 60V) of 12 cycles with a pulse repetition frequency of 300 ms. This frequency was chosen based on good MB response compared to higher frequency (>3 MHz). Figure 7-10 (a-d) shows the response of a trapped MB during constant insonation for 86 seconds. The acoustic actuation resulted in the shrinking of the MB until complete dissolution. The measured pressure amplitude, using a fibre-optic hydrophone (Precision Acoustics, UK), was 100 KPa. During these experiments it was noticed that only a constantly insonified MB showed this behaviour, while short exposure times of several seconds caused no visible (camera with low framerate) effect.

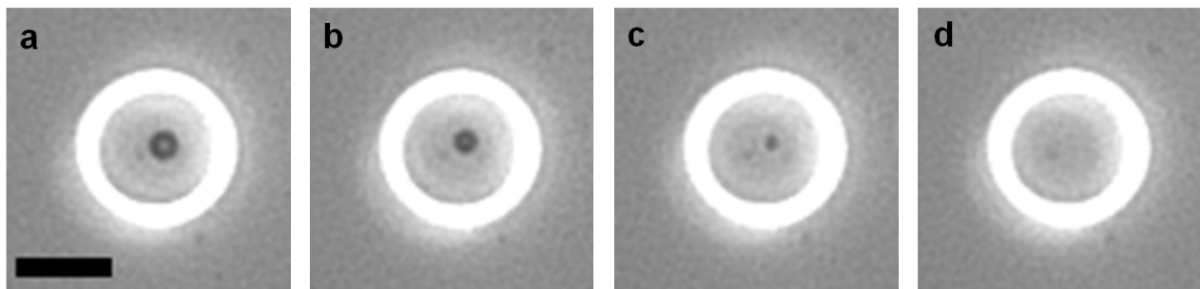


Figure 7-10: Microbubble (7 μm) response after activation of acoustic transducer (2.8 MHz, 60V, burst mode, 300ms) where (e) is 0 s, followed by 37 s (f), 73 s (g) and 86 s (h). Scale bar: 20 μm .

The resonance frequency of a simple gas bubble at low pressure amplitudes (e.g. standard atmospheric pressure) can be approximated by the simple harmonic oscillation. An expression for determining the resonance frequency of a MB of a certain size was developed by Medwin *et al.*³⁵⁰ However, it has been shown that the acoustic behaviour of structurally more complex MBs (e.g. encapsulation) is significantly altered. A shell (e.g. phospholipid) causes an increase in resonance frequency due its stiffness and an increase in damping due to its viscosity.³⁵¹ Therefore, the simple analytical expression given by Medwin *et al.* resulted in lower frequency values while in fact higher frequencies should be assumed for SonoVue MBs. As mentioned above, SonoVue MBs responded at 2.8 MHz with size changes as shown in Figure 7-10. This agrees well with previous studies where similar resonance frequencies for populations of SonoVue MBs were found to be 3 MHz and 2.9 MHz.^{339, 349} Also, a non-linear MB oscillation mode called ‘compression-only’ has been identified in these

studies and could be an explanation for the observed MB shrinkage when constantly insonified. A more detailed description of this non-linear behaviour is given below.

The response to a particular frequency was investigated for MBs of different sizes. A range of MBs were selectively trapped, isolated and arranged in an array. It has to be noted that the OET chip can be of great benefit for this, as the whole process from injecting the MBs to specifically selecting individual MBs can be performed at relatively short time scales of around 10 to 15 minutes. In Figure 7-11a, MBs with sizes of 4.0 μm to 9.0 μm were held in ring patterns before insonation at 2.8 MHz (60 V). The array arrangement was chosen to avoid bubble-bubble interaction. In previous studies it has been shown that the MB response to an ultrasound signal was altered in the presence of nearby MBs.³⁵² The MB oscillation when insonified can induce non-inertial cavitation (e.g. microstreaming) and Bjerknes forces. These effects may influence single bubble studies when inter-MB distances are small ($< 40 \mu\text{m}$ ³⁵²). The following image sequences (Figure 7-11) show time points during insonation. In Figure 7-11b, after 1.21 minutes, the right column of the array is empty indicating complete MB dissolution. Subsequently, in Figure 7-11c and 7-11d, the remaining MBs disappeared after 1 min 45 s and 3 min 45 s. The size change for every MB was measured during insonation. Figure 7-12 shows the change in MB diameter over time. The dissolution time of MBs increased with increasing MB diameter. For instance, a 4 μm MB was dissolved after 25 s while 230 s were needed to completely dissolve the 9 μm MB.

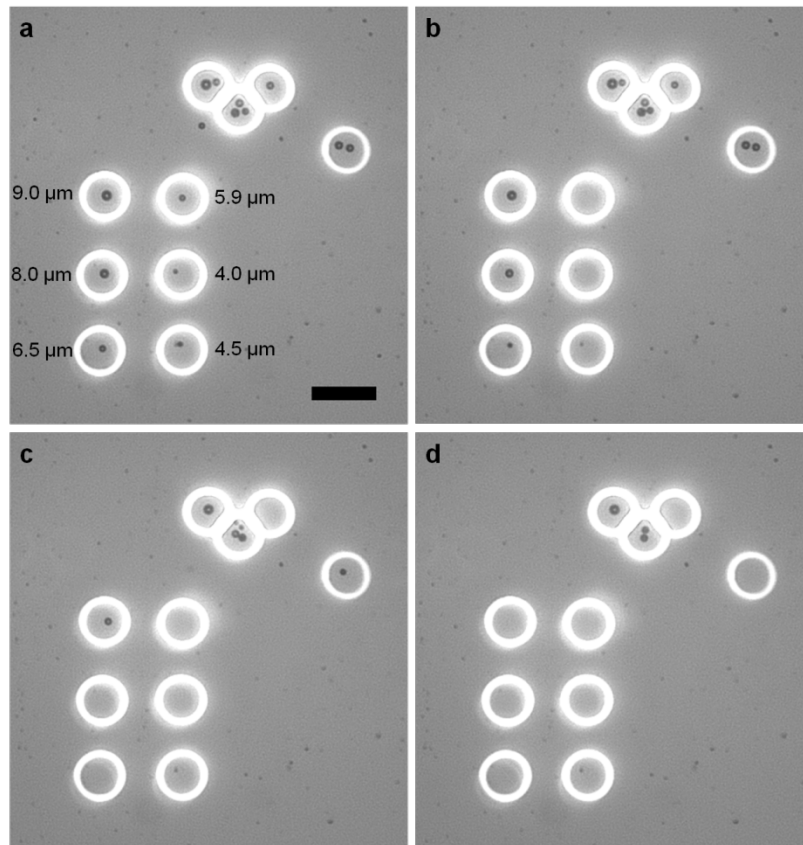


Figure 7-11: (a) Trapping of different sized microbubbles in dielectrophoretic trap at 70 KHz and 10 V. (b-d) Insonation (2.8 MHz, 60V, burst mode 12 cycles, 300 ms) of microbubbles (b) after 1.21 min (c) 1.45 min and (d) 3.45 min. Scale bar 200 μm .

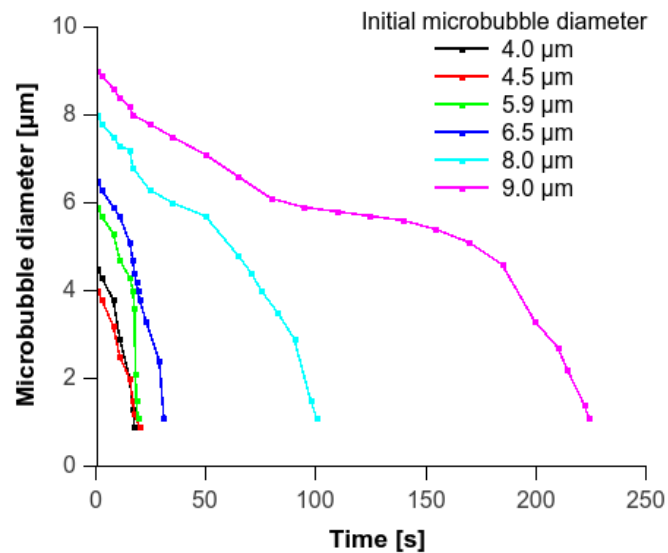


Figure 7-12: Change in microbubble diameter over time when acoustically actuated at 2.8 MHz using 60 V. Microbubbles were kept in dielectrophoretic trap at 70 KHz and 10V.

From the experiments above it can be concluded that the SAW device actuation was able to insonify MBs of different sizes using a single frequency and acoustic pressure amplitude.

The stimulation led to MB shrinkage until dissolution but sudden impulsion in the form of inertial cavitations was not observed. This can be associated to a lack of acoustic energy generated by the SAW device and a limited output voltage generated by the amplifier resulting in ultrasound pulses with pressures of 100 kPa, which can be considered as a low acoustic pressure.^{349, 353}

The shrinkage of the MBs could be attributed to acoustically driven diffusion. The rate of diffusion, which is dependent on the shell material as well as concentration gradient of the gas, can be significantly affected during insonation because of the changing pressure over time and the motion of the gas liquid interface.³⁵³ MBs usually undergo forced expansions and compressions when insonified. During the expansion phase an increased inward diffusion can dominate over the outwards diffusion. However, during the compression phase the outwards diffusion can dominate. This phenomenon has been observed in studies by Cha and Henry³⁵⁴. A decrease in diameter of a lipid-shelled MB (MP1950) during insonation (2.25 MHz, 240 kPa) has also been observed in a study by Chomas *et al.*³⁵³ Similar to the observation in this study, MB shrinkage was only stimulated when the ultrasound was switched on. No decrease was observed after insonation showing that the shell of the MB was intact and the size changes were because of acoustically driven diffusion. Interestingly, a single frequency and pressure amplitude can be applied to destruct MBs of different sizes. Chomas *et al.* used bubbles in the range of 3 μm to 6 μm . Here, destruction of MBs of 4 μm to 9 μm in diameter was demonstrated. This indicates that a frequency or pressure dependency in regards to the size based MB response was absent under the given conditions. In fact, an onset of MB vibration at resonance and off-resonance for certain pressures has been shown by Emmer *et al.*³⁵⁵ An acoustic pressure threshold of 30 kPa to 120 kPa for different lipid-shelled MB (2 μm to 11 μm) was necessary for stimulated MB oscillation.

Alternatively to the concept of forced expansions and compressions with net diffusions out of the bubble, a recent study has shown that SonoVue MB undergo a compression-only mode when insonified.³⁵⁶ Here the MBs compress more than they expand. This non-linear behaviour has been explained by pressure induced buckle and folding of the lipid monolayer which results in easier compression than expansion.³⁵⁷ More specifically, it is understood that a 3D collapse of the monolayer occurs when the phospholipid monolayer is compressed beyond its saturated phospholipid concentration.³⁵⁸ Hence, this could possibly lead to a directed diffusion when the gas pressure in the MB increases during the compression phase while being at rest between the compression phases. More gas is forced out of the bubble

during the compression phase induced by a steep concentration gradient along the MB/liquid interface. Moreover, work on the compression-only behaviour by de Jong *et al.*³⁵⁹ has shown that there is no clear dependency on the initial bubble radius, the applied frequency or the pressure amplitude which corresponds partially to the first results seen in this study. However, the explanation has to be handled with care as a model by Marmottant *et al.*³⁶⁰ was successfully used to relate the compression-only behaviour with the change in surface tension during the buckling of the monolayer. The phospholipid concentration at the gas/liquid interface affects the surface tension. A change in the bubble radius (change in lipid concentration) changes the surface tension. The compression-only mode is then associated with a reduction of the surface tension due to a decreasing MB radius. But the reduced surface tension disagrees with the phenomenon of acoustically driven diffusion because in the buckling mode the surface tension is considered to be close to zero which counts for the longevity of MBs and counteracts the diffusion out of MBs.

Last but not least, rupturing of the phospholipid shell after many cycles of expansions and compression may offer another explanation. When the shell material breaks up, the surface of the MB is partially uncovered. This can promote the release of gas out of the MB core.

In summary, the initial experiments using this manipulation platform showed promising results in terms of individual MB handling and insonation but also raised lots of interesting question in terms of the observed phenomena. Currently, a lack of measurement equipment, for optical (e.g. high speed camera system) and acoustical investigations (e.g. transducer for attenuation and scattering measurements) inhibit a detailed characterisation but will be tackled for future studies which focus on single MBs as well as MB-cell interactions. The latter especially might benefit from the enhance MB control given by the proposed micromanipulation system.

7.4. Conclusion

We proposed a novel micromanipulation platform for the parallel characterisation of individual or grouped MBs during ultrasound excitation. It was demonstrated that an optoelectronic tweezer device can be applied to selectively trap and isolate single MBs of different sizes within a heterogeneous sample. Using a voltage of 10 V at 70 KHz, we were able to transport MBs of different sizes (2.7 μm to 7.1 μm) with speeds of 2.5 $\mu\text{m/s}$ to 11 $\mu\text{m/s}$. Moreover, insonation of MBs was achieved by coupling a surface acoustic wave from a SAW device into the optoelectronic chip. The successful actuation after ultrasound

activation was identified through MB size changes. The exposure to the alternating acoustic pressure field caused an increased diffusion of SF₆ from the MB core into the surrounding liquid until total dissolution. Primarily, it was suggested that an acoustically driven diffusion out of the bubble during compression cycles is the underlying mechanism. Alternatively, shell defects due to the mechanical load can contribute to the diffusion. The diffusion in terms of diameter change was shown for MBs of different sizes. The total dissolution time was a function of the size of the MB under the applied experimental conditions which agrees with the proposed diffusion mechanism.

The advantage of the proposed system can be summarized as follows. The introduced concept provides a microfluidic environment for controlled experiments contained in one device with visual inspection through a microscope. Furthermore, the capability of patterning light in arbitrary shapes to form non-uniform electric fields enables precise MB control. The parameters of the optoelectronic chip can be tuned in terms of field strength or chip geometry to be able to work with different sized MBs. The ultrasound transducer works in a frequency range relevant for medical concepts and moreover, a wider range of frequencies can be applied simply by changing the slanted electrode design.

At the moment, a disadvantage is that only low acoustic energy is coupled into the chip producing low acoustic pressures. It would be desirable to have a tuneable system which is able to create high acoustic pressures in order to induce microstreaming, inertial cavitation effects and asymmetric bubble collapse. To solve this problem, the first step would be the replacement of double sided tape and the use of more rigid material such as SU8 to reduce the energy loss due to acoustic absorption. In addition, transducer output can be improved by using a different electrode design with an increased number of electrodes creating a better coupling efficiency into the piezoelectric substrate and hence into the optoelectronic chip.

The study of single MB behaviour is of course only the first step towards the understanding of more complex phenomena. In reality the MB behaviour is influenced by many factors such as the presence of nearby MBs which may alter the way the cavitation process takes place. Starting from understanding simple systems (single MB studies) followed by a stepwise subsequent increase in the complexity (adding MBs) can help to decipher the underlying relationships that explain the observed phenomena. In future, we hope that the developed system may be used for such an approach as well as for the study of MB and cell interactions to aid the development of drug delivery or controlled tissue damage.

8. Summary

Micromanipulations platforms have gained increased attention over the last decades. They enable handling of particles in minute samples within microfluidic compartments and demonstrate promising routes to enhance procedures in important fields such as analytical chemistry and medical diagnosis. Non-contact approaches based on externally applied force fields allow researchers to probe and alter particle states in a gentle, precise and controlled manner. Among them, especially forces generated by acoustic and electric fields received the attention of researchers developing lab on a chip, micro total analysis and point of care systems. This is evident by the vast amount of literature dealing with physical phenomena such as dielectrophoresis and acoustophoresis applied to miniaturised systems. Each of these methods has its merits. Ideally, a system that combines it all (“eierlegende Wollmilchsau”) would be of great benefit for the scientific community.

The thesis introduced a concept for a unified platform that enabled the use of acoustic and electric fields for particle manipulations in microfluidic environments. In particular, optoelectronic tweezing (OET), also known as light induced dielectrophoresis was fused with acoustic tweezing, also known as acoustophoresis, on a versatile system. The system can be divided into two individual physical units. The first one represents the OET unit which integrated light induced electric fields into a robust microfluidic chip. The OET chip not only operated as room for electric field generation but also as transverse resonator to confine acoustic fields. These fields were the result of travelling surface acoustic waves excited by a piezoelectric transducer which defined the second unit.

The first experimental chapter focused on the development and characterisation of the OET unit. A fabrication protocol was first designed that enabled the integration of OET into a robust microfluidic chip. A conventional OET device consists of a photoconductor substrate parallel aligned to a second electrode substrate. In this work amorphous silicon (aSi) and indium tin oxide (ITO) were used as substrates and assembled to a composite structure using SU8 negative photoresist as bonding agent as well as frame to define the microfluidic channel. Briefly, SU8 was sandwiched between the electrodes substrate followed by a photolithography step to allow cross linking induced bonding and defining of the microchannel features. The protocol was adjusted at different fabrication steps to be able to alter the depth of the microfluidic channels. Here it was found that changing spin-coating

speeds as well as adjusting soft baking and exposure times for a set of SU8 versions (3050, 3025) yielded SU8 thicknesses in the range of 15 μm to 70 μm . The OET chips were characterised by profile measurements and microscope techniques. The latter one included scanning electron microscopy (SEM) which enabled detailed investigations of the cross-sections of fabricated chips. It is mentioned in the literature that an ideal transverse resonator contains flat and vertical side walls to create standing waves efficiently.⁵¹ However, SEM imaging revealed curved channels walls and deviations from the lateral mask layout dimensions. This has been associated to the unusual sandwiching process in combination with refraction issues during the UV-exposure through several adjacent layers leading to an increase in the lateral dimension by 5 % to 10 %. Nonetheless, the developed fabrication protocol allowed the production of robust channels of high bonding area and strengths using materials which are biocompatible and resistant to chemical and physical strain. The novel chip fabrication process can be applied to different substrates and may find its usage where classical PDMS soft lithography for microfluidics is not applicable.

However, a critical note has to be made concerning a process step within the fabrication protocol which included the developing times of the unexposed SU8 features. The developing took place through inlet and outlet holes in the top ITO substrate. The exposure to the developer solution was spatially limited and mainly diffusion controlled which increased the overall chip fabrication time up to several days for long and narrow microfluidic features. An improved protocol may include the use of ultrasound (MHz range) assisted developing as suggested in the literature.³⁶¹

The performance of fabricated OET chips were experimentally characterised by particle manipulation experiments under continuous flow and device simulations in COMSOL. The velocity of particles before being trapped at virtual electrodes was used as figure of merit and parameter to determine the dielectrophoretic force experienced by the particle. Particle velocities and corresponding dielectrophoretic forces in the range of tens of $\mu\text{m/s}$ to hundreds of $\mu\text{m/s}$ and several pN to tens of pN were achieved by adjusting device and operational parameters including the voltage amplitude, the conductivity of the liquid medium, the depth of the microchannel as well as virtual electrode width and transparency defined in the image projecting software.

The performance of the OET chip improved by an increased voltage amplitude, by lowering the liquid medium conductivity, by decreasing the substrate gap distance while increasing the optical intensity and width of the virtual electrode patterns. Simulations showed that the electric field magnitude in the liquid medium rose according to these parameters and that the

vertical field components may be responsible for characteristic device behaviour. The latter one describes a linear trend observed when increasing the voltage amplitude. The DEP force scales with gradient of the electric field squared which is proportional to the applied voltages. A square dependence was expected, however, the observed linear relationship was associated with a dominating vertical component of the DEP force inducing particle lifting over the potential barrier.

The OET unit as part of the joined micromanipulation platform was individually applied to demonstrate useful microfluidic functions. This included the focussing of particles into precise single particle streams by oblique virtual electrodes as well as sorting of particles of different diameters (3 μm , 6 μm , 10 μm) into channels defined by virtual electrodes. A significant sample throughput required higher particle velocity and hence higher amplitudes applied to the OET chip to increase the DEP force. However, the voltage increase was accompanied with leakage fields in the absence of selective illumination. The photoconductor was not an ideal insulator switching voltage into the liquid medium even in the dark state. A uniform leakage field in the microchannel centre induced particle-particle interactions (pearl chaining). At the microchannel wall, the leakage field was disturbed by the presence of the insulating SU8 photoresist. The curved shape of the wall was expected to produce a rather non-uniform field and was verified by particle distribution near the channel, eventually. The leakage field influences the sorting as larger particles are loaded by smaller ones due to mutual DEP. Furthermore, particles in proximity to the wall undergo motions towards the wall as result of low field magnitudes near the insulator. Virtual electrode projections were not able to address these particles by means of DEP. The leakage field needs to be suppressed in future devices to make particle manipulation more reliable when using OET. A strategy to do so may involve a thicker photoconductive layer ($> 1 \mu\text{m}$) which increases the voltage drop in the dark state and reduces the field in the liquid medium. An attempt has been made to increase the aSi layer thickness but poor adhesion led to cracking and peeling of the layer making device fabrication difficult. An optimisation of the aSi deposition process needs to be undertaken to increase the layer stability. Amorphous silicon layers of more than 1 μm thickness have been achieved, preferably on silicon and oxide substrates.³⁶² Although ITO seems to be an ideal adhesion layer, exposure to elevated temperatures might reduce the surface oxygen³⁶³ which can affect the aSi layer stability.

The second experimental chapter describes the fabrication of the second unit, the surface acoustic wave (transducer), before introducing a novel concept where the first unit is applied as transverse resonator in form of a superstrate placed on the piezoelectric substrate. A SAW transducer consisting of interdigitated electrodes of varying pitch and gaps along the

aperture was developed. This kind of transducer is known as slanted IDT and allows the excitations of multiple frequencies (one at a time) as narrow SAW beams at specific positions in the aperture. The developed transducer design had a fundamental frequency response in the range of 3.7 MHz to 5.5 MHz and was used throughout this study.

The superstrate concept has been tested using disposable glass-polymer-glass composite chips, fabricated using the protocol developed in chapter 3. Although the microchannel was constructed by a polymer and curved channel walls were obtained a one-dimensional plane standing wave was evident at the fundamental resonance of the chip. Sufficient acoustic energy could be coupled into the chip enabling acoustophoretic particle manipulation. In fact, pressure amplitudes of 0.3 MPa to 3.1 MPa were measured when voltages of 5 V to 40 V were applied. The developed superstrate concept addressed the need for disposable substrates⁵³ used in conjunction with SAW based particle manipulation. SAW transducer and piezoelectric substrates are expensive units due to material and fabrication cost while superstrates can be made from cheaper composites or plastic materials. Furthermore, it was shown that the superstrate/transverse resonator concept has some benefits compared to standing surface acoustic wave (SSAW) manipulation in PDMS channels. These include easier device assembling as no precise position, bonding and aligning relative to the pressure nodes on the SAW substrates is required while keeping the benefits of SAW transducer such as high and wide frequency excitation and a planar device structure. The potential of this new concept has been demonstrated showing versatile particle patterning in a static fluid and also tuneable pressure node distribution under continuous flow. Moreover, the PAR force and acoustic streaming induced drag forces experienced by different particles enabled their separation. In particular, the developed strategies for separating trypanosomes from blood cells provide a very promising avenue to improve the enrichment of the parasite and the diagnosis of the disease associated with it.

Besides the outlined advantages of the superstrate concept there is plenty of room for optimisations and extensions. For instance, an alternative transducer design can be developed to try to increase the coupling efficiency into the piezoelectric substrate and the superstrate. At the moment relative high voltages are applied which might be inappropriate for certain system requirements (battery power devices in low resource environments). Moreover, a change to a superstrate completely made of plastics would be desirable which would reduce cost and also enables more rapid prototyping, although the acoustic energy transfer might be a concern and should be investigated. An advanced application might involve the use of several SAW transducers in sequence to allow for multiple microfluidic functions such as focussing, separation or merging. In summary, this chapter introduced the

superstrate concept and showed individual acoustophoretic applications while also laying the foundation of combining acoustic and electric fields in a single microfluidic chip.

The third experimental chapter presented the combined use of electric and acoustic fields under continuous flow. This provided the advantage of performing localized as well as more global particle manipulation with virtual electrodes being applied selectively to small microchannel sections while acoustic standing wave fields being applied along the channel length. Acoustic standing wave fields were well suited to rapidly concentrate particle samples into fixed pressure nodal planes before being addressed by virtual electrodes in form of selective sorting and guiding into channel outlets, pressure nodes or trapping and merging of particle aggregates. The application of locally applied virtual electrodes within a microchannel section can be exploited to support a more localised use of the PAR force as shown by sorting of different sized beads into virtual channels. However, the chapter outlined again that particle-particle interactions arising from leakage fields, patterned electric fields and even acoustic standing wave fields influence manipulation processes including particle focussing and sorting. A strategy to reduce such unwanted interactions may involve the increase in the photoconductor thickness and the introduction of an additional SAW transducer. This might reduce the amount of the field leaking into the liquid layer as most of the voltage drops across the photoconductor in the dark state which reduces pearl chaining effects. An additional acoustic standing wave across the channel height, generated by a second SAW, can be helpful to focus beads into one horizontal plane which also counteracts dipole-dipole interactions.

The fourth experimental chapter applies optoelectronic and acoustic tweezing to perform lysis of cells under continuous and static flow conditions. The lysis of cells is the first step in many bioanalytical investigations where cellular components (e.g. Proteins and DNA) are studied or quantified to characterise cell behaviour. Microfluidic approaches are of great advantage. The need of low sample requirements, reduced sample loss and contamination as well as fast processing can be addressed using on chip handling. In this work a shallow microchannel of 15 μm height was used to demonstrate continuous lysis of red blood cells by light induced electric fields. Simulation of the OET devices were used to investigate the electric field strength and analyse transmembrane potentials induced in red blood cells for the given conditions. Simulation results have been confirmed by successful lysis under static conditions where time-sensitive experiments showed that electric field exposure times of millisecond scales were sufficient to induce irreversible damage to the cells. These findings have been adapted to perform lysis under continuous flow. The OET device was acoustically actuated to form a single cell band along the pressure nodal plane in the microchannel

centre. The combined use of OET and acoustic tweezing enabled cell lysis efficiencies close to 100 % for cell concentrations of $60 \cdot 10^6$ cells/ml. Lysis was improved compared to single OET actuation partially because of removing cells from the shielding channel wall and possibly also due to exposure to high pressure amplitudes. The latter can cause sonoporation of the cell membrane as the result of strong membrane oscillation which can cause mechanical strain strong enough to rupture the bilipid layer. However, control experiments could not confirm sonoporation effects when cells were exposed to high pressure amplitudes and transfection agents. It was speculated that exposure to high pressure amplitudes within the standing wave might have been too short to induce sonoporation but despite this, minor mechanical strain induced by acoustic fields as well as flow induced shear stress could explain an enhanced lysis efficiency. Nonetheless, the presented concept showed lysis of dense cell samples in a microfluidic chip. It was suggested that even higher concentrated cell samples can be successfully lysed when the multi pressure node capability of the SAW device and increased field exposure times are utilized in future investigations.

Also part of this chapter, but in absence of ultrasound, lysis of single cells was demonstrated. It was shown that small virtual electrode spots of up to $2.5 \mu\text{m}$ generated high electric fields which allowed irreversible electroporation in red blood cells. The increased field strength which enabled successful lysis was linked to the reduced gap between the electrode substrates. The precise targeting of cells was carried out in dense population of cells. Neighbouring cells stayed intact owing to the fact that the high field regions were spatially well defined and dropped significantly with small distances from the spot centre. Moreover, this concept has been applied to suspension and adherent cells suspended in physiological buffer solutions. The use of high conductivity solutions in the OET chip impedes the creation of high field regions, as most of the voltage drops across the aSi layer. However, the presence of a cell alters the potential distribution at the interface significantly, as long as the cell is very close to the aSi surface. This has been investigated by simulations and experimentally verified for red blood cells and MCF7 cells adhered to the aSi surface. It is believed that the cell's membrane dominates the impedance at the interface at close distance. And that it generates voltage differences between the cell and the surrounding liquid sufficient for lysis. The complete lysis was achieved within 1 minute upon exposure to the field.

Although the single lysis concept works only for planar cell arrangements (no 3D tissue cell targeting), it may find its application in microfluidic cell culture devices which incorporate

molecular analysis (e.g. ELISA) techniques to identify intracellular components subsequent to single cell lysis steps.

The fifth experimental chapter demonstrated the use of the platform for selective handling of microbubbles (MB) by OET and MB insonation induced by a pressure field in the superstrate. MBs are promising therapeutic tools allowing *in vivo* delivery of chemical compounds (e.g. drugs) to points of need (e.g. tumour) where controlled MB destruction releases the compounds. However, the mechanism governing the MB acoustic field interaction and the impact of the insonified MB on biological cell are not well understood. For instance the influence of the applied insonation frequency on particles of different sizes is of interest to find optimise MB destruction parameters. Therefore, novel tools are required which allow the study of these mechanisms in controlled environments. Here, we showed size dependent MB actuation by non-uniform electric fields upon illumination. MBs were selected and isolated from a group to enable individual characterisation. In combination with a slanted SAW transducer, acoustic energy was coupled to the microfluidic compartment to insonify trapped MBs. The interaction with the sound field led to MB size changes possibly induced by acoustically driven diffusion. Although, the acoustic energy was too low to induce inertial cavitation and micro streaming effects, it is believed that this setup can be helpful for size dependent MB characterisations and MB and cell positioning to study ultrasound induced interaction effects (e.g. poration). An improvement in the transferred acoustic energy can be achieved by replacing of the polymeric adhesive (double sided tape) and the use of more inelastic materials (e.g. SU8). A more powerful wide frequency SAW transducer can be considered, too. The broadband frequency response of the SAW device is of particular interest, as it is able to probe the resonance point of various MB sizes.

9. Conclusion

The study was set out to develop a new microfluidic platform that integrates two popular micromanipulation methods. The combination of optoelectronic and acoustic tweezing aimed to overcome individual technological shortcomings and demonstrate the potential of a hybrid system for microfluidic functions. Optoelectronic tweezing provides the ability for very localised, precise and versatile manipulation while acoustic tweezing offers to manipulate cells and particles across large areas very efficiently.

An essential step towards the creation of a microfluidic platform was made by developing a device concept that enabled the introduction of optoelectronic tweezing into a microfluidic chip which, in addition, can be used as a microfluidic acoustic resonance cavity. The device development described in Chapter 3 is a novel and versatile fabrication process and has the potential to be applied in applications beyond this work. An improvement of the fabrication time should be investigated in future research to achieve a more efficient work flow.

The use of optoelectronic tweezing within a continuous microfluidic system was also demonstrated in Chapter 3. The characterization of the developed chips has shown that light induced dielectrophoresis was not limited to quiescent liquids but can be used for fast (e.g. 5 mm/s) and complex particle manipulation under pressure driven flow. A particular example was presented by a very localised sorting process of a complex particle mixture simply through generating a light pattern gradient. The integration concept demonstrated to be a very promising approach and improvements regards the photoconductor properties can enhance the functionality and may promote a more widespread use.

The link between the integration of optoelectronic and acoustic tweezing was made by introducing the surface acoustic wave technology to the microfluidic chip. Chapter 4 described the novel arrangement where a surface acoustic wave device was connected to the developed microfluidic chip to create the hybrid microfluidic platform. The creation of acoustic standing waves and the associated acoustic forces were investigated experimentally and theoretically by simulations. The flexibility of surface acoustic wave excitation at different frequencies, the simplicity of assembling the system as well as the potential of using the microfluidic chip as disposable unit showed some important advantages compared to other systems. The sole use of acoustic tweezing for complex particle handling was demonstrated by sorting particles and cells with good efficiencies. The strategy of using surface acoustic wave devices in conjunction with disposable and custom

microfluidic chips can be easily expanded by using a range of surface acoustic wave devices in a sequential manner. This would enable localised acoustic manipulation and hence localised control of particles within the microchannel chip.

Both micromanipulation methods were brought together in Chapter 5. It was demonstrated that optoelectronic tweezing can benefit from the acoustic actuation in form of acoustic standing waves. The rapid concentration of particles along the microchannel length using acoustic tweezing complemented the localised and confined manipulation by light induced electric fields. On the other side, optoelectronic tweezing can be used to control the localised enforcement of the acoustic manipulation of particles by competing with the acoustic force as shown by sorting experiments of particle mixtures into virtual microchannels. While the versatility of this system was indicated and potential applications were described, optimisations should be carried out to suppress unwanted effects such as leakage fields. This may include the change of the photoconductor properties as described above and the introduction of an additional acoustic transducer to achieve two-dimensional particle focussing.

The exceptional fine control of optoelectronic tweezing in the developed microchip was demonstrated in Chapter 6. In particular, a true single cell lysis approach based on small light beams was established that can be applied for cells suspended in physiological buffers. Lysis is a very important procedure for cellular studies when analysing the content of selective cells. Microfluidic approaches are ideal technologies for single cell investigations with high throughput. The lysis strategy presented here may be of use for future applications that includes a whole process line including sample preparation and content analysis. The electric field induced lysis was also combined with acoustic tweezing to demonstrate lysis under continuous flow. Again, it was shown that the acoustic actuation complemented the electrical actuation by pre-aligning the cell sample along the microchannel before lysis was induced locally by light induced electric fields. The acoustic counterpart may be even used as an additional way to break up the cell membrane in form of sonoporation once improvements in coupling of the acoustic energy more efficiently have been made.

Last but not least, Chapter 7 addressed challenges that are encountered when handling microbubbles. Therapeutic microbubbles are the focus of many studies due to their potential as drug delivery system. However, a lack of efficient manipulation systems that enable selection, isolation and rearrangement of microbubbles inhibit extensive fundamental studies. The microfluidic platform presented in this work was applied for selective microbubble handling using optoelectronic tweezing as well as insonation and destruction of

microbubbles using surface acoustic waves. The initial results demonstrated that the system could represent a valuable route to study bubble-bubble and bubble-cell interaction.

In summary, the thesis introduced a promising concept in the field of microparticle manipulation in microfluidics and will hopefully find the right attention to inspire students and researcher to develop new technologies or improve and extend existing ones.

10. References

1. Feynman, R.P. in American Physical Society, Vol. 23:5 (Caltech Engineering and Science, California Institute of Technology; 1960).
2. Manz, A., Graber, N. & Widmer, H.M. Miniaturized total chemical analysis systems: A novel concept for chemical sensing. *Sensors and Actuators B: Chemical* **1**, 244-248 (1990).
3. Vanapalli, S.A., Duits, M.H.G. & Mugele, F. Microfluidics as a functional tool for cell mechanics. *Biomicrofluidics* **3** (2009).
4. Streets, A.M. & Huang, Y. Microfluidics for biological measurements with single-molecule resolution. *Current opinion in biotechnology* **25**, 69-77 (2014).
5. DeMello, A.J. Control and detection of chemical reactions in microfluidic systems. *Nature* **442**, 394-402 (2006).
6. Culbertson, C.T., Mickleburgh, T.G., Stewart-James, S.A., Sellens, K.A. & Pressnall, M. Micro total analysis systems: fundamental advances and biological applications. *Anal Chem* **86**, 95-118 (2014).
7. Dittrich, P.S. & Manz, A. Lab-on-a-chip: microfluidics in drug discovery. *Nat Rev Drug Discov* **5**, 210-218 (2006).
8. Di Carlo, D., Irimia, D., Tompkins, R.G. & Toner, M. Continuous inertial focusing, ordering, and separation of particles in microchannels. *Proc Natl Acad Sci U S A* **104**, 18892-18897 (2007).
9. Spielman, L. & Goren, S.L. Improving resolution in coulter counting by hydrodynamic focusing. *Journal of Colloid and Interface Science* **26**, 175-182 (1968).
10. Martel, J.M. & Toner, M. Particle Focusing in Curved Microfluidic Channels. *Sci Rep-Uk* **3** (2013).
11. Yamada, M., Nakashima, M. & Seki, M. Pinched flow fractionation: continuous size separation of particles utilizing a laminar flow profile in a pinched microchannel. *Anal Chem* **76**, 5465-5471 (2004).
12. Yamada, M. & Seki, M. Hydrodynamic filtration for on-chip particle concentration and classification utilizing microfluidics. *Lab Chip* **5**, 1233-1239 (2005).
13. Davis, J.A. et al. Deterministic hydrodynamics: taking blood apart. *Proc Natl Acad Sci U S A* **103**, 14779-14784 (2006).
14. Luo, M.X., Sweeney, F., Risbud, S.R., Drazer, G. & Frechette, J. Irreversibility and pinching in deterministic particle separation. *Applied Physics Letters* **99** (2011).
15. Kuntaegowdanahalli, S.S., Bhagat, A.A., Kumar, G. & Papautsky, I. Inertial microfluidics for continuous particle separation in spiral microchannels. *Lab Chip* **9**, 2973-2980 (2009).
16. Ashkin, A., Dziedzic, J.M., Bjorkholm, J.E. & Chu, S. Observation of a single-beam gradient force optical trap for dielectric particles. *Opt Lett* **11**, 288 (1986).
17. Hatch, G.P. & Stelter, R.E. Magnetic design considerations for devices and particles used for biological high-gradient magnetic separation (HGMS) systems. *J Magn Magn Mater* **225**, 262-276 (2001).
18. Pohl, H.A. The Motion and Precipitation of Suspensoids in Divergent Electric Fields. *J. Appl. Phys.* **22**, 869-871 (1951).
19. Kundt, A. & Lehmann, O. Ueber longitudinale Schwingungen und Klangfiguren in cylindrischen Flüssigkeitssäulen. *Annalen der Physik* **229**, 1-12 (1874).
20. Molloy, J.E. & Padgett, M.J. Lights, action: optical tweezers. *Contemp Phys* **43**, 241-258 (2002).
21. Ashkin, A., Dziedzic, J.M. & Yamane, T. Optical Trapping and Manipulation of Single Cells Using Infrared-Laser Beams. *Nature* **330**, 769-771 (1987).

22. Bowman, R.W. et al. iTweezers: optical micromanipulation controlled by an Apple iPad. *J Optics-Uk* **13** (2011).
23. Kreysing, M.K. et al. The optical cell rotator. *Opt Express* **16**, 16984-16992 (2008).
24. Guck, J. et al. The optical stretcher: A novel laser tool to micromanipulate cells. *Biophysical Journal* **81**, 767-784 (2001).
25. Bustamante, C., Smith, S.B., Liphardt, J. & Smith, D. Single-molecule studies of DNA mechanics. *Current opinion in structural biology* **10**, 279-285 (2000).
26. Grier, D.G. A revolution in optical manipulation. *Nature* **424**, 810-816 (2003).
27. Korda, P.T., Taylor, M.B. & Grier, D.G. Kinetically locked-in colloidal transport in an array of optical tweezers. *Physical review letters* **89**, 128301 (2002).
28. MacDonald, M.P., Spalding, G.C. & Dholakia, K. Microfluidic sorting in an optical lattice. *Nature* **426**, 421-424 (2003).
29. Pamme, N. Magnetism and microfluidics. *Lab Chip* **6**, 24-38 (2006).
30. Kimura, T., Yamato, M. & Nara, A. Particle trapping and undulation of a liquid surface using a microscopically modulated magnetic field. *Langmuir* **20**, 572-574 (2004).
31. Winkleman, A. et al. A magnetic trap for living cells suspended in a paramagnetic buffer. *Applied Physics Letters* **85**, 2411-2413 (2004).
32. Zborowski, M., Malchesky, P.S., Jan, T.F. & Hall, G.S. Quantitative separation of bacteria in saline solution using lanthanide Er(III) and a magnetic field. *Journal of general microbiology* **138**, 63-68 (1992).
33. Lee, H., Purdon, A.M. & Westervelt, R.M. Manipulation of biological cells using a microelectromagnet matrix. *Applied Physics Letters* **85**, 1063-1065 (2004).
34. Zborowski, M. et al. Red blood cell magnetophoresis. *Biophys J* **84**, 2638-2645 (2003).
35. Miltenyi, S., Muller, W., Weichel, W. & Radbruch, A. High gradient magnetic cell separation with MACS. *Cytometry* **11**, 231-238 (1990).
36. Furdui, V.I. & Harrison, D.J. Immunomagnetic T cell capture from blood for PCR analysis using microfluidic systems. *Lab Chip* **4**, 614-618 (2004).
37. Rida, A. & Gijs, M.A. Manipulation of self-assembled structures of magnetic beads for microfluidic mixing and assaying. *Anal Chem* **76**, 6239-6246 (2004).
38. Inglis, D.W., Riehn, R., Austin, R.H. & Sturm, J.C. Continuous microfluidic immunomagnetic cell separation. *Applied Physics Letters* **85**, 5093-5095 (2004).
39. Junho, J., Shen, J. & Grodzinski, P. Micropumps based on alternating high-gradient magnetic fields. *Magnetics, IEEE Transactions on* **36**, 2012-2014 (2000).
40. Wirix-Speetjens, R. & De Boeck, J. On-chip magnetic particle transport by alternating magnetic field gradients. *Magnetics, IEEE Transactions on* **40**, 1944-1946 (2004).
41. Lee, H., Purdon, A.M., Chu, V. & Westervelt, R.M. Controlled Assembly of Magnetic Nanoparticles from Magnetotactic Bacteria Using Microelectromagnets Arrays. *Nano Letters* **4**, 995-998 (2004).
42. Pamme, N. & Manz, A. On-Chip Free-Flow Magnetophoresis: Continuous Flow Separation of Magnetic Particles and Agglomerates. *Analytical Chemistry* **76**, 7250-7256 (2004).
43. Østergaard, S., Blankenstein, G., Dirac, H. & Leistiko, O. A novel approach to the automation of clinical chemistry by controlled manipulation of magnetic particles. *J Magn Magn Mater* **194**, 156-162 (1999).
44. Robert, D. et al. Cell sorting by endocytotic capacity in a microfluidic magnetophoresis device. *Lab Chip* **11**, 1902-1910 (2011).
45. Hayes, M.A., Polson, N.A., Phayre, A.N. & Garcia, A.A. Flow-Based Microimmunoassay. *Analytical Chemistry* **73**, 5896-5902 (2001).
46. Kwakye, S. & Baeumner, A. A microfluidic biosensor based on nucleic acid sequence recognition. *Analytical and Bioanalytical Chemistry* **376**, 1062-1068 (2003).

47. Sun, T. & Morgan, H. in *Electrokinetics and Electrohydrodynamics in Microsystems*, Vol. 530. (ed. A. Ramos) 1-28 (Springer Vienna, 2011).
48. Khoshmanesh, K., Nahavandi, S., Baratchi, S., Mitchell, A. & Kalantar-Zadeh, K. Dielectrophoretic platforms for bio-microfluidic systems. *Biosens Bioelectron* **26**, 1800-1814 (2011).
49. Pethig, R. Dielectrophoresis: Status of the theory, technology, and applications. *Biomicrofluidics* **4**, 022811-022835 (2010).
50. Lenshof, A. & Laurell, T. Continuous separation of cells and particles in microfluidic systems. *Chem Soc Rev* **39**, 1203-1217 (2010).
51. Laurell, T., Petersson, F. & Nilsson, A. Chip integrated strategies for acoustic separation and manipulation of cells and particles. *Chem Soc Rev* **36**, 492-506 (2007).
52. Lin, S.C., Mao, X. & Huang, T.J. Surface acoustic wave (SAW) acoustophoresis: now and beyond. *Lab Chip* **12**, 2766-2770 (2012).
53. Ding, X. et al. Surface acoustic wave microfluidics. *Lab Chip* **13**, 3626-3649 (2013).
54. Hayward, R.C., Saville, D.A. & Aksay, I.A. Electrophoretic assembly of colloidal crystals with optically tunable micropatterns. *Nature* **404**, 56-59 (2000).
55. Chiou, P.Y., Ohta, A.T. & Wu, M.C. Massively parallel manipulation of single cells and microparticles using optical images. *Nature* **436**, 370-372 (2005).
56. Valley, J.K., Jamshidi, A., Ohta, A.T., Hsu, H.-Y. & Wu, M.C. Operational Regimes and Physics Present in Optoelectronic Tweezers. *J Microelectromech Syst* **17**, 342-350 (2008).
57. Adachi, S. *Optical properties of crystalline and amorphous semiconductors : materials and fundamental principles*. (Kluwer Academic Publishers, Boston; 1999).
58. Jamshidi, A. in *Electrical Engineering and Computer Sciences*, Vol. Dissertation (University of California,, Berkeley; 2009).
59. Schwarz, R., Wang, F. & Reissner, M. Fermi-Level Dependence of the Ambipolar Diffusion Length in Amorphous-Silicon Thin-Film Transistors. *Applied Physics Letters* **63**, 1083-1085 (1993).
60. Lipson, A., Lipson, S.G. & Lipson, H. *Optical physics*, Edn. 4th. (Cambridge University Press, Cambridge ; New York; 2011).
61. Cheng, I.F., Liu, S.-L., Chung, C.-C. & Chang, H.-C., Vol. 12 95-105 (Springer Berlin / Heidelberg, 2012).
62. Choi, W., Nam, S.-W., Hwang, H., Park, S. & Park, J.-K. Programmable manipulation of motile cells in optoelectronic tweezers using a grayscale image. *Appl. Phys. Lett.* **93**, 143901-143903 (2008).
63. Lee, S., Park, H.J., Yoon, J.S. & Kang, K.H. Optoelectrofluidic field separation based on light-intensity gradients. *Biomicrofluidics* **4** (2010).
64. Lin, W.-Y., Lin, Y.-H. & Lee, G.-B. Separation of micro-particles utilizing spatial difference of optically induced dielectrophoretic forces. *Microfluidics and Nanofluidics* **8**, 217-229 (2010).
65. Zhu, X., Yi, H. & Ni, Z. Frequency-dependent behaviors of individual microscopic particles in an optically induced dielectrophoresis device. *Biomicrofluidics* **4**, 13202-13202 (2010).
66. Ohta, A.T. et al. Dynamic Cell and Microparticle Control via Optoelectronic Tweezers. *Microelectromechanical Systems, Journal of DOI - 10.1109/JMEMS.2007.896717* **16**, 491-499 (2007).
67. Ohta, A.T. et al. Optically Controlled Cell Discrimination and Trapping Using Optoelectronic Tweezers. *Selected Topics in Quantum Electronics, IEEE Journal of DOI - 10.1109/JSTQE.2007.893558* **13**, 235-243 (2007).
68. Chau, L.H. et al. Self-rotation of cells in an irrotational AC E-field in an opto-electrokinetics chip. *PLoS One* **8**, e51577 (2013).
69. Hwang, H. & Park, J.-K. Rapid and selective concentration of microparticles in an optoelectrofluidic platform. *Lab Chip* **9**, 199-206 (2009).

70. Ohta, A.T. et al. Trapping and Transport of Silicon Nanowires Using Lateral-Field Optoelectronic Tweezers. *2007 Conference on Lasers & Electro-Optics/Quantum Electronics and Laser Science Conference (Cleo/QELS 2007), Vols 1-5*, 1451-1452 (2007).
71. Pauzauskie, P.J., Jamshidi, A., Valley, J.K., Satcher, J.J.H. & Wu, M.C. Parallel trapping of multiwalled carbon nanotubes with optoelectronic tweezers. *Appl. Phys. Lett.* **95**, 113104-113103 (2009).
72. Hwang, H. et al. Reduction of nonspecific surface-particle interactions in optoelectronic tweezers. *Appl. Phys. Lett.* **92**, 024108-024103 (2008).
73. Park, S.Y., Kalim, S., Callahan, C., Teitell, M.A. & Chiou, E.P.Y. A light-induced dielectrophoretic droplet manipulation platform. *Lab on a chip* **9**, 3228-3235 (2009).
74. Hsu, H.-y. et al. Phototransistor-based optoelectronic tweezers for dynamic cell manipulation in cell culture media. *Lab Chip* **10**, 165-172 (2010).
75. Wang, W., Lin, Y.-H., Wen, T.-C., Guo, T.-F. & Lee, G.-B. Selective manipulation of microparticles using polymer-based optically induced dielectrophoretic devices. *Appl. Phys. Lett.* **96**, 113302-113303 (2010).
76. Yang, S.M. et al. Dynamic manipulation and patterning of microparticles and cells by using TiOPc-based optoelectronic dielectrophoresis. *Opt Lett* **35**, 1959-1961 (2010).
77. Neale, S.L. et al. Trap profiles of projector based optoelectronic tweezers (OET) with HeLa cells. *Opt Express* **17**, 5232-5239 (2009).
78. Hwang, H. et al. Interactive manipulation of blood cells using a lens-integrated liquid crystal display based optoelectronic tweezers system. *Electrophoresis* **29**, 1203-1212 (2008).
79. Choi, W., Kim, S.-H., Jang, J. & Park, J.-K. Lab-on-a-display: a new microparticle manipulation platform using a liquid crystal display (LCD). *Microfluidics and Nanofluidics* **3**, 217-225 (2007).
80. Jeorrett, A.H. et al. Optoelectronic tweezers system for single cell manipulation and fluorescence imaging of live immune cells. *Opt Express* **22**, 1372-1380 (2014).
81. Zarowna-Dabrowska, A. et al. Miniaturized optoelectronic tweezers controlled by GaN micro-pixel light emitting diode arrays. *Opt. Express* **19**, 2720-2728 (2011).
82. Neale, S.L., Witte, C. & Cooper, J.M. in European Optical Society Annual Meeting Aberdeen, UK; (2012).
83. Hughes, M.P. *Nanoelectromechanics in engineering and biology*. (CRC, Boca Raton, Fla.; 2003).
84. Jones, T.B. *Electromechanics of particles*, Edn. Digitally printed 1st pbk. (Cambridge University Press, Cambridge ; New York; 2005).
85. Huang, Y., Holzel, R., Pethig, R. & Wang, X.B. Differences in the AC electrodynamics of viable and non-viable yeast cells determined through combined dielectrophoresis and electrorotation studies. *Physics in medicine and biology* **37**, 1499-1517 (1992).
86. Becker, F.F. et al. Separation of human breast cancer cells from blood by differential dielectric affinity. *Proc Natl Acad Sci U S A* **92**, 860-864 (1995).
87. Yang, J. et al. Dielectric properties of human leukocyte subpopulations determined by electrorotation as a cell separation criterion. *Biophys J* **76**, 3307-3314 (1999).
88. Gimsa, J., Muller, T., Schnelle, T. & Fuhr, G. Dielectric spectroscopy of single human erythrocytes at physiological ionic strength: dispersion of the cytoplasm. *Biophys J* **71**, 495-506 (1996).
89. Menachery, A. et al. Counterflow Dielectrophoresis for Trypanosome Enrichment and Detection in Blood. *Sci Rep-Uk* **2** (2012).
90. Ha, C., Ou-Yang, H.D. & Pak, H.K., Vol. 7507 750702-750702-750708(2009).
91. Lau, A.N.K. et al. Antifouling coatings for optoelectronic tweezers. *Lab Chip* **9**, 2952-2957 (2009).

92. Yang, S.-M. et al. Light-driven manipulation of picobubbles on a titanium oxide phthalocyanine-based optoelectronic chip. *Appl. Phys. Lett.* **98**, 153512-153513 (2011).
93. Hoeb, M., Rädler, J.O., Klein, S., Stutzmann, M. & Brandt, M.S. Light-induced dielectrophoretic manipulation of DNA. *Biophys J* **93**, 1032-1038 (2007).
94. Lin, Y.-H. & Lee, G.-B. Optically induced flow cytometry for continuous microparticle counting and sorting. *Biosens Bioelectron* **24**, 572-578 (2008).
95. Chiou, P.Y., Ohta, A.T. & Wu, M.C. Continuous optical sorting of HeLa cells and microparticles using optoelectronic tweezers. *IEEE/LEOS Optical MEMs 2005: International Conference on Optical MEMs and Their Applications*, 83-84 (2005).
96. Hung, S.H., Lin, Y.H. & Lee, G.B. A microfluidic platform for manipulation and separation of oil-in-water emulsion droplets using optically induced dielectrophoresis. *Journal of Micromechanics and Microengineering* **20** (2010).
97. Ohta, A.T. et al. Motile and non-motile sperm diagnostic manipulation using optoelectronic tweezers. *Lab Chip* **10**, 3213-3217 (2010).
98. Valley, J.K. et al. Preimplantation mouse embryo selection guided by light-induced dielectrophoresis. *PLoS One* **5**, e10160-e10160 (2010).
99. Lin, Y.H. et al. The application of an optically switched dielectrophoretic (ODEP) force for the manipulation and assembly of cell-encapsulating alginate microbeads in a microfluidic perfusion cell culture system for bottom-up tissue engineering. *Lab on a chip* **12**, 1164-1173 (2012).
100. Hwang, H., Park, Y.H. & Park, J.K. Optoelectrofluidic control of colloidal assembly in an optically induced electric field. *Langmuir* **25**, 6010-6014 (2009).
101. Hwang, H. & Park, J.-K. Measurement of molecular diffusion based on optoelectrofluidic fluorescence microscopy. *Anal Chem* **81**, 9163-9167 (2009).
102. Hwang, H. & Park, J.-K. Dynamic light-activated control of local chemical concentration in a fluid. *Anal Chem* **81**, 5865-5870 (2009).
103. Chiou, P.Y., Ohta, A.T., Jamshidi, A., Hsu, H.Y. & Wu, M.C. Light-actuated ac electroosmosis for nanoparticle manipulation. *J Microelectromech S* **17**, 525-531 (2008).
104. Valley, J.K. et al. Parallel single-cell light-induced electroporation and dielectrophoretic manipulation. *Lab Chip* **9**, 1714-1720 (2009).
105. Lin, Y.-H. & Lee, G.-B. An optically induced cell lysis device using dielectrophoresis. *Appl. Phys. Lett.* **94**, 033901-033903 (2009).
106. Kremer, C. et al. Shape-Dependent Optoelectronic Cell Lysis. *Angewandte Chemie International Edition* **53**, 842-846 (2014).
107. King, L.V. On the Acoustic Radiation Pressure on Spheres. *Proceedings of the Royal Society of London. Series A - Mathematical and Physical Sciences* **147**, 212-240 (1934).
108. Yosioka, K. & Kawasima, Y. Acoustic radiation pressure on a compressible sphere. *Acustica* **5**, 167-173 (1955).
109. Gorkov, L.P. On the Forces Acting on a Small Particle in an Acoustical Field in an Ideal Fluid. *Sov. Phys. Dokl.* **6**, 773-773 (1962).
110. Barnkob, R., Augustsson, P., Laurell, T. & Bruus, H. Measuring the local pressure amplitude in microchannel acoustophoresis. *Lab Chip* **10**, 563-570 (2010).
111. Lenshof, A., Evander, M., Laurell, T. & Nilsson, J. Acoustofluidics 5: Building microfluidic acoustic resonators. *Lab on a chip* **12**, 684-695 (2012).
112. Manneberg, O., Svennebring, J., Hertz, H.M. & Wiklund, M. Wedge transducer design for two-dimensional ultrasonic manipulation in a microfluidic chip. *Journal of Micromechanics and Microengineering* **18**, 095025-095025 (2008).
113. Groschl, M. Ultrasonic separation of suspended particles - Part I: Fundamentals. *Acustica* **84**, 432-447 (1998).

114. Wiklund, M., Green, R. & Ohlin, M. Acoustofluidics 14: Applications of acoustic streaming in microfluidic devices. *Lab Chip* **12**, 2438-2451 (2012).
115. Muller, P.B., Barnkob, R., Jensen, M.J. & Bruus, H. A numerical study of microparticle acoustophoresis driven by acoustic radiation forces and streaming-induced drag forces. *Lab Chip* **12**, 4617-4627 (2012).
116. Evander, M. et al. Noninvasive acoustic cell trapping in a microfluidic perfusion system for online bioassays. *Anal Chem* **79**, 2984-2991 (2007).
117. Manneberg, O. et al. A three-dimensional ultrasonic cage for characterization of individual cells. *Appl. Phys. Lett.* **93**, 063901-063903 (2008).
118. Shi, J., Huang, H., Stratton, Z., Huang, Y. & Huang, T.J. Continuous particle separation in a microfluidic channel via standing surface acoustic waves (SSAW). *Lab Chip* **9**, 3354-3359 (2009).
119. Lippmann, G. Principe de la conservation de l'électricité. *Annales de chimie et de physique* **24**, 145-145 (1881).
120. Evander, M., Lenshof, A., Laurell, T. & Nilsson, J. Acoustophoresis in wet-etched glass chips. *Anal Chem* **80**, 5178-5185 (2008).
121. Jönsson, H. et al. Particle separation using ultrasound can radically reduce embolic load to brain after cardiac surgery. *Ann Thorac Surg* **78**, 1572-1577 (2004).
122. Jönsson, H., Nilsson, A., Petersson, F., Allers, M. & Laurell, T. Particle separation using ultrasound can be used with human shed mediastinal blood. *Perfusion* **20**, 39-43 (2005).
123. Petersson, F., Aberg, L., Swärd-Nilsson, A.-M. & Laurell, T. Free flow acoustophoresis: microfluidic-based mode of particle and cell separation. *Anal Chem* **79**, 5117-5123 (2007).
124. Petersson, F., Nilsson, A., Holm, C., Jonsson, H. & Laurell, T. Continuous separation of lipid particles from erythrocytes by means of laminar flow and acoustic standing wave forces. *Lab Chip* **5**, 20-22 (2005).
125. Petersson, F., Nilsson, A., Jönsson, H. & Laurell, T. Carrier medium exchange through ultrasonic particle switching in microfluidic channels. *Anal Chem* **77**, 1216-1221 (2005).
126. Burguillos, M.A. et al. Microchannel acoustophoresis does not impact survival or function of microglia, leukocytes or tumor cells. *PLoS One* **8**, e64233 (2013).
127. Augustsson, P., Barnkob, R., Wereley, S.T., Bruus, H. & Laurell, T. Automated and temperature-controlled micro-PIV measurements enabling long-term-stable microchannel acoustophoresis characterization. *Lab on a chip* **11**, 4152-4164 (2011).
128. Persson, J., Augustsson, P., Laurell, T. & Ohlin, M. Acoustic microfluidic chip technology to facilitate automation of phage display selection. *FEBS J* **275**, 5657-5666 (2008).
129. Yasuda, K. et al. Using acoustic radiation force as a concentration method for erythrocytes. *J. Acoust. Soc. Am.* **102**, 642-645 (1997).
130. Kapishnikov, S. Continuous particle size separation and size sorting using ultrasound in a microchannel. *Journal of Statistical Mechanics: Theory and Experiment* **2006**, P01012---P01012 (2006).
131. Brown, G.C. & Mussett, A.E. *The inaccessible earth.* (Allen & Unwin, London ; Boston; 1981).
132. Liu, Y. & Lim, K.-M. Particle separation in microfluidics using a switching ultrasonic field. *Lab Chip* **11**, 3167-3173 (2011).
133. Jung, B., Fisher, K., Ness, K.D., Rose, K.A. & Mariella, J.R.P. Acoustic particle filter with adjustable effective pore size for automated sample preparation. *Anal Chem* **80**, 8447-8452 (2008).
134. Hammarström, B. et al. Non-contact acoustic cell trapping in disposable glass capillaries. *Lab Chip* **10**, 2251-2257 (2010).
135. Hammarstrom, B., Laurell, T. & Nilsson, J. Seed particle-enabled acoustic trapping of bacteria and nanoparticles in continuous flow systems. *Lab on a chip* **12**, 4296-4304 (2012).

136. Lilliehorn, T. et al. Trapping of microparticles in the near field of an ultrasonic transducer. *Ultrasonics* **43**, 293-303 (2005).
137. Guo, S.S. et al. Ultrasonic particle trapping in microfluidic devices using soft lithography. *Appl. Phys. Lett.* **92**, 213901-213903 (2008).
138. Ratier, C. & Hoyos, M. Acoustic programming in step-split-flow lateral-transport thin fractionation. *Anal Chem* **82**, 1318-1325 (2010).
139. Harris, N.R., Hill, M., Keating, A. & Baclet-Choulet, P. A lateral mode flow-through PMMA ultrasonic separator. *International Journal of Applied Biomedical Engineering* **5**, 8pp (2012).
140. Gonzalez, I. et al. A polymeric chip for micromanipulation and particle sorting by ultrasounds based on a multilayer configuration. *Sensor Actuat B-Chem* **144**, 310-317 (2010).
141. Wixforth, A. Acoustically driven microfluidic applications for on-chip laboratories. 778-783 (2009).
142. Hribšek, M., Tošić, D. & Radosavljević, M. Surface Acoustic Wave Sensors in Mechanical Engineering. *FME Transactions* **38**, 7 (2010).
143. Ding, X. et al. On-chip manipulation of single microparticles, cells, and organisms using surface acoustic waves. *Proc Natl Acad Sci U S A* **109**, 11105-11109 (2012).
144. Bourquin, Y., Reboud, J., Wilson, R. & Cooper, J.M. Tuneable surface acoustic waves for fluid and particle manipulations on disposable chips. *Lab Chip* **10**, 1898-1901 (2010).
145. Yeo, L.Y. & Friend, J.R. Ultrafast microfluidics using surface acoustic waves. *Biomicrofluidics* **3**, 12002 (2009).
146. Shi, J. et al. Three-dimensional continuous particle focusing in a microfluidic channel via standing surface acoustic waves (SSAW). *Lab Chip* **11**, 2319-2324 (2011).
147. Gronewold, T.M. Surface acoustic wave sensors in the bioanalytical field: recent trends and challenges. *Anal Chim Acta* **603**, 119-128 (2007).
148. Jonathan, D.A. et al. High-throughput, temperature-controlled microchannel acoustophoresis device made with rapid prototyping. *Journal of Micromechanics and Microengineering* **22**, 075017 (2012).
149. Nordin, M. & Laurell, T. Two-hundredfold volume concentration of dilute cell and particle suspensions using chip integrated multistage acoustophoresis. *Lab Chip* **12**, 4610-4616 (2012).
150. Nam, J., Lee, Y. & Shin, S. Size-dependent microparticles separation through standing surface acoustic waves. *Microfluidics and Nanofluidics*, 1-10 (2011).
151. Zeng, Q., Chan, H.W.L., Zhao, X.Z. & Chen, Y. Enhanced particle focusing in microfluidic channels with standing surface acoustic waves. *Microelectronic Engineering* /05 **87**, 1204-1206 (2010).
152. Johansson, L., Enlund, J., Johansson, S., Katardjiev, I. & Yantchev, V. Surface acoustic wave induced particle manipulation in a PDMS channel-principle concepts for continuous flow applications. *Biomed Microdevices* (2011).
153. Johansson, L. et al. Surface acoustic wave-induced precise particle manipulation in a trapezoidal glass microfluidic channel. *Journal of Micromechanics and Microengineering* **22** (2012).
154. Friend, J. & Yeo, L.Y. Microscale acoustofluidics: Microfluidics driven via acoustics and ultrasonics. *Rev. Mod. Phys.* **83**, 647-704 (2011).
155. Reboud, J. et al. Shaping acoustic fields as a toolset for microfluidic manipulations in diagnostic technologies. *Proc Natl Acad Sci U S A* **109**, 15162-15167 (2012).
156. Wilson, R. et al. Phononic crystal structures for acoustically driven microfluidic manipulations. *Lab Chip* **11**, 323-328 (2011).
157. Piyasena, M.E. & Graves, S.W. The intersection of flow cytometry with microfluidics and microfabrication. *Lab on a chip* **14**, 1044-1059 (2014).

158. Piyasena, M.E. et al. Multinode Acoustic Focusing for Parallel Flow Cytometry. *Anal Chem* (2012).
159. Shi, J., Mao, X., Ahmed, D., Colletti, A. & Huang, T.J. Focusing microparticles in a microfluidic channel with standing surface acoustic waves (SSAW). *Lab Chip* **8**, 221-223 (2008).
160. Wood, C.D. et al. Formation and manipulation of two-dimensional arrays of micron-scale particles in microfluidic systems by surface acoustic waves. *Applied Physics Letters* **94**, - (2009).
161. Shi, J. et al. Acoustic tweezers: patterning cells and microparticles using standing surface acoustic waves (SSAW). *Lab Chip* **9**, 2890-2895 (2009).
162. Ding, X. et al. Tunable patterning of microparticles and cells using standing surface acoustic waves. *Lab Chip*, -- (2012).
163. Neild, A., Oberti, S., Radziwill, G. & Dual, J. Simultaneous positioning of cells into two-dimensional arrays using ultrasound. *Biotechnol Bioeng* **97**, 1335-1339 (2007).
164. Bernassau, A.L. et al. Two-dimensional manipulation of micro particles by acoustic radiation pressure in a heptagon cell. *IEEE transactions on ultrasonics, ferroelectrics, and frequency control* **58**, 2132-2138 (2011).
165. Bernassau, A.L., Courtney, C.R.P., Beeley, J., Drinkwater, B.W. & Cumming, D.R.S. Interactive manipulation of microparticles in an octagonal sonotweezer. *Applied Physics Letters* **102**, - (2013).
166. Courtney, C.R.P. et al. Dexterous manipulation of microparticles using Bessel-function acoustic pressure fields. *Applied Physics Letters* **102**, - (2013).
167. Courtney, C.R.P. et al. Independent trapping and manipulation of microparticles using dexterous acoustic tweezers. *Applied Physics Letters* **104**, - (2014).
168. Bernassau, A.L., Gesellchen, F., Macpherson, P.G., Riehle, M. & Cumming, D.R. Direct patterning of mammalian cells in an ultrasonic heptagon stencil. *Biomed Microdevices* **14**, 559-564 (2012).
169. Bernassau, A.L., Macpherson, P.G., Beeley, J., Drinkwater, B.W. & Cumming, D.R. Patterning of microspheres and microbubbles in an acoustic tweezers. *Biomed Microdevices* **15**, 289-297 (2013).
170. Gesellchen, F., Bernassau, A.L., Dejardin, T., Cumming, D.R. & Riehle, M.O. Cell patterning with a heptagon acoustic tweezer--application in neurite guidance. *Lab Chip* **14**, 2266-2275 (2014).
171. Adams, J.D. & Soh, H.T. Tunable acoustophoretic band-pass particle sorter. *Appl Phys Lett* **97**, 064103-064103 (2010).
172. Liu, Y., Hartono, D. & Lim, K.-M. Cell separation and transportation between two miscible fluid streams using ultrasound. *Biomicrofluidics* **6**, 12802-1280214 (2012).
173. Kumar, M., Feke, D.L. & Belovich, J.M. Fractionation of cell mixtures using acoustic and laminar flow fields. *Biotechnol Bioeng* **89**, 129-137 (2005).
174. Ai, Y., Sanders, C.K. & Marrone, B.L. Separation of Escherichia coli bacteria from peripheral blood mononuclear cells using standing surface acoustic waves. *Anal Chem* **85**, 9126-9134 (2013).
175. Nam, J., Lim, H., Kim, D. & Shin, S. Separation of platelets from whole blood using standing surface acoustic waves in a microchannel. *Lab Chip* **11**, 3361-3364 (2011).
176. Jo, M.C. & Guldiken, R. Active density-based separation using standing surface acoustic waves. *Sensors and Actuators A: Physical* **187**, 22-28 (2012).
177. Nam, J., Lim, H., Kim, C., Yoon Kang, J. & Shin, S. Density-dependent separation of encapsulated cells in a microfluidic channel by using a standing surface acoustic wave. *Biomicrofluidics* **6**, 24120-2412010 (2012).
178. Bengtsson, M. & Laurell, T. Ultrasonic agitation in microchannels. *Anal Bioanal Chem* **378**, 1716-1721 (2004).

179. Jo, M.C. & Guldiken, R. Dual surface acoustic wave-based active mixing in a microfluidic channel. *Sensors and Actuators A: Physical* **196**, 1-7 (2013).
180. Franke, T., Braunmüller, S., Schmid, L., Wixforth, A. & Weitz, D.A. Surface acoustic wave actuated cell sorting (SAWACS). *Lab Chip* **10**, 789-794 (2010).
181. Franke, T., Abate, A.R., Weitz, D.A. & Wixforth, A. Surface acoustic wave (SAW) directed droplet flow in microfluidics for PDMS devices. *Lab Chip* **9**, 2625-2627 (2009).
182. Huang, K.W., Su, T.W., Ozcan, A. & Chiou, P.Y. Optoelectronic tweezers integrated with lensfree holographic microscopy for wide-field interactive cell and particle manipulation on a chip. *Lab Chip* **13**, 2278-2284 (2013).
183. Thalhammer, G. et al. Combined acoustic and optical trapping. *Biomedical optics express* **2**, 2859-2870 (2011).
184. Bassindale, P.G., Phillips, D.B., Barnes, A.C. & Drinkwater, B.W. Measurements of the force fields within an acoustic standing wave using holographic optical tweezers. *Applied Physics Letters* **104**, - (2014).
185. Prentice, P., Cuschieri, A., Dholakia, K., Prausnitz, M. & Campbell, P. Membrane disruption by optically controlled microbubble cavitation. *Nat Phys* **1**, 107-110 (2005).
186. Chung, Y.-C., Chen, P.-W., Fu, C.-M. & Wu, J.-M. Particles sorting in micro-channel system utilizing magnetic tweezers and optical tweezers. *J Magn Magn Mater* **333**, 87-92 (2013).
187. Adams, J.D., Thévoz, P., Bruus, H. & Soh, H.T. Integrated acoustic and magnetic separation in microfluidic channels. *Appl Phys Lett* **95**, 254103-254103 (2009).
188. Glynne-Jones, P. & Hill, M. Acoustofluidics 23: acoustic manipulation combined with other force fields. *Lab Chip* **13**, 1003-1010 (2013).
189. Wiklund, M. et al. Ultrasonic standing wave manipulation technology integrated into a dielectrophoretic chip. *Lab Chip* **6**, 1537-1544 (2006).
190. White, R.M. & Voltmer, F.W. DIRECT PIEZOELECTRIC COUPLING TO SURFACE ELASTIC WAVES. *Appl. Phys. Lett.* **7**, 314-316 (1965).
191. Hwang, H., Lee, D.-H., Choi, W. & Park, J.-K. Enhanced discrimination of normal oocytes using optically induced pulling-up dielectrophoretic force. *Biomicrofluidics* **3**, 14103-14103 (2009).
192. Lin, Y.-H. & Lee, G.-B. An integrated cell counting and continuous cell lysis device using an optically induced electric field. *Sensors and Actuators B: Chemical* **145**, 854-860 (2010).
193. Huang, K.W., Wu, T.H., Zhong, J.F. & Chiou, P.Y. in Solid-State Sensors, Actuators and Microsystems Conference, 2009. TRANSDUCERS 2009. International DOI - 10.1109/SENSOR.2009.5285793 1594-1597.
194. Yang, S.-M., Yu, T.-M., Liu, M.-H., Hsu, L. & Liu, C.-H. Moldless PEGDA-Based Optoelectrofluidic Platform for Microparticle Selection. *Advances in OptoElectronics* **2011**, 8-8 (2011).
195. Huang, K.W., Sattar, S. & Chiou, P.Y. in Solid-State Sensors, Actuators and Microsystems Conference (TRANSDUCERS), 2011 16th International DOI - 10.1109/TRANSDUCERS.2011.5969436 1300-1303.
196. del Campo, A. & Greiner, C. SU-8: a photoresist for high-aspect-ratio and 3D submicron lithography. *Journal of Micromechanics and Microengineering* **17**, R81-R81 (2007).
197. Voskerician, G. et al. Biocompatibility and biofouling of MEMS drug delivery devices. *Biomaterials* **24**, 1959-1967 (2003).
198. Nemani, K.V., Moodie, K.L., Brennick, J.B., Su, A. & Gimi, B. In vitro and in vivo evaluation of SU-8 biocompatibility. *Mat Sci Eng C-Mater* **33**, 4453-4459 (2013).
199. Iz, S.G., Ertugrul, F., Eden, E. & Gurhan, S.I. Biocompatibility of glass ionomer cements with and without chlorhexidine. *European journal of dentistry* **7**, S89-93 (2013).
200. Hwang, I.-T., Ahn, M.-Y., Jung, C.-H., Choi, J.-H. & Shin, K. Micropatterning of Mammalian Cells on Indium Tin Oxide Substrates Using Ion Implantation. *Journal of Biomedical Nanotechnology* **9**, 819-824 (2013).

201. Rushe, N. et al. Cytocompatibility of novel tin oxide thin films. *Journal of materials science. Materials in medicine* **16**, 247-252 (2005).
202. Dahmen, C. et al. Surface functionalization of amorphous silicon and silicon suboxides for biological applications. *Thin Solid Films* **427**, 201-207 (2003).
203. Kotzar, G. et al. Evaluation of MEMS materials of construction for implantable medical devices. *Biomaterials* **23**, 2737-2750 (2002).
204. Williams, J.D. & Wang, W. Using megasonic development of SU-8 to yield ultra-high aspect ratio microstructures with UV lithography. *Microsystem Technologies* **10**, 694-698 (2004).
205. Li, D. Encyclopedia of microfluidics and nanofluidics. (Springer, New York; 2008).
206. Lin, C.H., Lee, G.B., Fu, L.M. & Hwey, B.H. Vertical focusing device utilizing dielectrophoretic force and its application on microflow cytometer. *J Microelectromech S* **13**, 923-932 (2004).
207. Holmes, D., Morgan, H. & Green, N.G. High throughput particle analysis: Combining dielectrophoretic particle focussing with confocal optical detection. *Biosensors & Bioelectronics* **21**, 1621-1630 (2006).
208. Khoshmanesh, K. et al. Dielectrophoretic manipulation and separation of microparticles using curved microelectrodes. *Electrophoresis* **30**, 3707-3717 (2009).
209. Huh, D., Gu, W., Kamotani, Y., Grotberg, J.B. & Takayama, S. Microfluidics for flow cytometric analysis of cells and particles. *Physiological measurement* **26**, R73-98 (2005).
210. Godin, J. et al. Microfluidics and photonics for Bio-System-on-a-Chip: A review of advancements in technology towards a microfluidic flow cytometry chip. *J Biophotonics* **1**, 355-376 (2008).
211. Xuan, X.C., Zhu, J.J. & Church, C. Particle focusing in microfluidic devices. *Microfluidics and Nanofluidics* **9**, 1-16 (2010).
212. Hu, X.Y. et al. Marker-specific sorting of rare cells using dielectrophoresis. *P Natl Acad Sci USA* **102**, 15757-15761 (2005).
213. Sochol, R.D., Li, S., Lee, L.P. & Lin, L.W. Continuous flow multi-stage microfluidic reactors via hydrodynamic microparticle raiting. *Lab on a chip* **12**, 4168-4177 (2012).
214. Kim, U., Qian, J.R., Kenrick, S.A., Daugherty, P.S. & Soh, H.T. Multitarget Dielectrophoresis Activated Cell Sorter. *Analytical Chemistry* **80**, 8656-8661 (2008).
215. Brzobohaty, O. et al. Experimental and theoretical determination of optical binding forces. *Opt Express* **18**, 25389-25402 (2010).
216. Kang, K.H. & Li, D.Q. Dielectric force and relative motion between two spherical particles in electrophoresis. *Langmuir* **22**, 1602-1608 (2006).
217. Kovach, K.M., Capadona, J.R., Gupta, A.S. & Potkay, J.A. The effects of PEG-based surface modification of PDMS microchannels on long-term hemocompatibility. *Journal of biomedical materials research. Part A* **102**, 4195-4205 (2014).
218. Bruus, H. Acoustofluidics 7: The acoustic radiation force on small particles. *Lab Chip* **12**, 1014-1021 (2012).
219. Weiser, M.A.H. & Apfel, R.E. Extension of acoustic levitation to include the study of micron-size particles in a more compressible host liquid. *The Journal of the Acoustical Society of America* **71**, 1261-1268 (1982).
220. Vanherberghen, B. et al. Ultrasound-controlled cell aggregation in a multi-well chip. *Lab Chip* **10**, 2727-2732 (2010).
221. Woodside, S.M., Bowen, B.D. & Piret, J.M. Measurement of ultrasonic forces for particle-liquid separations. *AIChE J.* **43**, 1727-1736 (1997).
222. Wiklund, M., Spégel, P., Nilsson, S. & Hertz, H.M. Ultrasonic-trap-enhanced selectivity in capillary electrophoresis. *Ultrasonics* **41**, 329-333 (2003).
223. Johansson, L., Johansson, S., Nikolajeff, F. & Thorslund, S. Effective mixing of laminar flows at a density interface by an integrated ultrasonic transducer. *Lab Chip* **9**, 297-304 (2009).

224. Manneberg, O., Vanherberghen, B., Onfelt, B. & Wiklund, M. Flow-free transport of cells in microchannels by frequency-modulated ultrasound. *Lab Chip* **9**, 833-837 (2009).
225. Wiklund, M., Toivonen, J., Tirri, M., Hanninen, P. & Hertz, H.M. Ultrasonic enrichment of microspheres for ultrasensitive biomedical analysis in confocal laser-scanning fluorescence detection. *J. Appl. Phys.* **96**, 1242-1248 (2004).
226. Saito, M., Kitamura, N. & Terauchi, M. Ultrasonic manipulation of locomotive microorganisms and evaluation of their activity. *J. Appl. Phys.* **92**, 7581-7586 (2002).
227. Coakley, W.T. et al. Cell-cell contact and membrane spreading in an ultrasound trap. *Colloids Surf B Biointerfaces* **34**, 221-230 (2004).
228. Hodgson, R.P., Tan, M., Yeo, L. & Friend, J. Transmitting high power rf acoustic radiation via fluid couplants into superstrates for microfluidics. *Appl. Phys. Lett.* **94**, 024102-024103 (2009).
229. Seemann, K.M., Ebbecke, J. & Wixfort, A. Alignment of carbon nanotubes on pre-structured silicon by surface acoustic waves. *Nanotechnology* **17**, 4529---4529 (2006).
230. Johansson, L., Enlund, J., Johansson, S., Katardjiev, I. & Yantchev, V. Surface acoustic wave induced particle manipulation in a PDMS channel-principle concepts for continuous flow applications. *Biomedical Microdevices* **14**, 279-289 (2012).
231. Yantchev, V. A micromachined Stoneley acoustic wave system for continuous flow particle manipulation in microfluidic channels. *Journal of Micromechanics and Microengineering* **20**, 035031---035031 (2010).
232. Tan, M.K., Yeo, L.Y. & Friend, J.R. Rapid fluid flow and mixing induced in microchannels using surface acoustic waves. *Epl-Europhys Lett* **87** (2009).
233. Bruus, H. Acoustofluidics 7: The acoustic radiation force on small particles. *Lab on a chip* **12**, 1014-1021 (2012).
234. COMSOL in COMSOL Multiphysics Modelling Guide - Acoustics, Edn. 3.3 US; 2006).
235. Bruus, H. Acoustofluidics 2: Perturbation theory and ultrasound resonance modes. *Lab on a chip* **12**, 20-28 (2012).
236. Wang, S.X. et al. Stiffness controlled SU-8-based nanocomposites: application for 1 GHz matching layer conception. *2008 Ieee Ultrasonics Symposium, Vols 1-4 and Appendix*, 678-681 (2008).
237. Dual, J. & Schwarz, T. Acoustofluidics 3: Continuum mechanics for ultrasonic particle manipulation. *Lab on a chip* **12**, 244-252 (2012).
238. Schmid, L., Wixforth, A., Weitz, D.A. & Franke, T. Novel surface acoustic wave (SAW)-driven closed PDMS flow chamber. *Microfluidics and Nanofluidics* **12**, 229-235 (2012).
239. Hagsater, S.M. et al. Acoustic resonances in straight micro channels: Beyond the 1D-approximation. *Lab on a chip* **8**, 1178-1184 (2008).
240. Manneberg, O. et al. Spatial confinement of ultrasonic force fields in microfluidic channels. *Ultrasonics* **49**, 112-119 (2009).
241. Mitchell, R.F. & Read, E. Suppression of Bulk Wave Radiation from Surface Acoustic Wave Devices. *Sonics and Ultrasonics, IEEE Transactions on* **22**, 264-269 (1975).
242. Kakio, S., Hishinuma, K. & Nakagawa, Y. Suppression of bulk wave radiation from leaky surface acoustic waves by loading with thin dielectric films. *J Appl Phys* **87**, 1440-1447 (2000).
243. Koskela, J., Plessky, V.P. & Salomaa, M.T. Suppression of the leaky SAW attenuation with heavy mechanical loading. *Ieee T Ultrason Ferr* **45**, 439-449 (1998).
244. Li, R.C.M. & Alusow, J.A. Suppression of Bulk-Scattering Loss at Saw-Resonator Reflectors. *Electron Lett* **13**, 580-581 (1977).
245. Ebata, Y. in *Ultrasonics Symposium, 1988. Proceedings., IEEE 1988* 91-96 vol.911988).
246. Panda, P.K. Review: environmental friendly lead-free piezoelectric materials. *J Mater Sci* **44**, 5049-5062 (2009).

247. Dual, J. & Moller, D. Acoustofluidics 4: Piezoelectricity and application in the excitation of acoustic fields for ultrasonic particle manipulation. *Lab on a chip* **12**, 506-514 (2012).
248. Lighthill, J. Acoustic Streaming. *J Sound Vib* **61**, 391-418 (1978).
249. Nelson, C.M. & Chen, C.S. Cell-cell signaling by direct contact increases cell proliferation via a PI3K-dependent signal. *FEBS letters* **514**, 238-242 (2002).
250. Tang, J., Peng, R. & Ding, J. The regulation of stem cell differentiation by cell-cell contact on micropatterned material surfaces. *Biomaterials* **31**, 2470-2476 (2010).
251. Garcia, A.J., Vega, M.D. & Boettiger, D. Modulation of cell proliferation and differentiation through substrate-dependent changes in fibronectin conformation. *Molecular biology of the cell* **10**, 785-798 (1999).
252. Xu, T., Jin, J., Gregory, C., Hickman, J.J. & Boland, T. Inkjet printing of viable mammalian cells. *Biomaterials* **26**, 93-99 (2005).
253. Schiele, N.R. et al. Laser-based direct-write techniques for cell printing. *Biofabrication* **2**, 032001 (2010).
254. Torisawa, Y.S., Mosadegh, B., Cavnar, S.P., Ho, M. & Takayama, S. Transwells with Microstamped Membranes Produce Micropatterned Two-Dimensional and Three-Dimensional Co-Cultures. *Tissue engineering. Part C, Methods* (2010).
255. Krasovitski, B., Frenkel, V., Shoham, S. & Kimmel, E. Intramembrane cavitation as a unifying mechanism for ultrasound-induced bioeffects. *P Natl Acad Sci USA* **108**, 3258-3263 (2011).
256. Ankrett, D.N. et al. The effect of ultrasound-related stimuli on cell viability in microfluidic channels. *Journal of nanobiotechnology* **11**, 20 (2013).
257. Carugo, D. et al. Contrast agent-free sonoporation: The use of an ultrasonic standing wave microfluidic system for the delivery of pharmaceutical agents. *Biomicrofluidics* **5**, 44108-4410815 (2011).
258. Rodamporn, S., Harris, N.R., Beeby, S.P., Boltryk, R.J. & Sanchez-Elsner, T. HeLa cell transfection using a novel sonoporation system. *IEEE transactions on bio-medical engineering* **58**, 927-934 (2011).
259. Stich, A., Abel, P.M. & Krishna, S. Human African trypanosomiasis. *BMJ* **325**, 203-206 (2002).
260. Moore, S., Shrestha, S., Tomlinson, K.W. & Vuong, H. Predicting the effect of climate change on African trypanosomiasis: integrating epidemiology with parasite and vector biology. *Journal of the Royal Society, Interface / the Royal Society* **9**, 817-830 (2012).
261. Biéler, S. et al. Improved detection of *Trypanosoma brucei* by lysis of red blood cells, concentration and LED fluorescence microscopy. *Acta Tropica* **121**, 135-140 (2012).
262. Mitashi, P. et al. Human african trypanosomiasis diagnosis in first-line health services of endemic countries, a systematic review. *PLoS neglected tropical diseases* **6**, e1919 (2012).
263. Lenshof, A., Magnusson, C. & Laurell, T. Acoustofluidics 8: Applications of acoustophoresis in continuous flow microsystems. *Lab on a chip* **12**, 1210-1223 (2012).
264. Thévoz, P., Adams, J.D., Shea, H., Bruus, H. & Soh, H.T. Acoustophoretic synchronization of mammalian cells in microchannels. *Anal Chem* **82**, 3094-3098 (2010).
265. Ravula, S.K. et al. A microfluidic system combining acoustic and dielectrophoretic particle preconcentration and focusing. *Sensors and Actuators B: Chemical* **130**, 645-652 (2008).
266. Walling, M.A. & Shepard, J.R. Cellular heterogeneity and live cell arrays. *Chem Soc Rev* **40**, 4049-4076 (2011).
267. Smith, Q. & Gerecht, S. Going with the flow: microfluidic platforms in vascular tissue engineering. *Current opinion in chemical engineering* **3**, 42-50 (2014).
268. Manz, A. et al. Planar chips technology for miniaturization and integration of separation techniques into monitoring systems: Capillary electrophoresis on a chip. *Journal of Chromatography A* **593**, 253-258 (1992).
269. Sims, C.E. & Allbritton, N.L. Analysis of single mammalian cells on-chip. *Lab Chip* **7**, 423-440 (2007).

270. Rau, K.R., Quinto-Su, P.A., Hellman, A.N. & Venugopalan, V. Pulsed laser microbeam-induced cell lysis: time-resolved imaging and analysis of hydrodynamic effects. *Biophys J* **91**, 317-329 (2006).
271. Quinto-Su, P.A. et al. Examination of laser microbeam cell lysis in a PDMS microfluidic channel using time-resolved imaging. *Lab Chip* **8**, 408-414 (2008).
272. Marentis, T.C. et al. Microfluidic sonicator for real-time disruption of eukaryotic cells and bacterial spores for DNA analysis. *Ultrasound in medicine & biology* **31**, 1265-1277 (2005).
273. Tandiono, T. et al. Sonolysis of Escherichia coli and Pichia pastoris in microfluidics. *Lab Chip* **12**, 780-786 (2012).
274. Kim, Y.C., Kang, J.H., Park, S.-J., Yoon, E.-S. & Park, J.-K. Microfluidic biomechanical device for compressive cell stimulation and lysis. *Sensors and Actuators B: Chemical* **128**, 108-116 (2007).
275. Di Carlo, D., Jeong, K.H. & Lee, L.P. Reagentless mechanical cell lysis by nanoscale barbs in microchannels for sample preparation. *Lab on a chip* **3**, 287-291 (2003).
276. Kim, J., Johnson, M., Hill, P. & Gale, B.K. Microfluidic sample preparation: cell lysis and nucleic acid purification. *Integrative biology : quantitative biosciences from nano to macro* **1**, 574-586 (2009).
277. Schilling, E.A., Kamholz, A.E. & Yager, P. Cell lysis and protein extraction in a microfluidic device with detection by a fluorogenic enzyme assay. *Anal Chem* **74**, 1798-1804 (2002).
278. Heo, J., Thomas, K.J., Seong, G.H. & Crooks, R.M. A microfluidic bioreactor based on hydrogel-entrapped E. coli: cell viability, lysis, and intracellular enzyme reactions. *Anal Chem* **75**, 22-26 (2003).
279. Kim, S.H., Yamamoto, T., Fourmy, D. & Fujii, T. An electroactive microwell array for trapping and lysing single-bacterial cells. *Biomicrofluidics* **5**, 24114 (2011).
280. Lu, H., Schmidt, M.A. & Jensen, K.F. A microfluidic electroporation device for cell lysis. *Lab Chip* **5**, 23-29 (2005).
281. Mernier, G., Piacentini, N., Braschler, T., Demierre, N. & Renaud, P. Continuous-flow electrical lysis device with integrated control by dielectrophoretic cell sorting. *Lab Chip* **10**, 2077-2082 (2010).
282. Tsong, T.Y. Electroporation of cell membranes. *Biophys J* **60**, 297-306 (1991).
283. Weaver, J.C. Electroporation of cells and tissues. *Plasma Science, IEEE Transactions on* **28**, 24-33 (2000).
284. Weaver, J.C. Electroporation: a general phenomenon for manipulating cells and tissues. *Journal of cellular biochemistry* **51**, 426-435 (1993).
285. Weaver, J.C. & Chizmadzhev, Y.A. Theory of electroporation: A review. *Bioelectrochemistry and Bioenergetics* **41**, 135-160 (1996).
286. Weaver, J.C. & Mintzer, R.A. Decreased Bilayer Stability Due to Transmembrane Potentials. *Phys Lett A* **86**, 57-59 (1981).
287. Tarek, M. Membrane electroporation: A molecular dynamics simulation. *Biophysical Journal* **88**, 4045-4053 (2005).
288. Teissie, J., Golzio, M. & Rols, M.P. Mechanisms of cell membrane electropermeabilization: A minireview of our present (lack of ?) knowledge. *Bba-Gen Subjects* **1724**, 270-280 (2005).
289. Tekle, E., Astumian, R.D. & Chock, P.B. Selective and Asymmetric Molecular-Transport across Electroporated Cell-Membranes. *P Natl Acad Sci USA* **91**, 11512-11516 (1994).
290. Klenchin, V.A., Sukharev, S.I., Serov, S.M., Chernomordik, L.V. & Chizmadzhev, Y.A. DNA Electrophoresis Plays a Significant Role in Electrostimulated DNA Translocation. *Biol Membrany* **8**, 769-777 (1991).
291. Neumann, E., Kakorin, S. & Toensing, K. Fundamentals of electroporative delivery of drugs and genes. *Bioelectrochemistry and Bioenergetics* **48**, 3-16 (1999).

292. Valero, A. et al. Gene transfer and protein dynamics in stem cells using single cell electroporation in a microfluidic device. *Lab on a chip* **8**, 62-67 (2008).
293. Faurie, C., Golzio, M., Phez, E., Teissie, J. & Rols, M.P. Electric field-induced cell membrane permeabilization and gene transfer: Theory and experiments. *Eng Life Sci* **5**, 179-186 (2005).
294. Wang, H.Y. & Lu, C. Electroporation of mammalian cells in a microfluidic channel with geometric variation. *Analytical Chemistry* **78**, 5158-5164 (2006).
295. Diez-Silva, M., Dao, M., Han, J., Lim, C.T. & Suresh, S. Shape and Biomechanical Characteristics of Human Red Blood Cells in Health and Disease. *MRS bulletin / Materials Research Society* **35**, 382-388 (2010).
296. Kinoshita, K., Jr. & Tsong, T.Y. Voltage-induced pore formation and hemolysis of human erythrocytes. *Biochimica et biophysica acta* **471**, 227-242 (1977).
297. Abiror, I.G. et al. 246 - Electric breakdown of bilayer lipid membranes I. The main experimental facts and their qualitative discussion. *Bioelectrochemistry and Bioenergetics* **6**, 37-52 (1979).
298. Chernomordik, L.V. et al. The electrical breakdown of cell and lipid membranes: the similarity of phenomenologies. *Biochimica et biophysica acta* **902**, 360-373 (1987).
299. Serspersu, E.H., Kinoshita, K., Jr. & Tsong, T.Y. Reversible and irreversible modification of erythrocyte membrane permeability by electric field. *Biochimica et biophysica acta* **812**, 779-785 (1985).
300. Ward, M., Wu, J. & Chiu, J.F. Ultrasound-induced cell lysis and sonoporation enhanced by contrast agents. *The Journal of the Acoustical Society of America* **105**, 2951-2957 (1999).
301. Khanna, S., Amso, N.N., Paynter, S.J. & Coakley, W.T. Contrast agent bubble and erythrocyte behavior in a 1.5-MHz standing ultrasound wave. *Ultrasound in medicine & biology* **29**, 1463-1470 (2003).
302. Lee, Y.H. & Peng, C.A. Enhanced retroviral gene delivery in ultrasonic standing wave fields. *Gene therapy* **12**, 625-633 (2005).
303. Lindström, S. & Andersson-Svahn, H. Overview of single-cell analyses: microdevices and applications. *Lab Chip* **10**, 3363-3372 (2010).
304. Ryan, D., Ren, K. & Wu, H. Single-cell assays. *Biomicrofluidics* **5**, 21501 (2011).
305. Zong, C., Lu, S., Chapman, A.R. & Xie, X.S. Genome-wide detection of single-nucleotide and copy-number variations of a single human cell. *Science* **338**, 1622-1626 (2012).
306. Flatz, L. et al. Single-cell gene-expression profiling reveals qualitatively distinct CD8 T cells elicited by different gene-based vaccines. *Proc Natl Acad Sci U S A* **108**, 5724-5729 (2011).
307. Amantonico, A., Urban, P.L. & Zenobi, R. Analytical techniques for single-cell metabolomics: state of the art and trends. *Anal Bioanal Chem* **398**, 2493-2504 (2010).
308. Lin, Z. & Cai, Z. Cell lysis methods for high-throughput screening or miniaturized assays. *Biotechnology journal* **4**, 210-215 (2009).
309. Di Carlo, D., Ionescu-Zanetti, C., Zhang, Y., Hung, P. & Lee, L.P. On-chip cell lysis by local hydroxide generation. *Lab Chip* **5**, 171-178 (2005).
310. Church, C., Zhu, J., Huang, G., Tzeng, T.R. & Xuan, X. Integrated electrical concentration and lysis of cells in a microfluidic chip. *Biomicrofluidics* **4**, 44101 (2010).
311. Han, F. et al. Fast electrical lysis of cells for capillary electrophoresis. *Anal Chem* **75**, 3688-3696 (2003).
312. Kemmerling, S. et al. Single-cell lysis for visual analysis by electron microscopy. *Journal of structural biology* **183**, 467-473 (2013).
313. Nashimoto, Y. et al. Measurement of gene expression from single adherent cells and spheroids collected using fast electrical lysis. *Anal Chem* **79**, 6823-6830 (2007).
314. Brown, R.B. & Audet, J. Current techniques for single-cell lysis. *Journal of the Royal Society, Interface / the Royal Society* **5 Suppl 2**, S131-138 (2008).

315. Nan, L., Jiang, Z. & Wei, X. Emerging microfluidic devices for cell lysis: a review. *Lab Chip* **14**, 1060-1073 (2014).
316. Nevill, J.T., Cooper, R., Dueck, M., Breslauer, D.N. & Lee, L.P. Integrated microfluidic cell culture and lysis on a chip. *Lab Chip* **7**, 1689-1695 (2007).
317. Giaever, I. & Keese, C.R. Monitoring fibroblast behavior in tissue culture with an applied electric field. *Proc Natl Acad Sci U S A* **81**, 3761-3764 (1984).
318. Hong, J., Kandasamy, K., Marimuthu, M., Choi, C.S. & Kim, S. Electrical cell-substrate impedance sensing as a non-invasive tool for cancer cell study. *The Analyst* **136**, 237-245 (2011).
319. Trommler, A., Gingell, D. & Wolf, H. Red blood cells experience electrostatic repulsion but make molecular adhesions with glass. *Biophys J* **48**, 835-841 (1985).
320. Seidl, J., Knuechel, R. & Kunz-Schughart, L.A. Evaluation of membrane physiology following fluorescence activated or magnetic cell separation. *Cytometry* **36**, 102-111 (1999).
321. Calliada, F., Campani, R., Bottinelli, O., Bozzini, A. & Sommaruga, M.G. Ultrasound contrast agents: basic principles. *European journal of radiology* **27 Suppl 2**, S157-160 (1998).
322. Ibsen, S., Schutt, C.E. & Esener, S. Microbubble-mediated ultrasound therapy: a review of its potential in cancer treatment. *Drug design, development and therapy* **7**, 375-388 (2013).
323. Dayton, P.A. et al. Optical and acoustical dynamics of microbubble contrast agents inside neutrophils. *Biophys J* **80**, 1547-1556 (2001).
324. Collis, J. et al. Cavitation microstreaming and stress fields created by microbubbles. *Ultrasonics* **50**, 273-279 (2010).
325. Bouakaz, A., Versluis, M. & de Jong, N. High-speed optical observations of contrast agent destruction. *Ultrasound in medicine & biology* **31**, 391-399 (2005).
326. Miller, M.W., Miller, D.L. & Brayman, A.A. A review of in vitro bioeffects of inertial ultrasonic cavitation from a mechanistic perspective. *Ultrasound in medicine & biology* **22**, 1131-1154 (1996).
327. Koch, S., Pohl, P., Cobet, U. & Rainov, N.G. Ultrasound enhancement of liposome-mediated cell transfection is caused by cavitation effects. *Ultrasound in medicine & biology* **26**, 897-903 (2000).
328. Zhao, Y.Z. et al. Phospholipids-based microbubbles sonoporation pore size and reseal of cell membrane cultured in vitro. *Journal of drug targeting* **16**, 18-25 (2008).
329. Christiansen, J.P., French, B.A., Klibanov, A.L., Kaul, S. & Lindner, J.R. Targeted tissue transfection with ultrasound destruction of plasmid-bearing cationic microbubbles. *Ultrasound in medicine & biology* **29**, 1759-1767 (2003).
330. Schlachetzki, F. et al. Observation on the integrity of the blood-brain barrier after microbubble destruction by diagnostic transcranial color-coded sonography. *Journal of ultrasound in medicine : official journal of the American Institute of Ultrasound in Medicine* **21**, 419-429 (2002).
331. Kheiriloom, A. et al. Acoustically-active microbubbles conjugated to liposomes: characterization of a proposed drug delivery vehicle. *Journal of controlled release : official journal of the Controlled Release Society* **118**, 275-284 (2007).
332. Huang, S.L. Liposomes in ultrasonic drug and gene delivery. *Advanced drug delivery reviews* **60**, 1167-1176 (2008).
333. Porter, T.R., LeVeen, R.F., Fox, R., Kricsfeld, A. & Xie, F. Thrombolytic enhancement with perfluorocarbon-exposed sonicated dextrose albumin microbubbles. *American heart journal* **132**, 964-968 (1996).
334. Molina, C.A. et al. Microbubble administration accelerates clot lysis during continuous 2-MHz ultrasound monitoring in stroke patients treated with intravenous tissue plasminogen activator. *Stroke; a journal of cerebral circulation* **37**, 425-429 (2006).

335. van der Meer, S.M. et al. Microbubble spectroscopy of ultrasound contrast agents. *The Journal of the Acoustical Society of America* **121**, 648-656 (2007).
336. Tang, M.X. & Eckersley, R.J. Frequency and pressure dependent attenuation and scattering by microbubbles. *Ultrasound in medicine & biology* **33**, 164-168 (2007).
337. Emmer, M. et al. Pressure-dependent attenuation and scattering of phospholipid-coated microbubbles at low acoustic pressures. *Ultrasound in medicine & biology* **35**, 102-111 (2009).
338. Kimmel, E., Krasovitski, B., Hoogi, A., Razansky, D. & Adam, D. Subharmonic response of encapsulated microbubbles: conditions for existence and amplification. *Ultrasound in medicine & biology* **33**, 1767-1776 (2007).
339. de Jong, N., Emmer, M., van Wamel, A. & Versluis, M. Ultrasonic characterization of ultrasound contrast agents. *Medical & biological engineering & computing* **47**, 861-873 (2009).
340. Sijl, J. et al. Combined optical and acoustical detection of single microbubble dynamics. *The Journal of the Acoustical Society of America* **130**, 3271-3281 (2011).
341. Thomas, D.H. et al. Single microbubble response using pulse sequences: initial results. *Ultrasound in medicine & biology* **35**, 112-119 (2009).
342. Morgan, K.E. et al. Experimental and theoretical evaluation of microbubble behavior: effect of transmitted phase and bubble size. *IEEE transactions on ultrasonics, ferroelectrics, and frequency control* **47**, 1494-1509 (2000).
343. Zhou, Y., Yang, K., Cui, J., Ye, J.Y. & Deng, C.X. Controlled permeation of cell membrane by single bubble acoustic cavitation. *Journal of Controlled Release* **157**, 103-111 (2012).
344. Sankin, G.N., Yuan, F. & Zhong, P. Pulsating tandem microbubble for localized and directional single-cell membrane poration. *Physical review letters* **105**, 078101 (2010).
345. Lim, K.Y. et al. Nonspherical laser-induced cavitation bubbles. *Physical review. E, Statistical, nonlinear, and soft matter physics* **81**, 016308 (2010).
346. Pawar, S.D., Murugavel, P. & Lal, D.M. Effect of relative humidity and sea level pressure on electrical conductivity of air over Indian Ocean. *J Geophys Res-Atmos* **114** (2009).
347. Shih, R. et al. Flow-focusing regimes for accelerated production of monodisperse drug-loadable microbubbles toward clinical-scale applications. *Lab Chip* **13**, 4816-4826 (2013).
348. van Liew, H.D. & Burkard, M.E. Behavior of bubbles of slowly permeating gas used for ultrasonic imaging contrast. *Investigative radiology* **30**, 315-321 (1995).
349. van der Meer, S.M. et al. Highly non-linear contrast agent oscillations: the compression-only behavior. *Ultrason*, 974-976 (2005).
350. Medwin, H. Counting Bubbles Acoustically - Review. *Ultrasonics* **15**, 7-13 (1977).
351. Dejong, N., Hoff, L., Skotland, T. & Bom, N. Absorption and Scatter of Encapsulated Gas Filled Microspheres - Theoretical Considerations and Some Measurements. *Ultrasonics* **30**, 95-103 (1992).
352. Schutt, C.E., Ibsen, S.D., Thrift, W. & Esener, S.C. The influence of distance between microbubbles on the fluid flow produced during ultrasound exposure. *The Journal of the Acoustical Society of America* **136**, 3422-3430 (2014).
353. Chomas, J.E., Dayton, P., Allen, J., Morgan, K. & Ferrara, K.W. Mechanisms of contrast agent destruction. *Ieee T Ultrason Ferr* **48**, 232-248 (2001).
354. Cha, Y.S. & Henry, R.E. Bubble-Growth during Decompression of a Liquid. *J Heat Trans-T Asme* **103**, 56-60 (1981).
355. Emmer, M., van Wamel, A., Goertz, D.E. & de Jong, N. The onset of microbubble vibration. *Ultrasound in medicine & biology* **33**, 941-949 (2007).
356. De Jong, N. et al. "Compression-only" behavior of phospholipid-coated contrast bubbles. *Ultrasound in Medicine and Biology* **33**, 653-656 (2007).

357. Lipp, M.M., Lee, K.Y.C., Takamoto, D.Y., Zasadzinski, J.A. & Waring, A.J. Coexistence of buckled and flat monolayers. *Physical review letters* **81**, 1650-1653 (1998).
358. Sijl, J. et al. "Compression-only" behavior: a second-order nonlinear response of ultrasound contrast agent microbubbles. *The Journal of the Acoustical Society of America* **129**, 1729-1739 (2011).
359. de Jong, N. et al. "Compression-only" behavior of phospholipid-coated contrast bubbles. *Ultrasound in medicine & biology* **33**, 653-656 (2007).
360. Marmottant, P. et al. A model for large amplitude oscillations of coated bubbles accounting for buckling and rupture. *Journal of the Acoustical Society of America* **118**, 3499-3505 (2005).
361. del Campo, A. & Greiner, C. SU-8: a photoresist for high-aspect-ratio and 3D submicron lithography. *Journal of Micromechanics and Microengineering* **17**, R81-R95 (2007).
362. Chung, C.K., Tsai, M.Q., Tsai, P.H. & Lee, C. Fabrication and characterization of amorphous Si films by PECVD for MEMS. *Journal of Micromechanics and Microengineering* **15**, 136-142 (2005).
363. Mason, M.G. et al. Characterization of treated indium-tin-oxide surfaces used in electroluminescent devices. *J Appl Phys* **86**, 1688-1692 (1999).